# *An Investigation into using Laser Micro Channelling to Assist Fibre Integration via Ultrasonic Consolidation*

***Simona Masurtschak***

Doctoral Thesis

Submitted in partial fulfilment of the requirements for the award of

Doctor of Philosophy

Loughborough University

December 2013

# Abstract

Ultrasonic Consolidation (UC) is a layer-by-layer metal-based additive manufacturing process. Bonding between two layers is accomplished by energy transmission in form of ultrasonic oscillations inducing localised plastic deformation. The benefit of localised plastic deformation and bonding below melting temperatures has been effectively used for fibre integration. Thus, UC presents a feasible alternative to other metal-manufacturing processes as well as an attractive method for novel engineering materials production such as smart structures.Yet, high volume fibre embedding has been shown to result in delamination of foils and greater porosity at the bonding interfaces due to insufficient plastic flow around the fibres. Furthermore, post-functionality of delicate fibre types was limited.

In this study a novel hybrid approach aiming to reduce the necessary plastic flow around fibres and high fibre volume embedding is presented. Laser-processed channels and melt manipulation to form shoulder-like structures at the channel edges were explored in terms of their aid for secure and accurate high volume Silicon Carbide (SiC) fibre integration using low amplitudes and contact pressures.

In the first part of the study, a fiber laser was used to investigate the feasibility of channel manufacturing and melt manipulation into UC samples by varying specific laser parameters. In the second part, high volumes of SiC fibres (up to 10.5 %) were embedded within the channels and ultrasonically processed. The influence of the channels, shoulders and high fibre volumes of was analysed in terms of positioning, possible damages and bond formation.

The investigations showed that channel and shoulder manufacturing is possible. Compelling evidence for accurate positioning of high fibre volumes with the aid of the channels was found. The intention to reduce plastic flow during bond formation for high volume fibre embedding has been shown to be difficult due to the shoulder material modification during laser processing.

# Acknowledgement

I would like to thank my supervisor, Russell Harris, for his advice and guidance. There are few people who are able to think in such a concise way. I would also like to thank my second supervisor, Ross Friel, for all the genuine support and help. I wouldn't have been this far without him.

Many thanks to Jonathan Lawrence, Pete Wileman, Andy Sandaver, Dave Britton, Mark Capers, Shaun Fowler and especially Dr. Arnold Gillner and Joachim Ryll (Fraunhofer ILT). Good knowledge is hard to find.

I would also like to thank my family. I can only imagine how difficult it must have been dealing with me. Every one of you is precious and deserves a medal. I have to especially thank my Dad for being the most amazing person. I am happy if I have inherited a quarter of his strength.

*„Kopf hoch, auch wenn der Hals dreckig ist."*

I also have to thank Seidemann, Thomas and Volker. It is hard to find friends that will stay for life. I found the best ones.

*"No sense of doubt or what you could achieve"*

-Taken from the song "Papillon" by Editors-

# Table of Contents

# Publications

## Journal Papers

1. *Fiber Laser Induced Surface Modification/Manipulation of an Ultrasonically Consolidated Metal Matrix*. Masurtschak, S., Friel, R.J., Gillner, A., Ryll, J., Harris, R.A., 2012. Journal of Materials Processing Technology, 213(10), pp.1792-1800.

2. *Laser-Machined Micro-Channel Effect on Microstructure and Oxide Formation of Ultrasonically Processed Aluminium*. Masurtschak, S., Friel, R.J., Gillner, A., Ryll, J., Harris, R.A., 2013. ASME Journal of Engineering Materials and Technology. Accepted for Publication.

3. *On the assistance of laser processed channels in metal matrices for secure fibre placement and positioning during ultrasonic consolidation*. Masurtschak, S., Friel, R.J., Harris, R.A., 2013. Submitted to Proceedings of the Institution of Mechanical Engineers, Part B: Journal of Engineering Manufacture.

4. *Influence of Laser-Processed Structures and High Volume Fibre Integration on Bond Quality for Ultrasonic Consolidation*. Masurtschak, S., Friel, R.J., Harris, R.A. (final preparation).

5. *Hardness Investigation of a Laser-processed Aluminium Alloy for Use in Smart Material Structures*. Masurtschak, S., Friel, R.J., Harris, R.A. (final preparation).

## Conference Papers

1. *Smart Material Structures by Ultrasonic Consolidation*. Fitzgerald, C., Masurtschak, S., Edmonds, H. Ultrasonic Additive Manufacturing Technology Symposium, Ohio, Columbus, USA, 19.-21. October 2009.

2. *Enabling dissimilar fibre embedding and explicit fibre layout in ultrasonic consolidation*. Friel, R.J., Masurtschak, S., Harris, R.A. 21st International Conference on Adaptive Structures and Technologies, ICAST 2010, Pennsylvania, USA, 4.-6. October 2010.
3. *Enabling techniques for secure fibre positioning in ultrasonic consolidation for the production of smart material structures*. Masurtschak, S., Harris, R.A. In: Tomizuka, M., ed., Sensors and Smart Structures Technologies for Civil, Mechanical, and Aerospace Systems, SPIE Proceedings Vol. 7981, 11.-15. March 2012, San Diego, California, USA.

# Collaborations

Within the scope of this thesis, Simona Masurtschak collaborated with the Fraunhofer Institute for Laser Technology (ILT) in Aachen, Germany. Work was carried out for two weeks (December 2011) on the Trumpf TruFiber 300 W laser at the ILT. The studies were funded by the EPSRC/IMCRC through grant number EPSRC IMCRC 275.

In October 2009, Simona Masurtschak spend a week at Solidica Inc. in Ann Arbour, USA to learn about the latest trends in UC research and how to operate the UC Formation machine. During this visit, she attended the 2nd Ultrasonic Additive Manufacturing Technology Symposium (20.-21. October 2009), at the Edison Welding Institute in Columbus, Ohio.

# Nomenclature

| | |
|---|---|
| A | Area of contact for hardness measurement |
| $A_f$ | Area of focused spot |
| AC | Alternating Current |
| Al | Aluminium |
| AlN | Aluminium Nitride |
| α | Thermal diffusivity |
| AM | Additive Manufacturing |
| $Al_2O_3$ | Aluminium Oxide |
| Au | Gold |
| BPP | Beam Parameter Product |
| BZ | Base Zone |
| C | Carbon |
| Cc | Contact Compliance |
| CAD | Computer Aided Design |
| CDRX | Continuous Dynamic Recrystallisation |
| CNC | Computer Numerical Controlled |
| $CO_2$ | Carbon Dioxide |
| Cu | Copper |
| CW | Continuous Wave |
| $D_0$ | Input radius at the lens |
| $d_f$ | Focused spot size |
| DPSS | Diode-Pumped Solid State Laser |
| DRX | Dynamic Recrystallisation |
| EDX | Energy-Dispersive X-ray Spectroscopy |
| $E_i$ | Young's modulus (Indenter) |
| $E_s$ | Young's modulus (Sample) |
| $E_r$ | Reduced Modulus |
| f | Focal Length |
| FBG | Fibre Bragg Gratings |

| | |
|---|---|
| Fe | Iron |
| FZ | Fusion Zone |
| H | Hardness |
| HAZ | Heat-Affected Zone |
| $h_f$ | Final plastic depth |
| $h_c$ | Contact depth |
| $h_{max}$ | Maximum indentation depth |
| HeNe | Helium-Neon |
| HPD | High Power Diode |
| I | Power Density |
| λ | Lambda (Thermal conductivity) |
| λ | Lambda (Wavelength) |
| $L_B$ | Physically Bonded Area |
| LMA | Large Area Mode |
| $L_T$ | Total Interface Length |
| LWD | Linear Weld Density |
| $M^2$ | Beam Quality Factor |
| MEMS | Microelectromechanical systems |
| Mg | Magnesium |
| MMC | Metal Matrix Composite |
| Mn | Manganese |
| Nd:YAG | Neodymium-Doped Yttrium Aluminum Garnet |
| Ni | Nickel |
| NA | Numerical Aperture |
| O | Oxygen |
| π | Pi |
| PCF | Photonic Crystal Fibre |
| $P_f$ | Power input from laser |
| $P_{max}$ | Peak load for nanoindentation |
| PMZ | Partially Melted Zone |
| R | Reflectivity |
| RM | Rapid Manufacturing |

| | |
|---|---|
| $S_a$ | Areal Surface Roughness |
| SEM | Scanning Electron Microscopy |
| SFF | Solid Freeform Fabrication |
| Si | Silicon |
| SiC | Silicon Carbide |
| SMA | Shape Memory Alloy |
| TEM | Transverse Electromagnetic Modes |
| θ | Beam Divergence Angle |
| Ti | Titanium |
| UC | Ultrasonic Consolidation |
| UMW | Ultrasonic Metal Welding |
| USW | Ultrasonic Welding |
| VHP-UAM | Very High Power-Ultrasonic Additive Manufacturing |
| $V_i$ | Poisson's ratio (Indenter) |
| $V_s$ | Poisson's ratio (Sample) |
| Zn | Zinc |

# List of Figures

# List of Tables

# Chapter 1.
# Introduction

## 1.1 Subject Domain

Ultrasonic Consolidation (UC) is a metal-based additive/subtractive hybrid manufacturing technology from which complex three-dimensional structures can be fabricated (White, 2003b). Sequential layers of metal foils are joined by application of pressure and ultrasonic oscillations. A computer numerical controlled (CNC) milling head trims the 3D part after a (variable) number of layers. As opposed to other additive manufacturing (AM) processes, geometric accuracy and surface finish depend on the CNC milling which overcomes layer-thickness accuracy and stair stepping effects as observed for other AM processes (Gibson et al., 2010).

Bonding is accomplished by energy transmission from the sonotrode to the interface of the two metal foils via mechanical oscillation. The combination of interfacial shear forces and contact pressure results in elastic-plastic deformation of the metal foils (Daniels, 1965; Yang et al., 2009).

Two key aspects have been identified for UC: Bonding is achieved at temperatures below the melting temperatures of the consolidated foils (typically ≤ 50 % of melt temperature) (Kong et al., 2004b) and highly localised plastic flow occurs during ultrasonic excitation (Langenecker, 1966). These aspects can be used to allow components which are prone to damage or sensitive to high temperatures to be embedded via UC (Cheng et al., 2007). Research on embedding structural elements demonstrated the integration of optical fibres (Kong and Soar, 2005a; Mou at al., 2009), shape memory alloys (SMA) (Kong and Soar, 2005b; Hahnlen et al., 2009; Friel and Harris, 2010) and reinforcing

SiC fibres (Yang et al., 2007; Li and Soar, 2009a). UC is also capable of bonding dissimilar materials (Janaki Ram et al., 2007a) and materials which are metallurgically incompatible in fusion processes (Matsuoka, 1994).

UC is still a relatively immature process which presents several areas for further understanding and improvement such as: bonding quality, interfacial bonding phenomena, plastic flow behaviour, further embedding of objects and use of UC in industrial applications.

## 1.2 Gap in the Knowledge

Metal matrix composite (MMC) fabrication has been employed to create smart material structures (Schaller, 2003). However, the delicacy of embedded components and post-fabrication functionality has demonstrated smart material fabrication limitations primarily due to the occurrence of high pressures, high temperatures and interfacial reactions (Kong et al., 2004b; Kong and Soar, 2005b, Siggard et al., 2006).

UC presents an attractive alternative for the production of smart material structures. It combines high dimensional accuracy, solid-state welding and the ability to fabricate complex 3D structures (Friel and Harris, 2013). Fibre integration has been successfully demonstrated for low volume fractions of SiC, SMA and optical fibres (Kong and Soar, 2005a; Li and Soar, 2009a; Hahnlen and Dapino, 2010). For efficient MMC fabrication, high volume fractions of fibres would be needed for efficient controlling, sensing and actuating. Higher volume fibre integration can be achieved by increasing the amplitude of the sonotrode oscillation which enables higher plastic flow and void closure around the fibres (Kong, 2005; Friel, 2011). However, it has been shown that some delicate materials may be damaged by high amplitudes and contact pressures (Cheng et al., 2007). To efficiently integrate high fibre volumes yet avoiding high amplitudes which could harm the integrity and post-functionality of the fibres, a method that allows secure and accurate high fibre volume embedding while inducing sufficient plastic flow with low amplitudes must be realised.

## 1.3 Theoretical Approach of the Dissertation

To enable high volumes of fibres to be embedded within UC foils, an approach combining laser micro processing and UC was proposed. A laser was used to process channels into UC samples in which fibres were to be placed. The approach is displayed schematically in Figure 1.1.

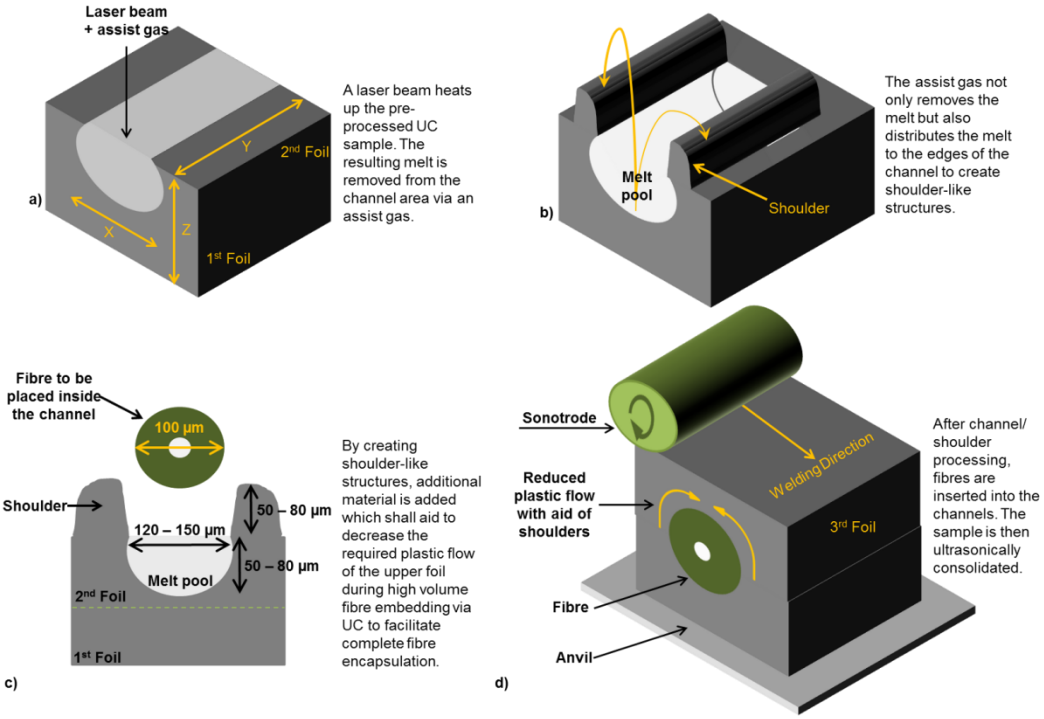


**Figure 1.1 Theoretical approach of using laser processed channels and UC for fibre embedding**

A laser was employed to melt a channel into the previously UC processed metal matrix (a). The molten material was removed from the channel via the assist gas pressure and displaced from the melt pool and distributed to the sides of the channel boundary in the form of shoulders (b). By creating the shoulders, additional material was added at the edges of the channel which was theorised to aid the fibre placement and reduce the level of plastic flow required for full encapsulation of the fibre into the matrix material during UC. The channel width and depth as well as the shoulder height were to be controlled by laser/material interaction. By selecting a fibre diameter (100 µm) beforehand, a guideline for the intended channel and shoulder geometries was given (c). The channel was

supposed to be slightly wider than the fibre that would be embedded to comfortably accommodate the fibre. The shoulder height was supposed to be the depth of the channel in order to match the displaced molten material as well as to enable sufficient aid for plastic flow reduction of the upper foil. Fibres will be placed inside the laser-processed channels and a new foil layer will be bonded on top via UC. The new foil layer will experience a decrease in plastic flow due to the aid of the additional material added by creating the shoulders (d).

## 1.4 Context of the Subject

### 1.4.1 Smart Structures

Smart structures or smart composites are materials which have the ability to adapt to their environment (internally or externally) by monitoring and altering their structure (Spillman JR et al., 1996; Wei et al., 1998; Galea and Baker, 2001). For a structure to adapt to the surroundings, a sensor or an actuator or both combined must be embedded so that either closed loop feedback or immediate response to external stimuli is possible (Chung, 1998; Balta et al., 2005). There are many types of sensors and actuators such as piezoelectric materials, magnetostrictive materials, microelectromechanical (MEMS) systems, SMA or optical fibres which can be embedded (Tzou et al., 2004).

The application of smart structures offers a variety of advantages: new product capabilities, structural health monitoring, self-repair, noise and vibration control, energy harvesting and greater safety by damage detection (Flatau and Chong, 2002; Hurlebaus and Gaul, 2006). For this reason, the application of smart structures can be found in many areas such as civil engineering, automobile and aeronautical engineering as well as medical engineering (Boller, 2000; Wu and Schetky, 2000; Hartl and Lagoudas, 2007; Sohn, 2007). A schematic drawing of smart structure applications for civil engineering such as the development of bridges is displayed in Figure 1.2. The manufacturing of metallic smart structures can be carried out by MMC fabrication techniques. The

fabrication of MMC's can be grouped into three different processes: diffusion, solid-state and liquid processes (Kainer, 2006). However, for the fabrication of MMC's there are the following issues: high fabrication costs, fabrication-related problems such as component distribution and multiple manufacturing steps and material interactions such as poor wettability and mixing (Clyne and Withers, 1993).

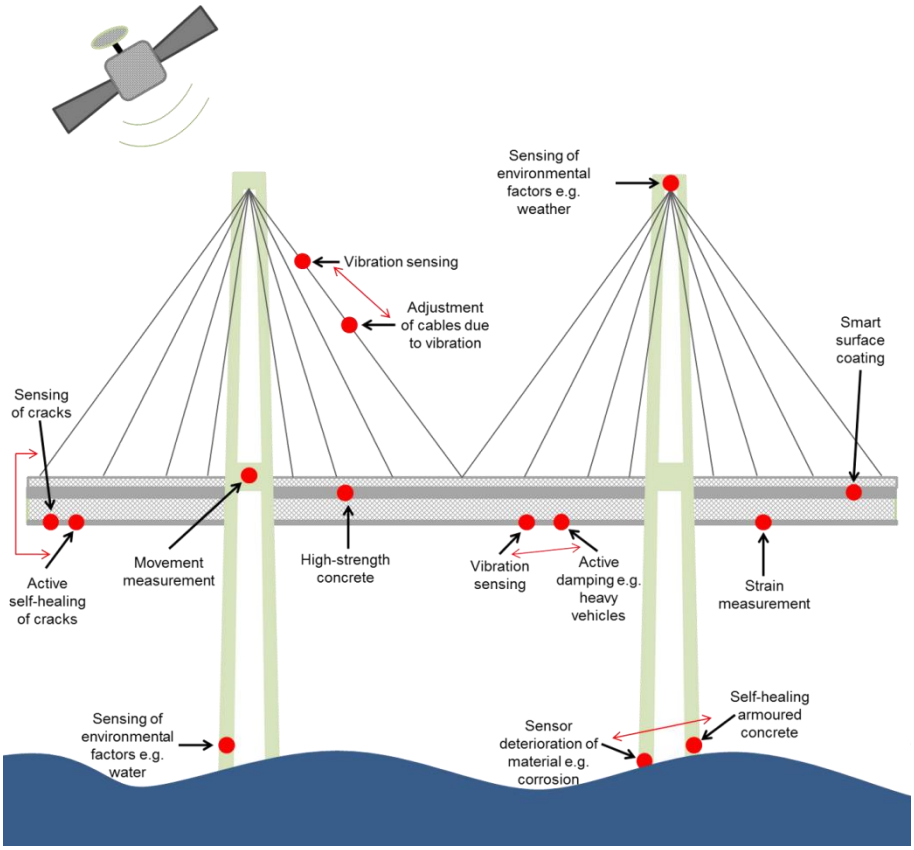


**Figure 1.2 Smart structure applications for bridges**

High temperatures, high pressures and thermal imbalance between the reinforcement and matrix material may cause residual stresses, reinforcement fractures or damage (Nakamura and Suresh, 1993; Wan et al., 2000). Two examples are: firstly, optical fibres may exhibit failure such as cracking due to high pressures and temperatures (Li and Prinz, 2003) and secondly, during SMA integration the transformation effect may be lost due to high temperatures (Recarte et al., 2004). Additionally, during high temperature processing, chemical reactions at the interfaces between the reinforcements and matrix

have been observed which can degrade mechanical properties of the MMC or harm the integrity of reinforcements (Lindroos and Talvitie, 1995; Hamada et al., 1998; Yu-Qing, 1998).

### 1.4.2 Laser Micro-Processing

Laser technology has been a growing industry in material processing and the global market for laser systems has reached a record high of €7.2 billion in the year 2011 (Mayer, 2012). The development of ultrashort pulses in the femtosecond regime in 1987 attracted new applications for laser processing (Hecht, 2010). New laser sources such as high repetition rate short pulse lasers with ps- and fs-pulse duration, fiber, excimer and diode pumped solid-state (DPSS) lasers have enabled processing technologies in the micrometre and nanometre range (Paschotta, 2007, Chong et al., 2010).

Laser micro processing can be found in many industries nowadays such as automotive, aerospace and electronic and electrical industry (Meijer, 2004; Dubey and Yadava, 2008). Applications of laser micro processing can be found in printed circuit boards, flat panel displays, solar cells, micro joining, micro tooling as well as basic micro cutting, drilling and welding operations (Gower, 2000; Halbwax et al., 2008; Tamaoki et al. 2010). The reason for an increased application in micro machining is the low heat/energy input preventing material property change and elimination of mechanically induced material damage or distortion as well as tool wear, flexibility and high selectivity (Gillner et al., 2005).

Fiber lasers appear to be an increasingly promising tool for micro processing due to excellent beam qualities, nearly diffraction-limited beams and high brightness which allow the focusing of the laser to small spot sizes (Tünnermann et al., 2005; Limpert et al., 2007; Beyer et al., 2012). Additionally, fiber lasers offer compactness, high conversion efficiency, long lifetime and low optical maintenance. Current fiber laser systems can reach up to 4 kW output power (Kliner et al., 2011). The fiber laser has been shown to be a reliable tool for micro materials processing such as drilling, cutting or milling (Kleine et al.,

2002; Hoult et al., 2006; Franke et al., 2007; Poprawe et al., 2010; Gabzdyl and Brodsky, 2010).

Utilisation of the fiber laser due to the inherent advantages of the fibres for channel manufacturing appears to be a promising tool to further the use of UC as a manufacturing technique for solid state MMC and eventually for novel hybrid processing of smart material structures.

## 1.5 Research Goals

In order to elaborate on current gaps in the knowledge, the following research goals were defined:

- → Experimental investigation of channel fabrication feasibility via the use of laser technologies with accompanying analytical investigation of the heat-affected zone (HAZ) after laser channelling.
- → Experimental investigation of melt manipulation and shoulder fabrication via the use of a laser with accompanying analytical investigation of the shoulder geometry and composition.
- → The fabrication of higher volumes of channels/shoulders for fibre integration.
- → Integration of fibres and investigation of the accuracy of positioning of fibres. The assessment of the fibre integrity after UC.
- → Investigation of the proposed shoulder features to aid and enhance the bond formation in samples.

## 1.6 Research Approach and Structure of Investigation

The research approach, and hence the structure of the dissertation, was divided into four stages which are summarised here and displayed in Figure 1.3. The first stage was focused on the understanding of the fundamental background and metallurgical impact of UC combines with laser processing on 3003 H18

aluminium (Al) alloy. The first stage was concluded with the development of the hypothesis which served as a driver for the following experimentation.

For the second stage the feasibility of channel and shoulder formation via laser processing onto a UC sample surface was investigated. The second stage of research was presented in chapters four and five:

*(Stage 2 – Chapter 4)*

→ Initial research work on an SPI 200 W redPower fiber laser was carried out by varying power, gas pressure, traverse speed and gas type. The different impacts on the material were classified. Influences of the different variables were analysed to identify the potential of a fiber laser for channel and shoulder creation. The resultant microstructure was analysed in terms of influence of the variables on the HAZ formation.

*(Stage 2 – Chapter 5)*

→ The results of chapter four indicated that manufacturing of the desired channel geometry was possible. However, the shoulder formation and hence the distribution of the melt pool was difficult to control. In order to fully investigate the shoulder influence on the plastic flow during UC, a different approach to produce channels/shoulders was developed. The work was carried out on a Trumpf TruFiber 300 W fiber laser during a research exchange visit to Fraunhofer ILT, Aachen, Germany. Distinct channel/shoulder geometries were produced by varying power, traverse speed, gas pressure and multiple laser passes. As multiple passes resulted in a different heat input into the material, the resultant microstructure was analysed in terms of influence of the variables on HAZ formation.

The third stage served as a transition between stage 2 and stage 4 as the laser processing results were used in order to manufacture samples which could be further investigated in terms of fibre embedding and UC influence.

*(Stage 3 – Chapter 6)*

→ A strategy for production of high quantities of channels on a UC sample for two orientations was developed. To compare the influence of embedding higher quantities of fibres on bonding, production of samples containing 8 and 24 channels was carried out. The manufactured samples were then analysed to investigate the possibility of stable and consistent channel production.

The fourth stage covered the fibre placement into the laser processed channels and embedment via UC.

*(Stage 4 – Chapter 7)*

→ SiC fibres were inserted into the pre-manufactured channels and consolidated via UC while keeping the amplitude, pressure and speed constant. The influence of the channels and fibres on bond formation (macroscopic) was studied and analysed. Analysis of precise positioning of the fibres within the channels/shoulders, as well as their appearance post-UC for different embedding directions was carried out.

*(Stage 4 – Chapter 8)*

→ Bond formation at the interfaces was studied by analysing features and changes introduced by laser processing – in particular the role of the assist gas on oxide formation. The role of plastic deformation and the aid of the shoulder to enhance plastic flow around the fibres during UC were investigated for samples with and without fibres. Possible changes in the microstructure by laser processing were studied via hardness testing.

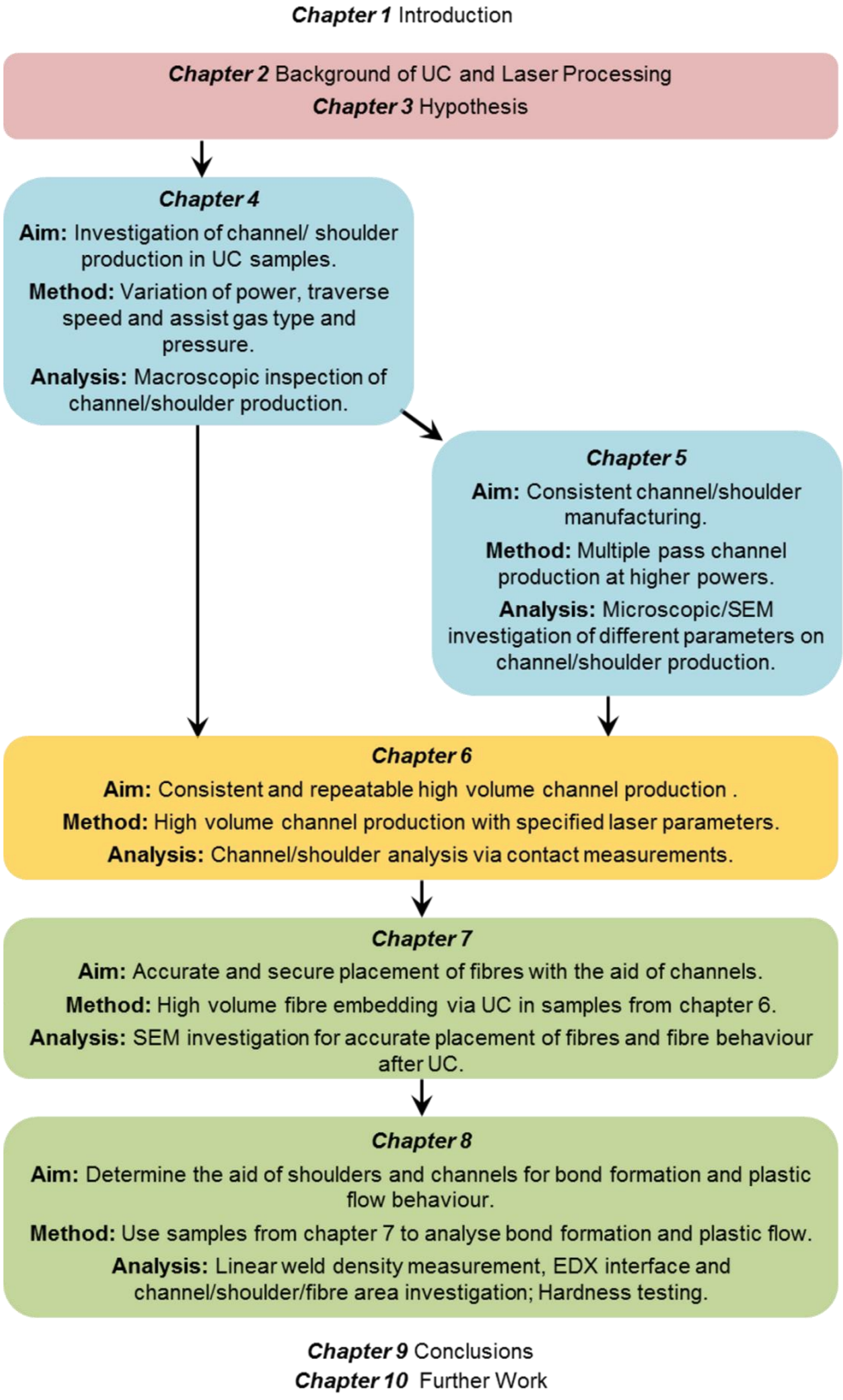


**Figure 1.3 Structure of dissertation**

# Chapter 2.
# Background

## 2.1 Ultrasonic Consolidation

### 2.1.1 Introduction

Additive manufacturing (AM), also known as rapid manufacturing (RM) or solid freeform fabrication (SFF) has its roots in a number of processes developed in the late 1980s (Levy et al., 2003). It has since been classified as a revolutionary set of processes for product development and manufacturing (Kruth, 1998; Levy, 2010). AM technologies are based on the following principle: a 3D CAD model is generated which is sliced into layers and converted to an STL file which an AM machine can use to directly manufacture the part – layer by layer.

Many AM processes have been developed over the past 20 years which can be classified into three categories: liquid-based, powder-based and solid-based (Hopkinson et al., 2006). Examples of AM processes are Stereolithography, Selective Laser Sintering, 3D-Printing and Fused Deposition Modelling. AM offers many benefits such as manufacturing of complex geometries and customised products and fast production of these. However, in terms of metal additive manufacturing, the vast majority of the processes are based on thermal fusion or melting of the materials (which could alter the microstructures or make delicate component embedding difficult (Kong, 2005).

Ultrasonic metal welding (USW) has been commercially developed since the 1950s (Neppiras, 1965). USW is based on the joining of metal materials by

applying ultrasonic oscillations and pressure and is classified as a solid-state joining process (Kearns, 1980).

### 2.1.2 Basic Concepts of Ultrasonic Consolidation

The process of Ultrasonic Consolidation (UC) combines ultrasonic metal welding and computer numerical controlled (CNC) milling techniques - thus allowing part manufacturing by additive and subtractive techniques (White, 2003b). The process was invented and patented by Dr. Dawn White in 2000 (White, 2003a) and is commercially provided by Fabrisonic LLC, Columbus, USA.

An overview of the three-dimensional (3D) part manufacturing steps is displayed in Figure 2.1.

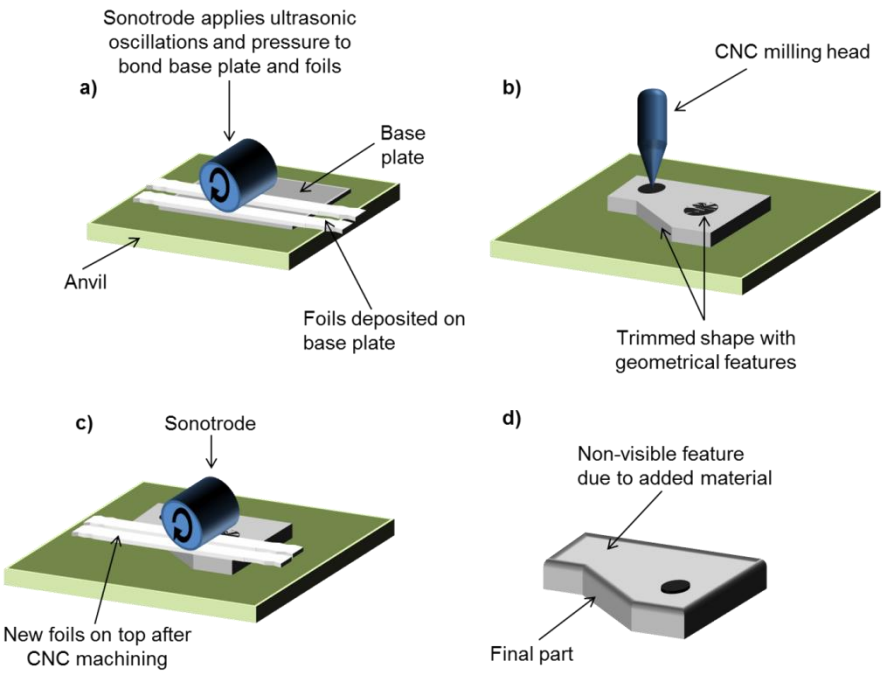


**Figure 2.1 Schematic overview of the single process steps in UC to produce a 3D part**

On the anvil (see Figure 2.1 a)), a base plate is placed. The base plate is used to prevent adhesion between the foil and the anvil. Manufacturing is performed by supplying metal foil layers from a foil-feed mechanism. The strips of metal foil are then ultrasonically consolidated by applying ultrasonic oscillations and

pressure via a cylindrical sonotrode which transmits continuous oscillations to the metal foils (de Vries, 2004). This is done for a sequence of foils. A three-axis CNC milling head is used to machine the foils to the required shape and shape 3D contour (Figure 2.1 b)). After the machining a new set of foils is consolidated (Figure 2.1 c)). The required 3D solid part is produced from a computer-aided (CAD) model by sequential consolidation of foils and CNC machining (Figure 2.1 d)).

Bonding is achieved by the combination of ultrasonic oscillations and contact pressure. The combination of oscillating shear forces and contact pressure forces enables the formation of dynamic frictional stresses at the interfaces of the foils surfaces (Daniels, 1965; O'Brien, 1991), which is detailed in Figure 2.2. The stresses produce metallurgical bonds by disruption and displacement of surface contaminants and plastic metal flow (White, 2003b).

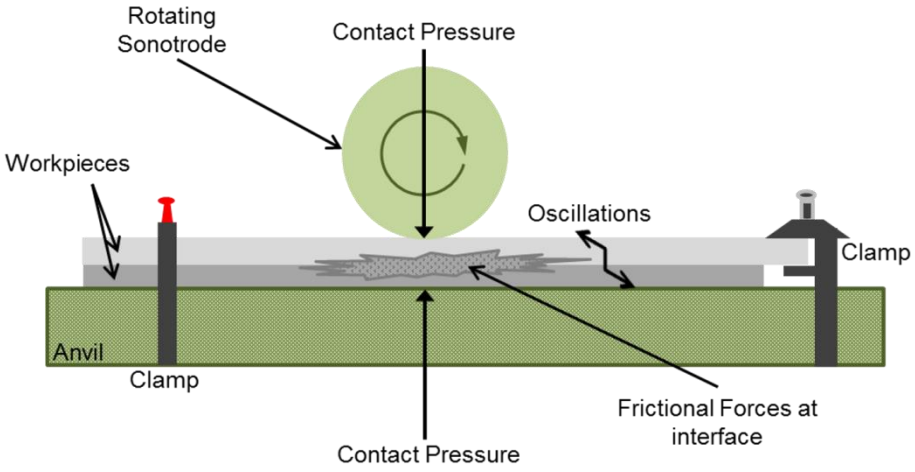


**Figure 2.2 Interaction of process variables acting upon workpieces and resulting forces at interface (Hahnlen et al., 2009)**

The crux of UC and also the major difference to other additive manufacturing processes is that it produces bonds with highly localised temperatures generally below 50% of the melting point of the joined metals (Jones and Powers, 1956; Okada et al., 1963; de Vries, 2004; Johnson et al., 2011). Other benefits for UC include:

- → the ability of welding a variety of materials – including those which are difficult to thermally weld
- → the ability to produce complex 3D structures and to integrate complex internal features
- → high dimensional accuracy due to CNC milling without further finishing processes
- → component embedding such as fibres, SMA, fibre bragg gratings (FBG)
- → low melting temperatures and low pressures but highly localised plastic flow lay the foundations for secure component embedment

The oscillations are applied to the workpieces via four components which transform mains electrical energy into high frequency mechanical energy. The single components of a UC machine (power supply, transducer, booster and sonotrode) are demonstrated in Figure 2.3.

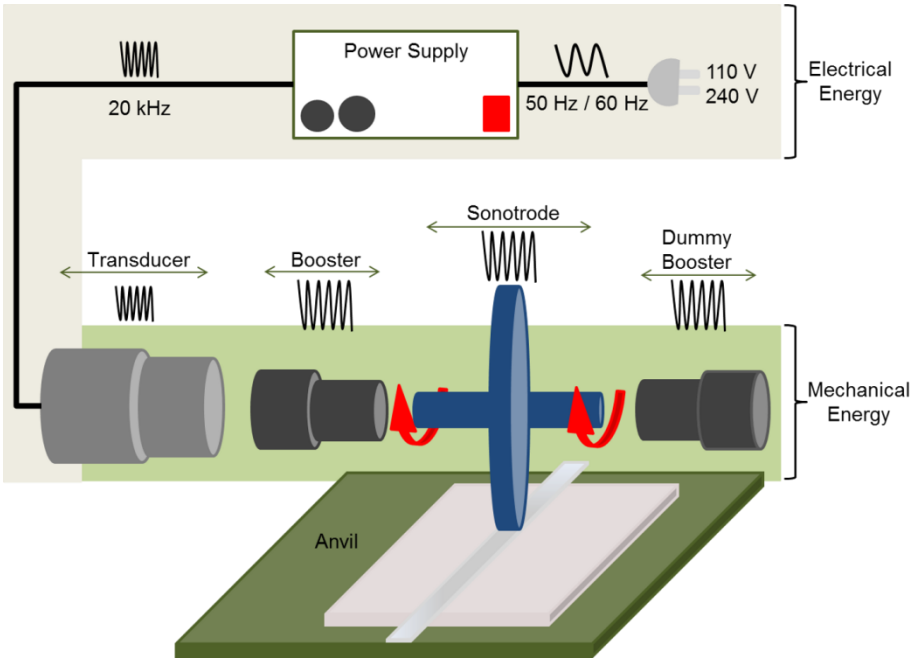


**Figure 2.3 Transformation of electrical in mechanical energy via single components of UC**

***The power supply*** converts alternating current (AC) of 100 V or 240 V at frequencies of 50 Hz or 60 Hz into high frequency electrical energy of 20 kHz with the possibility to increase the frequencies to 60 kHz or more (Hulst, 1972;

Shoh, 1975). The high frequency is then coupled into the transducer which is part of the ultrasonic stack together with booster and sonotrode. The power supply additionally allows the amplitude of vibration to be adjusted (Pohlmann and Lehfeldt, 1966). In general, an increase in amplitude increases the ultrasonic energy delivered to the workpiece which aids the welding quality by increasing the plastic flow (Yang, 2008).

***The transducer*** converts the high frequency electrical energy into mechanical vibrations at the same frequency. It consists of piezoelectric elements, which after stimulation by power input, will exhibit the piezoelectric effect thus periodically changing dimensions in transversal or longitudinal direction in accord with the oscillations (Iula et al., 2006). The efficiency of converting electric energy into mechanical vibrations by piezoceramics is above 90% (Friel, 2011).

***The booster*** or displacement amplifier (amplifying the displacement of the piezoceramics) is used to either decrease or increase the amplitude generated by the transducer. The shape of the booster defines the reduction or increase of the amplitude. For UC conical shapes are used with a larger transducer input and smaller sonotrode output to boost the amplitude.

***The sonotrode*** is in direct contact with the workpiece and couples mechanical vibrations between two objects. The sonotrode is therefore the connection between the transducer to the workpiece in terms of ultrasonic amplitude. For efficiently inducing oscillations and guaranteeing a long working life, the resonance frequency of the sonotrode is tuned to be concordant with the deployed transducer frequency. The amplitude is the displacement of the sonotrode at the workpiece surface and is measured in micrometre (µm). The surface of the sonotrode is textured to decrease power loss and increase welding efficiency (Daniels, 1965). The anvil, which serves as a counterpart to the sonotrode, is textured as well which helps preventing slippage of the workpieces (Daniels, 1965). The combination of anvil and pneumatic actuation of the sonotrode are also necessary to deliver contact pressure to the workpiece.

### 2.1.3 Commercially available Equipment

The commercially available equipment has expanded significantly over the last five years. Three standard models are currently available by Fabrisonic LLC: the SonicLayer™ R200, 4000 and 7200. In Figure 2.4 the SonicLayer™ 4000 is displayed which was invented in 2001 and launched in 2004. Each are equipped with an automated tape feeding system. Additionally, the 4000 and 7200 versions incorporate an integrated 3D milling system.

The key features of the systems and main differences between the SonicLayer™ 4000 and 7200 are graphically depicted in Figures 2.3 and 2.5. The smaller version works with a power of 4.5 kW and one transducer, the bigger version works with a power of 9 kW induced by two transducers. The transducers work in a “push-pull” system (Graff et al., 2010), 180° out of phase with each other (Sriraman et al., 2011).


**Figure 2.4 Fabrisonic SonicLayer™ 4000**

The development of the high power UC machine, referred to as very high power ultrasonic additive manufacturing (VHP-UAM) was driven by the demand for higher amplitudes (de Vries, 2004) and normal forces to increase the plastic flow between bonds (Schick et al., 2010). The SonicLayer™ 7200 is able to

apply amplitudes up to 52 µm and normal forces up to 15 kN (Sriraman et al., 2010).

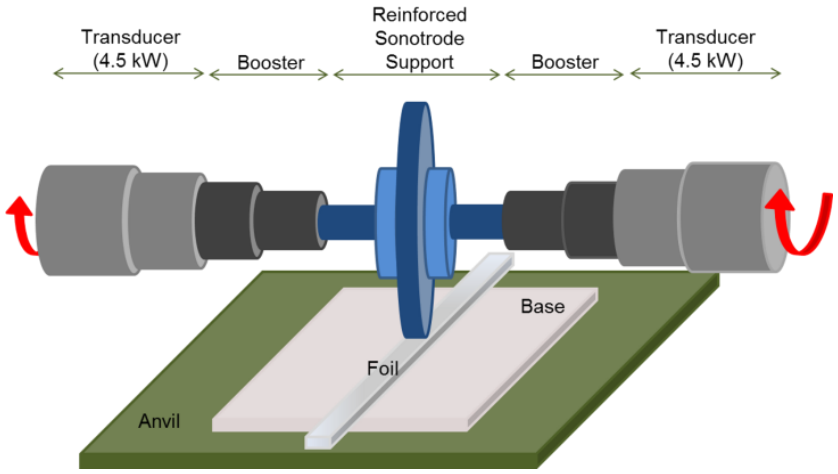


**Figure 2.5 Set-up of VHP-UAM system**

### 2.1.4 Current UC Research Equipment at Loughborough University

At Loughborough University, research was conducted on the Alpha 2 UC machine which was supplied by Solidica, INC. (USA) in 2009. However, research on an older version (Alpha 1) has been conducted since 2003 at Loughborough University (Kong et al., 2003). In Figure 2.6 the Alpha UC machine is shown.

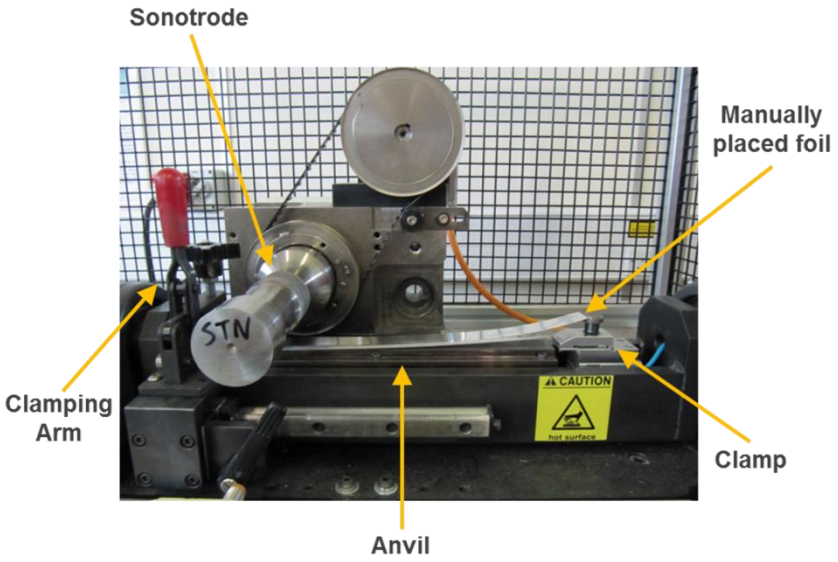


**Figure 2.6 Front view of alpha UC machine with manually placed foil**

The Alpha 2 UC machine is a modified version of the SonicLayer™ 4000 and in terms of set-up is comparable to the SonicLayer™ R200. Both exhibit an open platform in order to access the single components and to manually feed the material which allows basic research on smaller samples. Conversely to the SonicLayer™ R200, a CNC milling system is not incorporated in the Alpha UC machine, however it can be integrated as an optional extra. The Alpha UC machine is operated with an input power of 3.3 kW and works at a constant frequency of 20 kHz. The Alpha UC machine consists of the following components displayed in Figures 2.6 and 2.7:

- → A 20 kHz *power supply* (Branson BCA 900) to generate and modulate frequencies of 50 Hz from a main power source of 240 V.
- → The 20 kHz *transducer* (Branson 902JA) which contained a converter to convert the frequency into mechanical vibration.
- → A titanium 2.0:1 *booster* (20 kHz, 900 series) to increase the ultrasonic amplitude of the mechanical vibrations.
- → A tool steel *sonotrode* (AmTech W1A90A27) to transmit the ultrasonic amplitude/energy to the workpiece. The *sonotrode* surface area which is in contact with the workpiece has been Electro Discharge Machined (EDM) resulting in 5.89 µm average roughness ($R_a$).
- → A support *anvil* which can be heated up to a temperature of 149°C.
- → A *pneumatic cylinder* to generate the contact pressure of the sonotrode to the workpiece.
- → A *precision motor* which is used to control the rotation and traverse speed of the sonotrode.

A control panel (see Figure 2.7 b)) allows the user to manually control weld speed, contact pressure and oscillation amplitude. The coaction of these parameters affects the bonding process. For every material and machine an optimum process window exists (Kong et al., 2003; Kong et al., 2004a; Janaki Ram et al., 2006b; Kulakov and Rack, 2009).

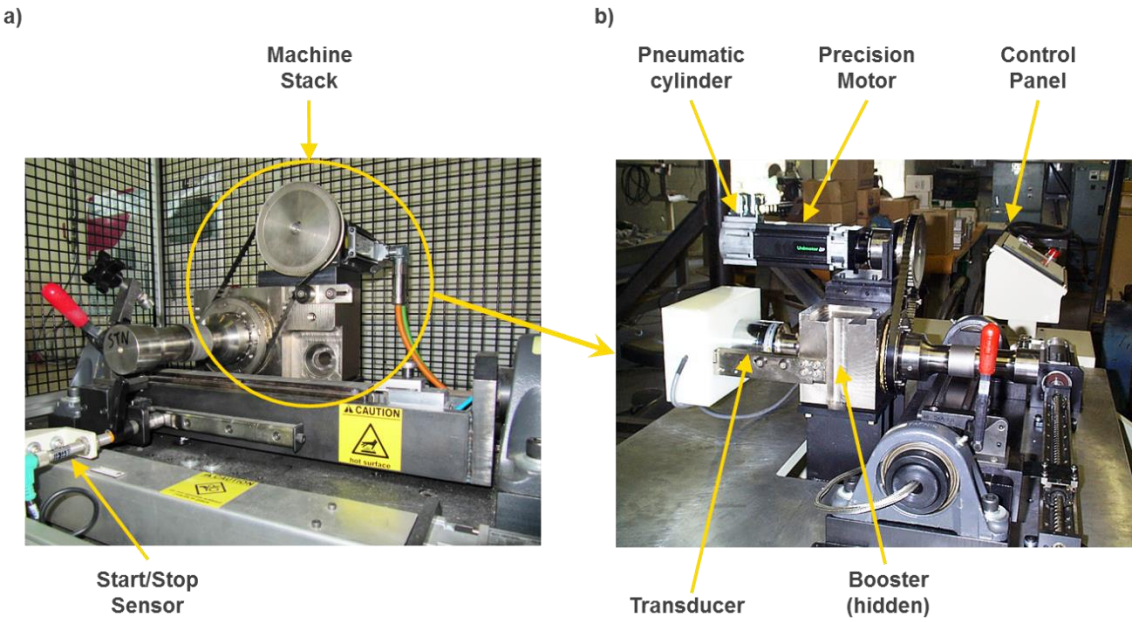


**Figure 2.7 Alpha UC machine a) front view and b) side view showing drive system**

Kong et al. (2004a) conducted studies on the Alpha 1 UC machine and found that optimum welding speed for Al 3003-H18 ranged between 27.8 mm/s and 43.5 mm/s, contact pressure between 103 kPa and 276 kPa and amplitude between 6.8 µm to 14.3 µm. The three main variables are explained below.

→ The *weld speed* is defined as the sonotrode traverse speed across the workpiece at which welding is performed. For the Alpha UC machine, the *weld speed* can be varied within a range of 0 to 100 mm/s.

→ The *contact pressure* is transmitted to the sonotrode by a pneumatic cylinder in order to hold the workpieces in close *contact* between sonotrode and anvil. *Contact pressures* can be varied between 0 to 690 kPa. However, contact forces at the workpiece could only be varied between 100 to 2000 N.

→ The *oscillation amplitude* refers to the longitudinal oscillatory movement of the sonotrode. The oscillatory movement of the sonotrode is required to from bonds between the workpieces. The amplitude can be varied between 12 to 21 µm.

→ The *temperature* refers to the temperature of the anvil. It can be increased from room temperature to 149°C.

### 2.1.5 Bonding Theories

The theory of bond formation during consolidation of metals is still subject to debate and investigation by a number of research groups globally. In summary, four main theories have been developed and discussed since the 1970s (Joshi, 1971; Yang et al., 2009), these are mechanical interlocking between foils, diffusion bonding, metal melting accompanied by recrystallisation and atomic bonding – each of which will be discussed below. Additionally, recent research has suggested newer bonding theories which will be discussed below as well.

***Mechanical Interlocking***

The theory of mechanical interlocking between two metals during ultrasonic metal welding was introduced by Joshi (1971). He showed that during welding of Al and gold (Au), the softer Au flows around the harder Al. A schematic representation of mechanical interlocking can be seen in Figure 2.8.

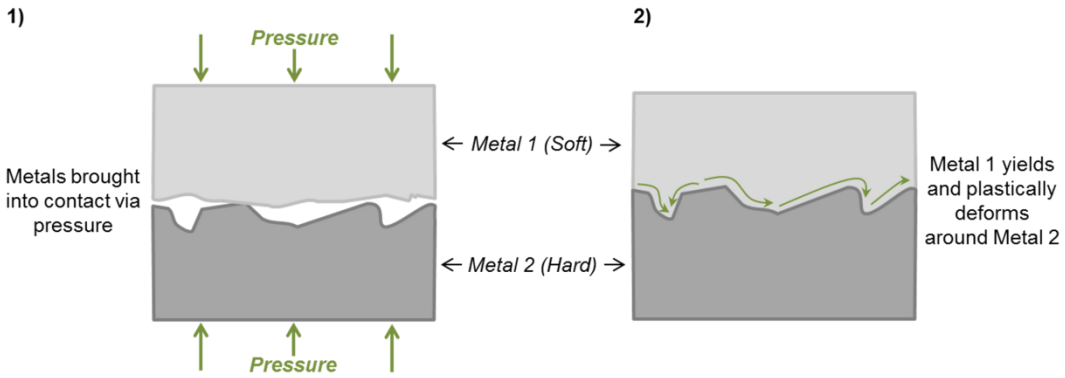


**Figure 2.8 Mechanical interlocking due to 1) normal forces lead to 2) deformation of the softer material around the harder material**

Mechanical interlocking between two metals has been shown to be effected by a large difference in hardness of the materials. Janaki Ram et al. (2007b) and Yang et al. (2009) found an absence of interlocking between the metal combinations of Al and nickel (Ni) and Al and copper (Cu). Hopkins et al. (2010)

suggested bonding by mechanical interlocking for Al and titanium (Ti) whose difference in hardness is larger than for Al/Ni and Al/Cu. Johnson et al. (2011) suggested the theory of mechanical interlocking for bonding of Al 3003 T0 foils due to an increase in hardness in the upper surface of the foils. Kumar (2010) found deformation of Al around stainless steel foils.

### *Diffusion Bonding*

In diffusion bonding, contact pressure results in deformation of the mating surfaces combined with a modest increase of temperature between the interfaces due to frictional forces, the surfaces coalesce into one and form a new interface (ASM, 1993) which is shown in Figure 2.9.

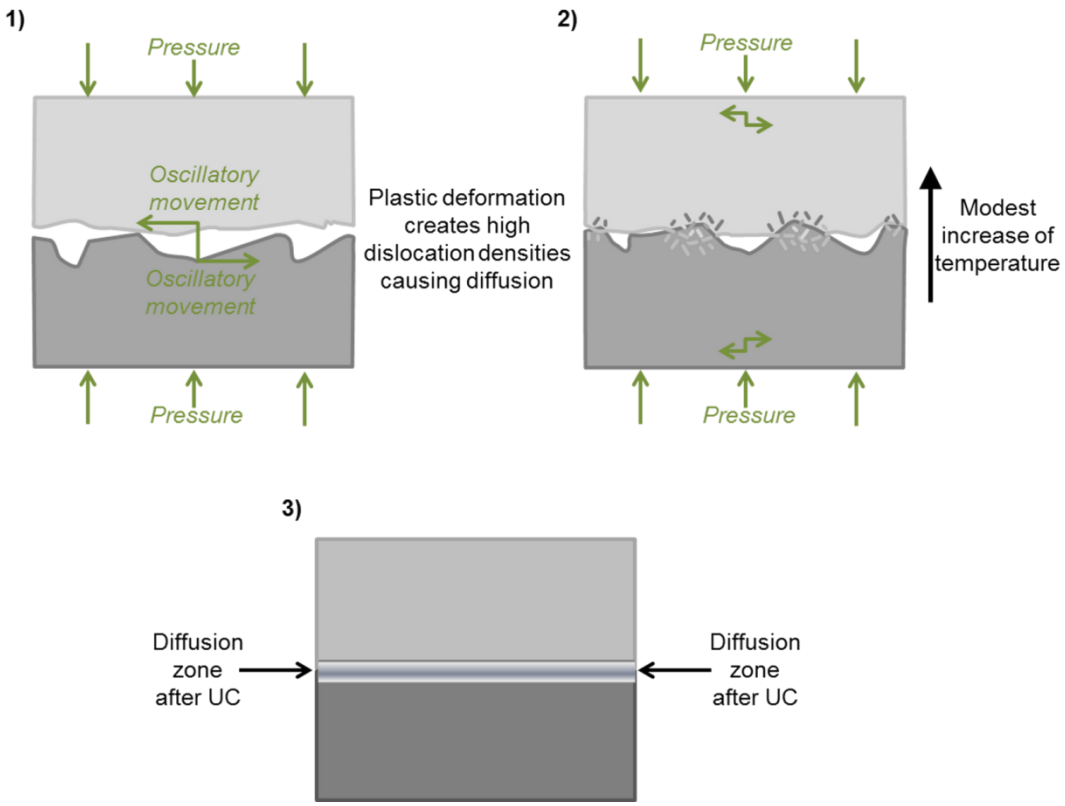


**Figure 2.9 Diffusion bonding by plastic deformation and modest temperature increase**

It has been stated by some authors that the appearance of diffusion bonding seems unlikely as small temperatures and little residence time of the sonotrode precludes diffusion bonding (Yang et al., 2009; Johnson et al., 2011). Additionally, especially for materials which exhibit a strong oxide layer, the

oxide layer would inhibit diffusion to take place (ASM, 1993; Johnson et al., 2011). However, Okada et al. (1963) found a 50 µm diffusion zone of copper and titanium. Gunduz et al. (2005) found that high deformation strain rates caused an enhanced diffusivity of Al into Zn and vice versa. Yang et al. (2009) concluded that diffusion, although not responsible for bonding, may contribute to bonding.

### *Thermal Melting*

Although it is generally agreed that USW is considered as a solid-state welding process (Jones and Powers, 1956; Daniels, 1965; White, 2003b; de Vries, 2004), many researchers have conducted studies on the occurrence of highly localised metal melting. Thermal melting is schematically displayed in Figure 2.10.

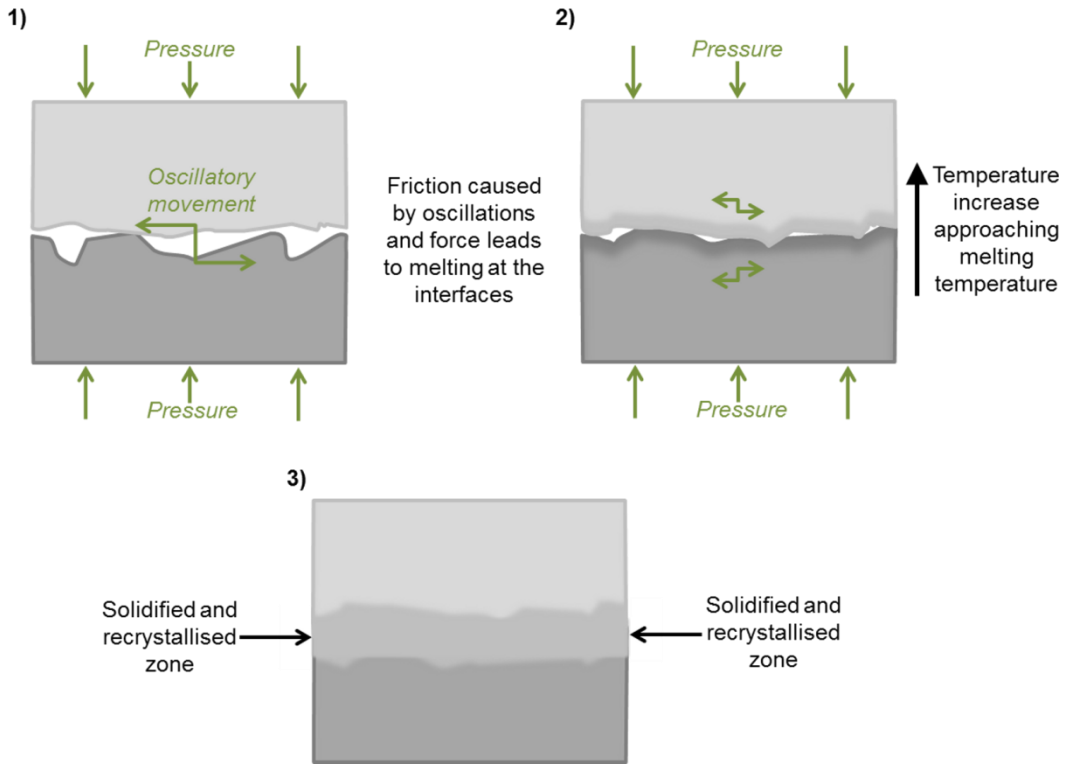


**Figure 2.10 The occurrence of melting is possible due to 1) applying normal and oscillating forces which lead to 2) an increase in temperature and a 3) solidified and recrystallised zone**

The motive for conducting thermal melting studies has been due to frictional effects within the weld interface provoked by applying normal and oscillating

forces during UC. Many studies using different metals have been concerned with measuring the temperature rise within the weld interfaces (Jones and Powers, 1956; Weare et al., 1960; Joshi, 1971; de Vries, 2004; Cheng et al., 2007; Cheng and Li, 2007; Yang et al., 2009; Schick et al., 2011). Nevertheless, all recorded temperatures were noticed to be below the melting temperatures of the various materials. However, as the recorded temperatures were observed at specific locations within the interface, the appearance of localised melting cannot be excluded. This argument is reinforced by Gunduz et al. (2005) who observed localised melting during bonding of Al and Zn.

***Atomic Bonding***

It has been stated that since a number of studies found no indication of melting between two metals which endorsed the argument that UC is a solid-state process and consequently suggests that atomic forces are responsible for bond formation. Atomic bonding or the so called “surface effect” has been suggested by several authors (Langenecker, 1966; Hulst, 1972; O’Brien, 1991; White, 2003b; Kong et al., 2005; Yang et al., 2006; Yang et al., 2009) and is the predominant theory for bond formation as it can be universally applied to various metal combinations.

Yang et al. (2006) stated that two conditions must be fulfilled to produce solid-state metallurgical bonding: firstly, atomically clean surfaces need to be established and secondly, the surfaces need to be held in intimate contact. In Figure 2.11, the steps to produce atomic bonding are displayed. In the first step, the surfaces of the metals are brought into intimate contact by initiating contact pressure from the sonotrode and the anvil. Contact however is only applied at certain points due the metal’s roughness which originates from oxide layers and surface asperities. The second step starts when normal and oscillating shear forces act in conjunction producing interfacial stresses at the contact points leading to cracking and breaking up of the oxide layers (Yang et al., 2007). The second step is completed when metal due to plastic deformation from underneath extrudes through the cracks aiding the dispersal of oxide particles along the interface and thus producing bonding of atomically clean surfaces.

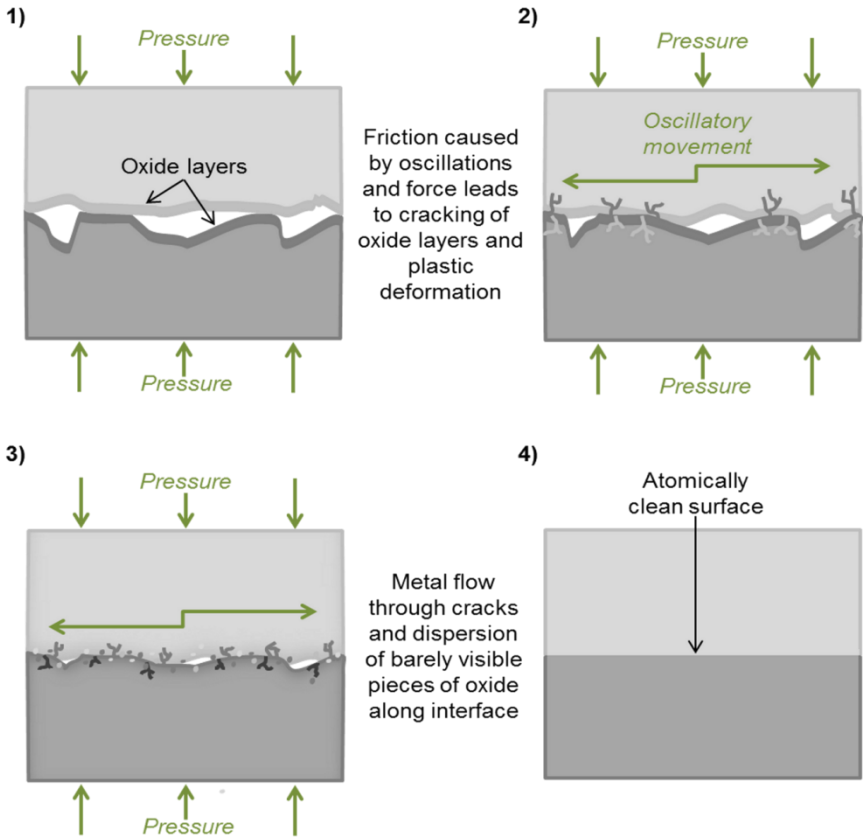


**Figure 2.11 Formation of atomic bonds by dispersal of oxide particles and plastic deformation**

During the third step, the contact points increase and grow in size due to plastic deformation. As a result, an increase of bonded contact points is achieved which eventually in the fourth step leads to metallurgical bonding of atomically clean interfaces.

### *Newer bonding theories*

Further to the main bonding theories, the characterisation of the interface microstructure between bonded foils has been part of several investigations in order to fully understand the bond formation which led to the proposal of new UC bonding theories which are under investigation (Johnson, 2008; Dehoff and Babu, 2010; Johnson et al., 2011). These bonding theories are based on dislocation movement and plastic behaviour and have been investigated by characterisation of the grain structure around the interfaces of the foils after UC.

On the contrary to the dispersion and elimination of the surface oxides for atomic bonding, Kong et al. (2003) found that oxide clusters still exist after bonding. It was proposed that brittle ceramic bonds were formed. This theory supported earlier findings by Matsuoka (1994) who successfully welded metals to ceramics by obtaining an approximate strength to that of the base metal. The existence of the oxide clusters has also been observed by Li and Soar (2009b) who suggested both, metal and ceramic bonding at the interfaces was taking place.

Work on oxide layer existence after bonding has been carried out by Dehoff and Babu (2010) and Johnson et al. (2011). Both observed a persistent oxide layer via focussed Ion beam imaging as can be seen in Figure 2.12.

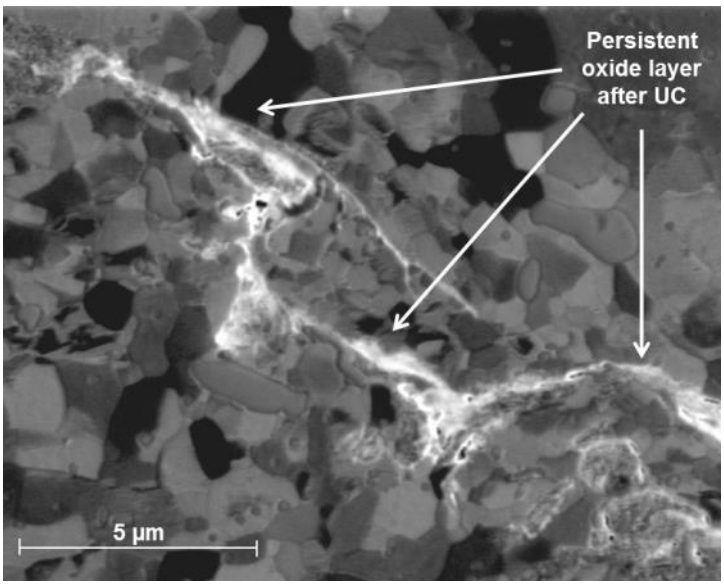


**Figure 2.12 Oxide layer detected via FIB (Johnson, 2008)**

Further substantiation for oxide existence after UC was found by measuring higher oxygen concentrations via EDX along the weld interface and around voids (Domack and Baughman, 2005; Brodyanski et al., 2005; Janaki Ram et al., 2007b; Johnson et al.; 2007). It has been proposed that oxide layers along the weld interface would significantly weaken the strength of the bond due to the brittleness of the oxides (Kong et al., 2003; Dehoff and Babu, 2010).

### *Bauschinger Effect*

Johnson (2008) suggested that bonding may have occurred by the "Bauschinger Effect". This effect describes the uniaxial loading of a sample beyond the yield stress and unloading to zero. Reloading of the sample will result in lower yield stress than the original and subsequent loadings will result in further reduction of yield stress and hence, softening of the material (Sowerby et al., 1979; Bannantine, Comer and Handrock, 1990). The appearance of the "Bauschinger Effect" evolves from effects such as dislocation interactions and dislocation pile-ups at grain boundaries (Jordon et al., 2007; Johnson, 2008). Johnson (2008) hypothesised changes in dislocation densities and sub-grain sizes within a deformation affected zone indicate the "Bauschinger Effect". He found grain size variations in a deformation affected zone with the smallest sub-grain region at the weld interface which had been in contact with the sonotrode and caused increased amount of cold work. Grain size reduction towards the weld interface has also been suggested in earlier studies by Allameh et al. (2005), Brodyanski et al. (2005) and Siu et al. (2011).

### *Dynamic Recrystallisation*

Following the bonding theory of thermal melting, bonding by recrystallisation has been intensively discussed in the last three years – especially for the VHP-UAM process. The key element for recrystallisation is the change of stored energy via dislocation movement. Recrystallisation is based on the formation of new grains and grain orientation variation due to deformation (Humphreys and Hatherly, 2004). Dynamic recrystallisation is based on the generation of new grains and grain orientation variation during deformation accompanied by high temperatures (Humphreys and Hatherly, 2004). Mariani and Ghassemieh (2010) found a 10 µm thick bonding zone in which they suggested were newly recrystallised grains at the interface and low-angle boundaries at the outer edges were observed. They suggested that deformation occurred via dislocation glide due to frictional forces and proposed continuous dynamic recrystallisation (CDRX) due to high-angle grain boundaries. Dehoff and Babu (2010) suggested bonding via recrystallisation due to variations in grain

orientation. Furthermore, sub-grains suggested a high amount of dislocation content which would account for bonding due to dynamic recrystallisation (DRX) at elevated temperatures possibly due to friction.

Research on the VHP-UAM has been primarily carried out by the Ohio State University and the Edison Welding Institute. Research suggests that dynamic recrystallisation is the originator for bonding (Sriraman et al., 2010; Sojiphan et al., 2010; Fujii et al., 2011; Sriraman et al., 2011; Sriraman et al., 2012). Most of the above mentioned authors found that samples after deformation showed a reduction in grain size, a change in crystallographic texture and high angle disorientations of the grains (Sriraman et al., 2010; Sojiphan et al., 2010; Fujii et al., 2011).

As proposed by Langenecker (1966), acoustic softening of the material is caused by the combination of ultrasonic irradiation and contact pressure. On the contrary, plastic deformation and the resultant dislocation movement during UC causes work hardening and strength increase in the material due to an increase in dislocation density. To test the appearance of softening and hardening of UC samples, Kong et al. (2005) carried out microhardness tests. He found softening for low contact pressures and hardening for higher contact pressures (10 % increase compared to original foil) accompanied with equal or higher weld strength. Matsuoka and Imai (2009) found an increase in hardness in the vicinity of the interface. Schick et al. (2010) found a hardness and tensile strength increase for UC samples due to grain refinement. For UAM-VHP bonding, Sojiphan et al. (2010) showed that the material softens rather than hardens which has been attributed to the recrystallisation mechanism. This argument was reinforced by Sriraman et al. (2010) who found a grain size reduction and lower hardness values compared to the original foils. They also stated that the hardness decrease is not uniform along the weld interface which may be due to inhomogeneous plastic deformation and contact pressure distribution due to the texture of the sonotrode.

### 2.1.6 Parameters Affecting Bonding in Ultrasonic Consolidation

Bond formation between metals depends on the coaction of the process variables (Yang, 2008) and the physical and chemical properties of the materials (Joshi, 1971; Daniels, 1965; Yang, 2008; de Vries, 2004). As already mentioned in section 2.1.4, the three main variable process parameters are weld speed (welding time), amplitude and contact pressure. Additionally, temperature and sonotrode topology have to be considered with regards to bond formation.

***The welding speed*** is the speed of the sonotrode travelling over the workpiece. The *welding time* is the time frame during which normal and oscillating forces are applied to the workpiece and bond formation occurs. Ergo, the *welding time* and *welding speed* are related and in combination with ultrasonic power, the ultrasonic energy delivered to the workpiece is determined. Kong et al. (2003) stated that a decrease in weld speed would increase the ultrasonic energy delivered to the workpiece at a given contact pressure and amplitude which could lead to higher levels of strain-hardening. Additionally, excessive speeds will cause inadequate bonds and insufficient speeds will cause a disproportionate amount of ultrasonic energy delivered into the workpiece which may cause excessive friction and temperature Kong et al. (2004a).

***The oscillation amplitude*** is directly controlled by the power supply and dictates the thickness of the interface area, density of the bonding area, the size of the deformed area (Joshi, 1971) and the amount of elastic/plastic deformation between the workpieces (Jones and Powers, 1956). In general, higher amplitudes deliver greater amounts of ultrasonic energy to the workpieces which facilitates plastic deformation and results in better bonds (Weare et al., 1960; Kong et al., 2004a; Yang et al., 2006; Tuttle, 2007; Yang et al., 2009; Li and Soar, 2009a; Zhang et al., 2009; Hopkins et al., 2010; Friel and Harris, 2010; Hopkins et al., 2012). Unbonded areas due to the surface roughness and potential voids can be reduced by an increase in plastic deformation.

***The contact pressure*** serves two purposes: Firstly, to initiate intimate contact between the welded materials so that ultrasonic vibrations can be applied to the workpiece (Joshi, 1971) and secondly, to enhance plastic deformation (Yang et al., 2009). However, bond formation can only be performed in combination with the oscillating forces. Both determine the dynamic interfacial stresses at the interfaces which facilitate oxide removal and plastic flow (Yang et al., 2009). In general, higher contact pressures increase the bonding area and decrease the void volume (Friel and Harris, 2010). However, an excessive contact pressure can produce severe deformation at the interface area due to the high interfacial stresses (Kong, 2005a; Yang et al., 2007). Low contact pressures may cause slippage of the workpieces and poor welds (Kong, 2005a).

***The temperature of the anvil*** can be varied as mentioned in section 2.1.4. An increase in bond formation and a reduction of voids was reported with increased anvil temperatures for aluminium foils (Janaki Ram et al., 2006a; George and Stucker, 2006). Increased temperatures due to friction play a major role in ultrasonic welding as low stresses are reduced and atomic diffusion and recrystallisation is enhanced (O'Brien, 1993). Furthermore, strain hardening may be reduced due to plastic deformation (Janaki Ram et al., 2006a).

***Sonotrode topology*** directly influences the induced roughness to the workpiece. In Figure 2.13 two different sonotrode topologies and the corresponding workpiece surfaces with areal surface roughness values ($S_a$) are shown. Texturing of the sonotrode is integrated to efficiently transfer ultrasonic energy to the workpiece by oscillations and contact pressure and to induce sufficient plastic flow for bonding (Johnson, 2008; Li and Soar, 2009b; Edmonds and Harris, 2010). A roughened surface helps preventing energy loss by reducing the occurrence of sliding (Weare, 1967; Yang, 2008). However, a roughened sonotrode also leaves an imprint of the topology on the top surface of the material (Kulakov and Rack, 2010; Yang et al., 2009; Harris and Friel, 2010) and may consequently affect bonding of subsequent layers (Edmonds and Harris, 2010).

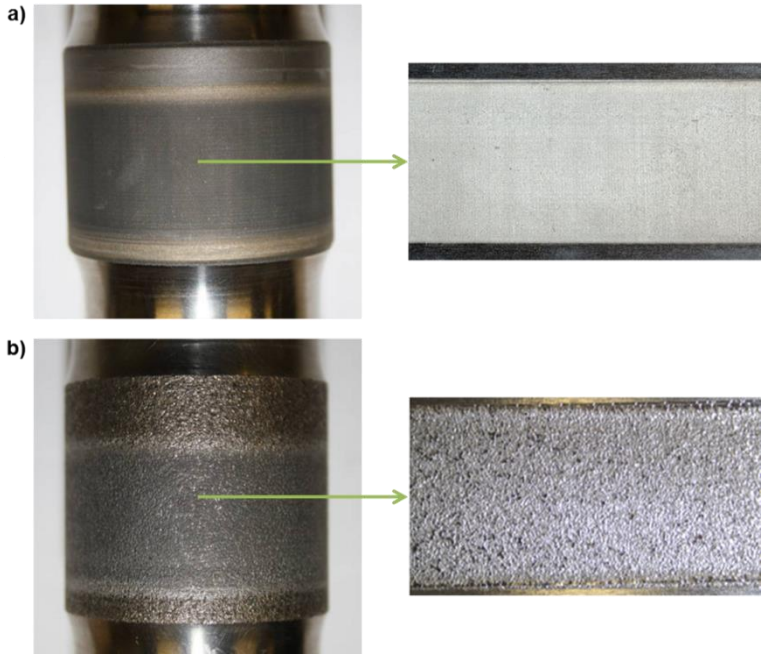


**Figure 2.13 Different sonotrode topologies a) smooth topology ($S_a$ = 4.97 µm) and b) rough topology ($S_a$ = 18.87 µm) (Edmonds and Harris, 2011)**

It has been stated that higher surface roughness (see Figure 2.13 b)) increases the possibility of interlaminar defects as void levels increase at the interfaces (O'Brien, 1993; Li and Soar, 2009b; Edmonds and Harris, 2010; Friel and Harris; 2010). An attempt to decrease the workpiece roughness has been made by Yang et al. (2006) by removing 30 µm of the consolidated surface which resulted in a decrease of interlaminar voids.

***Bonding quality***

In order to represent the bonding quality between the interfaces of two foils, Kong et al. (2003) introduced the microstructural linear weld density (LWD) analysis. LWD analysis is based on the formation and amplification of contact points during UC. It is described as the percentage of the physically bonded area ($L_B$) to the total interface length ($L_T$) (Janaki Ram et al., 2006a). For this reason the LWD can be seen as a representation of unbonded areas to bonded areas.

$$\text{LWD } [\%] = \left(\frac{L_B}{L_T}\right) \times 100 \qquad (1)$$

Janaki Ram et al. (2006b) stated that the formation of contact points is strongly dependent on the interaction of the process parameters. An increase in amplitude and contact pressure and a reduction of the weld speed advance LWD (Kong, 2003; Janaki Ram et al., 2006a; Janaki Ram, 2006b). Kulakov and Rack (2009) found that the weld speed has a minimal effect on LWD. Yang (Yang et al., 2010) expanded the LWD analysis by developing an analytical model which takes into account the energy transmission from the oscillating sonotrode to the bonding interface and may be used to evaluate the LWD. However, directly relating the LWD to mechanical properties has been proven difficult (Kong et al., 2003; Kong et al., 2004a; Janaki Ram et al., 2006a; Friel, 2010; Hopkins et al., 2012) and propositions about mechanical properties have to be treated carefully.

### 2.1.7 Ultrasonic Consolidation Capabilities

As UC can be seen as an additive manufacturing process with the additional ability of CNC milling, manufacturing of complex direct parts is one of the main capabilities (White, 2003b; George and Stucker, 2006; Johnson, 2009). Furthermore, UC has been proven to offer a variety of capabilities ranging from research on metal-matrix composites and multi-materials to successful manufacturing of smart structures (Robinson et al., 2006; Siggard et al., 2006; Cheng et al., 2007; Mou et al., 2008; Mou et al., 2009). The potential of UC for multi-material structures and metal-matrix composites will be explained below in greater detail.

***Multi-Material Structures***

Ultrasonic metal welding (UMW) can be applied to a variety of similar and dissimilar metal combinations (Daniels, 1965; Jones and Powers, 1956; O'Brien, 1991). As can be derived from Figure 2.14, Al-, Cu- and Fe alloys are the most versatile and researched materials up to now for UMW. In UC, an initial primary focus was the bond formation of Al foils (Kong et al., 2003; Kong et al. 2004a; Janaki Ram et al., 2006b).

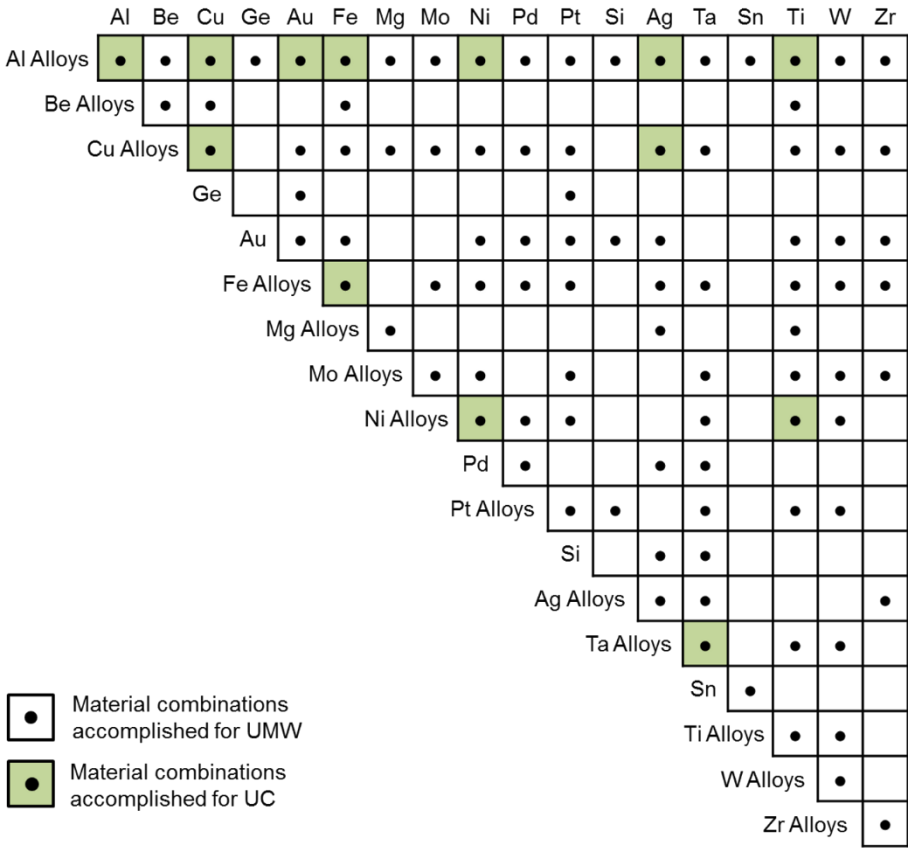


**Figure 2.14 Weldability of different metal combinations classed in UMW and UC (O'Brien, 1991; Johnson, 2009; Friel, 2011)**

In more recent years a variety of material combinations including reinforced materials have been investigated (Janaki Ram et al., 2007a; Obielodan et al., 2010).

### *Fibre Embedding*

UC benefits from two observed characteristic features which are advantageous and attractive for fibre embedment within metal matrices: Firstly, low temperature generation at the metal interfaces and secondly, acoustic softening of metals exposed to oscillations (Langenecker, 1966).

Langenecker (1966) found that ultrasonic irradiation reduces, as well as thermal energy, the static yield stress in metals necessary to initiate plastic flow which is displayed in Figure 2.15.

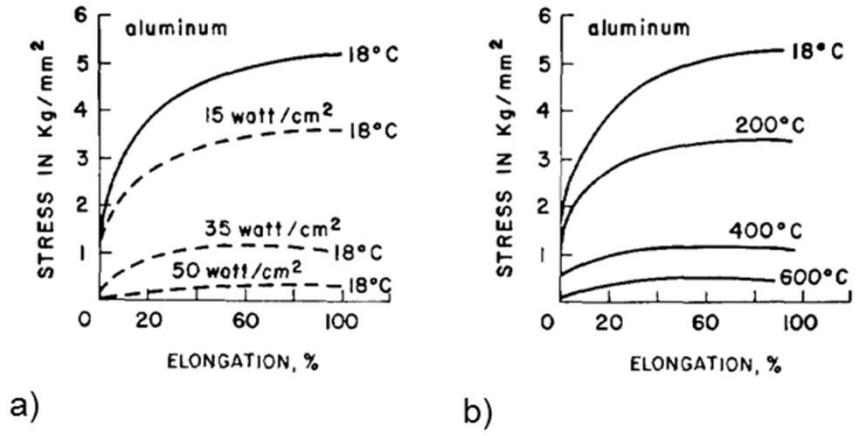


**Figure 2.15 Influence of ultrasound on static yield stress for Al single crystals: a) stress reduction by ultrasound (dashed curves indicate straining) and b) stress reduction by heat (Langenecker, 1966)**

However, less ultrasonic energy is needed to achieve stress reduction than thermal energy for the equal amount of stress reduction (Langenecker, 1966) due to a concentrated impact of ultrasound into dislocations. Eaves et al. (1975) reported a reduction of stress by 75% for ultrasonic irradiation and 45% for heating. The amount of ultrasonic energy applied determines the stress reduction in a metal. The mechanism of stress reduction by ultrasonic irradiation is caused by the activation of dislocations. The induced ultrasonic energy is preferentially absorbed into dislocations and grain boundaries, which are responsible for plastic deformation, and increases their mobility (Langenecker, 1966; Dawson et al., 1970; Hansson and Thölen, 1978). Kong (2005) introduced the term “volume effect” to describe the combination of ultrasonic softening by ultrasonic oscillations and contact pressure during UC. Superposition of both in combination with the friction-based surface effect (section 2.1.5) facilitates oxide layer break-up and activates large numbers of dislocations. Hence, high plastic deformation is achieved (Kong and Soar, 2005b). The volume effect has been found to be vital for UC bonding and has been subject of many studies (Izumi et al, 1966; Pohlman and Lehfeldt, 1966; Winsper et al., 1970; Joshi, 1971; Harman and Albers, 1977; Hansson and Thoelen, 1978; Kong, 2005; Siddiq and Ghassemieh, 2008; Siu and Ngan, 2011; Siddiq and El Sayed, 2012).

Significant stress reduction and enhanced plastic flow takes place immediately when ultrasound is applied (Langenecker, 1966). Fibre embedding via UC utilises this effect to immediately generate dislocation-induced plastic flow of the metal matrix surrounding the fibres (Kong and Soar, 2005b; Yang et al., 2006).

Successful research on fibre embedding has been conducted on various fibre types such as Silicon Carbide Fibres (SiC) (Kong, 2005; Yang et al., 2007; Li and Soar, 2007; Yang, 2008; Li and Soar, 2009a; Yang et al., 2010), shape memory alloys (SMA) (Kong et al., 2004b; Hahnlen et al., 2009; Friel and Harris, 2010; Hahnlen and Dapino, 2010), optical fibres (Kong, 2005; Kong and Soar, 2005) and FBG's ( Mou et al., 2008; Mou et al., 2009). A finite element model (FEM) based in SiC integration during UC has also been published (Siddiq and Ghassemieh, 2011).

Research showed that SMA fibres can be entirely encapsulated by the metal matrix without any voids or porosity by making use of the volume effect (Kong et al., 2004b) as shown in Figure 2.16.

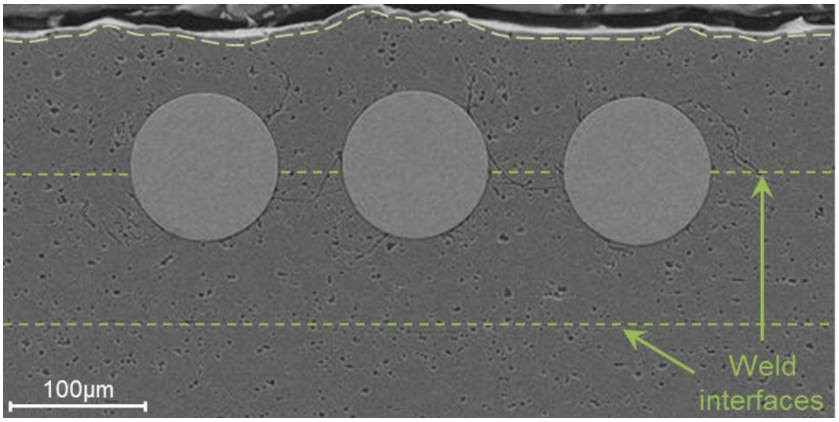


**Figure 2.16 Example of SMA fibres embedded in Al matrices (Kong, 2005)**

A possible explanation for an increased plastic flow around the fibres and hence better bond formation may be that the material surrounding the fibres experiences higher stresses originating from oscillations and contact pressure (Yang et al., 2007; Yang et al., 2009; Li and Soar, 2009a). However, during fibre pull-out tests and mapping studies, imprints of fibres within the matrix material

showed that fibres are mechanically/physically entrapped rather than metallurgical or chemical (Kong et al., 2004b; Kong, 2005; Yang et al., 2006).

In general, bonding appeared to be stronger when higher amplitudes and contact pressures were used (Kong et al., 2004b, Kong and Soar, 2005b, Yang et al., 2006). Consequently, low pressures and amplitudes entailed unbonded surfaces without encapsulation of the fibres or even separation of the foils. The fibres themselves seem to behave as stress risers (Yang et al, 2009) between the metal matrices which not only permit an increase of energy absorption into the upper foil but also allow energy to be transmitted through them which helps the deformation of the lower foil (Kong and Soar, 2005b; Friel and Harris, 2010). Yang et al. (2007) found when embedding softer materials than the matrix material, the component rather than the matrix is deformed. Additionally, the increase of oscillating and shear forces leads to higher dynamic interfacial stresses which enhance transfer from elasto-plasticity to visco-plasticity (Astashev and Babitsky, 1998; Kong and Soar, 2005a; Yang et al., 2006). Yang et al. (2006) stated that in addition to contact pressure, oscillations and weld speed, that fibre embedding direction influences bond formation during fibre embedment. Fibre placement plays an important role for the freedom of part manufacturing in UC. In general, during UC the workpiece experiences maximum shear stresses at an angle of 45° to the travelling direction of the sonotrode (Gao and Doumanidis, 2002; Johnson, 2008). Hence, fibres embedded in 45° direction experienced higher plastic flows than fibres placed at 0° or 90°. Hahnlen et al. (2009) found an increase of tensile strength for fibres embedded parallel to the weld interface but worse results for fibres perpendicular to the weld interface.

Research on fibre embedment has also demonstrated that higher amplitudes and contact pressures can lead to distortion of fibres, which is shown in Figure 2.17, or even breakage of fibres. This seems possible when considering that the fibres create high stresses by taking the shear and oscillation forces first. An increase in amplitude also means greater provided movement for the fibres. Ergo the fibres have more space to roll around. This can lead to displacement of the fibre itself (Friel and Harris, 2010; Hahnlen et al., 2010).

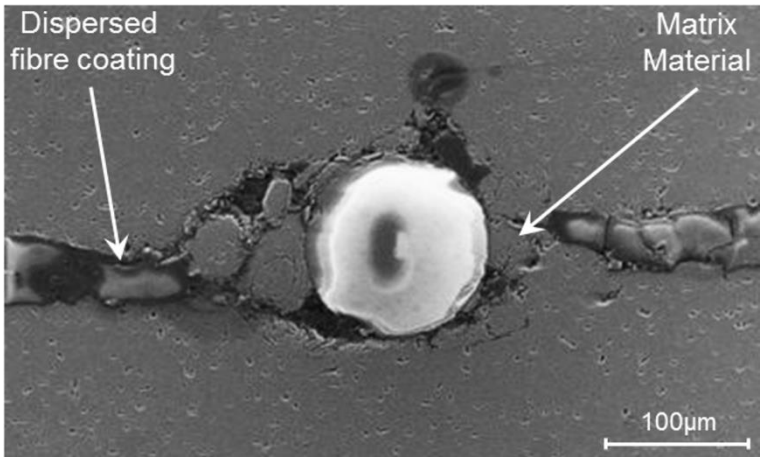


**Figure 2.17 Dispersed material around fibre (Kong, 2005)**

Fibre embedding of 10 fibres with a diameter of 375 µm (Friel, 2011) has been shown to result in increased amounts of plastic flow and good bond strength. However, research on high numbers of fibres (up to 40) with a diameter of 100 µm has been proven difficult (Kong, 2005; Li and Soar, 2007; Friel, 2011). Higher numbers of fibres constrained the delivery of sufficient energy to the interfaces and as a result plastic flow was insufficient to induce bond formation (Kong et al., 2004; Kong, 2005a; Li and Soar, 2007; Friel, 2010). In addition to the prevention of bond formation, higher volumes of fibres may as well constrain the metal to metal contact for sufficient foil bonding at the interfaces (Johnson, 2008; Friel, 2010).

### 2.1.8 Characterisation of the Fibre Microstructures

As opposed to microstructural studies on the interfaces of UC manufactured parts (see 2.1.5), relatively few studies have been concerned with the microstructural investigation of fibre embedment accompanied by plastic flow (Yang et al., 2007; Li and Soar, 2008; Friel and Harris, 2010; Yang et al., 2010).

Yang et al. (2010) classified four different regions around the fibre after push-out testing: zone 1 which is not influenced by the fibre, zone 2 and 3 which showed plastic deformation and the zone which showed an exact imprint of the fibre. In zone 3 (close to the fibre) brittle features were detected which indicated work-hardening. Li and Soar (2008) observed an increase in hardness in an

area 20 µm around embedded fibres. In this area, severely deformed grains were found (Li and Soar, 2008; Mariani and Ghassemieh, 2010). Friel and Harris (2010) found a decrease of grains which was highest above and below the fibre. The decrease of deformed grains reinforced the argument of the occurrence of highly localised plastic flow (section 2.1.7) and reinforced the suggestion of work-hardening around the fibres which increased the strength of fibre reinforced UC parts. Additionally, Friel and Harris (2010) stated that the combination of surface induced sub-grain refinement by the sonotrode and fibre embedment resulted in greater embedding of the fibres into the lower foil.

The hardness results of Li and Soar (2008) for SiC fibres also indicated that hard regions exist near the fibre harder than SiC itself. He suggested that the coating of the fibre may have been dispersed around the fibre after cracking which has also been shown by (Friel and Harris, 2010; Yang et al., 2010). Fibre cracking may be enhanced by the sonotrode hardening mechanism which enhances the fatigue of fibres by an increase in stress (Friel and Harris, 2010).

## 2.2 Laser Processing

### 2.2.1 Introduction

When Albert Einstein postulated the basics of quantum theory in 1916/1917, the concept of stimulated emission and thus the foundation for laser theory was born (Einstein, 1916; Einstein 1917). Stimulated emission is based on two principles: firstly, light is transported in bundles of photons and secondly, electrons occupy different energy levels (orbits) around a nucleus in an atom. Radiation is emitted when an excited electron leaves the higher energy level for a lower one. Einstein discovered that the presence of a photon causes an electron to descend from the excited state by emitting a photon exhibiting the same properties (frequency, phase, energy, polarisation and direction) as the first one – thus light is amplified. Laser (**L**ight **A**mplification by **S**timulated **E**mission of **R**adiation) theory utilises the principle of stimulated emission inside a cavity in which an active gain medium (gas, liquid, semiconductor, crystal or

solid) is pumped (optically or electrically) to an excited state. This causes population inversion and stimulated emission of the electrons which bounce back and forth in a resonator due to the use of a front and back mirror. Over 40 years after Einstein's discovery, Theodore Maiman discovered the first operational laser which utilised a ruby crystal as the gain medium pumped with flash lamps in 1960 (Maiman, 1960).

Ever since the 1960s, laser development and the invention of different laser sources, with the most popular ones being diode, solid state, $CO_2$, and fiber laser, followed a successful route and laser production has reached a market high in 2012 (Hausken, 2012) as can be seen from Figure 2.18.

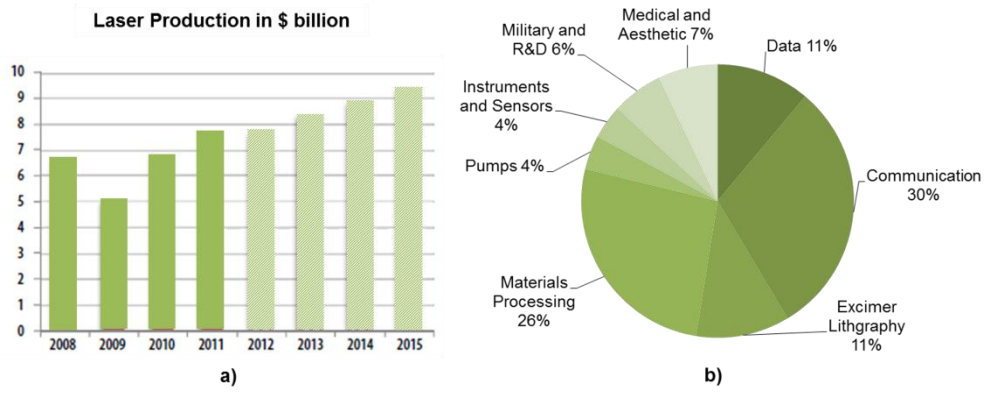


**Figure 2.18 Laser production until 2011 and forecast (a) and percentage of laser applications (b) (Hausken, 2012)**

Especially the on-going research on shorter pulse durations and optimisation of beam qualities (Hecht, 2010) have forced the laser's way into traditional materials processing techniques such as cutting, drilling, welding, soldering, hardening, brazing and marking (Tam et al., 1990; Fenoughty, 1994; Geiger, 1994; Steen, 2010). The advantages of laser processing in manufacturing are flexibility, machining rate and quality, automation, selectivity, reliability and maintenance (Hügel, 2000).

### 2.2.2 Fundamentals of Laser Beams

#### *Spatial Modes of Laser Beams*

A resonator produces electromagnetic waves within the cavity which are defined by the resonator geometry, alignment and spacing of the internal resonator optics, gain distribution, propagation properties of the active medium and the presence of apertures in the resonator (Ion, 2005). As the oscillation of the waves produces interference with each other, transverse standing wave patterns are formed which emerge from the cavity as a mode structure (Steen, 2003a) - Transverse Electromagnetic Modes (TEM).

The lowest order mode is Gaussian and described as $TEM_{00}$ (see Figure 2.19).

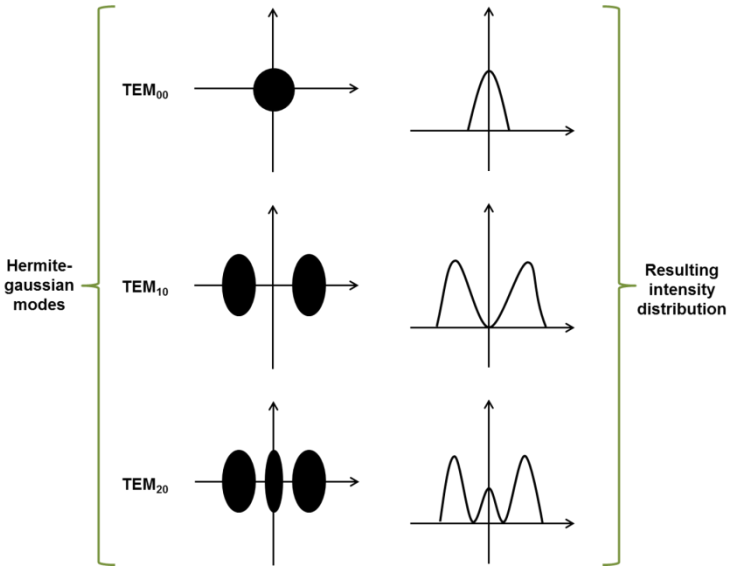


**Figure 2.19 Hermite-gaussian modes and their intensity distributions**

The TEM mode determines the intensity distribution caused by the beam diameter and divergence angle (see divergence). The Gaussian mode produces the smallest spot and narrowest beam divergence. Hence, this mode is desirable. However, real laser beams operate in higher order TEM modes (Kogelnik and Li, 1966) which can be described either as Hermite-Gaussian for rectangular resonators or Laguerre-Gaussian for symmetrical resonators (Carter, 1979; Phillips and Andrews, 1982).

For laser material interactions, the laser beam mode is of importance as the spatial distribution determines the irradiance intensity which influences the melt

pool shape, flow pattern and temperature distribution (Kantor et al., 1996; Farooq and Kar, 1999; Han and Liou, 2004).

### *Divergence*

The beam divergence (θ) is the measure of directionality of a laser beam (Falk, 1982; Ready and Farson, 2001). It measures the tendency of the beam to spread from the beam waist ($w_0$) in the far-field (Paschotta, 2008) as seen in Figure 2.20.

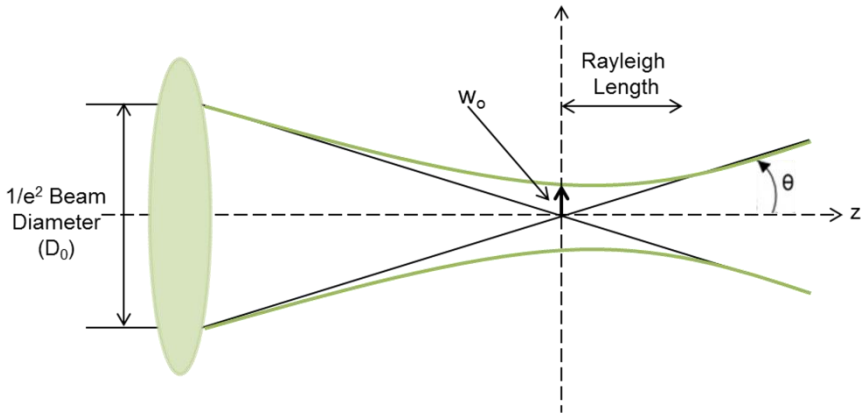


**Figure 2.20 Definition of beam waist and divergence half-angle**

For Gaussian beams, the beam radius is defined as the diameter at which the irradiance has fallen to $1/e^2$ or 13.5% of the intensity which is due to the infinite decrease of a Gaussian curve (Alda, 2003). A $TEM_{00}$ beam mode has the lowest beam divergence which results in small focused spot sizes and greater depth of focus (Ion, 2005). Higher TEM modes ($M^2 > 1$) exhibit a wider beam waist and angle of divergence (θ).

### *Brightness*

The brightness [$W/m^2sr$] of a laser is defined as the intensity of light at a particular location (Ion, 2005). The solid angle (sr) describes how the angle spreads out in three dimensions and is therefore measured in steradians (Hitz,

1989). Figure 2.21 shows that fiber lasers exhibit the highest brightness values up to a power of 10 kW.

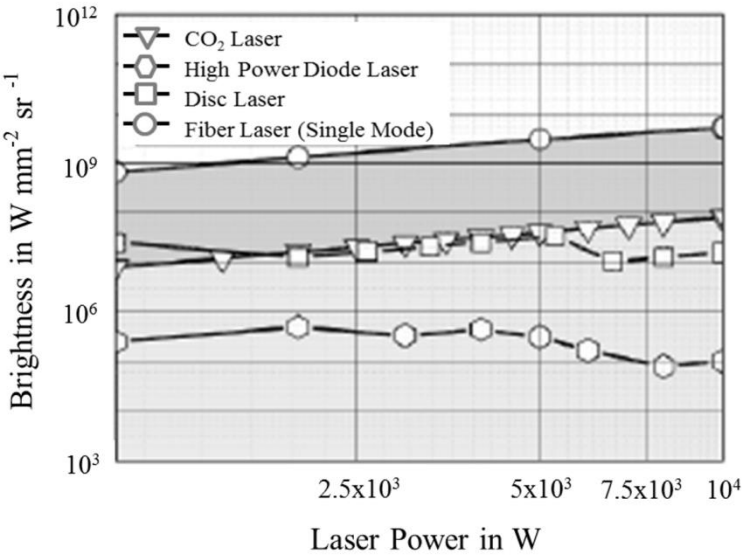


**Figure 2.21 Brightness of currently available $CO_2$, diode and solid-state lasers (Beyer et al., 2012)**

For laser processing applications, a high brightness value means that the laser source is able to provide a high intensity (Beyer et. al., 2012) as the intensity of a focused laser beam is directly proportional to the brightness (Ion, 2005).

### *Beam Quality*

The optical quality of a laser beam can be characterised by either the beam parameter product (BPP) or the beam quality factor $M^2$ (Parent et al., 1992). The $M_2$ factor indicates how close a laser mode is to being a single mode $TEM_{00}$ which is the Gaussian mode ($TEM_{00}$ = 1) (Siegmann, 1990). For this reason it can also be seen as the beam quality factor which determines the ability to focus a laser beam by spot size and focal length. It determines how many times wider the focused spot will be than the theoretical minimum. In general it can be said that the lower the $M^2$ value, the higher is the beam quality. For diffraction-limited beams $M^2$ is greater than 1. In Figure 2.22, the beam quality for various laser types according to their $M^2$ values can be seen.

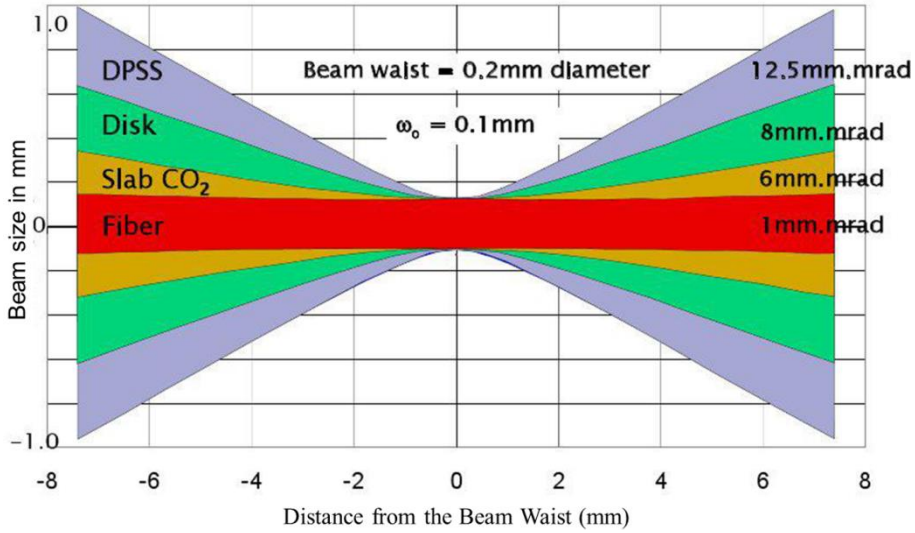


**Figure 2.22 BPP for various laser types (Kratky et al., 2008)**

The $M^2$ value varies with output power and can reach for example for a 400 W pulsed neodymium-doped yttrium aluminum garnet (Nd:YAG) laser up to $M^2$ = 150 (Ready and Farson, 2001). Fiber lasers usually exhibit $M^2$ values in the range of 1.2 – 1.5. The $M^2$ value can be measured from the evolution of the beam radius along the propagation axis which is called caustic of a beam. However, there are several other methods (Siegmann, 1998; Bouafia et al., 2004).

The BPP is of importance for fiber optics as a decrease in fibre diameter while maintaining the numerical aperture (NA) leads to a better BPP (Weber, 1998; Kratky et al., 2008). For a Gaussian beam the BPP is λ/π; hence for a fiber laser operating at a wavelength of 1.075 µm the minimum BPP would be 0.342 mm.mrad (Paschotta, 2008). The short wavelength of the fiber laser compared to other laser sources accounts for a small BPP. As the fiber laser at a given beam waist radius possesses the lowest beam divergence, it can be focused to a smaller spot size compared to other laser sources which lowers the BPP (Beyer et al., 2012). Vice versa, the higher the BPP, the lower is the beam quality (Hodgson and Weber, 1993).

***Focal Length and Focal Spot Size***

The focal length is the distance from the centre of the lens along the optical axis to the focal point (Ion, 2005). The effective focal length is the distance that is used by designers to calculate the curvature of the length (Ready and Farson, 2001). The focussed spot size is proportional to the focal length and the power density produced is proportional to the square of the length. Subsequently, short focal lenses give very high energy densities but are limited in their application due to a shallow working depth.

The focal spot size determines the maximum energy efficiency which can be delivered to the work piece for a given power. Hence, the focal spot size is an important parameter in laser material processing. For diffraction-limited beams $M^2$ is greater than 1. $M^2$ can be calculated from the spot size of a perfect Gaussian beam:

$$d_f\ [mm] = \frac{4 \times M^2 \times \lambda \times f}{\pi \times D_0} \tag{2}$$

where λ is the wavelength, f is the focal length and $D_0$ is the input beam radius at the lens (Nelson and Christ, 2012).

The power density of a laser beam at the surface of a material can be calculated as (Kaplan, 2011):

$$I\ \left[W/mm^2\right] = \frac{P_f}{A_f} \tag{3}$$

where $P_f$ is the power and $A_f$ is the area covered by the spot size.

### 2.2.3 Fiber Laser

In 1964, Charles Koester and Elias Snitzer presented the first fiber amplifier. This fiber system used a spring shaped coil of a fiber which was slipped around a linear flash lamp. Only a few milliwatt output power were gained due to an insufficient pumping source (Koester and Snitzer, 1964). Kao and Hockham (1966) proposed in 1966 that fiber optics in combination with diodes would be a good medium for laser beams due to low light loss. In 1970, the first step-index

fibre was manufactured (Beck et al., 2000) which led the way to pumping fibers with neodyminum in 1985 (Poole et al., 1985). In 1988, Snitzer developed a fiber multi-cladding geometry where pump light entered the outer core and then passed through the inner core which contained lasing ions (Snitzer, 1989). Here the optical gain occurred and light was confined to a focused spot with rarely a loss of energy. In the 1990's ytterbium was discovered to be a good pumping medium as it showed small photon energy defects and was efficient for diode pumping (Hanna et al., 1988; Hanna et al., 1990). The discoveries of new pumping mediums, the development of new pump sources and the continuous optimisation of fibre cladding led to an output power of 110W in 1990 for a single mode fiber and to 500 W in 2003 (Dominic et al., 1999; Limpert et al., 2003). In 2009 IPG reported continuous output power of 10 kW from a single-mode YB-fiber oscillator amplifier and 50 kW for multimode fibres (Richardson et al., 2010). Fiber laser revenues grew 114 % from 2008 to 2011 to $ 640 million and have a market share of 15 % in laser micro processing (Hausken, 2012).

***Fibre designs***

Fiber lasers can be classified as diode-pumped rare-earth-doped solid-state lasers as the active lasing medium is a crystal (Tünnermann et al., 2005). In contrast to conventional solid-state lasers, fibre lasers generate the wavelength in a doped fibre by pumping in direct connection to the fibre. Fibre designs can be classified into single mode, multi-mode and more recently large area mode (LMA) fibres. In Figure 2.23, a schematic graphic of a fiber laser and a multi-mode fibre are displayed. The pump source for the fiber laser is a semiconductor – generally in the form of diode bars or stacks (Endriz et al., 1992; Chen et al., 1996; Müller et al. 2006; Schröder et al., 2010; Xiao et al., 2012). Depending on the fibre design, the pump energy is either coupled directly into the core (single mode) or into a larger pump-cladding surrounding the core (multi-mode) (Paschotta, 2009). The fibre contains the active doping medium which enhances light amplification (Silfvast, 2004).

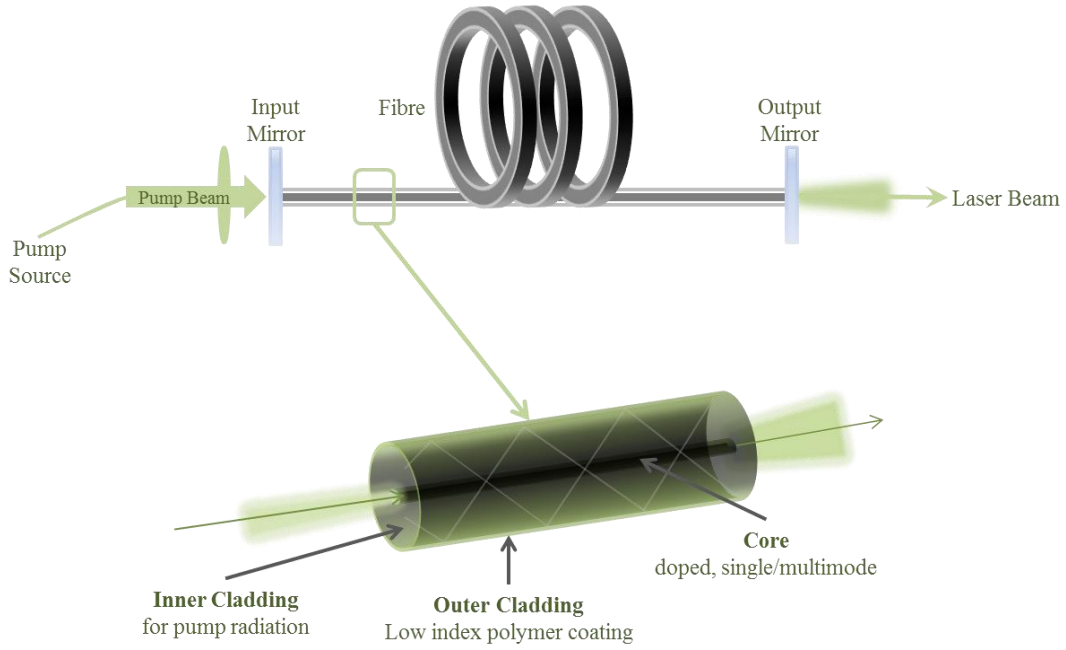


**Figure 2.23 Schematic overview of fiber laser and schematic multi-mode fibre structure**

Each end of the fibre is confined with dielectric mirrors or fibre-bragg gratings (FBG) which form the resonator cavity (Horley et al., 2007; Tünnermann et al., 2010).

Light guidance in an optical fibre is based on total internal reflection which is achieved by different refractive indexes of the core (higher index) and the cladding (lower index) of a fibre (Koester, 1966; Steen and Mazumder, 2010) which is the design of a single-mode fibre. The outer cladding usually consists of a polymer coating or solid glass (Horley et al., 2007). The core (2 µm to 10 µm) is usually made of fused silica, phosphate or fluoride glass which exhibits low attenuations of 10 dB/km (Tünnermann et al., 2000) so that light can be fully absorbed.

For stimulated emission and amplification of the light, the inner core of a fibre is doped with rare-earth dielectric materials such as erbium, neodymium, ytterbium, thulium, praseodymium or holmiu (Silfvast, 2004; Müller et al. 2006). $Yb^{3+}$ is usually the dopant material due to low quantum defect of 10 % and low intrinsic losses (Tünnermann et al., 2005; Müller et al., 2006). The output wavelength depends on the doped active medium (Tünnermann et al., 2000).

In a single-mode fibre, only one mode can propagate – the transverse fundamental mode. If the core diameter becomes larger, multiple modes can occur. Such multiple modes occur in double-clad fibres which are used to overcome output power limitations in single mode fibres which is due to the restriction of single pump diodes (Tünnermann et al., 2010). Double-clad fibres consist of three layers: a single-mode core doped with the rare-earth material, an inner silica cladding which serves as the pump core and an outer polymer cladding (Snitzer, 1989; Hecht, 2002; Canning, 2006). The advantage of double-clad fibres is that light can be coupled into the larger cladding core by low brightness high power diode lasers (Zenteno, 1993; Hand et al., 1996). The ratio of light coupled into the pump cladding is dependent on the size of the pump cladding and the numerical aperture between the silica and polymer coating (Müller et al., 2006). However, the disadvantage of the double-clad fibre design is the reduced absorption of pump light and hence, the reduced efficiency as some rays will never strike the doped fibre core (Tünnermann et al., 2000). For this reason, double-clad fibres with different core/cladding shapes have been developed (Limpert et al., 2007).

The above mentioned fibre designs are limited to powers barely exceeding an output of 100 W continuous wave (CW). For CW powers above 100 W and especially for higher power pulsed operation, nonlinear effects such as Raman-scattering and Brillouin scattering occur which can cause significant power loss (Smith, 1972; Beck et al., 2000; Hecht, 2002; Limpert et al., 2007). For fiber lasers, nonlinear effects scale as the product of power density and fiber length (Hansen et al., 2011). Hence, an increase in fibre core or shortening of the fiber length is desired for high power scaling (Limpert, 2006; Hansen et al. 2011). For this reason, large-mode area fibres (LMA) have been developed which use a bigger core diameter and by bending, operate in single mode (Koplow et al., 2000; Tünnermann, 2005; Müller et al., 2006). In Figure 2.24 a), a kidney-shaped fibre in coil form is displayed. Also displayed in Figure 2.24 b) is a photonic crystal fibre (PCF).

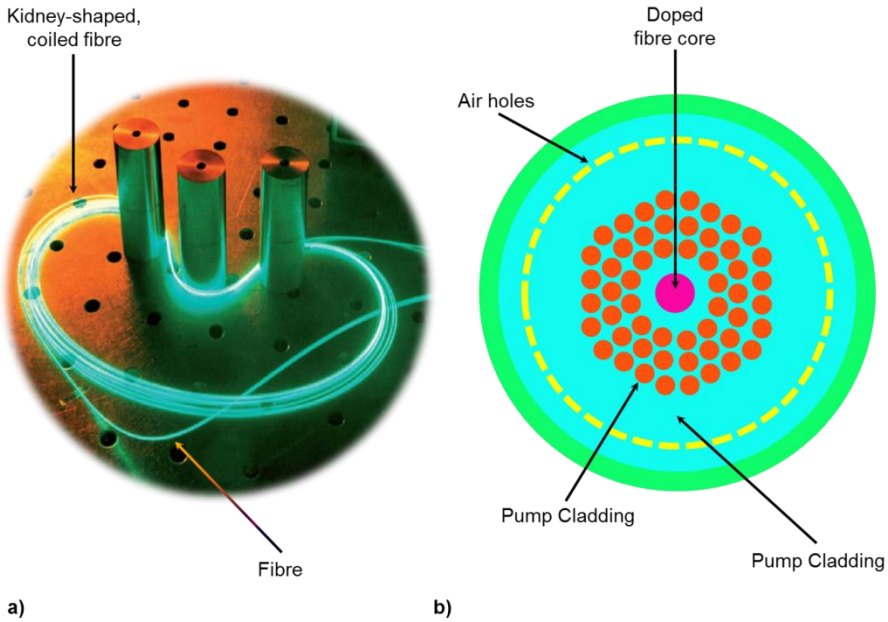


**Figure 2.24 Fibre types for non-linear effects reduction in fiber lasers a) large-area mode fibre; b) photonic crystal fibre (Tünnermann et al., 2010)**

PCF are fibres which possess high different refractive indexes due to the air holes while containing a single mode operation (Birks et al., 1997; Limpert et al., 2003; Knight, 2003; Canning, 2006).

The advances in fibre technology (especially the recent fibre designs) have led to several different fibre laser configurations which have expanded the range of output power into the kW range. Different fibre configurations are based on pulsing of lasers where the energy is held back and then superimposed to achieve a high peak power. A pulse is characterised by its peak power, shape, length and repetition rate (Ion, 2005). The main different fibre laser configurations for achieving high peak powers are based on amplification, q-switching and mode-locking (Ainslie, 1991; Paschotta et al., 1997; Limpert et al., 2002; Dawson et al., 2008; Limpert et al., 2009; Richardson et al., 2010; Wirth et al., 2011).

***Advantages of Fibre Lasers***

- Compactness – the complete laser process (including pump source and resonator) can be integrated in a waveguide and fibers can be bended or coiled.

- Maintenance-free – the optics are shielded from the environment and mechanic components are limited which avoids alignment and maintenance.
- Thermal properties – the thin and long fibre as a gain medium offers high thermal properties due to the high surface-to-volume ratio which offers high power scaling. Furthermore, large chillers for cooling can be avoided. Fibre lengths of several metres are possible due to low intrinsic losses. Thermal losses can become apparent for multi-mode fibres.

- Beam-quality is independent of input power because the fibre itself determines quality and characteristics. The mode guidance of the fibre ensures that the beam quality is independent of the output power.

- Wall-plug efficiency – fiber lasers offer small quantum defects between pump and output power (≥ 80% for Yb) (Kurkov, 2007). The wall-plug efficiency is 30% for ytterbium-fiber lasers.

- Bandwidth - fibre gain media have a large gain bandwidth due to strongly broadened laser transitions in glasses, permitting wide wavelength tuning ranges and/or the generation of ultrashort pulses.

***Disadvantages of Fiber Lasers***

- Power scaling – non-linear effects such Brillouin and Raman scattering can occur for very high core power intensities in combination with the narrow fibre core and long length of the fibre. These lower the achievable output power in single-mode fibres and pulse quality of mode-locked lasers

- Destruction threshold fibre - fibre light coupling at the end of the fibre is limited; coupling the amplified signal to the same end as pump source which requires alignment of fibre end and pump source
- Cavity length – high cavity lengths with long resonators are required as fibres exhibit a limited gain and pump absorption per unit length

### 2.2.4 Comparison of Different Laser Sources for Laser Processing

Table 2.1 gives an overview of different laser sources (**C**arbon **D**ioxide ($CO_2$), **D**iode-**P**umped **S**olid-**S**tate **L**aser, **H**igh-**P**ower **D**iode **L**aser and **E**xcited **D**imer (Excimer)) which are used in laser processing. Compared to the DPSS, HPD and Excimer lasers, the $CO_2$ laser operates at a longer wavelength. However, the $CO_2$ laser is an established source for multi-kilowatt processing (Steen, 2010).

**Table 2.1 Overview of different lasers for laser processing**

| | Fiber Laser | $CO_2$ | DPSSL | HPDL | Excimer |
|---|---|---|---|---|---|
| **Lasing Medium** | Semiconductor | Gas Mixture | Crystalline Rod | Semiconductor | Gas Mixture |
| **Wavelength** | 1.030 – 2.100 µm | 10.6 µm (9.6) | 1.064 µm | 0.2-1.6 µm | 193-350 nm |
| **Output Power/ Peak Power** | Up to 10 KW | Up to 50 kW (mostly 15 kW) | Up to 6 kW | Up to 10 kW | 10 – 30 MW |
| **Beam Quality** | 0.342 mm mrad | 3.7 mm mrad | 12 mm mrad | 85 mm mrad | Below 4 mm mrad |
| **Power Efficiency** | 80 % | Up to 10 % | 10-20 % | 30-50 % | 2 % |
| **Size** | Very small | Large | Small | Very Small | Medium |
| **Applications** | Welding; cutting; sintering; marking; drilling; heat treatments; Alloying | Cutting; Welding; Cladding; Multi-kW processes; Marking | Drilling; Cutting; Welding; Marking; Cladding; Semiconductors | Drilling; Welding; Cutting; Cladding; Hardening; High heat input Processes | Pulsed deposition; Ablation; Medical Applications; Photolithography Cleaning |
| **Advantages** | Compact; excellent beam properties; thermal properties; cost-effective | Faster processing due to high power; Processing of heavier-gauge materials; Lifetime | Short wavelength; Low Cooling; Narrow Optical Bandwidth; Lifetime Wide range of gain media | High Powers; Compact; Cost-effective; Energy-Efficient | Very short wavelength |
| **Disadvantages** | Power Scaling due to non-linear effects; destruction threshold fibres | High Wavelength High Cooling Rates | High cost per Watt Pump diodes are less robust than lamps Compromise between power and beam quality | High cost per Watt of pump power; instead often lamp-pumped; Diodes less robust than discharge lamps | Limited Lifetime Hazardous Expensive |
| **References** | Tuennermann, 2000; Mueller et al., 2006; Kurkov, 2007; Paschotta, 2008; Limpert et al., 2009; Richardson et al., 2010 | Powell and Kaplan, 2012; Ready and Farson 2001; Meijer, 2004; Powell, 1998; Du et al. 1995 | Kaplan, 2011;Killi et al., 2008; Giesen et al., 1994; Fan and Beyr, 1988; Fan, 1990; Beyr, 1988 | Woods, 2009; Timmermann et al., 2008; Poprawe and Schulz, 2003; Bachmann, 2003;Diehl, 2000; Li, 2000 | Wu, 2009; Junger and Schmidt, 2007; Hecht, 2008; Basting et al., 2002; Ewing, 2000 |

### 2.2.5 Current equipment at Loughborough University

Research at Loughborough University was conducted on a SPI redPower 200 W fiber laser (SP-200C-0002 CW / Modulated) provided by SPI Lasers UK Ltd., Southampton. The fiber laser operates at a central emission wavelength of 1075 nm with a variable output power of 10 W to 200 W. The basic optical and laser beam specifications can be seen in Table 2.2. Additionally the laser system is equipped with a helium-neon (HeNe) targeting laser which is used for optical cavity alignment. The HeNe targeting laser has an emission wavelength of 650 nm to 680 nm.

**Table 2.2 Specification of optical and beam parameters for SPI redPower 200 W laser**

| ***Parameter*** | ***Unit*** | ***Value*** |
|---|---|---|
| ***Optical Specifications*** | | |
| Rated output power | W | 200 |
| Central emission wavelength | nm | 1075 ± 5 |
| Output power tunability | % | 10 – 100 |
| Minimum average power | W | 20 |
| Frequency | Hz/kHz | 100 – 10 |
| Pulse duration | ms | 0.01 – 10 |
| Maximum peak power | W | < 10 x CW |
| ***Beam Specifications*** | | |
| Beam Diameter | mm | 5 ± 0.5 |
| Beam Divergence[2] | mrad | 0.32 |
| $M^2$ | - | < 1.1 |
| Beam Parameter Product (BPP) | mm.mrad | 0.38 |

In Figure 2.25 the SPI red Power fiber laser is displayed. The beam delivery unit is coupled into a fine cutting head with a fixed focal length of 50 mm (FS 50) developed by Precitec Group Daggenau, Germany. In order to avoid back reflections an isolator (SP-ISO) is attached to the beam delivery optics before the beam is coupled into a SP-BET 2.0 beam expander. The main cutting head

contains a focusing lens with a diameter of 20 mm (see Figure 2.26). The focal and beam position of the laser beam can be adjusted using horizontal and vertical devices on the cutting head. The processing gas is delivered via three apertures arranged in 120° position to each other below the focusing lens which allows protection of the focusing lens from dirt and plume during processing.

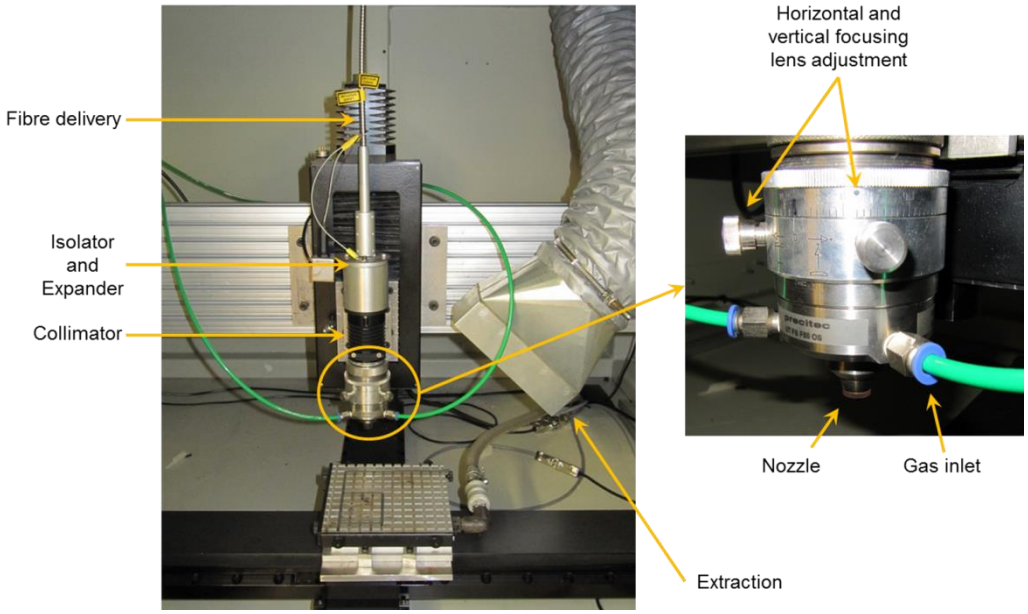


**Figure 2.25 Original fiber laser set-up**

Three different processing gases can be employed: air, oxygen and nitrogen which are delivered coaxially to the laser beam via a conical nozzle. Three different nozzle exits diameters were readily available (0.3 mm, 0.8 mm and 1 mm). Different nozzles sizes can show different characteristics such as insufficient gas flow and consumption for too large nozzles (Ion, 2005). Small nozzle diameters require precise alignment but may help localising the gas flow (Powell, 1998). The gas pressure can be regulated by the use of a gas flow meter. A water chiller unit is used to keep a temperature of 20 °C. Fumes produced while processing, are removed using an extraction system.

In Figure 2.26, a schematic representation of the laser set-up can be seen. The fiber laser contains multi-mode semiconductor laser diode emitters for pumping light into an active signal fibre which then is absorbed by active ions in the core. This type of fibre has been developed by SPI as the GTWave™ technology

(Grudinin et al., 2004). In GTWave™ technology, multi-mode fibres and the signal fibres are in contact with each other and surrounded by a low index polymer coating (Norman et al., 2004; Kurkov, 2007).

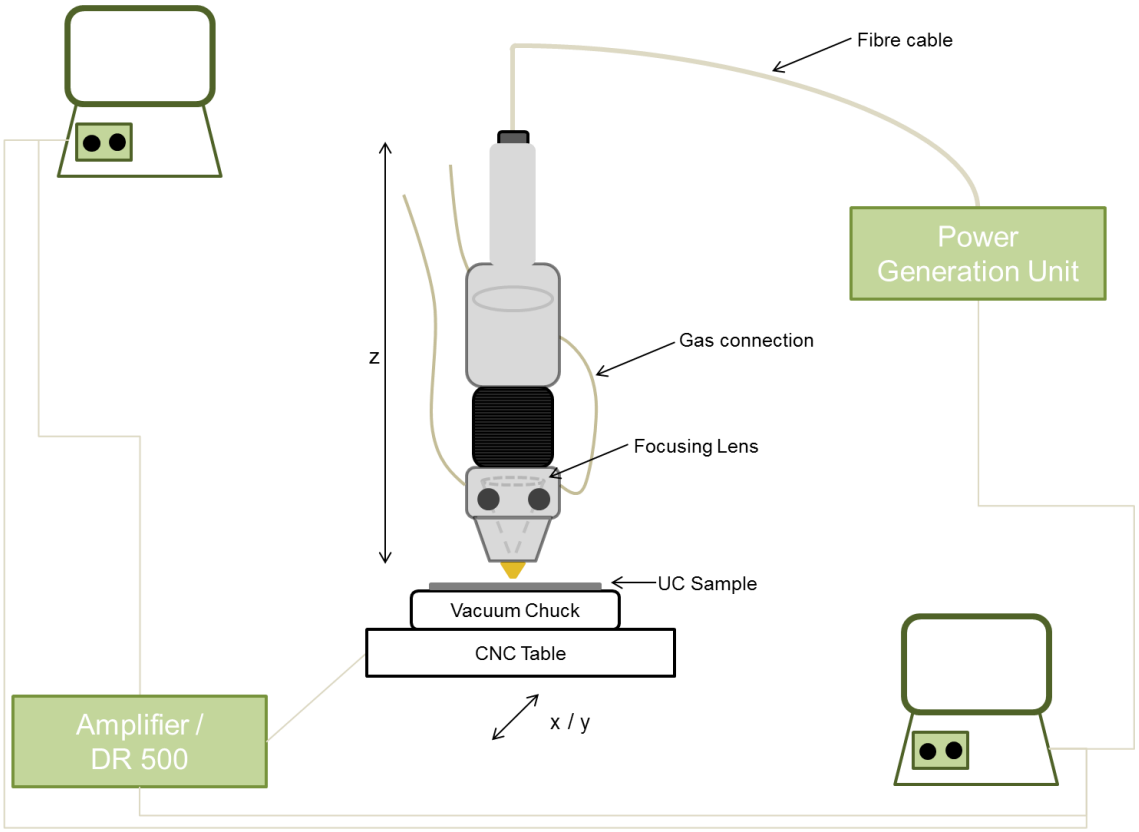


**Figure 2.26 Schematic overview of the fiber laser system**

To control the fiber laser, the laser is connected to a computer which runs the laser control software (GUI) to control the power output and operating mode. The GUI is also used for controlling the RPG 1000 Millennium pulse generator which modulates frequencies of up to 40 kHz and sets the pulse width. The pulse generator can be operated as gated, single shot and continuous. An Aerotech DR 500 amplifier is used to control the x- and y- position of a CNC table on which the sample is placed. The traverse speed can be set to 1 – 4000 mm/min. The amplifier is controlled by the U 500 board software which is run by a second PC. A vacuum plate above the CNC table is used to hold the sample in a stiff and flat position. Additionally to controlling the CNC table, the Aerotech DR 500 amplifier also controls the processing gases by sending a signal to the

solenoids whenever the gas is required. The processing gases can be used automatically or manually. To produce the required pattern for laser processing, the software Licon AlphaCam is used. The software allows the user to produce the necessary CNC code for running the Aerotech U 500 software.

### 2.2.6 Laser Grooving

The proposed theoretical model for channel/shoulder processing in section 1.4 resembles the laser grooving process (Chryssolouris et al., 1988b). Laser grooving is a 3D process in which a blind groove is generated by a laser beam and single or multiple laser passes as can be seen in Figure 2.27. A coaxial or off-axial gas jet is used to remove the molten or evaporated material from the groove (Choi and Chryssolouris, 1995a; O'Neill et al., 2001).

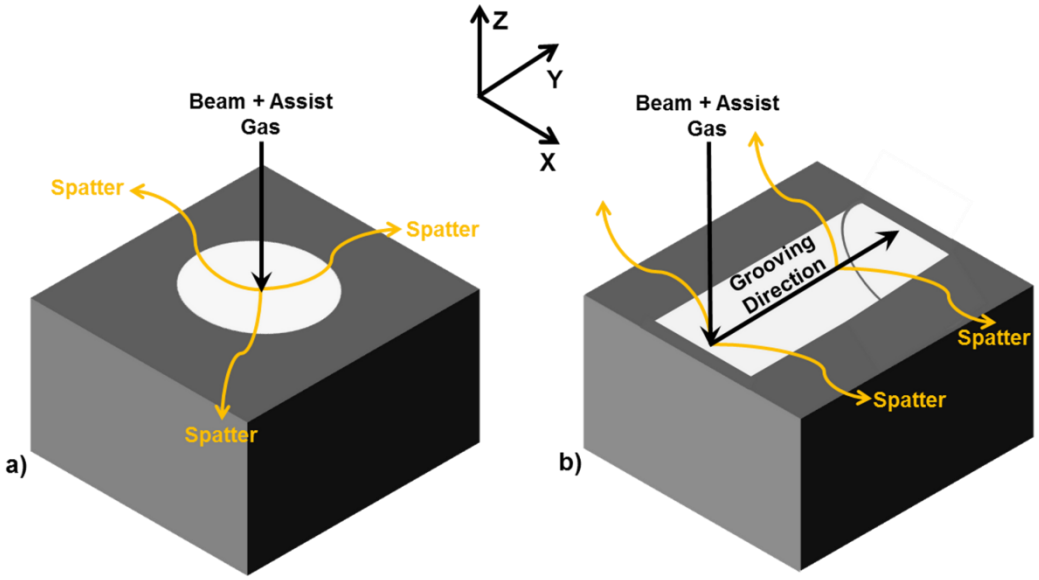


**Figure 2.27 Comparison of a) 2D drilling and b) 3D grooving process**

Laser grooving has been mainly researched for ceramics, composites and silicon structures (Chryssolouris et al., 1988b; Pan and Hocheng, 1996; Bai et al., 2006; Dhupal et al., 2008; Kam and Mazumder, 2008; Pecholt et al., 2008; Qi et al., 2009). For these difficult-to-machine materials (brittle, hard and inhomogeneity of composition), the laser presents a non-wear and non-contact

tool so that damage induced mechanically can be avoided (Hocheng and Pan, 1999).

Initial research in laser grooving has been carried out by Chryssolouris and Sheng (Chryssolouris et al., 1988b). A first attempt to theoretically model the achievable depth during groove processing was presented by Chryssolouris et al. (1988a) for ceramics. It was assumed that the material will be vaporised upon heating. It was found that an increase in power density created deeper cuts; an increase in traverse speed showed better groove qualities. Additionally, it was stated that the groove quality as well as the geometrical features depend on the beam profile and polarisation, spot size and depth of focus, focal point, assist gas and traverse speed. A model for composites and single-beam CW-experiments with a coaxial nitrogen gas jet was presented by Chryssolouris et al. (1988b). Additional to the main influencing parameters on laser grooving for ceramics, power density and the number of laser passes have to be considered as well. It was found that low powers and high traverse speeds minimise groove width and damage; a linear relationship between groove depth and power density was detected. The linear relationship has been stated by other authors (Choi and Chryssolouris, 1995b; Kumar and Gupta, 2010; Shamsaei and Ghoreishi, 2011). The theoretical model was developed further by Choi and Chryssolouris (1995a) integrating heat conduction. For aluminium oxide ($Al_2O_3$) processed with a CW laser and an off-axis gas jet, good agreement was achieved for the predicted depths with an absorptivity of 0.2. A theoretical model including the scanning direction and properties of composites was presented by Sheng and Chryssolouris (1995). They found that axial scanning showed and that the heat conduction reduced the energy for vaporisation and groove depth. In radial direction, grooves were found to be larger with less heat conducted away due to the composite properties. For both directions the width was twice the size of the beam diameter. A 3D finite element analysis for predicting the groove depth in combination with power, traverse speed and pulse frequency for steel was presented by Shamsaei and Ghoreishi (2011). It was found that low traverse speeds and decreasing the pulse frequency resulted in deeper grooves due to the increased energy provided in comparison

to fast speeds and shorter pulses which has also been stated by Stournaras et al. (2009).

Kumar and Gupta (2010) studied the influence of laser power, repetition rate, gas pressure and number of passes on grooving of steel and aluminium. They found that constant laser power and lower repetition rates resulted in deeper grooves due to the increase in energy as well as a saturation of depth for multiples passes due to insufficient energy at the bottom of the groove. Lallemand et al. (2000) found that the groove width is primarily dependent on the spot size. The groove depth as well as melt ejection is dependent on the gas jet angle. If the melt was not ejected an increase of the HAZ was observed. Mai and Lin (2003) found that with an increasing gas jet angle a two-peak profile was developed. They concluded that the pressure gradient which creates the shock wave to expel molten material was reduced with higher gas jet angles. In 2006, Mai and Lin investigated two different gas types for the laser grooving process and found that the resultant depth at different gas jet angles and traverse speeds was higher for oxygen than for nitrogen. O'Neill et al. (2001) investigated the use of two gas jets with two different gases (oxygen and nitrogen) on laser grooving and found that an optimum range of oxygen assist gas pressure exists. Chryssolouris et al. (1988a) stated that depending on the power of the gas jet, material will be ejected in different directions – the desirable direction is forward to minimise the time the molten material is in contact with the walls of the groove.

### 2.2.7 Laser Material Interactions for Aluminium Alloys

The material investigated in this thesis was an aluminium alloy. Hence, the following laser-material interactions will be confined to mainly laser-aluminium interactions. Aluminium can be classified in wrought and cast alloys (ASM, 1990). Wrought aluminum alloys can be further classified in heat treatable and non-heat treatable (ASM, 1993). The difference is that heat treatable aluminium alloys are strengthened by precipitation hardening and non-heat treatable alloys by work hardening and sold solution strengthening (ASM, 1993; Polmear, 2006;

Ryen, 2006). An overview of the different wrought aluminium alloys and their main alloying elements is given in Table 2.3. Due to their different responses to heat treatment and different alloying elements, the aluminium alloys experience different microstructural changes as will be discussed for the heat-affected zones (see section 2.2.9).

**Table 2.3 Overview of wrought aluminium alloys**

| **Non-heat treatable** | | **Heat treatable** | |
|---|---|---|---|
| International Alloy Designation System | Main Alloying Element | International Alloy Designation System | Main Alloying Element |
| 1xxx | 99% Al | 2xxx | Cu |
| 3xxx | Mn | 6xxx | Mg + Si |
| 4xxx | Si | 7xxx | Zn |
| 5xxx | Mg | | |
| 8xxx = Special alloy due to both mechanisms of hardening applicable. The main alloying element is Lithium. | | | |

***Reflectivity and Absorptivity***

Laser light impinging on a metal surface can either be reflected or absorbed. Reflectivity describes the portion of incident radiation that is reflected back by the surface of a material (Incropera and DeWitt, 2002). The light that is reflected is lost and not available for processing of a material. Absorptivity describes the amount of coupling incident energy into the material. This energy is transformed into thermal energy which is then used for laser processing (heating, melting, vaporisation). Reflectivity and absorptivity are linked to each other. The amount of absorbed light is proportional to 1-R (R is the reflectivity) for metal surfaces (Ready and Farson, 2001). Both, reflectivity and absorptivity are dependent on a number of beam and material parameters which determine the behaviour of the material during laser processing (Hecht, 2002; Bergström, 2005; Steen, 2003a; Bergström, 2007a):

*Beam Parameters:*

- → Wavelength [µm]
- → Angle of Incidence [degrees]
- → Polarisation (direction of electric field in light wave)
- → Intensity [W/m$^2$]

*Material Parameters:*

- → *Material Composition*
- → *Temperature [K]*
- → *Surface roughness [µm]*
- → *Surface impurities (oxides, grease, dirt etc.)*

In Figure 2.28, a graphic representing the absorption in relation to the wavelength can be seen.

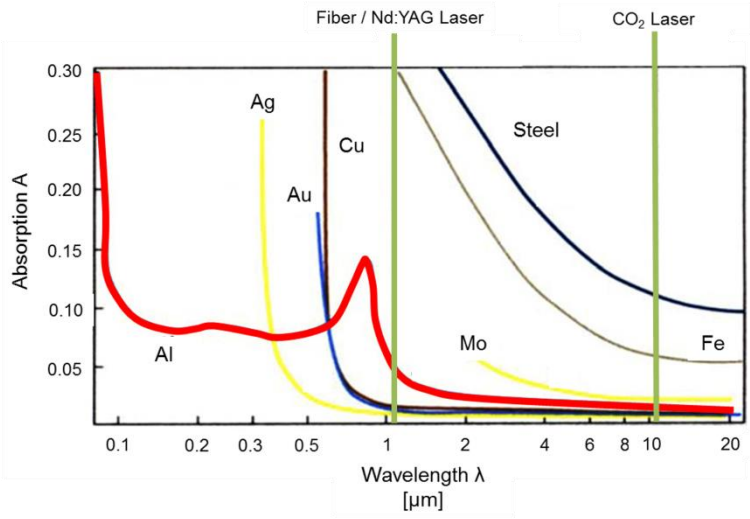


**Figure 2.28 Comparison of absorption for fiber/ Nd:Yag and $CO_2$ laser depending on the wavelength (Quintino et al., 2007)**

The fiber laser with a characteristic wavelength of 1.06 µm shows higher absorption values for aluminium than the CO2 laser with a characteristic wavelength of 10.6 µm (Duley, 1983; Xie and Kar, 1999; Kou, 2002; Quintino et al., 2007; Kwon et al., 2012). The reason for this is that shorter wavelengths exhibit more energetic photons which can be absorbed by a higher number of bound electrons (von Allmen, 1987; Steen 2010). Hence, reflectivity decreases and absorptivity is increased as the wavelength of the incident light decreases

(Steen, 2003a). At ambient temperature the absorption for as-received aluminium has been stated to be 16 % (Bergström et al., 2007a; Kwon et al., 2012), however, absorption may increase up to 20 % at the on-set of melting (increased surface temperature) for a wavelength of 1.06 µm (Xie and Kar, 1999; Pierron et al., 2007). For high powers (10 kW to 18 kW) along with increased surface temperatures, the beam gets trapped inside a keyhole (Patel and Brewster, 1990) as well as ionisation of plasma which defocuses the beam and leads to absorption values of 50 % to 93 % (Huntington and Eagar, 1993; Schneider et al., 2008; Pierron et al., 2007; Kawahito et al., 2012).

The reflectivity/absorption of an aluminium surface can also be influenced by the natural formation of an amorphous oxide film ($Al_2O_3$), with a thickness ranging from 2 nm to 10 nm (time-dependent), at ambient temperature (Cabrera and Mott, 1949; Mills, 1985). Due to its amorphous structure and the high melting point of 2300 K (Caristan, 2004) (melting point of aluminium = 933.15 K (Brandes and Brook, 1998)), the oxide layer can increase energy absorption by trapping the beam causing multiple reflections (Ursu et al. 1984; Patel and Brewster, 1990; Bergström et al., 2007b) as well as cause variations in absorptivity due to multiple reflections (Eagar and Huntington, 1983). Furthermore, purposefully induced surface oxidation can increase the absorption (Arata and Miyamoto, 1972; Xie and Kar, 1999). Increasing multiple reflections on the surface of aluminium can also be achieved by modifying the surface roughness in form of sandblasting, with sandpaper, texturisation or painting (Arata and Miyamoto, 1972; Eagar and Huntington, 1983; Xie and Kar, 1999; Sanchez-Amaya et al., 2011; Kwon et al., 2012).

The high reflectivity or low absorption of aluminium alloys presents a challenge in various laser processes such as welding, cutting and drilling as high power densities, approximately 1 x $10^6$ W/$cm^2$ (Shiganov et al., 2011) are required to initiate melting (Weckmann et al., 1997; Powell, 1998; Dausinger, 2000; Lujendijk, 2000; Tunna et al., 2005). High power densities are further required as aluminium exhibits two other challenging factors which are a high thermal conductivity ($\lambda$ = 238 W/mK) and thermal diffusivity ($\alpha$ = 8.8 $m^2$/s x $10^{-5}$) (Kou,

2002). This means that the heat input will quickly be conducted away from the irradiated surface which can not only prevent sufficient heat input for melting but also produces large heat-affected zones (Weckman et al., 1997; Xie and Kar, 1997; Ion, 2005; Riveiro et al., 2010a).

### 2.2.8 Melt Ejection Variables

In laser drilling of metals the melt removal mechanisms play an important role as melt can adhere around the channel periphery as spatter and at the walls and the bottom of the hole as a recast layer (McNally et al., 2004). Melt adherence is unwanted as finishing or cleaning of the surface is required because the produced melt can have a complete different structure than the main material (Kar and Mazumder, 1990; Steen, 2010). The control of melt ejection is wanted in this study as the shoulder structures shall consist of the melt ejected from the channel.

Melt removal mainly depends on the power intensity and the material properties (Körner et al., 1996; Voisey et al., 2003). It can be classified as melt ejection via melting and vaporisation when the melting temperature of the material is reached, vaporisation-induced melt ejection when the power density is sufficient to completely transform solid material into vapour (Semak and Matsunawa, 1997; Kudesia et al., 2002; Voisey et al., 2003) and explosive melt ejection when the boiling point of the material is passed which applies especially for short laser pulses (Yilbas and Sami, 1997; Xu and Willis, 2002; Porneala and Willis, 2006). Additionally, the assist gas may play an important role during melt ejection (Semak and Matsunawa, 1997). In Figure 2.29 the different melt ejection mechanisms are shown. For this study a) and b) have been identified as the dominant ejection mechanism.

In order to achieve melt ejection, a certain power density has to be reached otherwise the heat will be lost by conduction (Chun and Rose, 1970; Von Allmen, 1976, Körner et al., 1996, Zhang and Faghri, 1999).

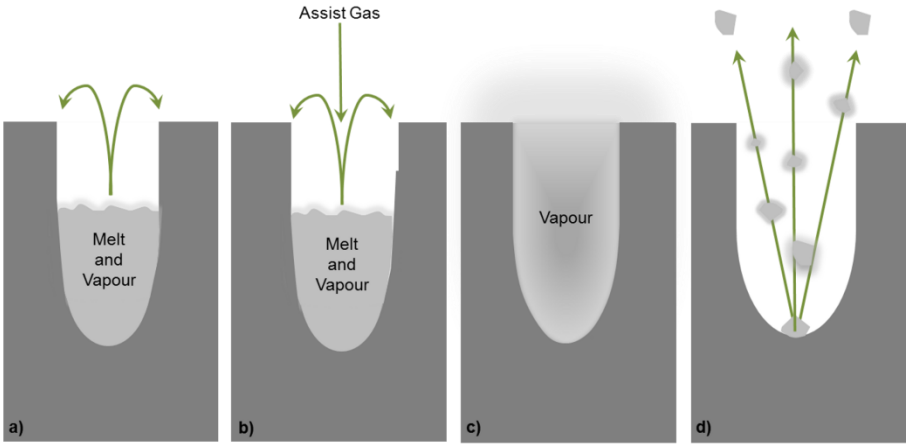


**Figure 2.29 Different melt ejection mechanisms a) recoil-induced melt and vapour ejection, b) with additional assist gas, c) vapour ejection and d) explosive ejection**

In 1976, von Allmen (1976) suggested that melt ejection starts when vaporisation of the metal will form a recoil pressure which causes a radial liquid motion. Hence, the surface tensions have to be overcome by the tangential pressure force (Chan et al., 1988; Basu and DebRoy, 1992; Semak et al., 2006). Until now this assumption is the basis for studies concerned with material removal. For aluminium, melt is removed as a liquid at low powers (Chan and Mazumder, 1987). A low melt ejection rate will be observed as high recoil pressures cannot be induced at low powers (Chan and Mazumder, 1987; Voisey et al., 2003). The quantity of melt ejection varies with the viscosity of the material, thermal conductivity (for CW processing), power density, spot size and traverse speed (Chun and Rose, 1970; Armon et al., 1989; Körner et al., 1996; Zhang and Faghri, 1999; Voisey et al., 2000; Solana et al., 2001). The thin layer of melt which is formed when the melting temperature has been reached will be acted on by the recoil pressure and form the recast layer after irradiation (Kar and Mazumder, 1990; Voisey et al, 2003). Ganesh et al. (1996) found that recast formation can affect the hole geometry. Kar and Mazumder (1990) stated that recast layers can be decreased when vaporisation is the dominant material removal mechanism as well as a decrease in spot size or increase in intensity.

If an assist gas is present, assist gas and recoil pressure will act together on melt expulsion (Semak and Matsunawa, 1997; Yilbas and Aleem, 2006). Low et al. (2000a) found that argon worked in tandem with the melting of material and

aided ejection in a radial manner whereas oxygen compensated the gas-jet assist due to the exothermic reaction (Powell et al., 2009). Furthermore, argon had a cooling effect on the melt whereas for oxygen cooling was negligible. However, oxygen reacted with the melt and increased the surface temperature (Semak and Matsunawa, 1997; Low et al., 2002). When an assist gas is used at low power densities (< 10 MW/cm$^2$) melt removal will be present. Schneider et al. (2007) found that assist gas will slow the melt ejection down which has also been observed by Tani et al. (2003). Kar et al. (1992) found that the assist gas is insignificant for depth and recast layer thickness.

As mentioned before, spatter is an unwanted characteristic of the laser drilling process. Additionally to the required removal, spatter can disturb the absorption in closely drilled holes which can lead to insufficient repeatability of the process (Low et al., 2001). Additionally, increasing spatter bonding strength has been observed for overlapped spatter resulting in insufficient removal for inert gases (Low et al., 2000b). Overlapping of spatter was observed for every pulse by Low and Li (2001). Spatter thickness increased with longer pulses and lower peak powers (Ng and Li, 2001).

Several authors have studied the influence of the assist gas pressure on the molten material: for steel, ejected particles were covered with an oxide layer when oxygen was used (Ivarson et al, 1991; Powell et al., 1993; Yilbas and Aleem, 2006). Chen et al. (2001) observed that steel will be less oxidised when air is used. For aluminium, a thin layer of aluminium oxide of ejected melt particles has been observed (Tunna et al., 2005; Baziz et al., 2006). Low et al. (2000a) observed that ejection sparks from an inert gas (argon) were smaller and less intense whereas the oxygen ejection sparks were larger and brighter owing to the exothermic reaction. The effect of different assist gas types on the spatter characteristics adhering next to the drilled hole were investigated by Low et al. (2000b): oxygen showed high spatter thickness and explosion-like spatter. Argon, nitrogen and air showed smaller thickness and uniform crater shapes which he owed to the inert nature of the assist gases. The spatter bonding strength was highest argon, nitrogen and air and lowest in oxygen as

this type of spatter was brittle in nature. An oxygen content of 40 % was found whereas argon showed no significant increase in oxygen content. The spatter for the other gases was thicker and brighter which led him to the conclusion that pure melt was ejected. Reg et al., 2011 found that larger spatter around drilled holes occurred for nitrogen and air in comparison to argon due to their partly-inert nature. Additionally, the hole diameter was smaller for argon than for air and nitrogen.

### 2.2.9 Microstructural Modification due to Laser Treatment

The heat input during laser processing has been shown to greatly affect the resulting microstructure and hence, the mechanical properties such as tensile strength or hardness. In laser welding, four different types of microstructural zones have been observed: the melted fusion zone (FZ), the partially melted zone (PMZ), the heat-affected zone (HAZ) which did not melt but was exposed to thermal cycles and the unaffected base metal (BZ) (David and Vitek, 1989; Zhao et al., 1999; David et al., 2003). The resultant microstructure is dependent on the solidification behaviour which is mainly controlled by the thermal gradient in the liquid, alloy composition, growth rate and undercooling due to rapid solidification (Savage et al., 1976; Lavernia et al., 1992; Kurz and Fisher, 1998; Mohanty and Mazumder, 1998; Ion, 2005). In general it can be said that pulsed laser processing creates smaller HAZ than CW laser processing. Due to the high thermal conduction gradient, laser processed aluminium will experience faster solidification than steel (Weckman et al., 1997).

For aluminium, studies concerned with the microstructure and the resulting mechanical properties have been mainly carried out for 2xxx, 5xxx and 6xxx alloys. Laser processing can result in planar, cellular (Bertelli et al. 2011, cellular-dendritic (Hirose et al., 1997; Venkat et al., 1997; Ramasamy and Albright, 2000; Pinto et al., 2003; Liu, 2005) or dendritic grains (Wong and Liang, 1997; Haboudou et al., 2003; Pakdil et al., 2011) depending on the solidification velocity from low to fast (Pfeiler, 2007). Hence, it has been shown that an increase in traverse speed during laser processing will induce finer

structures (such as dendrites) due to the lower heat input as well as decrease of the HAZ (Hegge and deHosson, 1990; Leech, 1989; Hirose et al., 1997; Venkat et al., 1997; Ramasamy and Albright, 2000). The solidification will start epitaxially from the bottom of the melt pool (highest thermal gradient) along the solid/liquid interface because the solidification speed at the bottom is zero will be the fastest at the solid/liquid interface (Savage, 1976; David et al., 1989; Kurz and Trivedi, 1994; Mohanty and Mazumder, 1998; Watkins et al., 1998: Pinto et al., 2003; Liu, 2005; Bertelli et al., 2011; Kalita, 2011).

Both types of wrought alloys (heat and non-heat treatable) show in general different mechanical properties after laser processing. Heat treatable alloys have been shown to lose their strength due to dissolution or coarsening of strengthening precipitates (ASM, 1993; Dausinger, 2000). Especially, the loss of strengthening alloying elements such as magnesium for the 6xxx series and overaging has been observed (Cieslack and Fuerschabch, 1988; Lujendijk, 2000; Ramasamy and Albright, 2000; Pakdil et al., 2011). The lowest strength is usually discovered in the HAZ (ASM, 1993; Hirose et al., 1997). Kalita (2011) observed for 2xxx and Sanchez-Amaya et al. (2009) for 5xxx the elimination of secondary phase precipitates in the laser melted region but found an uniform enrichment with copper via EDX maps. Liu et al. (2005) found for the 2xxx series in the FZ microsegregation of copper, magnesium, manganese and silicon which were rejected at the solid/liquid interface and a boundary layer of enriched alloying elements developed in the liquid ahead of the solidification front which was dependent on thermal gradient and solidification rate. Liu et al. (2005) also showed that an extended solid solubility was observed for copper due to rapid cooling. However, Pinto et al. (2003) showed an increase of hardness in the 2xxx series for the cellular structure and even higher values in the dendritic structure which he attributed to the fineness of the microstructure. De Mol van Otterloo et al. (1995) found an increase in hardness and suggested the same reasons as Pinto et al. (2003).

Non-heat treatable alloys have been shown to lose their strength due a reduction in solid solution strengthening. Cieslack and Fuerschbach (1988)

found that the 5xxx series loses strength due to the vaporisation of magnesium especially at lower welding speeds which was also observed by Blake and Mazumder (1985). Cieslack and Fuerschback also found a reduction in hardness in the FZ especially for slow welding speeds. The reduction in hardness was also observed by Moon and Metzbower (1993). Both attributed the hardness reduction to magnesium loss. Contrary, Haboudou et al. (2003) found for CW welding of 5083 an increase of hardness of nearly 10 % Vickers which was noticed by Venkat et al. (2003) as well. Haboudou et al. (2003) suggested that the fine dendritic structure in the equiaxed zone is responsible for the hardness increase which was observed and stated as well by Wong et al. (1997) for 4xxx due to precipitated silicon crystals. Khaleeq-ur-Rahman et al. (2010) showed that hardness increases in pulsed operation.

McCafferty et al. (1981) studied laser surface melting of 3xxx and found finely dispersed second-phase particles in a layered aluminium structure which was observed for 5xxx by Sanchez-Amaya et al. (2009) as well. Juarez-Islas et al. (1988) observed solid solubility extension for manganese due to rapid solidification but without microsegregation in 3xxx. Solute enrichment and solid solubility extension was also noticed by Wong and Liang (1997) for 4xxx. The dendritic structure will have high solute segregations which will consist of (Fe,Mn)$Al_6$ for 1xxx and 3xxx alloys; Si for 4xxx alloys; and $Mg_3Al_2$ for 5xxx alloys for non-heat treatable alloys (ASM, 1993; David et al., 2003).

## 2.3 Summary

The background showed that bond formation for various embedded fibre types was stronger for higher oscillation amplitudes and pressures as higher interfacial stresses will enhance the visco-plasticity of the material (Kong et al., 2004b, Kong and Soar, 2005b, Yang et al., 2007). Consequently, low oscillation amplitudes and pressure resulted in incomplete encapsulation of fibres or separation of the foils (Kong et al., 2004b; Li and Soar 2007; Friel, 2011).

Yet, it has also been shown that higher amplitudes and pressures may lead to distorted or broken fibres as well as interfacial reactions and displacement

between fibres (Kong and Soar, 2005a; Friel and Harris, 2010; Hahnlen and Dapino, 2010; Yang et al., 2010). Research concerned with high volume fibre integration has been proven difficult as insufficient energy was delivered to the interfaces to induce plastic flow and/or prevention of sufficient metal-to-metal contact for bonding (Kong et al., 2004b; Kong, 2005; Li and Soar, 2007; Johnson, 2008; Friel, 2011).

In order to further smart structure research, a method enabling secure and accurate integration of high fibre volumes by preferably lowering oscillation amplitudes and contact pressure is necessary.

The demands for accurate and secure fibre integration of possibly different sizes can be met by laser processing of grooves. Fiber lasers have been shown to be an attractive solution for laser processing in the micrometre range due to their beam qualities (Tünnermann, 2005; Limpert et al., 2007; Kratky et al., 2008; Beyer et al., 2012).

A large proportion of the literature on laser grooving has been focused on theoretical predictions for composite or ceramic materials (Chryssolouris et al., 1988b; Choi and Chryssolouris, 1995b) and relatively few on metals (Kumar and Gupta, 2010). Especially laser grooving of aluminium (and the inherent thermal properties) in conjunction with controlled melt/spatter manipulation for new structures rather than reduction of spatter (Kar and Mazumder, 1990; Low et al., 2001; Steen, 2010) has not been investigated before.

# Chapter 3.
# Research Approach

## 3.1 Problem Definition

Research into UC as a suitable method for fibre integration into metal matrices has been successfully shown over the past decade and thus the potential for future smart material fabrication has been established (Kong and Soar, 2005b; Yang et al., 2007; Li and Soar, 2009a; Friel and Harris, 2010; Hahnlen and Dapino, 2010). Yet, an increase in fibre volume has been shown to result in greater porosity at the fibre/foil and foil/foil interfaces and delamination of the foils due to insufficient plastic flow around the fibres and limited foil/foil oscillatory movement (Kong, 2005; Friel, 2011). Hence, high volume fibre integration when compared to traditional MMC processing techniques is restricted (Nair et al., 1985; Clyne and Withers, 1993; Armstrong et al., 1998). An increase in plastic flow might be enhanced by an increase in amplitude and contact pressure (Yang et al., 2009). However, delicate fibre types might lose their integrity due to pressure and oscillation movement. Furthermore, to adequately integrate fibres, the provision of fixed fibre boundaries is needed to prevent movement and damage of the fibres.

## 3.2 Hypothesis

*"It was hypothesised that a new approach for fibre embedment had the potential to securely and accurately consolidate while lowering the necessary plastic flow for fibre encapsulation. Laser-processed channels in the micrometre range can be fabricated into post-UC aluminium metal matrices by variation of laser power*

*[W], traverse speed [mm/s] and gas pressure [MPa]. The heat input of the laser will induce melting of the aluminium which can be distributed to the channel boundaries, by help of the assist gas, to form solidified shoulders. During integration of high quantities of fibres via UC, the shoulder will aid encapsulation of fibres by reducing the required amount of plastic flow and enhancing bond formation. The fabricated channels into post-UC samples will aid both secure positioning and maintain the integrity of high quantities of fibres during integration via UC."*

## 3.3 Research Approach

To determine the benefit of the channels/shoulders for integration of high quantities of fibres during UC, work was carried out in four stages:

**Stage 1:** Proof of the basic theory for channel/shoulder processing via a laser into UC samples:

→ Initial study to determine the influence of defined laser process parameters on single pass channel/shoulder formation; Experimental investigation of multiple passes to allow control of channel/shoulder geometries.

→ Analysis by macroscopic inspection of the channel/shoulder appearance as well as microscopic and scanning electron microscopy (SEM) inspection of the resultant geometrical features.

***Stage 2*:** Confirmation of consistency of multiple laser produced channels/shoulders:

→ Analysis of multiple channels/shoulders geometries for different gas types by non-contact and contact measurement techniques.

**Stage 3:** Evaluation of precise and secure integration of fibres with aid of channels:

→ Analysis (post-UC) of accurate placement of fibres by measuring the distances between the fibre cores; SEM inspection of fibre appearance.

**Stage 4:** Assessment of assistance of channels/shoulders for bond improvement:

→ Analysis of bonding quality after fibre embedding via LWD; determination of plastic flow behaviour around fibres and weld interface via SEM and energy dispersive x-ray spectroscopy (EDX).

# Chapter 4.
# Initial Study of Channel/Shoulder Formation by Fiber Laser Processing

## 4.1 Introduction

Chapter 4 details the initial study to investigate the use of a fiber laser as a possible aid to manufacture channels within an ultrasonically consolidated metal matrix. As shown in section 2.2.2, fiber lasers offer a high brightness and a high beam quality (Kratky et al., 2008; Richardson et al., 2010; Beyer et. al., 2012). Hence, a fiber laser offered the potential to apply high intensities to small areas which was favourable for the purpose of manufacturing a high number of narrow channels within a small area.

Chapter 4 was aimed at gaining fundamental knowledge of channel manufacturing for further UC purposes. An influential analysis via an Ishikawa diagram taking into account all possible parameters for laser processing as well as results from 2.2.6 and 2.2.8 suggested that power [W], traverse speed [mm/s] and gas pressure [MPa] would be the most influential variables on channel/shoulder manufacturing. The pre-UC processed Al 3003-H18 UC samples were radiated by variation of these parameters in order to understand their influence on channel formation. Additionally, the influence of three different gas types (air, nitrogen and oxygen) on aiding channel creation was examined. The samples were then macroscopically and microscopically inspected.

## 4.2 Methodology

### 4.2.1 Sample Preparation for Laser Processing via UC

The samples for laser processing were prepared by using the Alpha 2 UC machine introduced in section 2.1.4. All experiments were conducted on samples consisting of Al alloy 3003-H18. Al 3003-H18 was primarily chosen due to the utilisation in earlier UC studies concerned with bonding and fibre embedment (Kong, 2005; Yang et al., 2010). Hence, comparison of the results with earlier studies was warranted.

The fully strain-hardened alloy was supplied as a foil by United Aluminum, USA (24 mm wide and 100 µm thick) and had a nominal composition of: Al 97 wt %, Mn 1.2 wt %, Si 0.6 wt %, Fe 0.7 wt %, Cu 0.2 wt % (Kong, 2005). The properties of Al 3003-H18 can be seen in Table 4.1.

**Table 4.1 Material properties for Al 3003-H18 (ASM, 1990)**

| Material Property | Value |
|---|---|
| Tensile Strength [MPa] | 200 |
| Yield Strength [MPa] | 185 |
| Elongation [%] | 4-10 |
| Hardness [HB] | 55 |
| Shear Strength [MPa] | 110 |
| Liquidus temperature [°C] | 654 |
| Solidus temperature [°C] | 643 |

As mentioned in section 2.1.4, successful welding depends on the optimum combination of process parameters for the particular UC machine and material. Although a process window for Al 3003-H18 on the Alpha 1 UC machine had been established (Kong et al., 2004a), initial tests based on these parameters showed incomplete bonding for the Alpha 2 UC machine. Examples of differing welding outcomes for the Alpha 2 UC machine by variation of the contact pressure are given in Figure 4.1.

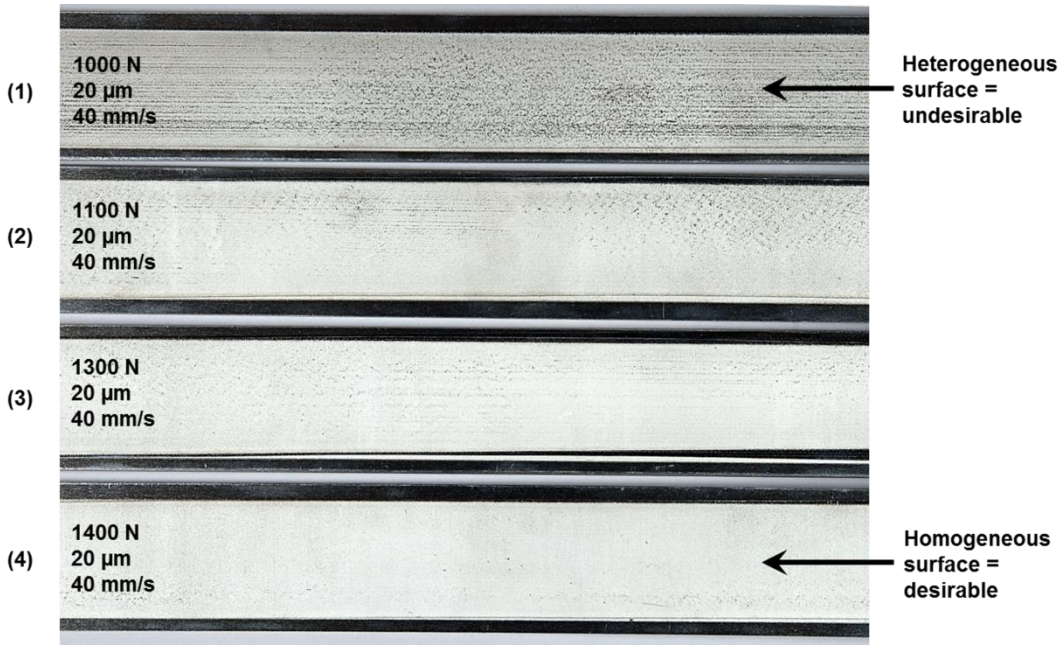


**Figure 4.1 Influence of different contact pressures on bond formation**

The heterogeneous surface for the first sample resembled the shiny surface appearance of the foil before UC processing. Additionally, the length of the sample exhibited weld lines. This meant that intimate contact and full bonding over the whole contact area was not established as some contact points remained unbonded (Yang et al., 2006). The fourth sample showed a homogeneous surface which meant that a higher pressure resulted in intimate contact and full bonding over the whole contact area was achieved.

For this study, all samples for laser processing were UC processed at a contact pressure of 1400 N, a weld speed of 40 mm/s and oscillation amplitude of 20 µm. The welding parameters were kept constant in order to limit the variety of influential parameters on laser processing. The samples were produced by firstly placing an Al 1050 supporting plate (330 x 29 x 1 mm) on the anvil. The supporting plate helped to prevent bending of the thin aluminium foil (Kong, 2005). A strip of Al 3003-H18 (approx. 400 mm long) was then placed above the supporting plate and finally consolidated to the supporting plate. After that, a second foil was welded to the already consolidated first foil. Two foils were considered adequate to allow sufficient thickness for laser processing of channels.

### 4.2.2 Influence Analysis

During the review of relevant laser literature, it became apparent that laser channel manufacturing will be a multi-parameter controlled process. To get an overview of all possible parameters and to eventually restrict the number of the variable parameters for channel manufacturing, an Ishikawa diagram was developed which can be seen in Figure 4.2.

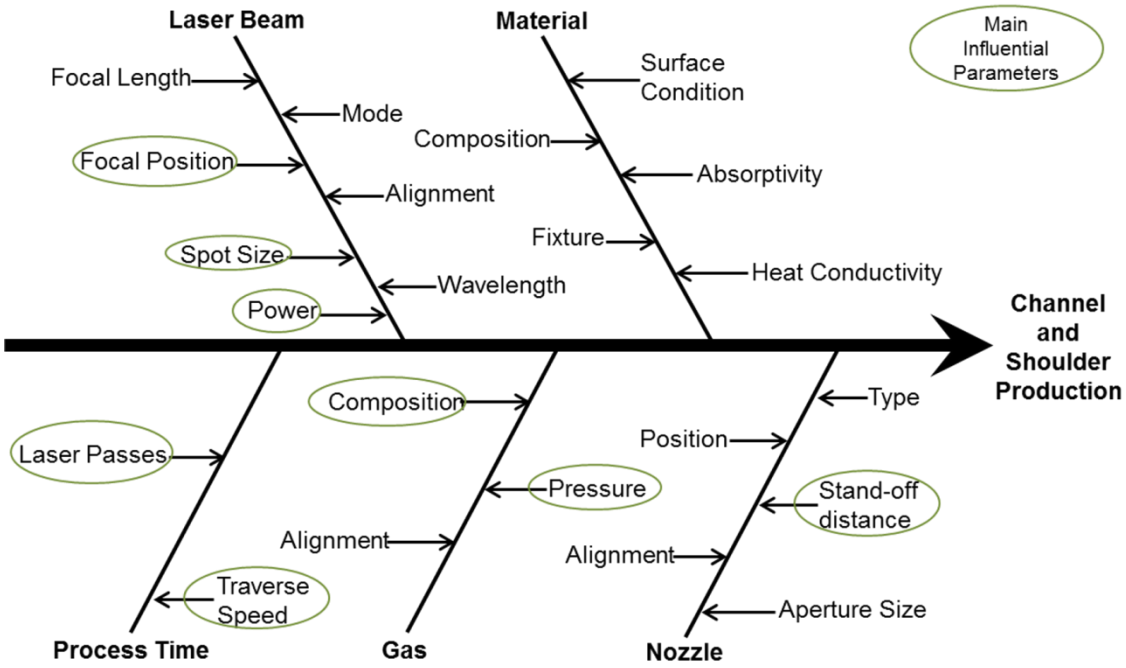


**Figure 4.2 Ishikawa diagram for influence analysis**

The main “causes” for channel and shoulder production were identified as laser beam interaction, material, process time, assist gas and nozzle. The “sub-causes” were classed in a) variable process parameters and b) fixed parameters influencing channel/shoulder formation. The fixed parameters included laser beam properties such as wavelength and material. It was already decided that the material to be used was Al 3003-H18 and the type of laser (fiber laser). Ergo parameters such as wavelength or composition of the material were fixed. The most influential, variable parameters were chosen based on the literature review in 2.2.6 and 2.2.8. Focal position and spot size were important as they defined the intensity of the laser beam and hence, the

smallest achievable channel sizes (Steen and Mazumder, 2010). The amount of laser passes and the traverse speed would define the amount of time the heat has to conduct into the Al and to influence the original microstructure. This was an important consideration as the HAZ was intended to be as small as possible in order to lower the influence on material characteristics (Venkat et al., 1997; Hirose et al., 1999). Additionally, the amount of laser passes as well as the traverse speed define the amount of heat to be produced for melting (Lallemand et al., 2000). The gas and recoil pressure define the amount of molten material which can be removed from the channel and hence, was important for the distribution of the molten material to form a shoulder (Semak and Matsunawa, 1997). Lastly, the gas type would have an influence on channel formation and furthermore may influence the bonding process during UC (Low et al., 2000b; Yang et al. 2006) as the gas composition may affect the material structures.

### 4.2.3 Laser Processing by Variation of Processing Parameters

Laser processing was carried out by using the SPI 200 W fiber laser already introduced in section 2.2.5. The UC sample was placed on the vacuum chuck which was fixed to the CNC table in order to hold the sample flat and in position during laser operation. The laser was then focused to a stand-off distance of 0.3 mm to the upper surface of the sample (Ready, 2001). The stand-off distance was chosen firstly due to the advice from SPI and secondly pre-tests showed that this stand-off distance gave best results for penetration. The theoretical spot size was calculated as 13.7 µm from Equation (2) with a focal length of 50 mm, an initial beam diameter of 5.5 mm and an $M^2$ value of 1.05. The values were supplied by SPI Lasers UK Limited. It was considered measuring the spot size however there was no equipment available due to the short focal length of the laser. The power density of the incident beam (see equation (4)) corresponded to 6.78 x $10^7$ W/$cm^2$ for 100 W and 1.36 x $10^8$ W/$cm^2$ for 200 W. All tests were carried out in CW mode. The pulsed option was considered, however pre-tests on pulsed output exhibited non-penetration of the material.

Laser processing was carried out by varying the main identified parameters: power, traverse speed and assist gas pressure. The varied parameters can be seen in Table 4.2. Power was varied in steps of 20 W beginning by 120 W – 200 W. The assist gas pressure was varied in steps of 0.2 MPa, 0.6 MPa and 1 MPa which corresponded to the highest gas pressure which could be achieved. The traverse speed was varied between 75 mm/min to 375 mm/min in steps of 100.

**Table 4.2 Overview processing parameters for process window**

| Nozzle type [mm] | Gas | Power [W] | Traverse Speed [mm/min] | Gas flow rate [MPa] |
|---|---|---|---|---|
| 0.8 | Air | 120-140 | 50-350 | 0.2; 0.6; 1 |
| 0.8 | Nitrogen | 120-200 | 50-350 | 0.2; 0.6; 1 |
| 0.8 | Oxygen | 120-200 | 50-350 | 0.2; 0.6; 1 |
| 0.8 | Air (black coating) | 120-200 | 50-350 | 0.2; 0.6; 1 |
| 1.0 | Air | 120-200 | 50-350 | 0.2; 0.6; 1 |

Two different types of nozzles (0.8 mm and 1 mm) were used for air in order to investigate whether there is an effect of the nozzle size on the channel layout. Additionally, a test where the aluminium sample was coated in black ink was carried out to investigate the influence of the reflectivity of the original foils. Three different gas types were investigated – nitrogen, compressed air and oxygen. The different gas types were investigated in order to understand their influence on channel processing. Nitrogen was chosen due to the inert nature, oxygen was chosen due to the ability to react exothermically and air was chosen due to the mixture of approximately 80 % nitrogen and 20 % oxygen which could also enhance an exothermic reaction (Charistan, 2004).

The samples were radiated by a single pass following the pattern shown in Figure 4.3. The pattern was created by using G-Code language which

controlled the CNC table's direction and speed. This ensured that consistency in channel length and traverse speed. A rectangular pattern was chosen to understand if channels would show the same characteristics in X- and Y direction.

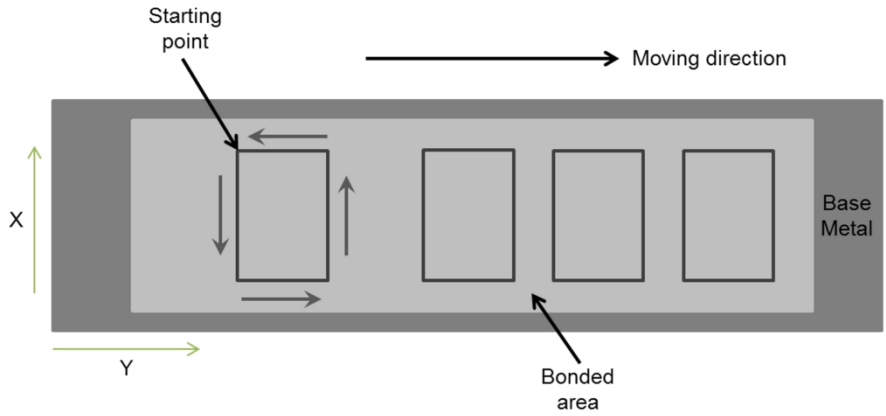


**Figure 4.3 Generated pattern for process window**

The reason for radiation in two directions was that, in case the channel appearance was the same for both directions, channels could be processed for two directions. Hence, fibres could be embedded in two directions to study the influence of fibre direction during UC. The laser radiation started at the indicated starting point, displayed in Figure 4.3 and followed the arrow direction (grey arrows) so that start and end point was the same.

Before the laser processing trials, the power output was measured. The results are displayed in Figure 4.4. The input power of the laser was set in between the available processing parameters for CW mode (10 W to 200 W). The output power was measured for various different set-ups as the output power proved to be less than the input. From Figure 4.4 it can be seen that the resulting output power was 30 % less for 200 W than the expected output power. Additionally, the output power was declining the higher the power input. It was reasoned that one of the power pumping units was faulty. This result was unexpected but due to the high cost of replacing of the part and the unavailability of other lasers operating at the standards of the fiber laser, experiments were carried out taking into consideration the lower power output.

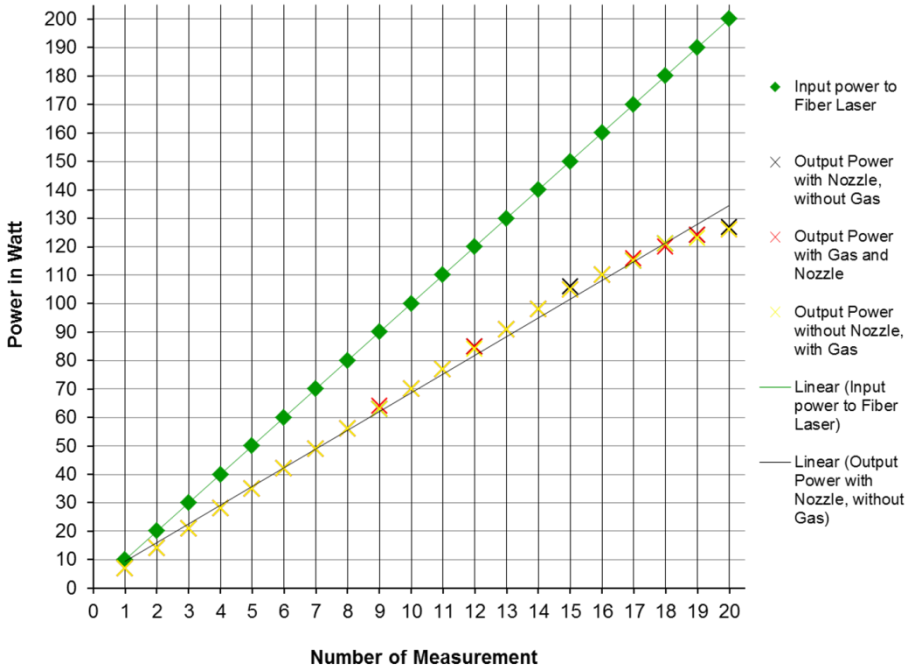


**Figure 4.4 Power output measurements for SPI 200 W redPower laser**

### 4.2.4 Macroscopic Inspection of Channel and Shoulder

To analyse the effects of the operating parameters upon processing quality, specimens were visually examined using two optical measurement devices. There were two measurement devices available: Alicona Infinite Focus by Alicona Imaging GmbH, Grambach, Austria and Zygo New View 700 Series supplied by Zygo Cooperation, Middelsfield, Connecticut, United States.

The Alicona Infinite Focus operates as an infinite focus microscope, whereas the Zygo New View operates as a white light interferometer. Both machines have in common that non-contact measurement is possible and 3D surface images can be generated. The difference between the two microscopes was that the Alicona Infinite Focus had the ability to focus to a lower depth. Additionally, the Alicona Infinite Focus had the advantage to measure steep flanks which was considered a necessary condition as it was hoped to create channels with exhibited steep sides. With the Zygo it was more difficult to measure the flanks and in order to properly analyse the channel geometry a program which calculated missing points was needed. Depending on availability and the characteristics of the channel depth, both machines were used. For

both machines a magnification lens of x10 was used. Table 4.3 shows the main operating characteristics.

**Table 4.3 Lens specifications for Zygo and Alicona Infinite Focus**

| Attribute | Zygo | Alicona |
|---|---|---|
| Lens magnification | x10 | x10 |
| Working Distance [mm] | 7.6 | 17.3 |
| HVFOV* [mm] | 0.70x0.53 | 1.429x1.088 |
| Optical Lateral Resolution [µm] | 2.19 | 1.1 |
| Sampling distance [µm] | 2.2 | 0.88 |
| Vertical Resolution [nm] | ≤0.1 | 100 |
| *Horizontal x vertical field of view. Size of imaged part. | | |

The laser processed specimens were positioned under the interferometer on a CNC gantry table. All specimens were mounted with an adhesive to a flat metal plate to ensure flatness of the specimen which may have been altered due to UC and heat treatment while laser processing. During all of the following visual inspections attention was focused on the extent of laser processing and not on shoulder features, as it was found difficult to generate appropriate depths.

The resulting data files were then analysed and interpreted with the Talymap Platinum Version 5 software. The following operations were carried out for every analysed sample.

→ Approximating non-measured points of the data file obtained from Alicona or Zygo measurements by using proven algorithms. This was especially necessary when using the Zygo as steep flanks were difficult to measure.

→ Levelling was used to remove the general slope of a profile which was the result of measurements that were not strictly horizontal due to laser processing and UC.

→ Generating a profile through the measured area to see if channels were created.

→ Generating a series of profiles: Used to see if the channel width and depth channels were consistent throughout their length.

→ 3D view: To give an overview of the whole channel/shoulder area.

Analysis of the channels was firstly conducted by categorising the samples into different groups by the channel appearance as can be seen in Figure 4.5.

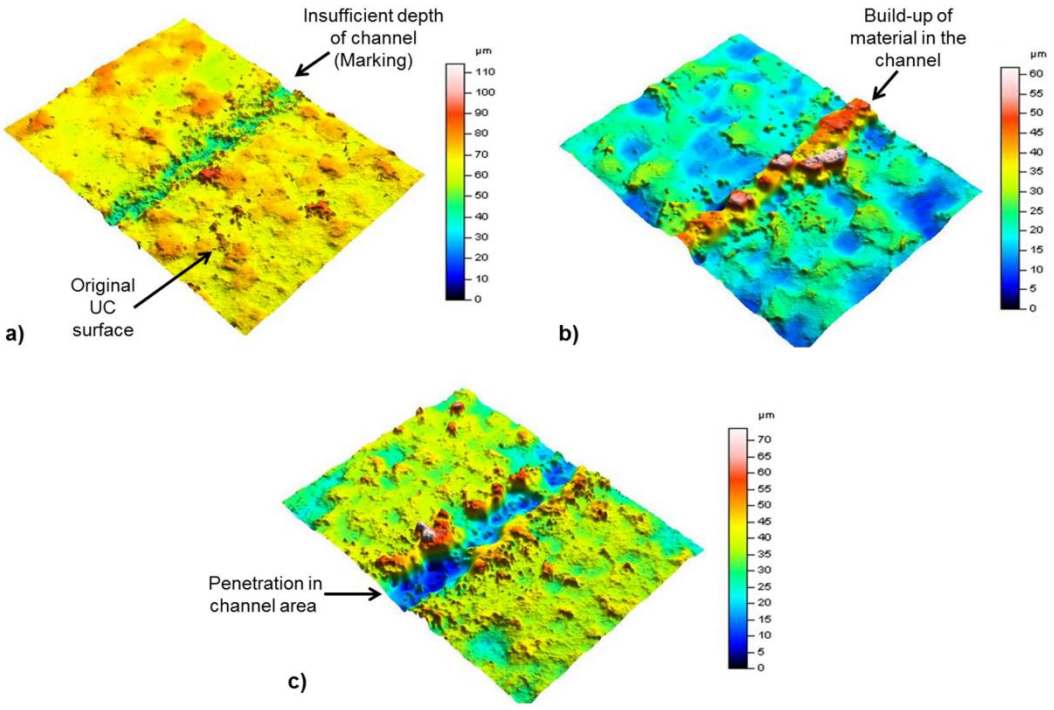


**Figure 4.5 Appearances of channels due to different influences a) marking, b) build-up and c) penetration**

The appearance was classified as a) marking, b) build-up and c) penetration. Marking meant that the laser had only a little effect on the channel creation. Build-up meant that material was either distributed on top of the channel or that the spatter was distributed unequally around the channel. Penetration meant

that a complete channel was created. Micrographs of the three different effects are shown in Figure 4.6.

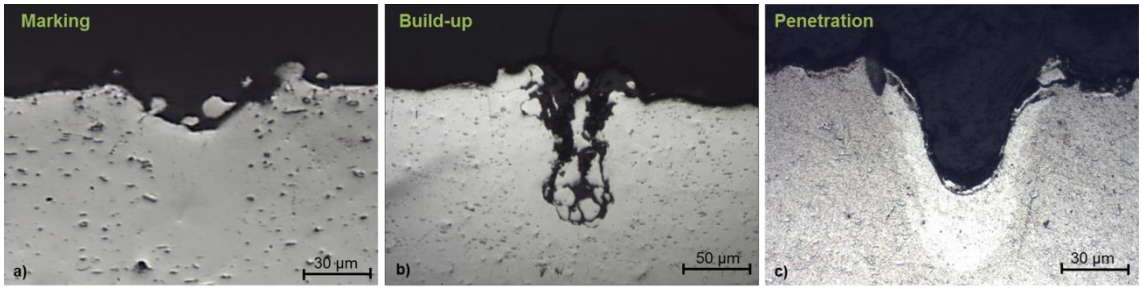


**Figure 4.6 Micrographs of a) marking, b) build-up of material and c) penetration**

The different effects were then compared to each other by obtaining a statistic overview to eliminate parameters for further laser processing. For further processing, only nitrogen and air were chosen as they gave the best penetration results which can be seen in Table 4.3 in section 4.3.2. The samples exhibiting penetration were then further analysed by measuring the width and depth of the channel and if applicable the width and depth of the shoulder. Analysis was carried out on the data received from the Zygo and Alicona.

Additionally, since the results for nitrogen and air varied, it was investigated whether the surface obtained from the UC manufacturing might be a possible influence on laser intensity. The inherent surface roughness after UC is displayed in Figure 4.7. The surface roughness of the foil material is purposefully induced while applying oscillations to the material as a natural part of the UC process (Li and Soar, 2009). The surface roughness varied constantly over the sample area. The arithmetic mean deviation value of the surface was stated to be Sa = 4.97 µm (Edmonds and Harris, 2011). As a result of this, the reflection of the laser beam could vary with the surface geometry while radiating.

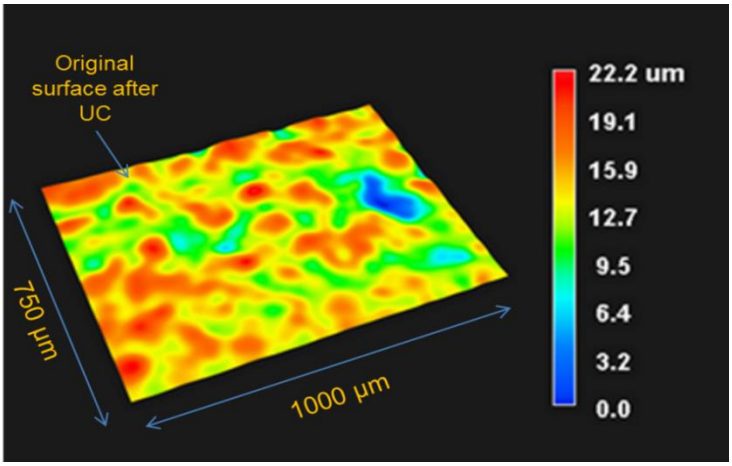


**Figure 4.7 Display of surface roughness measurement after UC**

To investigate the influence of the surface roughness, samples were roughened and polished manually. The first sample was produced using an abrasive SiC paper of P 120 with an average particle diameter of 125 µm, classified as fine. The sample was processed until the required roughness was achieved. For polishing, metal polish consisting of Aluminium oxide of 70-85 % was used. The liquid was applied to a cloth for polishing. The second sample was produced using an abrasive SiC paper of P 120 and then an abrasive SiC paper of P 240 with an average grain size of 58.8 µm.

### 4.2.5 Microscopic Inspection

The identification of the HAZ was carried out by microscopic inspection of the area surrounding the channel. Even though in laser welding, the HAZ is only one of four zones that develop during laser processing (see section 2.2.9), the term HAZ was used throughout the thesis to describe the whole area that was affected by the heat input of the laser. In order to inspect the HAZ, the samples were cross-sectioned perpendicular to the channel direction with a Struers Labotom cutting machine. They were then mounted into Buehler Konductomet II. The samples were then ground to 2400 grit SiC abrasive paper and then polished to a surface finish of 0.05 µm Ra with colloidal silica solution. The samples were then etched with Keller's reagent for 15 seconds in order to reveal details about the different HAZ. These zones were also visible before

etching as distinct darker regions around the channel area. However a more detailed inspection which involved revealing the microstructure was only possible via etching of the samples. To characterise the channels, shoulders and the HAZ, optical microscopy was carried out using an Olympus BX 60M microscope equipped with a JVC digital camera (2500 x 2000 pixel). A magnification of x 100 was used.

## 4.3 Results and Discussion

### 4.3.1 Statistical Distribution of the Channel Type after UC and Laser Processing

In Figure 4.8, the percentages of the occurring three effects (channel types) for the different tested samples can be seen. Samples produced with air and nitrogen for a nozzle size of 0.8 mm showed the highest penetration percentages – 48.3 % and 35 % respectively. 40 % (air) and 41.7 % (nitrogen) of the samples surfaces appeared as marking which accounted for insufficient penetration depth due to insufficient power and/or fast traverse speeds and/or high assist gas pressures which cooled the melt down to quickly to actually be displaced from the channel or hindered melting at all. The influence of the traverse speed and gas pressure on air samples showed that penetration was mainly achieved for speeds of 175 mm/min, 275 mm/min and 375 mm/min for medium to high gas pressure. The same applied for nitrogen samples, however with a gas pressure of 1 MPa samples were only marked possibly due to insufficient heat input. The use of a 1 mm nozzle for air showed compared to processing with a nozzle size of 0.8 mm, less penetration percentages (43 %). The reason for this may be that by using a wider aperture, the assist gas pressure was less localised. Higher traverse speeds let to marking of the material for all varied assist gas pressures. For this reason, the nozzle aperture of 0.8 mm was used for follow-up experiments (see 4.3.2). Oxygen and the black coating showed the same results for penetration – 13.3 %. In addition, the sample coated with black ink showed mainly marking characteristics (73.3 %). Penetration was only reached when the highest power was used for faster

travel speeds (375 mm/min) for all gas pressures. It was proposed that instead of coupling the laser beam efficiently into the material, the black coating hindered the penetration. The black coating served as an extra barrier for the beam to penetrate the material. The proposed effect of more efficiently coupling the beam into the aluminium was actually reversed; hence marking occurred but no penetration.

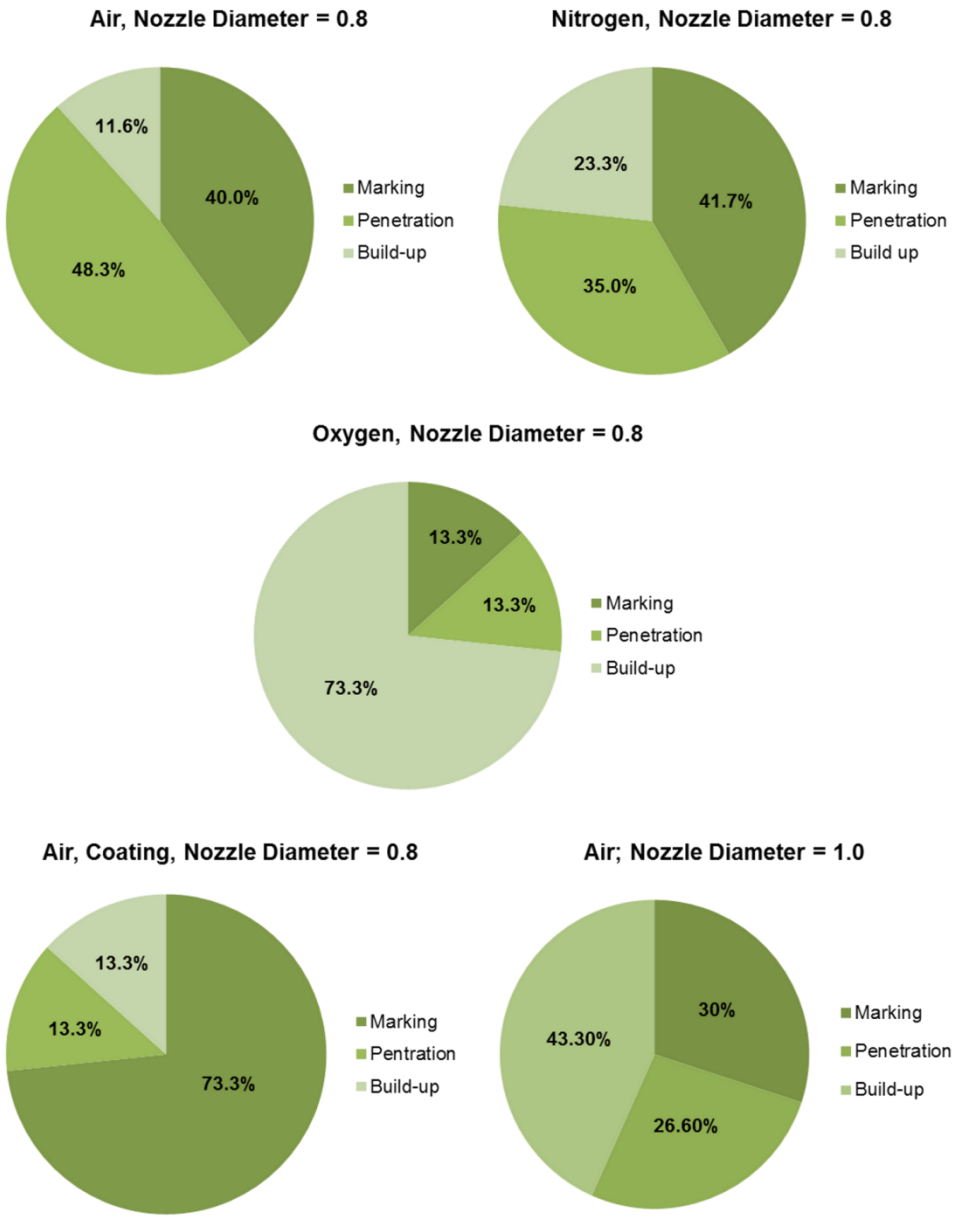


**Figure 4.8 Statistical overview of the appearances of the channels after laser processing**

In Figure 4.9, the build-up for oxygen is displayed. For 73.3 % of the oxygen samples, build-up of material was found. The build-up of material was believed to have happened due to the reactive nature of oxygen. Due to the oxidation reaction more heat is produced. However as mentioned in 2.2.8, oxygen can compensate the influence of the assist gas (Powell et al., 2009). Based on the theory of Powell et al., 2009, it was suggested for this study that the assist gas pressure was not strong enough to expel the material out of the channel and instead the material was piling up in the channel. Furthermore, aluminium may have reacted with the oxygen which could have caused a change towards a lower viscosity and a lower melt ejection rate. The results showed that penetration occurred randomly for all varied parameters.

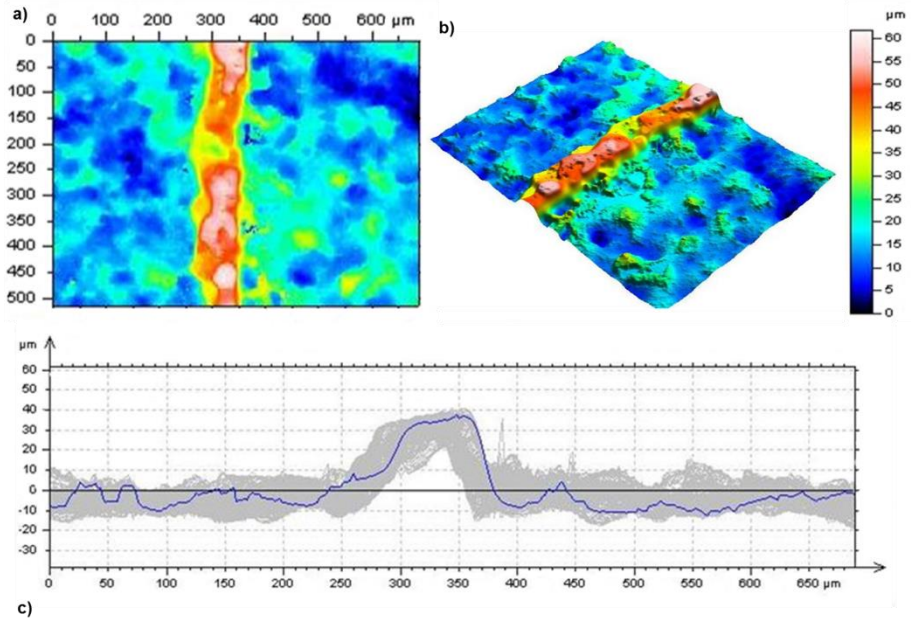


**Figure 4.9 Graphic representation of oxide build-up**

A study by Chen and Wang (2001) showed that the introduction of minute amounts of impurities (such as $N_2$) in $O_2$ drastically affected the keyhole depth and cutting results, to such a point that inert gases alone became more effective at creating a deeper keyhole. This provided an explanation for seeing deeper channels for nitrogen and air. As oxygen was only investigated to understand the exothermic reaction which could have caused deeper channels due to

higher heat input and oxygen only produced a small number of channels with penetration, it was therefore discarded from further experiments.

### 4.3.2 Variation of Process Parameters and Gas Types for Nitrogen and Air

For further investigations, nitrogen and air were chosen. The reason for choosing air was due to the fact that firstly, the penetration rate for air was higher than for nitrogen which can be seen in Figure 4.7. Secondly, it was readily available. Thirdly, it was suggested that air was able to induce more heat due to the partial reactive nature (Riveiro et al., 2011) for the case that penetration with nitrogen was not sufficient enough. Fourthly, particularly with regards to UC fibre embedding the study of two different gases on the bond formation was of special interest as bonding during UC is achieved when clean surfaces (free from oxides) create intimate metal contact. Air was expected to enhance oxide formation which was a way of comparison of two gases for bonding with regards to fibre embedding.

In Table 4.4, the processing parameters for air are displayed. As only marking for a gas pressure of 0.2 MPa was noticed, the results were not displayed in the table. This means that low gas pressure was insufficient to eject the material out of the channel area. For traverse speeds of 50 and 150 mm/s and a gas pressure of 0.6 MPa, penetration was achieved for low powers and higher powers of 120 W and 140 W caused build-up. For higher traverse speeds of 250 mm/s and 350 mm/s, marking was dominant for low powers and penetration for higher powers. Build-up was not caused for these speeds. Ergo, penetration of the sample was only achieved for higher speeds with higher powers. For a gas pressure of 1 MPa, penetration was achieved for low speeds for all powers. Higher traverse speeds led to penetration of the material for higher powers. However, for a speed of 350 mm/s only marking was achieved, thus the speed was too high for the beam to interact sufficiently with the material. The results showed that a higher gas pressure of 1 MPa, achieved a better overall penetration rate. Higher gas flows in addition to higher power and

traverse speeds possibly aided to cool down the molten material quicker which is the reason for less penetration.

**Table 4.4 Parameters and influences on material processed with air**

| Laser Parameters | | | Influence on the Material | | |
|---|---|---|---|---|---|
| Power [W] | Gas Pressure [MPa] | Traverse Speed [mm/s] | Marking | Penetration | Build-up |
| 60 | 0.6 | 50 | | X | |
| 80 | | | | X | |
| 100 | | | | X | |
| 120 | | | | | X |
| 140 | | | | | X |
| 60 | | 150 | | X | |
| 80 | | | | X | |
| 100 | | | | X | |
| 120 | | | | | X |
| 140 | | | | | X |
| 60 | | 250 | X | | |
| 80 | | | X | | |
| 100 | | | X | | |
| 120 | | | | X | |
| 140 | | | | X | |
| 60 | | 350 | X | | |
| 80 | | | X | | |
| 100 | | | X | | |
| 120 | | | | X | |
| 140 | | | | X | |
| 60 | 1 | 50 | | X | |
| 80 | | | | X | |
| 100 | | | | X | |
| 120 | | | | X | |
| 140 | | | | X | |
| 60 | | 150 | X | | |
| 80 | | | X | | |
| 100 | | | | X | |
| 120 | | | | X | |
| 140 | | | | X | |
| 60 | | 250 | X | | |
| 80 | | | X | | |
| 100 | | | | X | |
| 120 | | | | X | |
| 140 | | | | X | |
| 60 | | 350 | X | | |
| 80 | | | X | | |
| 100 | | | X | | |
| 120 | | | X | | |
| 140 | | | x | | |

In Table 4.5, the parameters and effects on channel creation using nitrogen as the assist gas are displayed. A gas pressure of 1 MPa showed only marking of

the material and was therefore discarded. It was concluded that higher gas pressures needed higher powers for penetration as nitrogen opposed to air lacked the additional heat input due to the exothermic reaction.

**Table 4.5 Parameters and influences of laser processing with Nitrogen**

| Laser Parameters | | | Influence on the Material | | |
|---|---|---|---|---|---|
| Power [W] | Gas Pressure [MPa] | Traverse Speed [mm/s] | Marking | Penetration | Build-up |
| 60 | 0.2 | 50 | X | | |
| 80 | | | X | | |
| 100 | | | | | X |
| 120 | | | | | X |
| 140 | | | | | X |
| 60 | | 150 | | X | |
| 80 | | | | X | |
| 100 | | | X | | |
| 120 | | | X | | |
| 140 | | | X | | |
| 60 | | 250 | | X | |
| 80 | | | | X | |
| 100 | | | | X | |
| 120 | | | | X | |
| 140 | | | | | X |
| 60 | | 350 | X | | |
| 80 | | | X | | |
| 100 | | | X | | |
| 120 | | | | X | |
| 140 | | | | X | |
| 60 | 0.6 | 50 | X | | |
| 80 | | | X | | |
| 100 | | | X | | |
| 120 | | | | | X |
| 140 | | | | | X |
| 60 | | 150 | | X | |
| 80 | | | | X | |
| 100 | | | | X | |
| 120 | | | | X | |
| 140 | | | | | X |
| 60 | | 250 | | X | |
| 80 | | | | X | |
| 100 | | | | X | |
| 120 | | | | | X |
| 140 | | | | | X |
| 60 | | 350 | X | | |
| 80 | | | | X | |
| 100 | | | | X | |
| 120 | | | | X | |
| 140 | | | | X | |

Additionally, an increase in gas pressure may have caused an increase in convectional heat losses from the aluminium, thus reducing full penetration.

This was supported by Gabzdyl and Brodsky (2010) who stated that increased flow rates increased heat losses of the processing material.

Nitrogen showed good results when processing with a gas pressure of 0.2 MPa and 0.6 MPa. The best results were observed for moderate speeds of 150 and 250 mm/s and lower powers. However, the results showed no conclusive relationship for any power input or transverse speeds for the $N_2$ gas jet. In order to understand the effect of penetration on the material, the width and depth of the channel were measured. In addition, for the case that a shoulder was observed, the width and height of the shoulder were measured.

Two diagrams for air and nitrogen for the channel and the shoulder are displayed in Figures 4.10 and 4.11. As both gas types showed best results for 250 mm/s and a gas flow of 0.6 MPa, the measurements for these parameters are presented. In Figure 4.10, the width and depth of the channel are displayed for air and nitrogen.

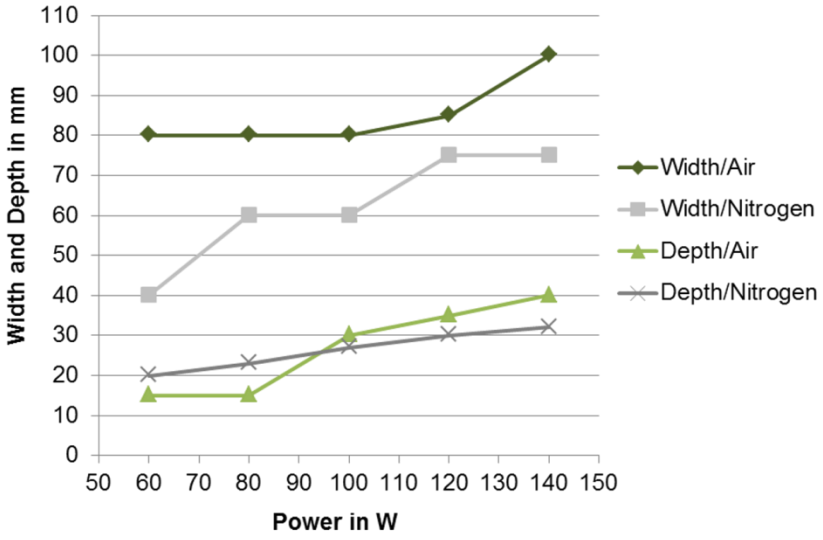


**Figure 4.10 Relationship between power and channel width and depth for a gas pressure of 0.6 MPa and a traverse speed of 250 mm/s**

It can be seen that the width of the channels was wide when compared to the depth for both gas types. For air an increase in power was noticed from 100 W onwards. For nitrogen, the width of the channel increased from 60 W. The depth of the channel for air increased from 15 µm to 40 µm for 140 W. For nitrogen,

the depth of the channel was 30 µm for 140 W. Both assist gases showed an increase in channel width and depth. Therefore for higher powers it would have been possible to generate deeper channels.

In Figure 4.11, the accompanying shoulder height and width for both assist gases is displayed. It can be seen that the shoulder was widest for the highest power applied. However, for both assist gases only a height of 15 µm maximum was achieved which was not sufficient for fibre embedding. As it was not possible to increase the power any further, it was decided that fibre embedding needed to be carried out with channels but without sufficient shoulder height.

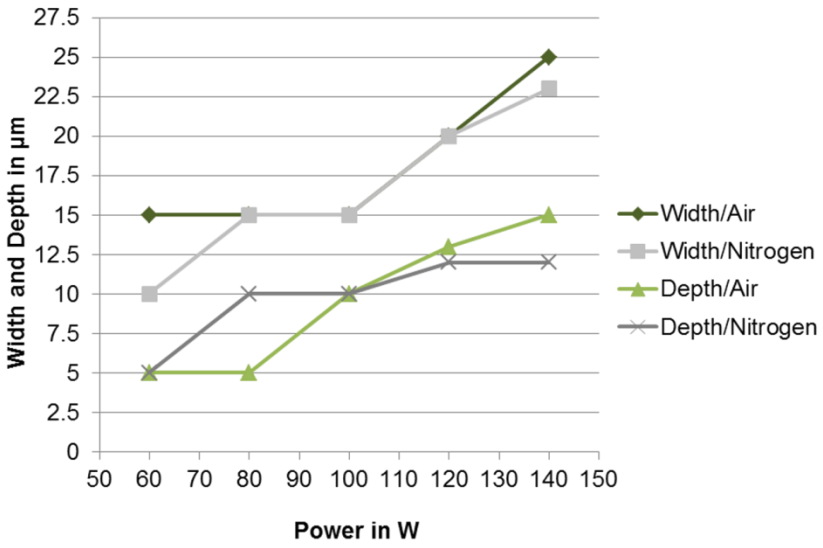


**Figure 4.11 Relationship between power and shoulder width and depth for a gas pressure of 0.6 MPa and a traverse speed of 250 mm/s**

In Figure 4.12, the HAZ for an air sample and for a nitrogen sample can be seen. Both channels were processed with a traverse speed of 200 mm/s, a power of 100 W and a gas pressure of 0.6 MPa. Both HAZ were uniformly formed around the channel. Considering, that the channel width was 40 µm for air and 20 µm for nitrogen, the HAZ was large and double the size of the channel widths. It was believed that due to the high heat conduction coefficient of aluminium, a considerable amount of heat was conducted into the surrounding material. Additionally, it can be observed that both channels were filled up with an unknown material which corresponded to build-up (see 4.3.1).

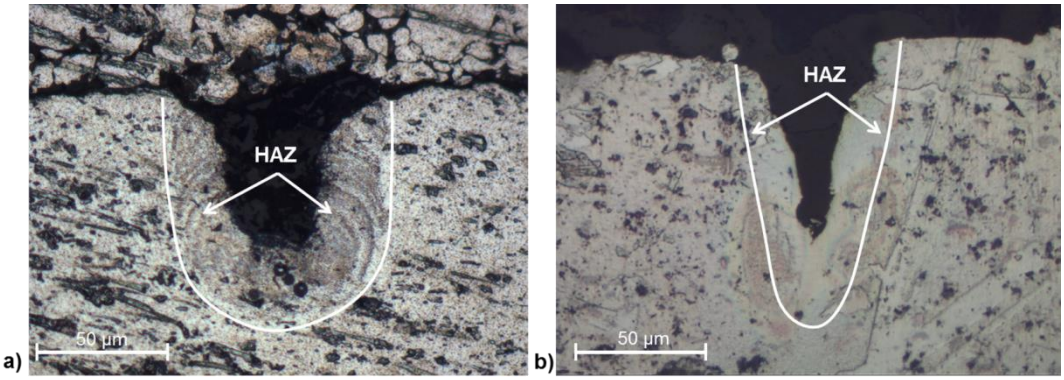


**Figure 4.12 HAZ distribution after laser processing for a) air and b) nitrogen**

It was believed that the material melted under the heat input of the laser and in the case of Al and air $Al_2O_3$ was formed as the material resembled brittleness. For nitrogen, the material inside the channel was observed to be less brittle and more homogeneous which may have been due to a lesser oxidation reaction.

### 4.3.3 Inspection of Polished Samples

The effects of the roughened and polished Al 3003-H18 samples can be seen in Table 4.6.

**Table 4.6 Overview of parameters and effects on polished samples**

| **Al3003-H18** | | | **P240** | | | | **P120** | | | |
|---|---|---|---|---|---|---|---|---|---|---|
| Laser Parameters | | | Influence on the Material | | | | Influence on the Material | | | |
| Gas Type: Air | | | | | | | | | | |
| Power (W) | Gas Pressure (MPa) | Traverse Speed (mm/s) | M | P | S | B | M | P | S | B |
| 60 | 10 | 175 | | | | X | | X | X | |
| 80 | | | | | | X | | X | | |
| 100 | | | | | | X | | X | | |
| 120 | | | | X | | X | | X | X | |
| 140 | | | | X | | X | | X | | |
| 60 | 10 | 275 | | | | X | | X | | |
| 80 | | | | | | X | | X | X | |
| 100 | | | | | | X | | X | X | |
| 120 | | | | | | X | | X | | X |
| 140 | | | | X | | X | | X | | X |

The rougher surface exhibited no marking effects but for nearly all powers and speeds a build-up of material. Penetration was only achieved at high powers of 120 W and 140 W for both speeds. The smoother surface showed on the contrary for all tests a penetration of the material. Additionally, for the rougher surface no indication of shoulder formation was seen (in Table 4.6 indicated as “S”). The smoother surface indicated shoulder formation, however for smaller powers. Hence, a smoother surface could have coupled the beam more efficiently into the material. This suggests that the rough surface of the UC sample hindered efficient coupling into the material as well as random coupling due to different angles of laser beam radiation which led to inconsistent channel width and channel depth due which has been suggested by Bergström et al. (2007b) and Huntington and Eagar (1993). There is no indication that higher speeds led to an increased penetration of the material. It was concluded that a smoother surface shows better results for channel creation as opposed to a rougher surface due to the multiple reflections caused on the surface which mislead the beam in the wrong direction.

In Figure 4.13, a graphic of the finer surface of Al 3003-H18 is displayed.

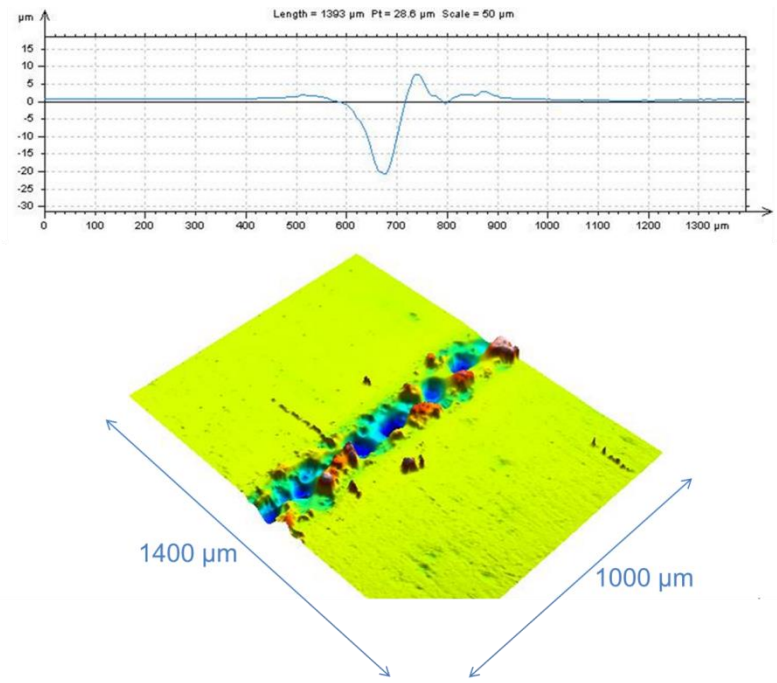


**Figure 4.13 Laser penetration of smoother Al 3003-H18 with 175mm/min, 140W, and 10l/min**

The diagram indicates that the surface is close to that of an unprocessed foil as the roughness value was found to be consistent over the whole area. A channel of a depth of 20 µm has been created. However, penetration of the channel is variable as several bumps in the channel can be noticed. It was suggested that the laser power output might vary along the channel length. When the material was penetrated more deeply, build-up was noticed next to the channel which indicated that the melt got dragged out of the channel and adhered next to it.

## 4.4 Review

The intention of chapter 4 was to gain fundamental knowledge for channel and shoulder manufacturing within an ultrasonically consolidated metal matrix with the support of a fiber laser.

The initial experiments were carried out by varying different parameters which were identified as the main influential parameters for channel processing via an Ishikawa diagram. These parameters were: power [W], traverse speed [mm/s], gas pressure [MPa] and gas type. The results showed that the rate of penetration could be classified into three categories: marking, penetration and build-up with penetration being the desired outcome as these samples showed the development of channel and shoulder features. Sample processing with air and nitrogen as the assist gas exhibited the best results for penetration, whereas oxygen showed mainly build-up with was attributed to the exothermic reaction between oxygen and aluminium. Hence, further experiments were carried out by using nitrogen and air. Two different assist gases were chosen firstly due to their different ionisation potential and secondly, to gain knowledge about the influence of the assist gas for future fibre embedding and on bond formation during UC.

Experiments carried out by using air and nitrogen as the main assist gases for channel manufacturing in this study showed that air exhibited a higher penetration rate (40 µm at a power of 140 W) for slower processing speeds due to the longer interaction time between the material and the laser beam. For nitrogen, the penetration rate was lower for the same laser powers (30 µm at a

power of 140 W) and it was assumed that samples would need higher laser powers in order to manufacture deeper channels as the exothermic reaction was missing. Both assist gases exhibited a similar height for the shoulders (~10 µm).

The results from chapter 4 showed promising results for channel/shoulder manufacturing by the use of a fiber laser. Especially, the width of the channels appeared in the desired range which showed that the narrow spot size of a fiber laser enables narrow processing capabilities. However, achieving the desired channel depth was challenging due to two main limiting factors: the loss of power (30 % of the input power) and lack of higher powers as well as the appearance of the metal matrix surface after UC which hindered stable penetration due to insufficient heat input for melting.

# Chapter 5.
# Channel and Shoulder Formation by Fiber Laser Processing

## 5.1 Introduction

The preliminary attempt in chapter 4 proved that the formation of channels and shoulders was challenging possibly due to the combination of lack of power and surface morphology of the UC samples. It was anticipated that higher powers or multiple scanning of a channel (both inducing more heat into the material) would benefit channel processing in Al 3003-H18 for fibre embedment. To expand the power range, experiments were carried out with a Trumpf TruFiber 300 W laser. The work on a different fiber laser offered the opportunity to expand the data set to encompass another laser manufacturer and thus to test the broader applicability of the experimental results.

Results from chapter 4 were taken into account for a remodelled set of experiments varying the power [W], traverse speed [mm/s] and gas pressure [MPa]. It was shown that the new approach of channel/shoulder processing via multiple passes in combination with a higher power input led to consistent channel/shoulder geometries. Nevertheless, multiple passes increased the heat input to the aluminium metal matrix and a considerable HAZ was detected. The HAZ was analysed in order to gain possible implications for future fibre embedding.

## 5.2 Methodology

### 5.2.1 Laser Processing

The already mentioned Trumpf TruFiber 300 W laser was located at the Fraunhofer Institute for Laser Technology ILT in Aachen, Germany. This laser was chosen due to the comparability with the SPI 200 W redPower fiber laser used for the experiments in chapter 4 whilst expanding the power range and allowing testing of wider applicability. The wavelength of the laser was 1.080 µm ± 0.5 µm. An image of the Trumpf TruFiber 300 W laser unit is shown in Figure 5.1. The laser could be operated in CW and pulsed mode (up to 1250 Hz). The power could be varied between 0 - 300 W (CW mode) and hence, added another 170 W to the power range compared to the possible power output in chapter 4.

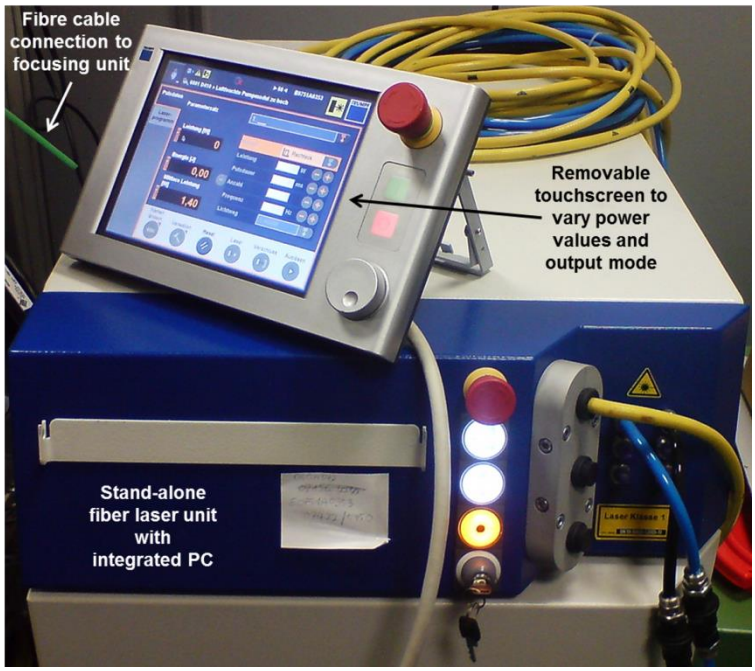


**Figure 5.1 Trumpf TruFiber 300W laser with removable touchscreen**

An external laser light cable for beam delivery (containing an optical fibre with a diameter of 50 µm) was used to connect the laser unit with the laser process head assembly. The 3-axes laser process head assembly can be seen in Figure

5.2. The process head was supplied by Haas Laser Technologies Inc. and consisted of a FCH-Series cutting head. The cutting head consisted of a manually adjustable Z-axis to allow positioning of the stand-off distance and focal position. The assist gas was supplied through a conical cutting nozzle with a diameter of 0.8 mm which was the size of the nozzle for mainly all laser experiments in chapter 4. The gas utilised throughout the experiments was compressed air. Due to time and expenditure constraints, nitrogen was not used.

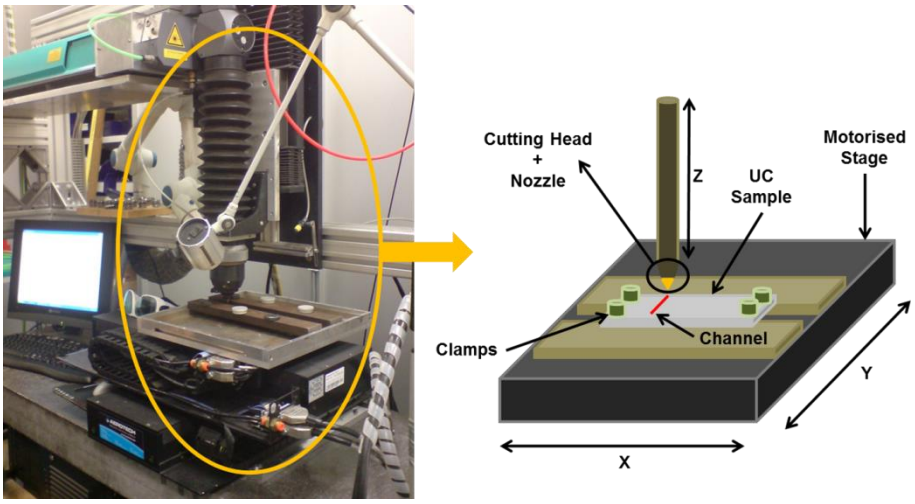


**Figure 5.2 Process head assembly/stage unit and schematic set-up for samples processed with Trumpf TruFiber 300W laser**

The experiments were carried out on Al 3003-H18 samples described and produced in section 4.2.1. The UC sample was fixed on an Aerotech CNC working table which could be operated in the X and Y direction via an A 3200 controller. The channel layout was programmed via NView software. For the following experiments, channels perpendicular to the UC welding direction were generated on the UC sample with a length of 15 mm.

A theoretical spot size of 13.8 µm was calculated by using equation (3) with a focal length of 50 mm, an initial beam diameter of 7.6 mm and $M^2$ = 1.2. The values were supplied by Fraunhofer Institute. It was considered measuring the spot size, however, due to time-limits and equipment availability, it was not possible to measure the spot size. The power density of the incident beam (see

equation (4)) corresponded to 1.48 x $10^8$ W/cm$^2$ for 200 W and 2.23 x $10^8$ W/cm$^2$ for 300 W. The beam was focused above the surface of the UC sample (Ready and Farson, 2001) and was kept at a constant stand-off distance of 0.4 mm. Different focal positions (0.2 mm, 0.3 mm, 0.4 mm and 0.5 mm) were tried throughout the experiments, however the most promising results were achieved at a focal position of 0.4 mm.

The experiments were carried out by varying the traverse speed (mm/s), power (W) and assist gas pressure (MPa). After initial experiments of one-time laser radiation which failed to show the desired results in terms of channel geometry, experiments were conducted to analyse the effect of multiple laser passes on channel geometry. These experiments were conducted by radiating the material surface three or five times. Results from single scans were taken into account and the parameters for multiple laser scans were refined accordingly. Table 5.1 details the range of varied parameters. The gas pressure was varied between 0.4 MPa and 0.8 MPa in order to determine the gas pressure effect on displacing the melt from the channel.

**Table 5.1 Varied parameters for multiple passes on Trumpf TruFiber 300 W**

| **Passes** [No] | **Gas Pressure** [MPa] | **Traverse Speed** [mm/s] | **Power** [W] |
|---|---|---|---|
| 3 | 0.4 | 100 | 150;200;250;280 |
| | | 200 | 150;200;250;280 |
| | | 500 | 150;200;250;280 |
| | 0.8 | 100 | 150;200;250;280 |
| | | 200 | 150;200;250;280 |
| | | 500 | 150;200;250;280 |
| 5 | 0.4 | 100 | 150;200;250;280 |
| | | 200 | 150;200;250;280 |
| | | 500 | 150;200;250;280 |
| | 0.8 | 100 | 150;200;250;280 |
| | | 200 | 150;200;250;280 |
| | | 500 | 150;200;250;280 |

### 5.2.2 Macroscopic Inspection

For examination of the 3D profile of the channels a Keyence digital microscope (VHX – 600 Series with a VH-Z100R lens) was employed. A magnification of x 300 was used to observe the channel geometry. This inspection was carried out at the ILT and allowed an in-situ observation of channel depth and shoulder height. As there were no facilities for microscopic inspection accessible, as well as a limited timeframe, conclusions for channel/shoulder formation and sample production (see section 6.2.2) were entirely based on this inspection. A self-defined preferable channel geometry served as a guideline for channel/shoulder formation. The desired parameters for channel geometry were: a width of 120 µm – 150 µm, a depth of 50 µm to 80 µm and a shoulder height of 50 µm to 80 µm. All the samples were examined with a built-in program. The height and the width of the channels were inspected as well as the shoulder height and width.

### 5.2.3 Microscopic Inspection

The sample preparation and microscopic inspection was carried out at Loughborough University and followed the sample preparation procedures described in section 4.2.5. The depths and heights of the channels were measured in order to compare the influences of the varied laser parameters. The samples were inspected at magnifications of x 100 and x 200 to exploit the whole channel area which was not possible at higher magnifications due to the width of the channels. The average channel widths were calculated by measuring five equally distributed points along the channel length. The average channel depths and shoulder heights were calculated by scanning the channel at five equally distributed points using a Taylor Hobson Talysurf CLI 2000 inductive gauge. These measurements were then compared to determine possible influences of the laser parameters.

Production of the channels via multiple laser passes was expected to have a more significant influence on the HAZ due to the high thermal conductivity of aluminium. For the reason of possibly altering the properties of the material, the

microstructure was studied at magnifications of x 200 and x 500 which was also able to reveal areas of particular interest such as the grain structure.

### 5.2.4 SEM and EDX Analysis of Samples

For a more detailed analysis at higher magnifications a field emission gun scanning electron microscope (FEGSEM) was utilised which allowed a closer inspection of the HAZ, solidified material and possible oxidisation effects due to the assist gas. Images of different features surrounding the channels and within the microstructure of the scanned tracks were taken using a Carl Zeiss (Leo / Cambridge) 1530 VP. The different areas of interest were selected in terms of the future fibre embedding and bonding process. Backscatter electron (BSE) images were taken which provided a clearer contrast of the microstructure. The tracks were then analysed with energy dispersive X-ray spectroscopy (EDX) to reveal detailed information about the distribution of alloying elements and hence, possible compositional changes. The EDX was integrated in the FEGSEM and an Oxford Instruments X-Max 80 $mm^2$ detector was used. The beam current was set to 20 keV which allowed quantifying the main alloying elements such as Aluminium (Al), Manganese (Mn), Iron (Fe) and Oxygen (O).

To analyse the resulting data the Oxford Instruments INCA Energy software, which was integrated into the FEGSEM, was used. EDX was performed by mapping the whole channel and adjacent microstructure area. Additionally, the oxide distribution along the channel interfaces and in particular within the shoulder area was closely inspected as this was of particular interest for further studies concerning the embedment of fibres and bond formation during UC. To understand possible influences of the laser on the microstructure such as distribution and potential loss of alloying elements, element spectra were taken from ten different points for five channels as displayed in Figure 5.3. The first four points for element acquisition were chosen in order to determine possible concentrations of oxygen along the inner part of the channel as this could affect bond formation and fibre embedment. Additionally, as will be shown in 5.3.3, the microstructure in this particular area changed and it was expected that

manganese concentrations would be higher due to the heat flow in the material. Points five and six were chosen because those regions showed no signs of element concentration. The last four points were chosen due to the variation of the microstructure.

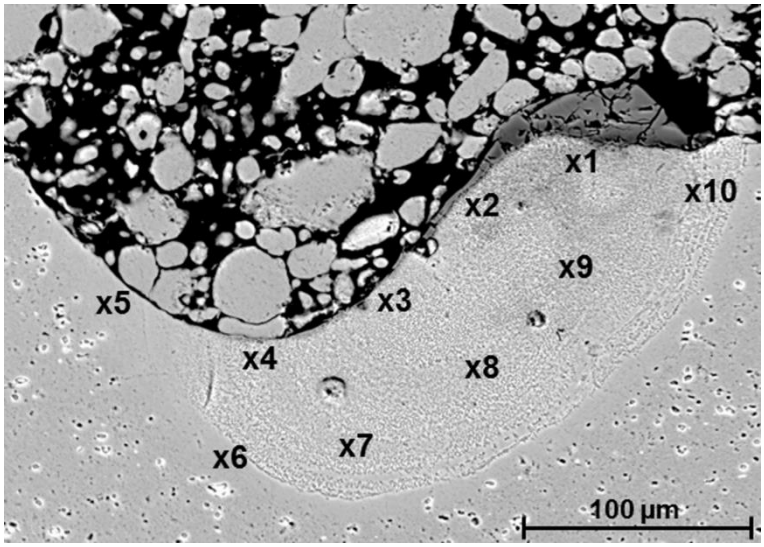


**Figure 5.3 Specific points within the HAZ for acquisition of element spectra for material composition**

## 5.3 Results and Discussion

### 5.3.1 Influence of Varied Parameters in Combination with Multiple Passes on Channel and Shoulder for Trumpf TruFiber 300 W

In the methodology section it was described that tests were carried out at traverse speeds of 100, 200 and 500 mm/min. However, the laser interaction obtained at a travel speed of 500 mm/min for samples was shown to be insufficient for channel creation. The reason for this was that the travel speed was too high to achieve sufficient melting and penetration depth. For this reason the following results are displayed for 100 mm/min and 200 mm/min. Figure 5.4 (a) and (b) displays the influences of laser power, travel speed and assist gas on the width and the depth of the channel. The channel was radiated three times. Figure 5.4 (a) shows that the channel width increased with higher laser power, which was due to the greater power density applied to the work piece.

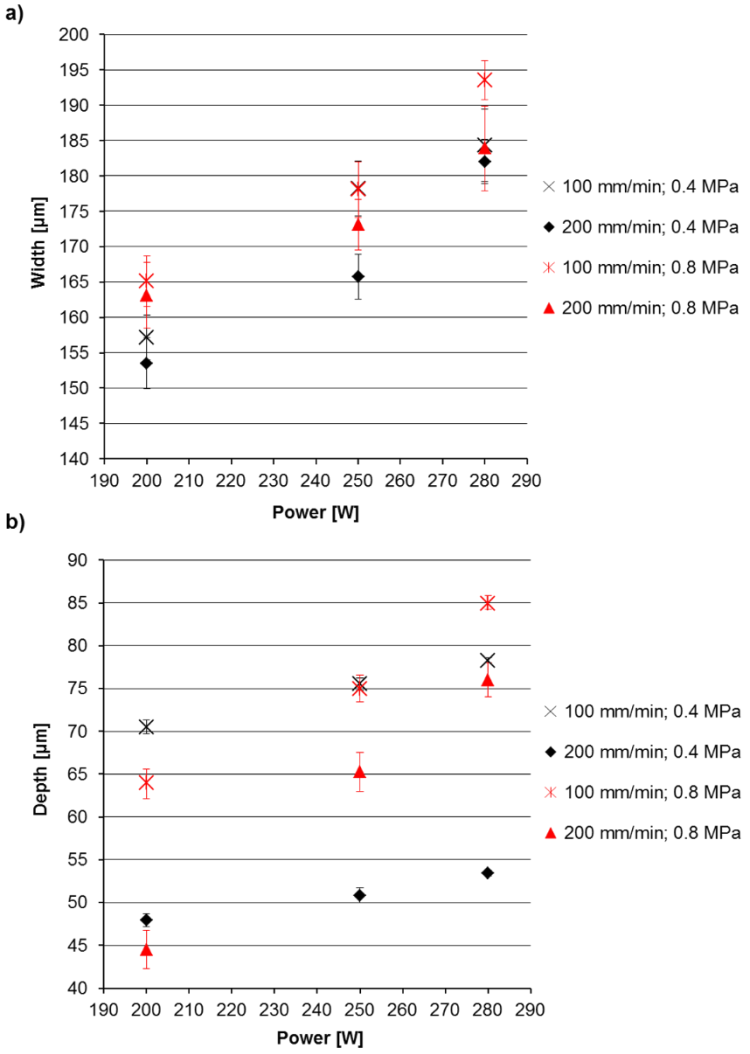


**Figure 5.4 Influence of power, traverse speed and gas pressure on the width (a) and the depth (b) of three times radiated channels**

The depth in Figure 5.4 (b) increased 10 µm for higher powers. As noticed for the width, the traverse speed significantly affected the depth. A comparison of the two different traverse speeds showed that the channel depth increased by nearly 40 % for a traverse speed of 100 mm/min. An increase of channel depth with lower traverse speeds has also been recognised by Choi and Chryssolouris (1995b). Further analysis of the penetration depth also revealed that the assist gas had only a minimal effect on the penetration. The difference between 0.4 MPa and 0.8 MPa was approximately 10 µm which indicated that the main process parameters influencing the depth of the channel were laser power density and the interaction time between the laser and material.

Results of the five laser pass experiments are shown in Figure 5.5 for the width (a) and depth (b) of the channels.

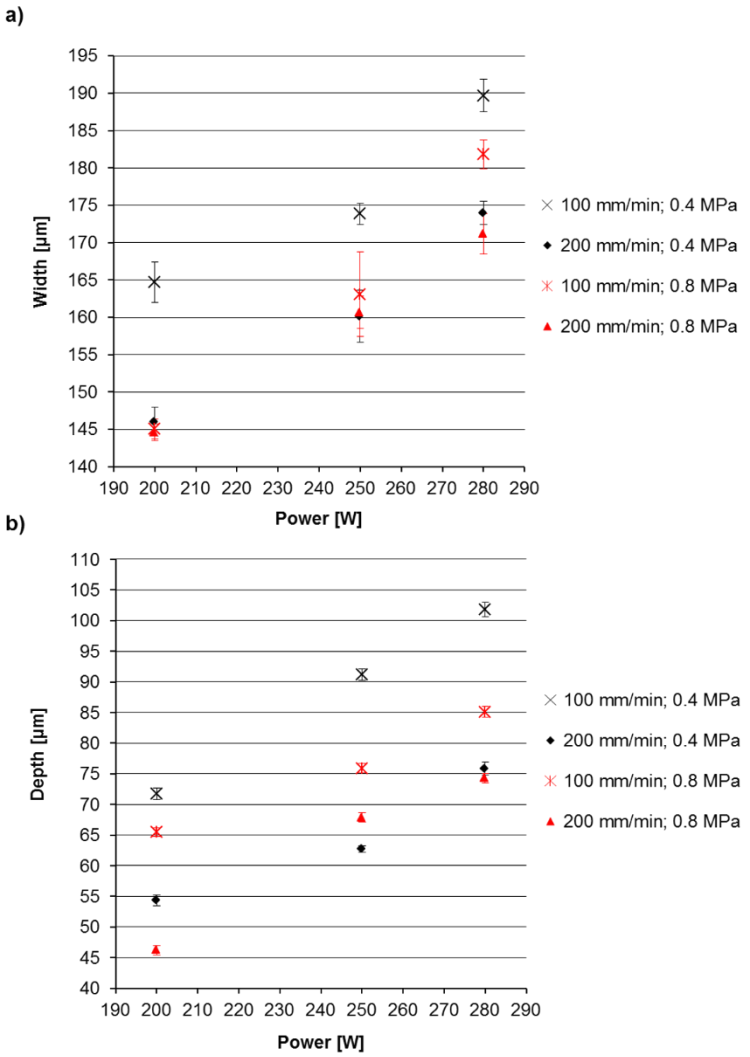


**Figure 5.5 Influence of power, traverse speed and gas pressure on the width (a) and the depth (b) of five times irradiated channels**

An increase in laser power resulted in a larger channel width (140 µm to 190 µm). Both three and five passes exhibited an approximately linear behaviour between power density and the width of the channel which was in agreement with previous theoretical work (Chryssolouris et al., 1988b; Kumar and Gupta, 2010).

Applying a slower processing speed of 100 mm/min to the work piece resulted in wider channels than when using a processing speed of 200 mm/min, (this

result was also obtained for three passes). This was another indication that a longer interaction time between the laser and Al 3003-H18 surface accounted for a wider channel. A decrease in traverse speed resulted in a longer interaction time between the laser and metal material, thus resulting in a larger melt area, which was subsequently expunged via the assist gas and therefore this created a wider channel.

It was interesting to note that an influence of the assist gas on channel width was not apparent for five passes. Since this behaviour correlated with three passes, it was interpreted that the assist gas may not be a major driving force for channel width. Furthermore, a comparison of the channel width for three and for five passes revealed that the channel width varied in the same range of 140 µm to 190 µm. Therefore it was suggested that the laser spot size, interaction time and laser power may have been the main contributing factors in determining the final channel width.

The channel depth of five pass samples increased with higher power as shown in Figure 5.5 (b). In comparison with three passes, Figure 5.4 (b), this increase was greater and increased further with a slower traverse speed. A linear relationship between the power and depth could be depicted. As with the 3 pass experiments it was noted that a slower traverse speed accomplished a deeper penetration into the material. The five pass experiments resulted in deeper channels than for the three pass experiments which suggested that the increased laser/material interaction time had an effect on channel deepening. Similar findings have been discovered in previous work (Mai and Lin, 2006). An explanation for this is that higher processing rates, i.e. more scans, led to a larger and deeper melt pool in which the beam was trapped and as result the channel became deeper. This would be in accordance to one and three scans compared to five scans; as the melt pool became larger, with more passes, the beam was more efficiently absorbed into the melt and as a result the channels deepened.

The influence of the assist gas on the channel depth for five passes did not appear to be as pronounced as for other processing parameters. Three passes

showed the depth to decrease by 10 µm between 0.4 MPa and 0.8 MPa respectively. It was concluded that a higher assist gas pressure caused the melt to cool down faster which prevented the channel from deepening.

Figure 5.6 illustrates the influence of power, traverse speed and assist gas on the shoulder creation for three passes (a) and five passes (b).

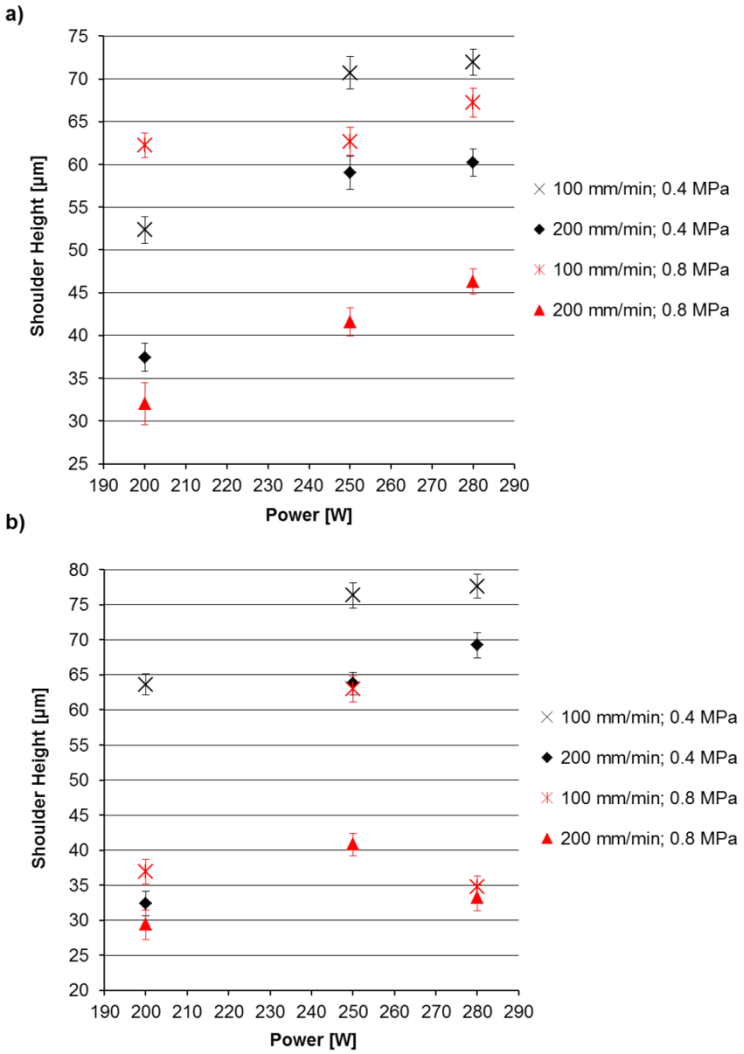


**Figure 5.6 Influence of power, traverse speed and gas pressure on the height of the shoulder established next to the channel (a) three passes and (b) five passes**

For three passes it was noted that the shoulder height for slower processing speeds was higher than for higher processing speeds. The height varied between 55 µm and 70 µm for both assist gas pressures. The same influence was noted for five passes with a range of 40 µm to 80 µm. Comparison of the

shoulder height and the channel depth demonstrated that there was a correlation between the two. A trend of an increasing shoulder height by increasing the laser power was obtained between 200 W and 250 W for 0.4 MPa. For 0.8 MPa, the same trend was noted for five passes but not for three passes, for which the shoulder height stayed similar for all three powers. The shoulder heights varied in the range of 10 µm between the highest shoulder for three passes (70 µm) and the highest shoulder for five passes (80 µm) as can be seen in Figure 5.6 (a) and (b). The majority of the melted material from the channel was deposited on the material surface at the side of the channel and therefore used for shoulder creation. This supports the generation of melt rather than vaporisation due to laser interaction.

The observed difference of shoulder formation from applying two different assist gas pressures was less than for the other processing parameters. A lower gas pressure of 0.4 MPa applied to the work piece resulted in a higher shoulder when compared to samples manufactured with 0.8 MPa. A reason for a lower gas pressure responsible for a higher shoulder may have been due to a slower cooling rate of the melt pool. Though the gas pressure did not appear to have as large an effect on channel depth and shoulder height as the other varied parameters, it was thought that it was the mechanism by which the melt pool was displaced from the channel onto the surface of the material.

As can be seen from the results, different widths and depth were produced by varying the laser parameters. This can be useful in the case that different fibre types with differing diameters will be embedded in order to create a closed-loop between the embedded fibres. Hence, with laser processing it would be possible to manufacture small channels for, for example optical fibres for sensing and wider channels to embed SMA as actuators.

### 5.3.2 Analysis of One-Sided Shoulder Formation

Figure 5.7 displays four channels for 3 and 5 passes at assist gas pressures of 0.4 MPa and 0.8 MPa taken with the Keyence VHX 600 Series. To facilitate the

comparison all channels displayed were processed with the same laser power and traverse speed.

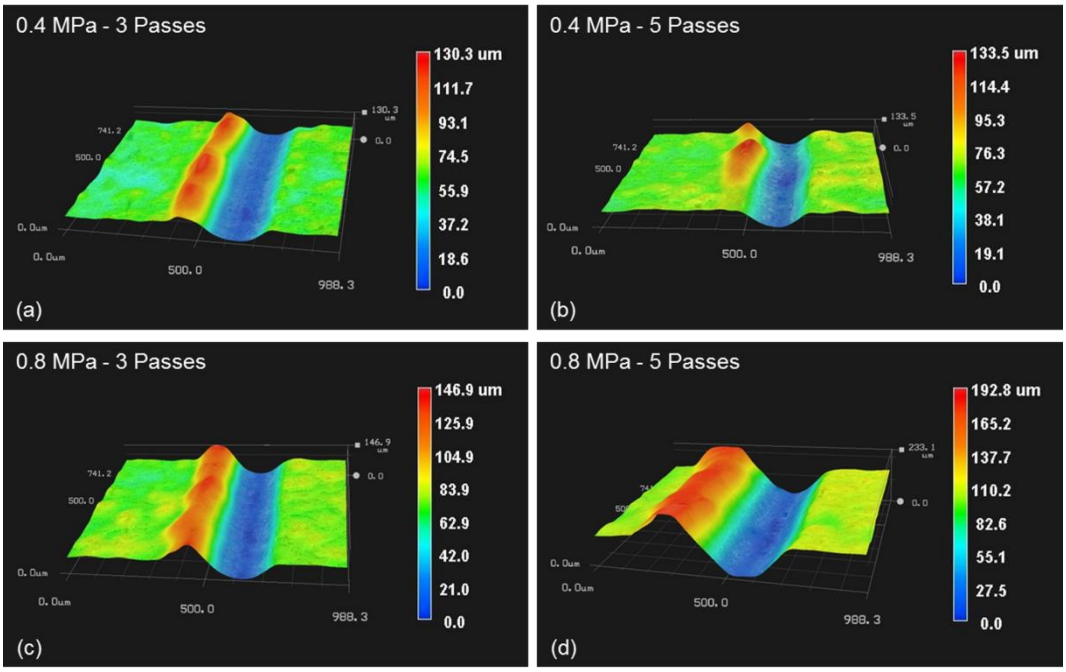


**Figure 5.7 Comparison influence of different gas pressures and passes (power: 280 W and traverse speed: 200 mm/min)**

It was observed that the channels exhibited a circular shaped channel profile which was considered an important factor for embedding circular fibres. The inside of the channels appeared as a smooth area without peaks or inconsistent channel depths. The shoulder feature was not found on both sides of the channel but instead occurred on one side of the channel. This was observed for every channel produced. It was also noted that the shoulder always appeared on the same side of the channel. The melt was built-up in accurate consistent paths to the side of the channel and additional material spatter was not apparent. It was unlikely that the beam would have caused this phenomenon as the channel showed a Gaussian-shaped outline and a Primes MicroSpot Monitor had been used before this study by Fraunhofer ILT to align the beam. This meant that the beam was aligned to the middle of the nozzle and was not clipping on the sides of the nozzle which would have caused a different power density distribution. However, two possible influences may have caused the shoulder to build up one-sided: a non-uniform heating of the melt-front, which

was reported and developed into a 3D model by Chan et al. (1988), and/or a non-uniform distribution of gas.

The non-uniform heating of the melt-front in the channel may be explained by the Gaussian distribution causing a higher heat input to the centre of the molten pool than at the channel boundaries. As a consequence a decrease in temperature towards the edges of the channel could have resulted in an increase in surface tension towards the channel boundaries. Due to the surface tension and wetting characteristics, the melt could have been pulled to either one side of the channel or the other.

The non-uniform distribution of gas could possibly be caused by air not flowing coaxially from the nozzle but instead flowing off-axially. It was possible that the air stream may have approached the material with an angle of less than 90º from the right side which in turn forced the melt to be built-up on the left side of the channel. Another possible explanation for the shoulder formation was based on the approach for side gas explanation stated by Kamimuki et al. (2002). The off-axis gas impinges on the channel wall and is converted back in the direction were it came from. This would have resulted in the build-up of the material under the gas inlet side. However, a substantiation for the shoulder formation due to non-uniform heating of the aluminium and the resulting surface tension gradients was established when test results performed at Loughborough University using a different laser setup demonstrated the same phenomena; suggesting it was not limited to the specific equipment used in this study. Further investigation on the assist gas flow was carried out by monitoring the impingement of the gas on a soft, rubber-like material which deformed upon application of the assist gas. The results further demonstrated that the material would rise at the left side of the laser spot, whereas the right side of the laser spot was not affected by the assist gas. In order to clarify and limit the possible influences of one-sided shoulder formation, an additional experiment was carried out: a square was radiated into a sample to determine the flow behaviour of the melt for different directions. As the laser remained stationary, a non-uniform distribution of gas through the nozzle would have resulted in

different melt flow behaviours depending on the direction. The results showed that the melt flow behaviour and consequently the shoulder position were again observed to be one-sided. For this reason the suggestion of non-uniform heating of the melt pool is an explanation for the one-sided shoulder formation.

As a one-sided shoulder differed from the expected two shoulders (see section 1.5) it was necessary to discuss the possible effect of a one-sided shoulder on future fibre embedding and ultrasonic consolidation. With regards to placement and positioning of fibres, the shoulder was not expected to interfere as the channel was used to securely position the fibres. The shoulder on one side may have an effect on the fibre embedment and the plastic flow characteristics during UC. The plastic flow around the fibre may be affected depending on the combination of the welding direction and positioning of the shoulder before or behind the fibres.

### 5.3.3 Microstructural Characterisation of the HAZ

Figure 5.8 a) corresponds to a 3D profile taken by the digital microscope of a channel produced by five laser passes. In Figure 5.8 b), a cross-section of a channel scanned five times by the laser is displayed. The shoulder and channel as well as the laser-affected zone underneath the channel are recognised.

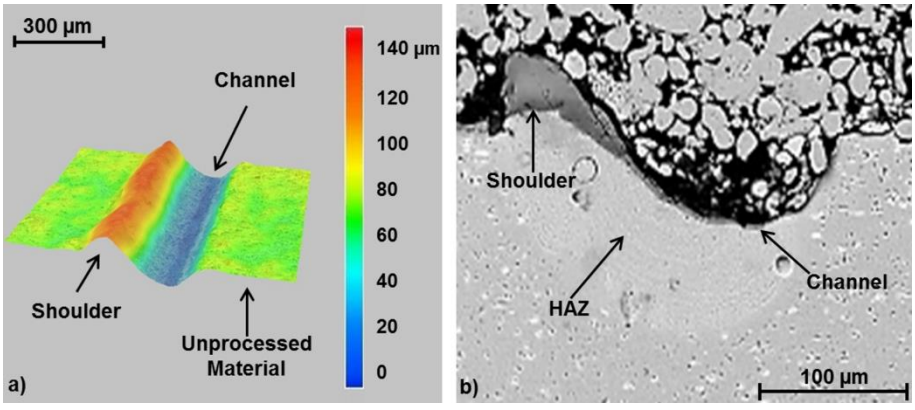


**Figure 5.8 Channel scanned five times: a) 3D image by digital microscope and b) cross-section**

In Figure 5.9 different microstructural areas surrounding the channel are displayed. Figure 5.9 a) represents the inner channel boundary with an attached

layer on top. Figure 5.9 b) represents the unmodified base metal which was not affected by the laser and exhibited the base alloy structure.

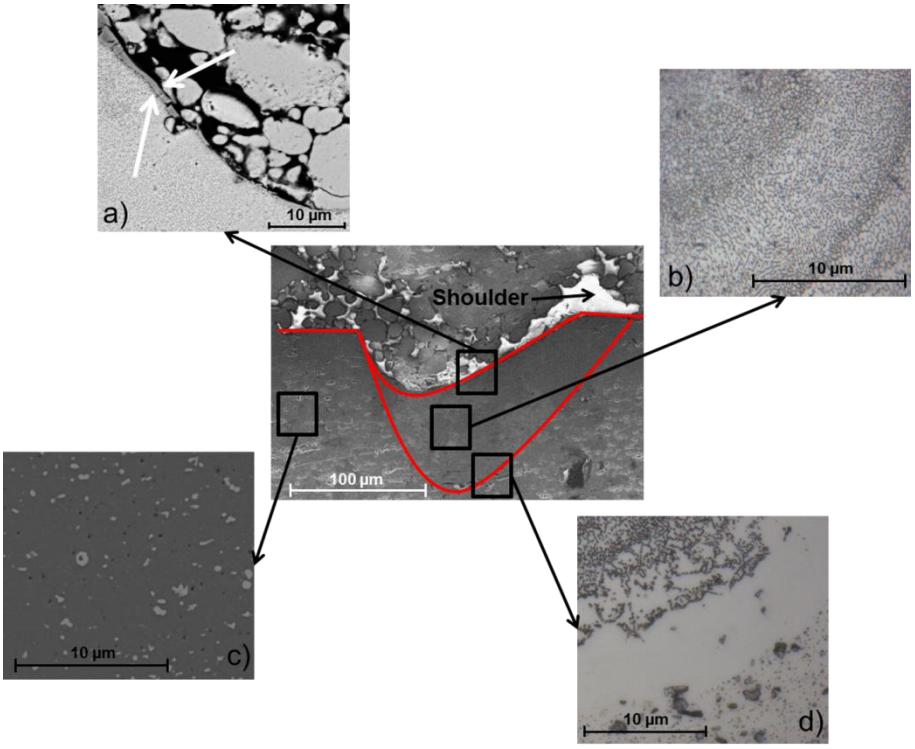


**Figure 5.9 Identification of different areas: a) attached layer, b) area with changed microstructure, c) base metal d) interface area between changed microstructure and base metal**

The HAZ was divided into two areas: Firstly, a zone exhibiting a different microstructure than the base metal (Figure 5.9 c)) and secondly, an interface area between the changed microstructure and the base metal (Figure 5.9 d)).

***Formation of Recast layer***

The attached layer seen in Figure 5.9 a) is suggested to be a recast layer consisting of melt that solidified after laser processing at the inner border of the channel. A recast layer is resolidified material that was not completely removed by assist gas and accumulates on the cut side in cutting or inside the hole in drilling. From Figure 5.8, it can be seen that the recast layer showed the same material characteristics as the shoulder. The recast was only noticed at the side of the channel which exhibited a lesser slope angle. On the other side the recast layer was hardly noticeable. In addition, the recast was noticed to be

thicker at the outer edge of the channel and gradually thinning out towards the lowest point in the channel. The thickness of the recast layer varied between 1 µm to 5 µm and was found to be adhered to the inner side of the channel as delamination was not found along the channel boundary.

***Interface between HAZ and Base Metal***

The zone displayed in Figure 5.9 d) was suggested to be a dispersoid/micro-segregation-free zone. The thickness of this zone was about 10 µm and it appeared as a white area without identifiable second phases or microstructure characteristics. The visible material was believed to be aluminium as the main alloying material. Mills (Mills, 1985) stated that the microstructure within a solidified alloy decreases when the rate of cooling increases. Hence, there will be a zone that is characterised by absence of dendritic or cellular micro-segregation. Comparison of Figure 5.9 d) and Figure 5.9 b) revealed the absence of dendritic or cellular structures. Meyer et al. (2000) showed that this zone is softer and experiences a reduction in hardness which is of importance for the mechanical characteristics of Al 3003-H18 as a UC manufactured component.

***The Heat-Affected Zone (HAZ)***

Figure 5.10 shows the microstructure after etching of the zone that experienced heat treatment by the laser and heat conduction for a channel scanned five times.

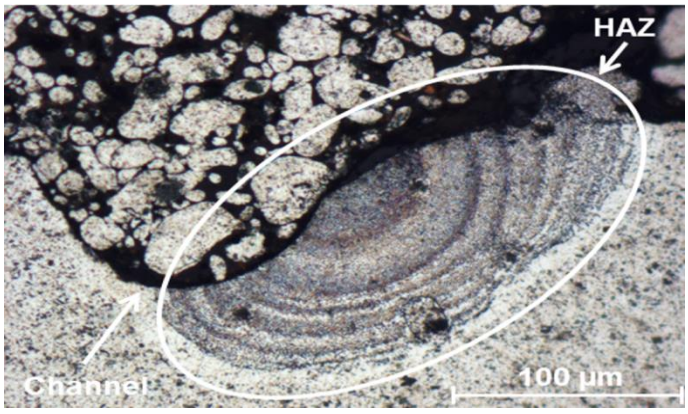


**Figure 5.10 Microstructure of the HAZ**

The HAZ was distinguished at one side of the channel, however exhibited a symmetrical shape. The channel however developed coaxially to the laser beam. It was believed that the surface tension gradients along the melt pool along with Marangoni convection and possible buoyancy forces were responsible for the shift of the HAZ as already discussed for the shoulder formation in section 5.3.2.

Figure 5.11 displays the microstructure of five laser passes at a higher magnification. It was observed that the microstructure alternated between darker and lighter regions which suggested that each time the laser traversed along the channel melt was produced and heat conducted into the material. It was predicted that every laser pass resulted in a microstructural combination of light and dark regions. Therefore, within the HAZ, single heat-affected microstructures were formed with specific melting and cooling cycles during every laser pass. The last microstructure to form after laser processing was possibly the dark, middle area. As opposed to the other single HAZ, this microstructural area exhibited the biggest area within the complete HAZ and it was anticipated that this area had more time for solidification due to the laser passes being completed. The other single HAZ were smaller but all with a similar appearance in size which is plausible as they had the same amount of time before the next laser pass.

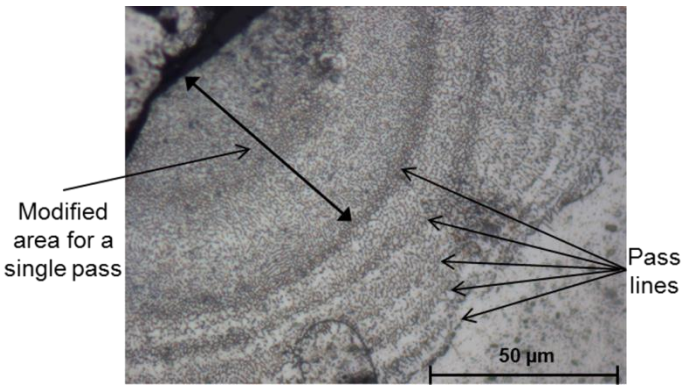


**Figure 5.11 HAZ displaying the five single laser pass lines and resulting modified areas**

In general, heat is conducted from the liquid into the solid metal due to the temperature gradient across the solid/liquid interface, so that the solid acts as a

heat sink. Hence, it was anticipated that for every laser pass resulting in more heat input and melt generation, further heat was conducted into the aluminium bulk. The HAZ formed accordingly due to the combination of heat input, assist gas and the relatively short time frame for solidification leaving the characteristic laser pass lines.

Further analysis of the microstructure with the optical microscope at higher magnifications revealed that the darker and lighter regions appeared to be of different microstructural characteristics which are shown in Figure 5.12.

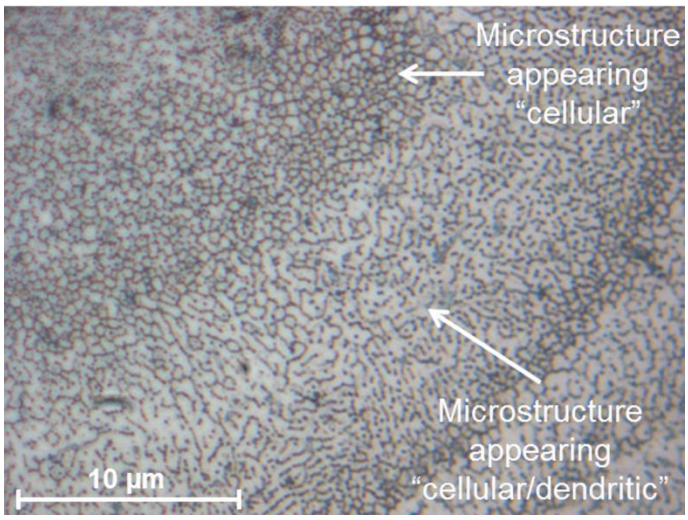


**Figure 5.12 HAZ revealing different microstructural characteristics for darker and lighter regions**

The dark areas appeared to be of a more cellular structure whereas the lighter areas appeared to be of a more cellular/dendritic structure. Comparison of Figure 5.11 and Figure 5.12 showed that the microstructure towards the outer border inside the channel was more pronounced (appearing cellular) and gradually decreased until the end of the HAZ inside the material (appearing cellular/dendritic). It was believed that the microstructure at the outer border of the channel solidified last. However, the use of optical microscope did not allow to clearly identify the type of microstructure formation (cellular, cellular dendritic or dendritic) during solidification. Different techniques such as electron backscatter diffraction in combination with EDX would be more suitable to allow the characterisation of the microstructure due to the ability to reveal grain

structure orientations which would have extended the scope of this thesis. The characteristic darker and lighter regions within the HAZ may be attributed to the amount of segregation of second phase particles. In general, when an alloy solidifies, solute which is the alloying element is rejected at the solidification front due to the higher solubility in liquid than in solid (Chalmers, 1977; Watkins et al., 1998). Therefore, it was believed that the darker areas seen in Figure 5.12 correspond to areas exhibiting a higher amount of Mn segregation as these areas solidified last, whereas the lighter areas exhibited a lesser amount of segregation as this area solidified before the darker one. therefore could be an indicator for an increase in hardness.

The amount of segregation could be an indicator for an increase in hardness within the HAZ which is substantiated by Juarez-Islas (1988) who found an increase in hardness after laser processing of Al 3003-H18. Pinto et al. (2003) reported cellular growth started at the bottom of the melt pool and due to instabilities during solidification, secondary dendritic arms were formed and an increase in hardness was found. A change in hardness would not only have altered the properties of Al 3003-H18, it may also affect future fibre embedment during UC. The hardness will be investigated in section 8.3.4.

As laser processing modified the microstructure of the UC sample around the channel area, it was reasoned to measure the distribution of the Mn by EDX point analysis. From the Al-Mn phase diagram it was observed that primary α(Al-$Mn_6$) and Al will be formed during cooling (Fink, 1949). Therefore, it was expected that the microstructure of the laser processed UC sample would exhibit those two phases. Additionally for a weight percentage of 1.2 % manganese (which is the concentration for Al 3003-H18), just below the eutectic point, the material will be composed of Al and α(Al-$Mn_6$) in which 1.8 % of manganese is dissolved. This is the limited solubility of manganese in aluminium at the eutectic point. Cooling then would lead to primary α-Al and a decrease in solubility of manganese.

The analysis of Point 1 can be seen in Figure 5.13. This point corresponded to a structure appearing cellular/dendritic. The manganese concentration is slightly

higher than 1.2 %, namely 1.3 %. A high content of oxygen (11 %) is noticed. A possible explanation may be the proximity of this point to the outer channel border as well as to the shoulder whose material consisted of oxygen and aluminium. It was possible that during grinding and polishing oxygen particles may have been dragged along.

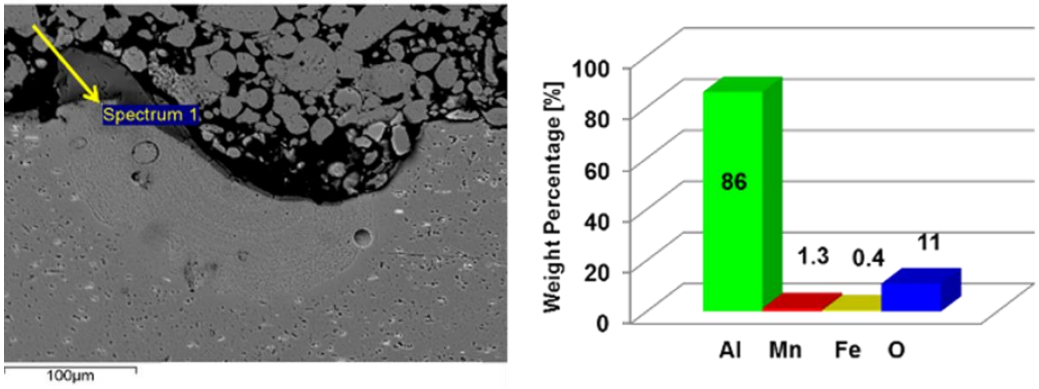


**Figure 5.13 Spectrum 1 (point) and according weight percentage distribution of main elements**

From Figure 5.14 which corresponds to point 3, it can be observed that the aluminium content increased to 95 % when compared to Figure 5.13. The reason may be less oxygen content of 2.3 % in the mixture.

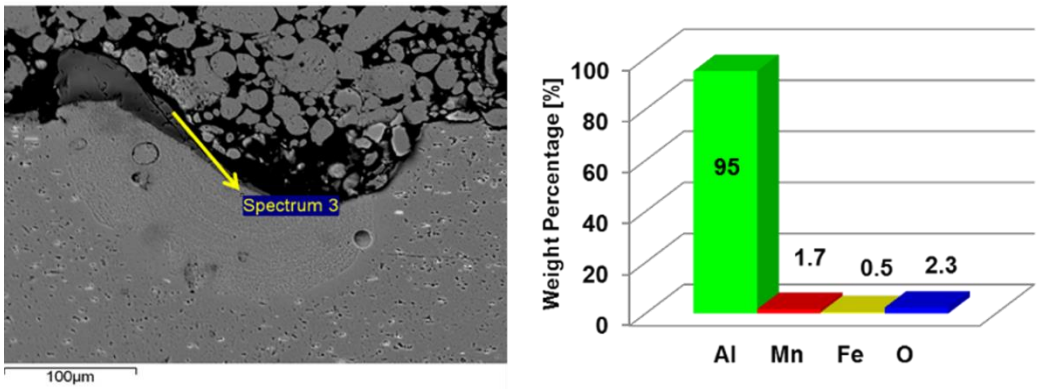


**Figure 5.14 Spectrum 3 (point) and according weight percentage distribution of main elements**

The reason that oxygen was measured again may attribute to the fact that this point was again situated close to the border of the channel and it was likely that oxides may have formed and the same explanations as for Figure 5.13 may be applicable here. Point three was of particular interest as future fibres will be

placed close to it - a difference in hardness or oxide formation may lead to failure or damage of fibres due to their delicacy.

Furthermore, this point corresponds to a drastic change in microstructure as the beam impinged here and microsegregation of Mn was expected to have occurred as this area would have solidified last. Indeed, the concentration was found to be 1.7 % for manganese which is nearly the highest percentage of manganese that can be dissolved (1.8 %) at the eutectic point in the Al-Mn phase diagram (Fink, 1949). Therefore it was expected that this area may have become harder than the surrounding and base material. The same result for manganese was expected for a point at the inner border of the HAZ which is shown in Figure 5.15. As this point corresponded to the inner HAZ border, it was likely that manganese got rejected from the solid and microsegregation took place because of the melting/cooling cycle of the passes. The manganese content was found to be 1.8 %. Moreover, there was no oxygen content detected in this point. This may be an indication that the oxygen content detected before was actually a product of grinding and polishing instead of mixing of oxides in the melt pool.

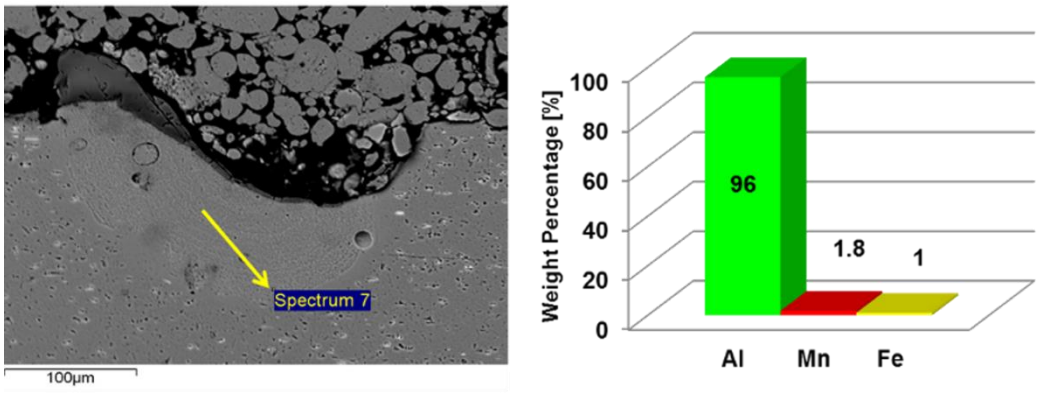


**Figure 5.15 Spectrum 7 (point) and according weight percentage distribution of main elements**

### 5.3.4 Analysis of the Shoulder

For a better understanding of the shoulder and the distribution of alloying elements in the HAZ, EDX maps were calculated from the channel area as can be seen in Figure 5.16.

Figure 5.16 shows that the shoulder mainly consists of oxygen. Furthermore, the recast layer was noticed to consist of oxygen as well. It was suggested that the molten material had been displaced with the aid of the assist gas. The molten material during irradiation and pressure reacted with the assist gas which resulted in the formation of aluminium oxide. The recast layer may then have formed because a part of the material flowed back into the channel due to the channel slope. The displacement theory would be supported by Semak and Matsunawa (1997) who suggested that that the assist gas pressure was mainly responsible for dross attachment to Al-Cu with the highest dross rate recognised for oxygen and air.

To clarify the existence of oxides and aluminium, EDX analysis was carried out. The X-Ray intensity distribution for oxygen was quite distinct, whereas the intensity for aluminium was less distinct. However, as aluminium was the main element in Al 3003-H18, it was believed that aluminium was still existent.

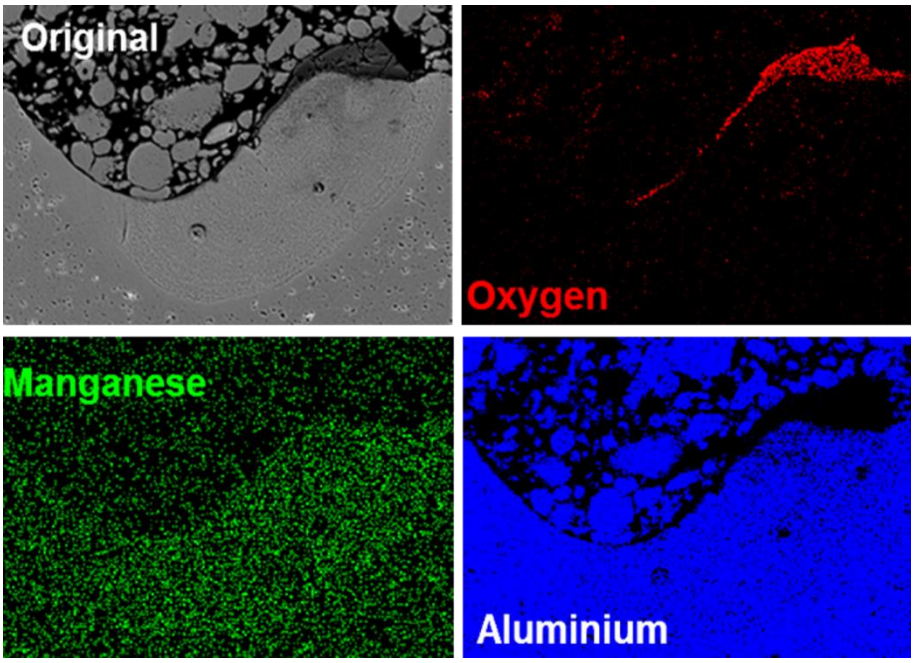


**Figure 5.16 EDX map of oxide formation within shoulder and manganese concentration in HAZ**

Further clarification was given by measuring the aluminium percentage for an area of the shoulder via EDX which is displayed in Figure 5.17. The measured ratio between oxygen (46.2 weight %) and aluminium (53.8 weight %) was

approximately that of aluminium oxide which contains 52.9 % aluminium and 47.1 % oxide. Hence, an exothermic reaction between the elements has occurred and aluminium oxide was formed which got displaced as the shoulder and recast layer. Low et al. (2000a) suggested that the recast layer consists of oxidised material and re-solidified melt. Additionally to the recast layer it was possible that an oxide layer had formed on top as the solidifying shoulder was exposed to the atmosphere. The same might have happened here, however verification is difficult due to the thickness of oxide layers in the nanometre range (Mondolfo, 1976).

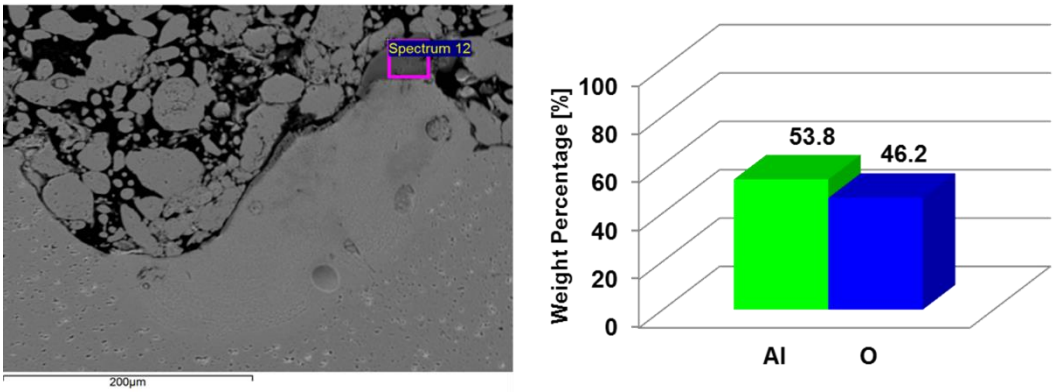


**Figure 5.17 Analysis of shoulder material and according weight percentage of Al and O**

The Al 3003-H18 material was completely exposed to the assist gas which possibly dispersed within the melt during displacement. This is endorsed by (Powell et al., 2009) who reported that during $CO_2$ cutting of iron, every spark removed was covered in a thin layer of iron-oxide. Additionally to the formation of aluminium oxide, the formation of aluminium nitride was suggested to have occurred as well. This was measured by the point analysis as well. However, no nitrogen was detected. The reason may have been detection limits for EDX or the absence of nitrogen. St-Onge et al. (2004) stated that aluminium has a higher affinity to oxygen than to nitrogen. This would endorse the formation of aluminium oxide instead of aluminium nitride.

## 5.4 Review

The results have shown that multiple passes of the laser led to a higher removal rate of material. This will be valuable knowledge for future applications as different fibre types have different diameters. Laser power density and traverse speed appear to be the most influential parameters for channel creation.

An increase in power resulted in a width and depth increase for the channel for both analysed pass investigations. Slower traverse speeds resulted in larger penetration depths due to the longer interaction time between the laser irradiation and material. The assist gas had less influence on the deepening of the channel than expected which was possibly due to the high cooling rate. Especially for a higher assist gas of 0.8 MPa, the melt cooled down to quickly during laser radiation. As expected the influence of a higher amount of passes resulted in deeper channels. This was desirable for further fibre embedding. However, deeper channels came with the drawback of an increase in width. To what extent this would play a role in fibre embedding would be investigated in chapter 7.

The produced channels showed a round-shaped profile which would facilitate the secure positioning and embedding of circular-profile fibres. The influence of the assist gas helped to disperse the melt, however an unexpected result of one shoulder being created instead of the proposed two shoulders was observed. It was believed that the surface tension gradient in combination with Marangoni forces had caused this shoulder built-up on one side. Beam and nozzle misalignment was excluded to be an influence as both were aligned beforehand. The possibility of the assist gas causing the built-up was suspended as experiments on the influence of the assist gas gave no indication of influence.

Multiple laser passes altered the microstructure surrounding the channel significantly. In comparison with a single laser pass experiments as seen in chapter 4, the laser-affected zone covered a larger area. This microstructure, possibly due to five laser passes resulted in darker and lighter areas which were

attributed to the melting/cooling cycles of each laser pass. The microstructure within the laser-affected zone appeared to be of cellular and cellular/dendritic nature. However, further work would be necessary to clarify the microstructure which would have extended the scope of the thesis. The darker and lighter regions corresponded to areas with different amounts of segregation of Mn due to solute rejection in the solid. EDX measurements showed that Mn-rich areas with up to 1.8 % Mn were formed which corresponds also to the maximum solvable manganese content in the eutectic phase of Al-3003. To what extent the microstructural changes and microsegregation changes the material properties such as hardness and the effect on fibre embedment for ultrasonically consolidated Al 3003 will be investigated in chapter 8.

The shoulder and the recast layer, exhibited high amounts of oxygen which is not favourable for UC bonding. The melt was exposed air and the assist gas. Therefore the melt was surrounded and infiltrated by both which led to solidified melt consisting of aluminium and oxides; hence, a different microstructure. As both, recast layer and shoulder will be in direct contact with the fibres and new foils, it is expected that bond formation and secure fibre integration will be influenced significantly. Especially, the influence of the modified shoulder microstructure, containing a high amount of oxides, on the plastic flow during bonding needs to be investigated as the original approach to promote plastic flow may not be given anymore.

# Chapter 6.
# Investigation of Higher Quantity Channel/Shoulder Production for Future Fibre Integration via UC

## 6.1 Introduction

Chapter 6 linked the laser processing of channels and shoulders (chapter 4 and chapter 5) and the integration of fibres into the pre-processed channels (chapter 7 and chapter 8). The results of chapter 4 and chapter 5 lay the basic groundwork for channel/shoulder manufacture and proved that channel processing within Al 3003-H18 samples was successful.

The primary concern of chapter 6 was the manufacturing of samples containing a high number of channels for fibre integration and hence defining the modus operandi for future high number fibre integration. For this the laser manufacturing limitations of high channel fabrication were explored. In order to ensure that channel/shoulder layout showed no variation for higher quantities, the repeatability and consistency of the channel and shoulder layout was investigated.

## 6.2 Methodology

### 6.2.1 Determination of a Strategy for High Volume Channel Production

The strategy for high volume channel production, necessary to allow future investigations on high volume fibre embedding, was based on five considerations as schematically displayed in Figure 6.1.

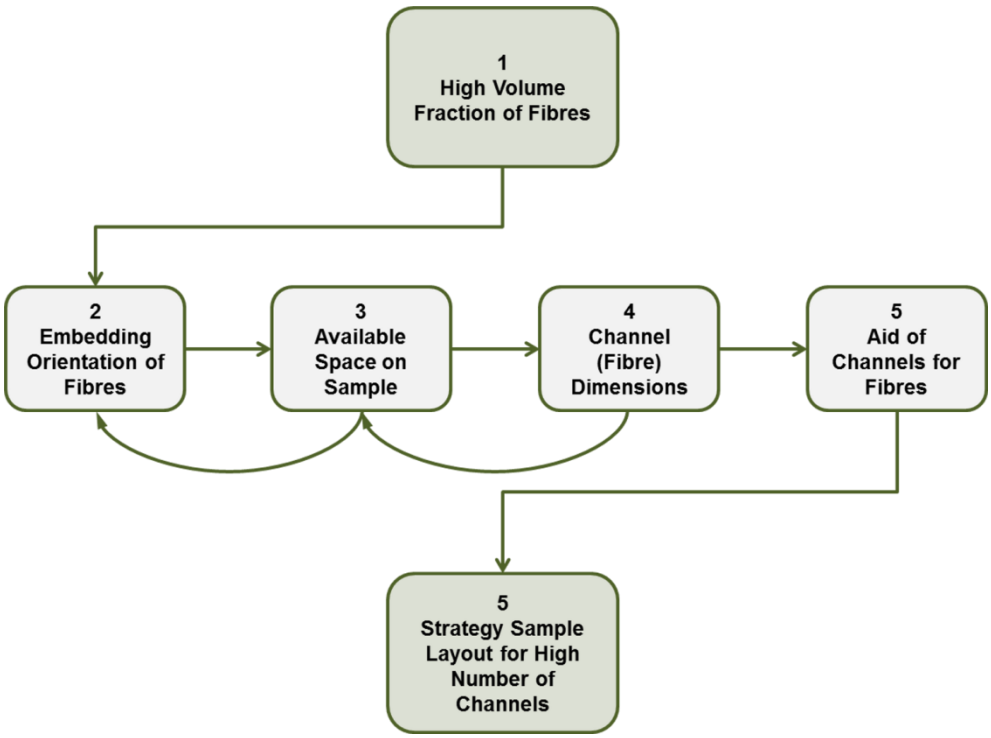


**Figure 6.1 Overview of the five interdependent considerations for sample production**

In order to investigate the value of the channels for secure positioning of fibres and plastic flow facilitation around the fibres by the shoulders when embedding a high volume fraction of fibres, the number of to-be produced channels needed to be defined. Li and Soar (2009a) embedded 33 fibres in Al 6061-O but without stating their effect on bond formation and condition after UC. Friel (2011) embedded up to 40 fibres into Al 3003-T0 matrices but only reported successful embedment for up to 30 fibres. Kong (2005) embedded 23 fibres into Al 3003-H18 without the aid of channels but observed delamination of foils. Both, Li and

Soar (2009a) and Friel (2011) used relatively soft materials when compared to Kong (2005). As the laser work was based on samples of Al 3003-H18, the work of Kong (2005) was used as a guideline for high volume fraction fibre embedding.

Additionally, to the investigation of high volume fibre embedment with the aid of channels and shoulders, the embedding orientation was of particular interest. The combination of channel, shoulder and fibre orientation would possibly influence plastic flow and bond formation during UC as reported by Yang et al. (2007). As two channel orientations had been investigated in chapters 4 and 5, fibre orientation was limited to parallel and perpendicular to the welding direction during UC.

The third consideration, available space on the sample, was limited by fibre orientation which lowered the amount of channels to be produced in parallel direction. Whereas the pre-laser sample length was set to 200 mm and theoretically a high amount of perpendicular channels could be processed, the width of the Al 3003 H18 foils was 24 mm. In Figure 6.2 these considerations are detailed. Fibre orientation also determined the channel length which in turn was limited for perpendicular channels due to the sample width which has been visually clarified in Figure 6.2 as well.

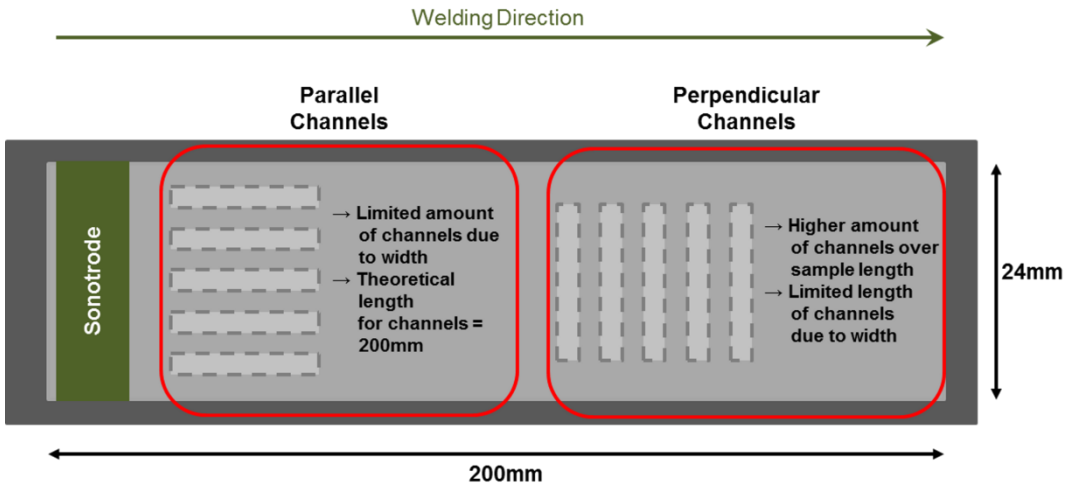


**Figure 6.2 Channel orientation on sample and corresponding considerations on space**

The fourth consideration for high volume channel production was the channel width which directly emerged from the to-be embedded fibre dimensions. At this point it was already decided to embed fibres with a diameter of about 100 µm (see section 7.2.2) which led to the consideration on how closely channels and shoulders could be produced without interference. The space available for channel production on the UC samples was limited due to the sample geometry with a width of 24 mm. This meant for channels produced parallel to the welding direction that the channels had to be produced within this range without overlap or interference. Both, overlap and interference were undesirable for the following reasons: Firstly, analysis of overlapping channels/shoulders would be difficult with regards to investigations on the plastic flow aiding the bond formation during UC. Additionally, analysis of the microstructures would be difficult for the same reason. Secondly, closely spaced channels would lower the overall space for the actual bond formation. For the case that shoulders overlap, the shoulder size would vary and bond formation would be completely dependent on the shoulder material and fibres. Thirdly, the shoulder on the channel periphery could cause a non-uniform absorption of the laser and disturb the production of the adjacent channel and change the consistency and repeatability of the process (Low et al., 2001).

Trials to determine the distances between adjacent channels without interference were carried out with the SPI redPower 200 W fiber laser on UC samples manufactured as described in section 4.2.1. The power was varied between 100 W and 120 W. The traverse speed was set to 275 mm/min and the gas pressure was set to 0.6 MPa. Air was chosen over nitrogen (even though both gases had been investigated in section 4) for the reason that these channels showed wider channels and wider shoulders. This meant that the distance between the channels would have to be wider in order to not interfere. The distances between the channels were chosen as followed: 0.25 mm, 0.5 mm, 0.75 mm, 1 mm, 2 mm and 4 mm which corresponded to a specified number of producible channels parallel to the welding direction as displayed in Table 6.1.

**Table 6.1 Overview of distances and corresponding producible number of channels**

| Distance between channels [a] [mm] | Producible number of channels [b] |
|---|---|
| 4 | 4 |
| 2 | 8 |
| 1 | 16 |
| 0.75 | 24 |
| 0.5 | 32 |

[a] based on an effective sample width of 21.12 mm and two 1 mm borders
[b] calculated from a foil width of 24 mm and an expected channel width of 0.12 mm.

The calculation of the producible number of channels was based on the supposition that the channel would exhibit a width of 0.12 mm based on the diameter of 100 µm and 0.02 mm space for secure embedding of the fibres. An extra 2 mm, 1mm on each side of the sample, was added to avoid channel production too close to the sample edge and radiation of the reflective base material by the laser to avoid beam reflection back into the cavity (Ready and Farson, 2001). For both power parameters three samples were produced with horizontal channels of a length of 200 mm which corresponded to the whole length of the UC sample. The reason for using the whole length was that this was a fast method for receiving an outlook on the consistency of the channel geometry.

The last consideration was based on the concern to explore the overall aid of the channels in terms of positioning, security and bonding. It appeared valuable to explore and compare a lower number of fibres for the case that high volume fractions of fibres embedded in the channels decrease the bond formation.

The combination of the results for producible channels, the aforementioned five considerations and the existing literature led to the decision to generate 24 channels with a distance of 750 µm between adjacent channels. Even though there was a possibility to produce 32 channels, it was suggested that the production of 24 channels ensured sufficient unprocessed space in between the

channels to investigate the bond formation in further work. To address the fifth consideration eight channels were chosen to serve as a representative of a low number of fibres.

### 6.2.2 Laser Processing of Final Samples

Laser processing was carried out for three different sets of samples. Two sets were processed by using the SPI 200 W redPower laser (see chapter 4) and one set was processed by using the Trumpf TruFiber 300 W laser. The reason for this was that research on channel processing had been carried out on two laser types by using two methods of channel fabrication. In Figure 6.3 the main influential factors for the decision to produce three sets of samples are listed. Two of the three sets of samples were manufactured using the SPI redPower 200 W laser. The difference between the sets was that two different assist gases were used – air and nitrogen.

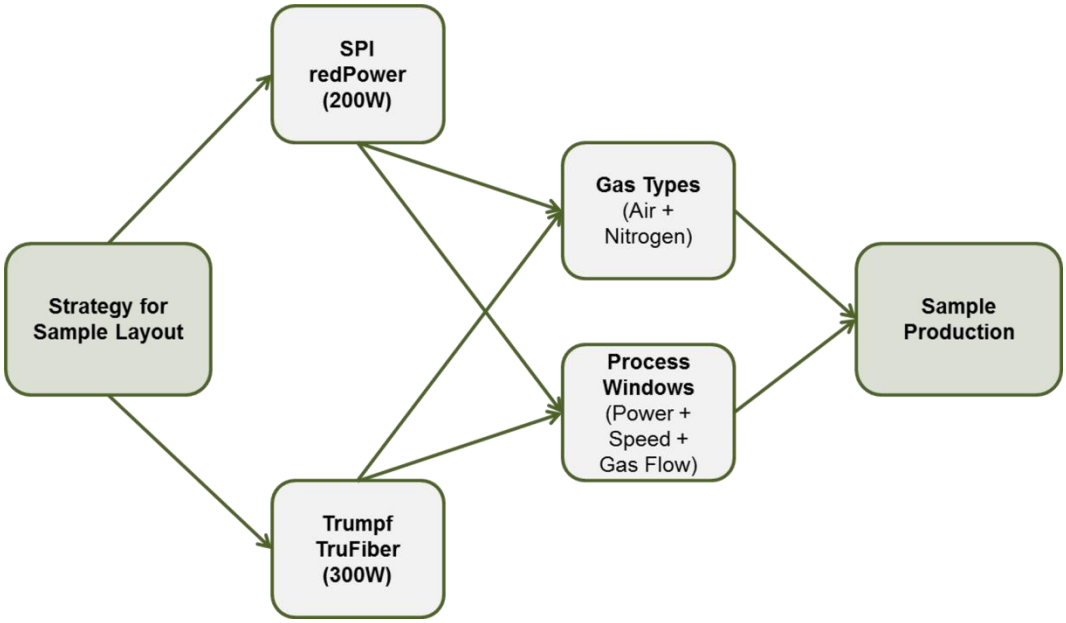


**Figure 6.3 Main laser factors for channel production**

It was postulated that different gas types would affect the bond formation in UC in differing ways. In particular air would likely aid the formation of oxides due to its oxygen content which was expected to have a weakening effect on bond formation. The third set of samples was manufactured by the Trumpf TruFiber

300 W laser with air and five passes. Three appropriate sets which complied with a diameter of 100 µm were chosen and can be seen in Table 6.2.

**Table 6.2 Overview of Parameters chosen for sample production for further fibre embedding**

| Laser Type | Parameters | | | |
|---|---|---|---|---|
| | *Power [W]* | *Speed [mm/min]* | *Gas Pressure [MPa]* | *Gas Type* |
| *SPI redPower* | 140 | 275 | 0.6 | Air |
| | 140 | 275 | 0.8 | Nitrogen |
| *Trumpf TruFiber* | 250 | 200 | 0.8 | Air |

The design of the channel patterns was carried out by programming the G-Code software to produce 8 and 24 channels in one go. Every set of samples was produced for 8 and 24 channels in parallel and perpendicular orientation with distances of 2 mm and 0.75 mm for the SPI fibre laser from the channel starting edge. For the Trumpf TruFiber laser, distances of 2 mm and 0.8 mm were chosen due to wider shoulders. The length of the channels was set to 15 mm due to the width limitation of the sample for perpendicular channel processing.

### 6.2.3 Exploration of Repeatability for Final Samples

In order to explore the repeatability, consistency and geometry of the manufactured channels, surface analysis was carried out. The analysis was conducted in two steps: The first step was carried out by using the Imagefield module of an Alicona InfiniteFocus Standard scanning microscope which has been described in 4.2.4. The Imagefield module allowed a non-contact method to scan the area which contained channels in one run on as-manufactured samples. The laser-processed sample was placed in a portable bench vice to hold it flat. The bench vice was then placed under a x10 magnification lens. An image was rendered by stitching multiple images of the area by variation of the

focus. The variation of focus was set to a z-Range of 700 µm which was sufficient to capture the total channel depth and shoulder height. The focus was set to autofocus. The microscope specifications can be seen in Table 6.3.

**Table 6.3 Lens Specifications for Alicona InfiniteFocus**

| Attribute | Alicona InfiniteFocus Specification |
|---|---|
| *Lens Magnification* | x10 |
| *Working Distance [mm]* | 17.3 |
| *HVFOV* [cm]* | 1.43 x 1.14 for 8 channels<br>1.55 x 2.22 for 24 channels |
| *Optical Lateral Resolution* | 1.1 |
| *Sampling distance [µm]* | 0.88 |
| *Vertical Resolution [nm]* | 100 |
| *Horizontal x Vertical Field of View (Size of Imaged Part) | |

For 24 channels, an area of 1.55 cm x 2.22 cm = 3.465 $cm^2$ was measured. For eight channels an area of 1.55 cm x 1.14 cm = 1.77 $cm^2$.

The resulting true colour 3D images were levelled by the integrated software in order to remove the general slope of the profile which was still visible even with a bench vice trying to hold the sample horizontally. Information of the shoulder height and channel depth was gathered by generation of 3D pseudo colour images of the channel area. The pseudo colour option was used due to its ability to show as-received grey true colour images in a coloured scale which allowed a better distinction of the channel depth and shoulder height.

The second step of surface analysis was carried out by contact measurement of the channel/shoulder profiles as described in section 5.2.2. Direct examination of the surface profile was desired as it allowed conclusions to be drawn of the surface profile itself. A tactile inductive gauge (Talysurf CLI 2000 Taylor Hobson Precision, Leicester, UK) with a diamond tip of 2 µm was traversed along the 8 or 24 channels. The machine and inductive gauge can be seen in Figure 6.4. A bench vice was again used to hold the sample flat.

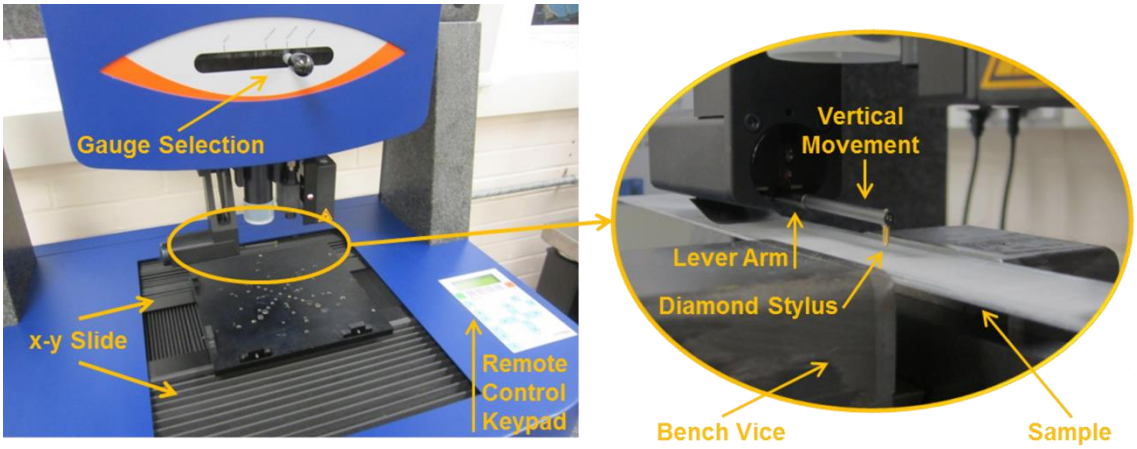


**Figure 6.4 Talysurf CLI 2000 and magnified image of the inductive gauge**

The inductive gauge range was set to medium which allowed coverage of a height movement in a range of 500 µm with a vertical resolution of 10 nm. The medium setting was necessary as the height of the channel/shoulder profile was in the range of 200 µm which had been identified by the images obtained from the measurements in step one.

For the trace of the stylus, the size of the area for 8 and 24 channels was calculated. This was necessary as the gauge was programmed to scan the channels at five equally distributed points. In Figure 6.5 a schematic representation of the five measurements for eight channels can be seen.

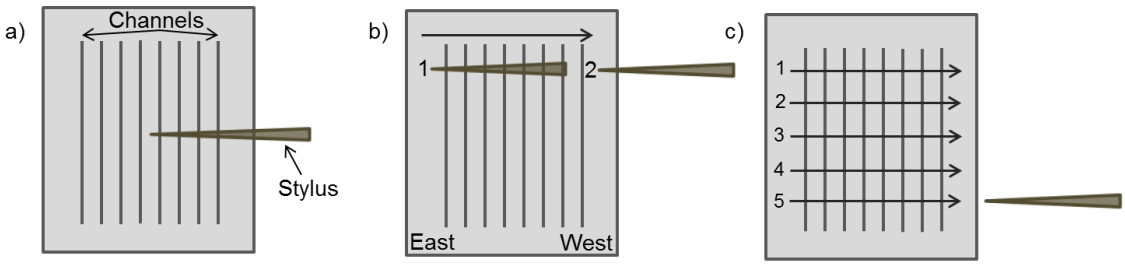


**Figure 6.5 Schematic overview of program for channel profile evaluation**

The starting scanning point was set to the middle of the sample. The stylus was traversed along the channels in east-west direction which corresponded to scanning channels perpendicularly with a scanning speed of 500 µm/s. Examination of the surface profile over the whole channel length at five random points, allowed an evaluation of the consistency and repeatability of the

channels/shoulder geometries. The as-received five scans of the surface profile are displayed in Figure 6.6. The scans were then analysed using the Talymap Platinum Version 5 software which has been described in 4.2.4.

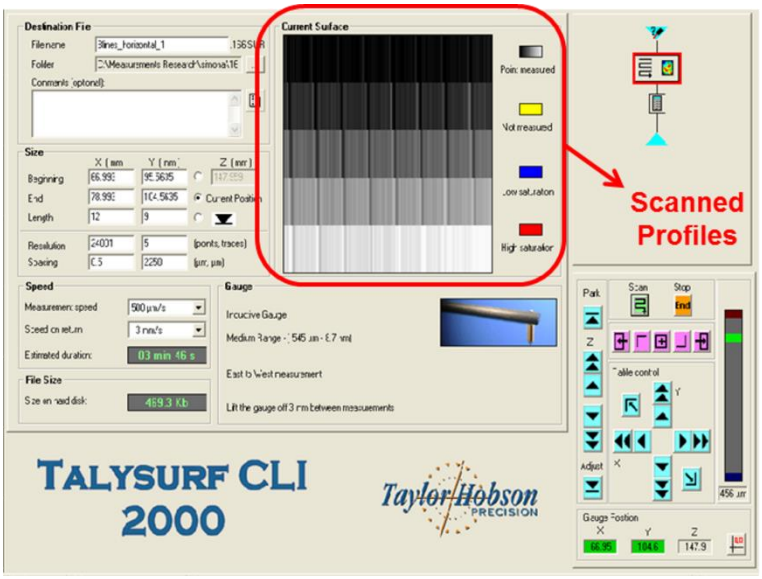


**Figure 6.6 As-received five scans of the surface profiles**

The scans were assembled to one image and levelled in order to remove the slope. For each of the five levelled surface profiles, profile measurement was carried out to allow the height and depth of the channel to be measured at the five specific points. After that a series of profiles was generated for the whole image in order to obtain an average profile for the five scanned tracks.

### 6.2.4 Quantification of the Shoulder and Channel Areas

The profiles of the samples produced by the Trumpf TruFiber 300 W laser were further investigated to analyse the consistency of the channel and shoulder formation. Those samples were chosen as they exhibited a well-defined and consistent channel and shoulder area. For this, a feature of the Talymap software “Surface of a Hole and a Peak” was employed in order to compare the shoulder and channel area. This was of particular interest as it was believed that the material was mainly melted as a result of the heat input by the laser (Semak and Matsunawa, 1997; Voisey et al., 2003) and deposited on each side

of the channel as a result of the gas and recoil pressure. Based on the literature it was believed that if the material got vaporised it would have been only a small amount (Chan and Mazumder, 1987). Quantifying the deposited material and comparing it to the channel hole was therefore an indication for melting.

In order to quantify the deposited material, the area covered by the shoulder (peak) and the area covered by the channel (hole) was measured; an example can be seen in Figure 6.7.

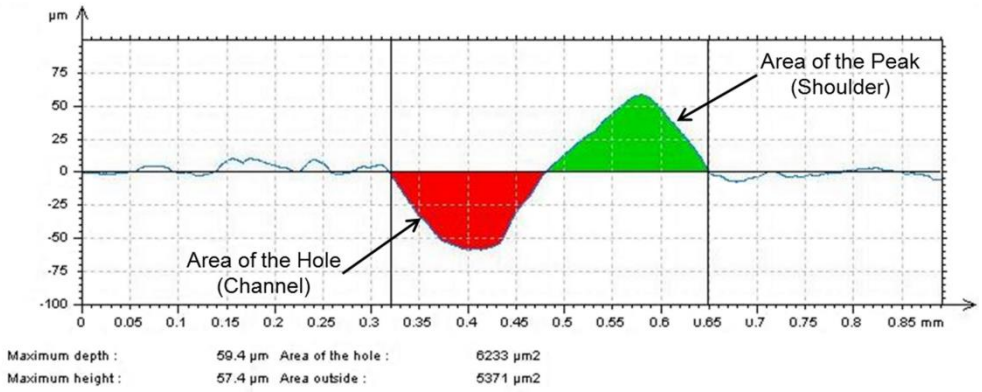


**Figure 6.7 Measurement of area covered by channel (red) and shoulder (green)**

For the analysis, ten randomly chosen samples either containing 8 or 24 channels manufactured with the Trumpf TruFiber 300 W laser were selected. From each of these samples six random channels and shoulders were analysed by using the hole under the mean line technique which means that the area of the channel and the area of the shoulder could be measured. The 60 measurements for the channel and the 60 measurements of the shoulder were then compared to each other to obtain an overview of the consistency. After that, the results of the channel and shoulder were compared to each other to see an influence and interdependence of the deposited material and channel hole.

## 6.3 Results and Discussion of Final Samples

### 6.3.1 Determination of the Possible Distances between Channels

The initial tests were carried out to study the influence of different distances between the channels as well as the behaviour of the laser to manufacture long (200 mm) and consistent channels. Figure 6.8 demonstrates a sample generated for air and two different powers (100 W and 120 W).

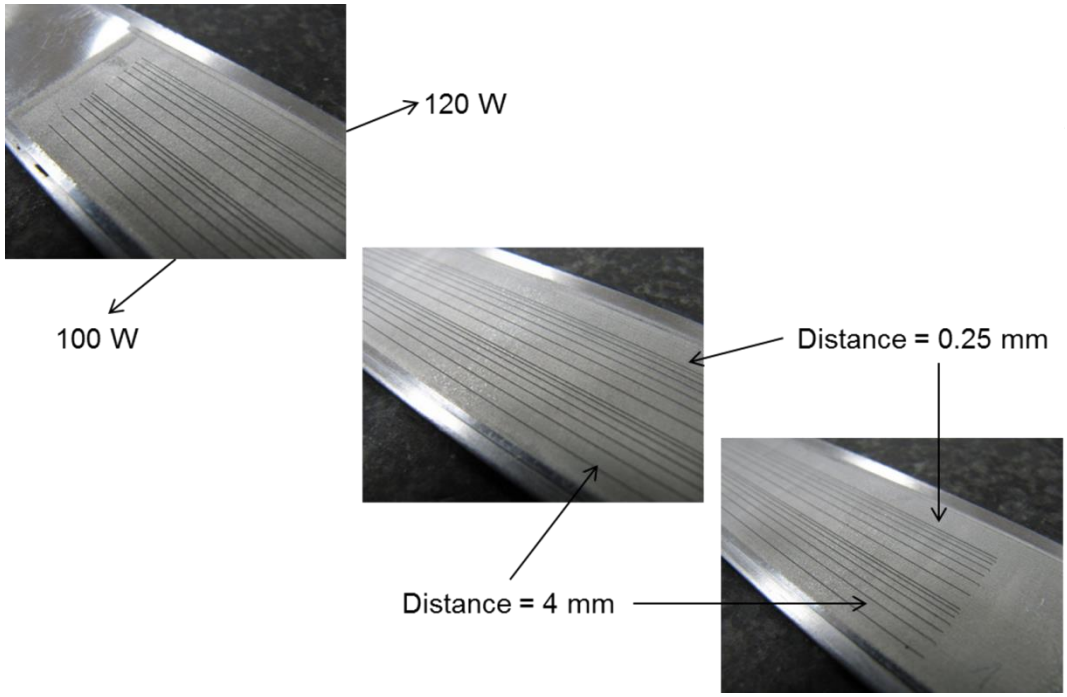


**Figure 6.8 Trial on influence of distance between the channels at two different powers**

Seven channels were produced with different distances ranging from 0.25 mm to 4 mm between adjacent channels. Analysis of the samples showed that no interference of adjacent channels and shoulders was noticed for every distance. The channel geometries appeared to be stable and consistent for the whole channel length. It was suggested that high volume channel production with distances up to 0.25 mm was possible. However, a distance of 0.25 mm would leave less space for bonding during UC as can be seen in Figure 6.8. This was considered to be an issue for channels produced by the Trumpf TruFiber 300 W laser as they exhibited wider channels and shoulders compared to channels

manufactured by the SPI Laser. To allow sufficient bonding space during fibre embedment via UC for all three sample sets and to obtain comparable results, a distance of 0.75 mm and 0.8 mm (Trumpf TruFiber) in between the 24 channels was chosen for laser processing in order to manufacture high volume fibre samples.

### 6.3.2 Non-Contact Inspection of High Volume Channels/Shoulders

Figures 6.9 to 6.11 show original images taken with a digital camera and non-true colour images for 24 channels for the three selected laser parameters. The non-true colour images were derived from the Alicona InfiniteFocus scanning microscope with a magnification of x10. An image of 24 channels generated by the SPI redPower 200 W Fiber laser for one-time radiation and air as an assist gas can be seen in Figure 6.9.

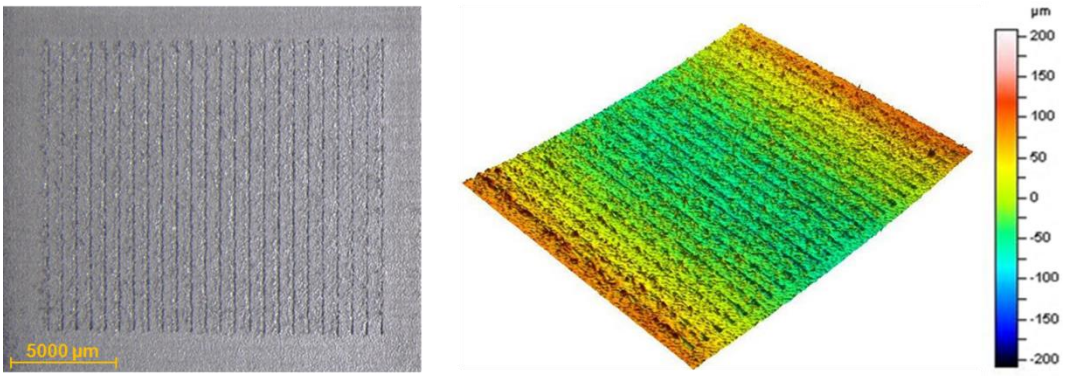


**Figure 6.9 Top view of original sample and resulting 3D non-true colour image with scale for 24 channels produced by SPI redPower laser for air**

The channels exhibited a fine and narrow outline. However, it was not possible to clearly identify any shoulders – clarification was needed by measuring the surface profile. It appeared that dross had adhered to the surface and in particular next to the channels which was an indication that shoulders had formed. Furthermore, it appeared that dross also adhered in the channels which could have lowered the geometric consistency of the channel. Removal of the dross by cleaning the sample with a cloth and acetone was unsuccessful. A comparison of the sample with samples exhibiting a high dross adherence from

section 4.3.2 showed that the dross on samples from 4.3.2 was easily removed by hand which was another indication for formation of shoulders. Dross adhesion and rough cut edges are a common problem when using air (Riveiro et al., 2010b).

Figure 6.10 shows 24 channels produced with nitrogen by the SPI redPower laser. A characteristic dark greyish to dark brown colouration is visible which is likely due to the formation of aluminium nitride (Faerber, 1995; Riveiro et al., 2010b; Reg et al., 2011).

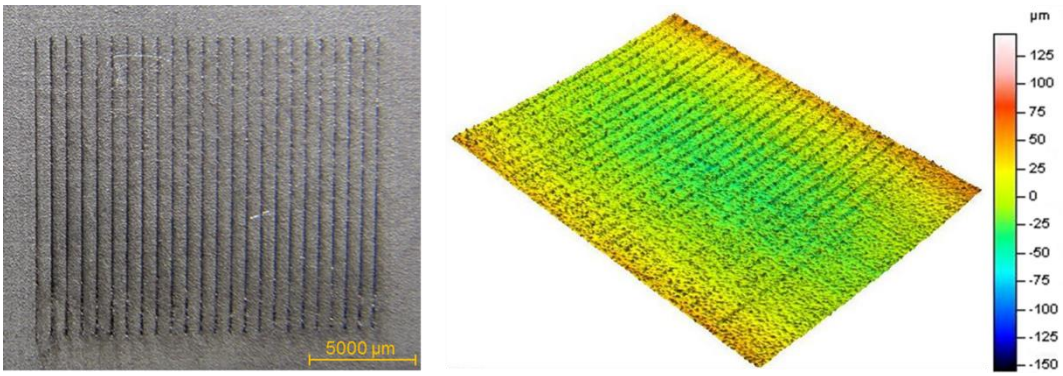


**Figure 6.10 Top view of original sample and resulting 3D image with scale for 24 channels produced by SPI redPower laser for nitrogen**

In comparison to the samples produced with air, the channels with nitrogen appeared more accurate with a distinct geometry. This was expected as nitrogen in laser cutting is commonly used when finer cut edges are needed (Caristan, 2004). Less dross, in particular next to the channels, was visible. The smaller amount of dross may be an indication for less distinct shoulder formation which will be discussed in 6.3.3. As noticed for air earlier, the consistency of the channels and shoulders was low. In addition, the channels seemed to be less deep and needed further analysis to clarify.

Figure 6.11 shows the channel outlines for 24 channels manufactured by the Trumpf TruFiber 300 W laser. Compared to the one-time radiated samples, the channels exhibited a clear geometry.

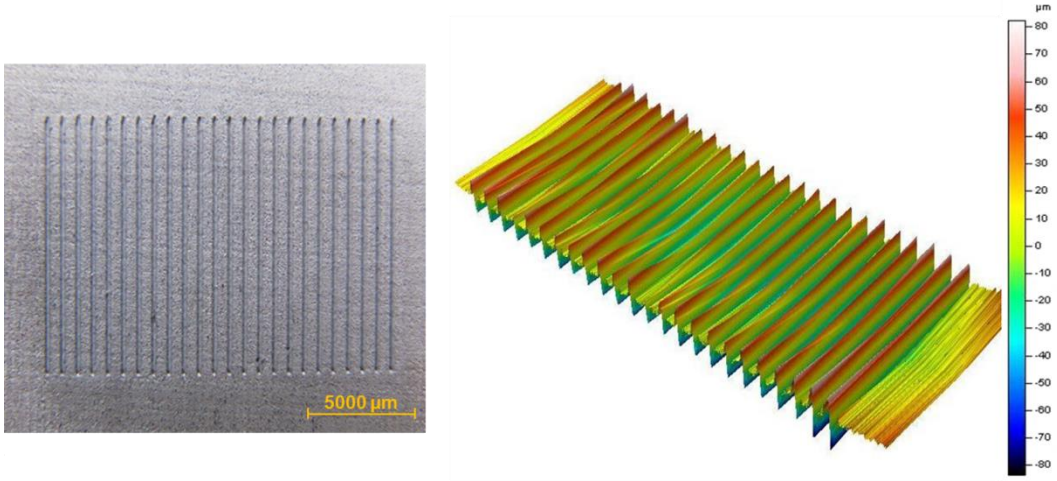


**Figure 6.11 Top view of original sample and resulting 3D image with scale for 24 channels produced by Trumpf TruFiber laser for air**

The original image showed no indication of a shoulder formed on the side of the channel. However, the non-true colour image revealed that shoulders were formed. A distinct difference between the height of the shoulders and the depth of the channels was detectable. Nearly no dross adherence was detected and unwanted spatter was not visible. In section 5.2.3 it was suggested that higher penetration rates achieved by multiple passes led to the complete melting of the channel and the material to be easily removed. Comparison with the one-time radiated channels indicated that one-time radiation may not have been sufficient enough to entirely melt the whole channel area which makes the appearance of the channels less consistent.

### 6.3.3 Contact Measurement for Repeatability of Channels/Shoulders

Figures 6.12 to 6.17 contain direct contact measurement results for 8 and 24 channels for the three sets of parameters. All of the figures exhibit channels processed in perpendicular direction. This was done for comparison reasons and was not related to better results than channels produced in the parallel direction. The appearance of the shoulder on either the left or right side of the channel is attributed to the fact on how the samples were placed into the bench vice. Depending on the placement and due to the fact that perpendicular channels are shown, the shoulder was either measured before the channel or

after the channel. The first non-true colour image shows the unlevelled surface and the second non-true colour image displays the surface after levelling. In the third image the series of the profiles is displayed. This allowed analysis of the consistency and geometry of the geometry of the channels.

In Figure 6.12 and 6.13 analysis of the channel/shoulder geometry for samples processed in the perpendicular direction with air by the SPI redPower laser is displayed. The five scanned tracks over the whole channel length were visible from the different and staggered colour profiles in the first images. The contact measurement technique clarified the shoulder formation in contrast to the non-contact technique in 7.3.2.

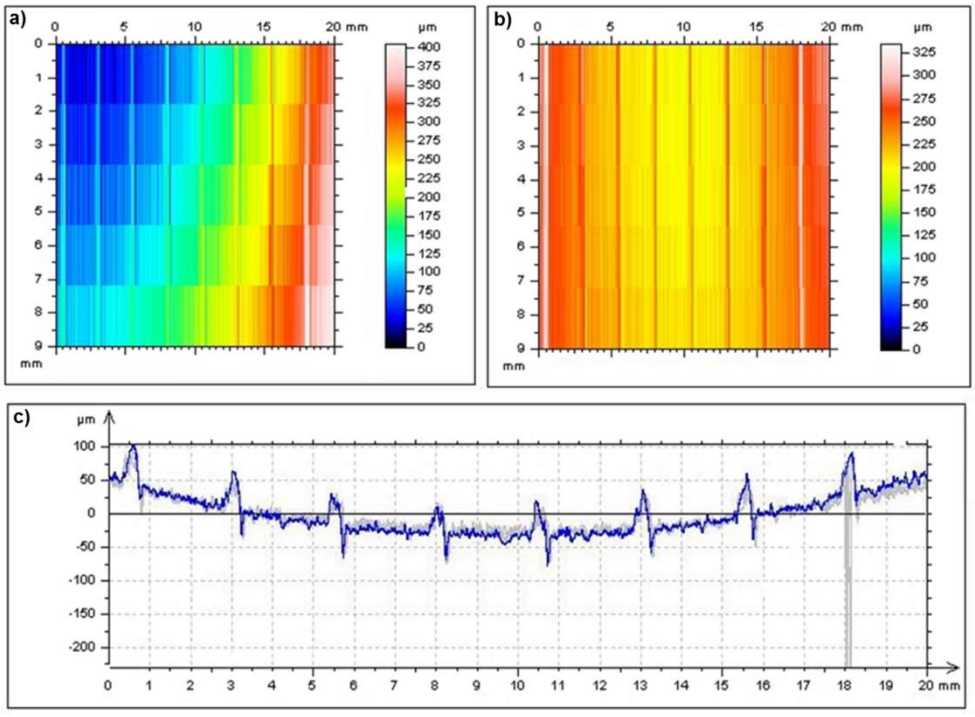


**Figure 6.12 Scanned surface of eight channels with an inductive gauge a) five scanned tracks (original) b) five scanned tracks (levelled) and c) series of profiles with mean average for air by SPI redPower laser**

As detailed in Figure 6.12, the eight processed channels exhibited the desired channels and shoulders, albeit the material being deposited on one side of the channel. This channel/shoulder outline was discovered for all the samples containing eight channels in parallel and perpendicular direction produced with

air. The depth values were measured between 40 µm to 50 µm. This was the maximum depth to be achieved for the channel creation with air and in accordance to the values measured in 4.3.2. It was interesting to note that the shoulders appeared to cover a larger area than the channel area which was unexpected as there was only melted material considered to be available for shoulder generation.

In Figure 6.13, an example of the 24 channels produced by the SPI redPower laser and air is displayed. It can be distinguished that the same channels and shoulders which were identified for 8 channels were also visible for 24 channels. The depth was measured to be in the range of 40 µm to 50 µm which was consistent with 8 channels.

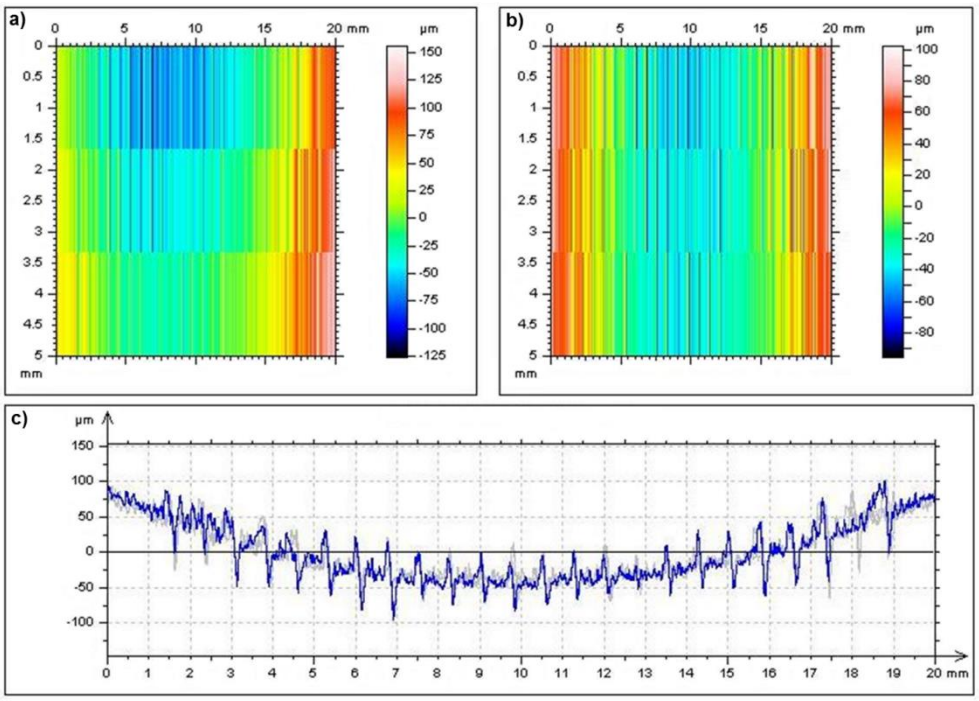


**Figure 6.13 Scanned surface of 24 channels with an inductive gauge a) five scanned tracks (original) b) five scanned tracks (levelled) and c) series of profiles with mean average for air by SPI redPower laser**

The overall consistency of the channels and shoulders which was noted for 8 channels was not applicable for 24 channels. Instead, a variety of different geometries was identified. These variations were classified as major and minor

variations. Non-penetration or partial penetration was considered to be a major variation as these failures could lead to insecure positioning of fibres and did not fulfil the purpose of the laser use. Minimal shoulders and fluctuations in the channel depth were considered to be minor variations which increased the possibility of insecure positioning. Two possible arguments were possible for the variety of channel/shoulder geometries. The first argument was that the laser may not have worked consistently. The second argument could be that dross or spatter from the melted material interfered with the processing of the next channel. Minor variations in the channel geometry were detected for nearly every sample containing 24 channels produced with air.

Figure 6.14 illustrates the scanned surface and profiles for eight channels produced by the SPI redPower laser and nitrogen.

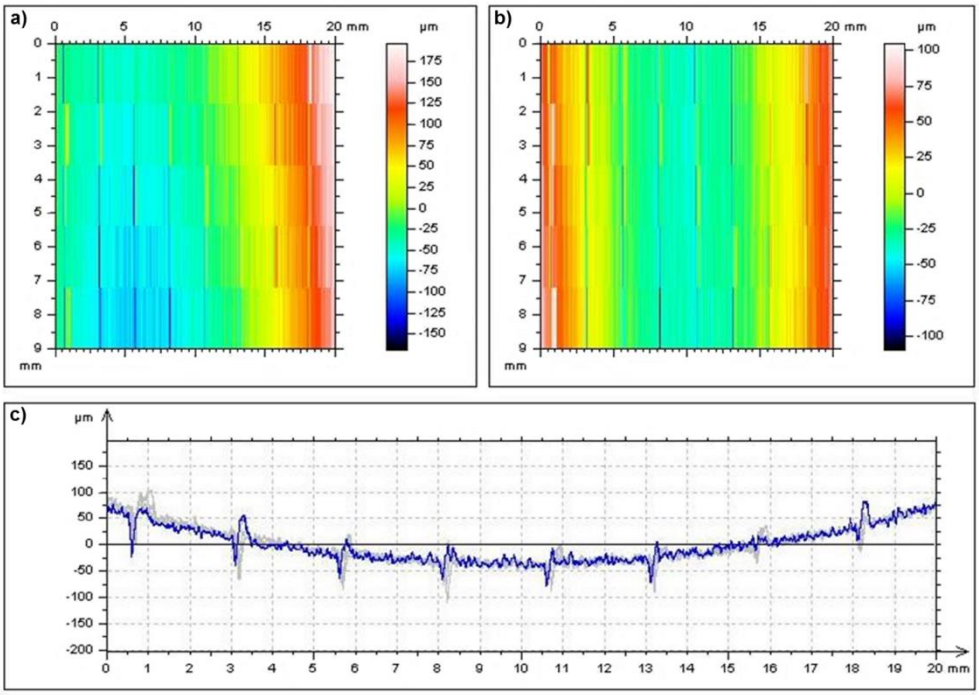


**Figure 6.14 Scanned surface of eight channels with an inductive gauge a) five scanned tracks (original) b) five scanned tracks (levelled) and c) series of profiles with mean average for nitrogen by SPI redPower laser**

The overall appearance of the channels/shoulders was nearly as distinct as for air. However, the channels were not as consistent in appearance and variations

in channel depth were noticed. The depth of the majority of channels ranged between 30 µm – 40 µm which complied with the results from 4.3.2.

The shoulders exhibited a less pronounced geometry and were sometimes non-existent which had previously been noted in 6.3.2. In general, channels produced with nitrogen were harder to manufacture than with air. A possible reason for this may have been that the high reflectivity of aluminium needed to be overcome by higher power. Air which contains about 20% oxygen was considered an external heat source and additional energy was applied to the work piece and resulted in slightly deeper and more consistent channels. Nitrogen as an inert gas contributed no external energy to the sample and was therefore possibly not able to melt the material sufficiently and consistently.

In Figure 6.15, the surface of a sample containing 24 channels and produced with nitrogen by the SPI redPower laser is displayed.

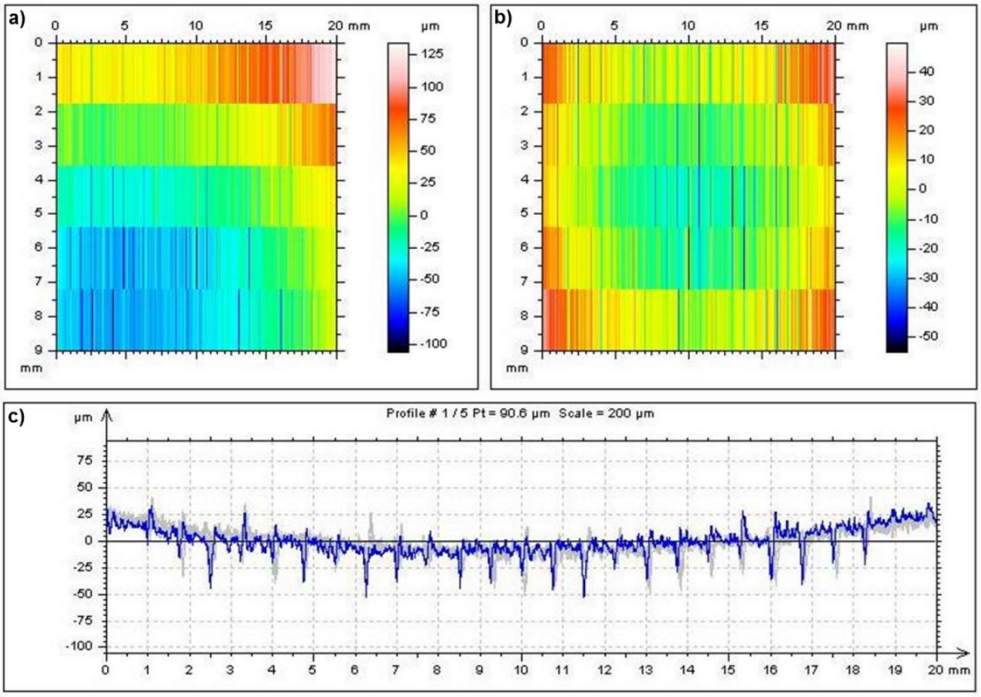


**Figure 6.15 Scanned surface of 24 channels with an inductive gauge a) five scanned tracks (original) b) five scanned tracks (levelled) and c) series of profiles with mean average for nitrogen by SPI redPower laser**

This profile was characteristic for 24 channels produced with nitrogen. A difference between the channel depths was obtained with a variation from 20µm to 60µm. It was considered that an increase in channels and decrease in distance between the channels compared to eight channels may have been responsible for a rougher profile appearance, although no interference between the channels had been identified. In addition, a colouration of the surface was noticed for both channel numbers as seen in Figure 6.10. This colouration may be an indication for surface oxidisation and formation of aluminium nitride (AlN) which might have interfered with consistent channel/shoulder manufacturing.

Figure 6.16 represents eight channels produced with the Trumpf TruFiber 300W laser. The channels were radiated five times.

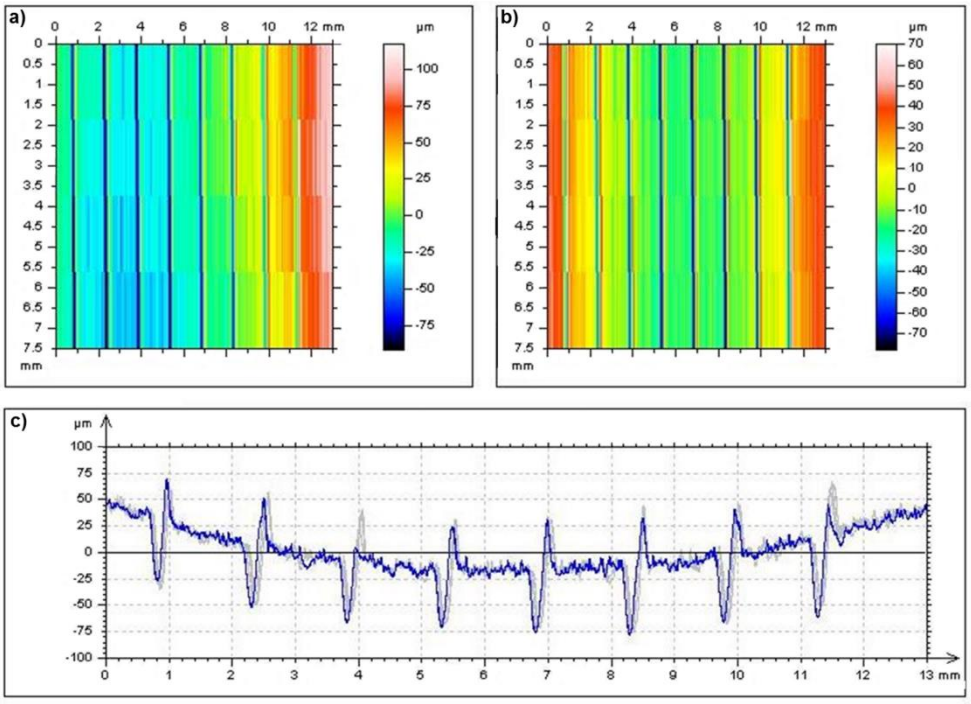


**Figure 6.16 Scanned surface of eight channels with an inductive gauge a) five scanned tracks (original) b) five scanned tracks (levelled) and c) series of profiles with mean average for air by Trumpf TruFiber laser**

As anticipated the channels and shoulders were clearly visible. Moreover, the overall appearance of the channels/shoulders was more distinct and easier to be analysed in comparison with the channels produced by the SPI redPower

fiber laser. The analysed channel depths varied between 65µm to 80µm and were therefore deeper than the one-time radiated channels. Furthermore, the channels exhibited highest consistency for channel processing and were in good agreement for fibre embedding. The width of the channels was larger than the before-mentioned channels as discussed in 5.3.5. The shoulders showed the same behaviour as the channels and were similarly consistent with a few exceptions in the shoulder height. The height of the shoulders (25 µm to 50 µm) was smaller than the channel depths which led to the suggestion that not all of the melted material was deposited (this is analysed further in section 6.3.5). Overall, the channels and shoulders shown in Figure 6.16 exhibited a promising geometry for fibre embedding.

In Figure 6.17, an example of 24 channels processed with the Trumpf TruFiber 300W laser is displayed. Again, the distinct channel/shoulder outlines were clearly visible. Analysis of the depth complied with the results for eight channels. A depth of 65µm to 80µm was obtained. Due to the higher heat input to the sample, the sample was curved more than for eight channels.

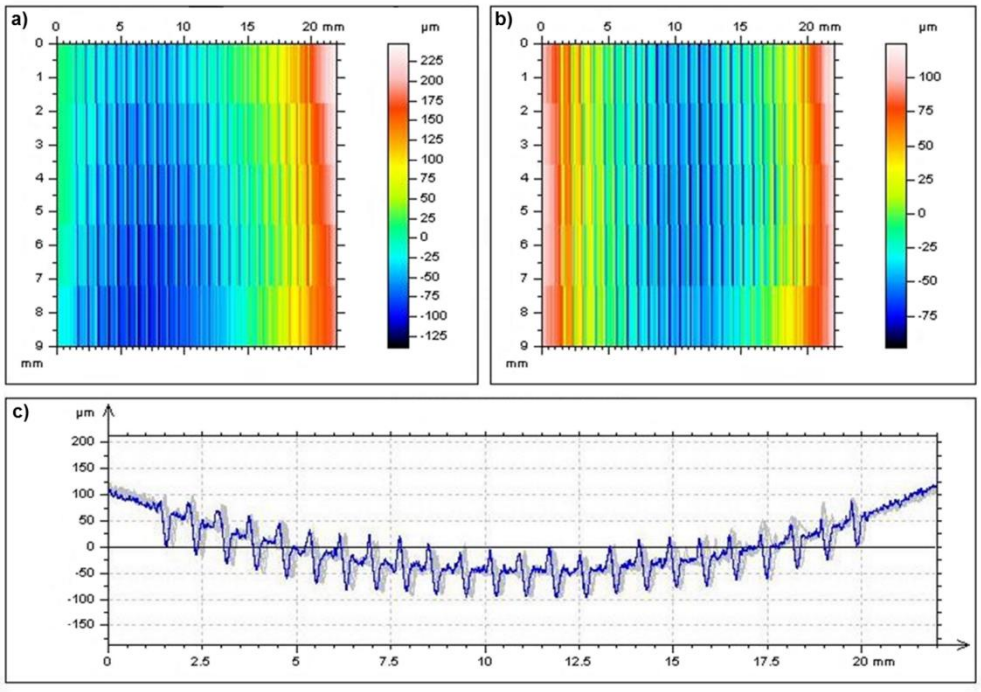


**Figure 6.17 Scanned surface of 24 channels with an inductive gauge a) five scanned tracks (original) b) five scanned tracks (levelled) and c) series of profiles with mean average for air by Trumpf TruFiber laser**

The same behaviour was detected in Figure 6.13, whereas for Figure 6.14 samples processed with nitrogen appeared less curved. This may be an indication that the heat input for nitrogen was less due to less available energy. In contrast to 24 channels with the SPI redPower laser, the shoulders are highly consistent. In addition, no defects of the shoulders such as non-shoulders were detected for any sample processed in both orientations.

Channel and shoulder manufacturing was carried out for all gas and laser types by applying different manufacturing approaches. The most promising appearance was observed for channels manufactured by the Trumpf TruFiber 300 W laser. The channels and shoulders did not interfere with each other which was a contribution to knowledge for further channel manufacturing processes. However, even though all processed channels showed an agreeable appearance for further work, it was considered to further the work only with two gas types.

### 6.3.4 Inspection of Channel and Shoulder Areas

To inspect the shoulder areas, six shoulder areas (peak areas) from ten randomly chosen samples containing either 8 or 24 channels all manufactured with the Trumpf TruFiber 300 W laser were selected. The 60 measurements of the calculated shoulder areas can be seen in Figure 6.18.

The range of the majority of the calculated areas was between 3000 $\mu m^2$ to 7000 $\mu m^2$. The single graphs of the ten samples showed no indication that the shoulder areas for one single sample were all in the same range as was expected. In fact, the range between the different measurements varied significantly and exhibited no straight lines which would have indicated that all shoulder areas on a single sample were consistent.

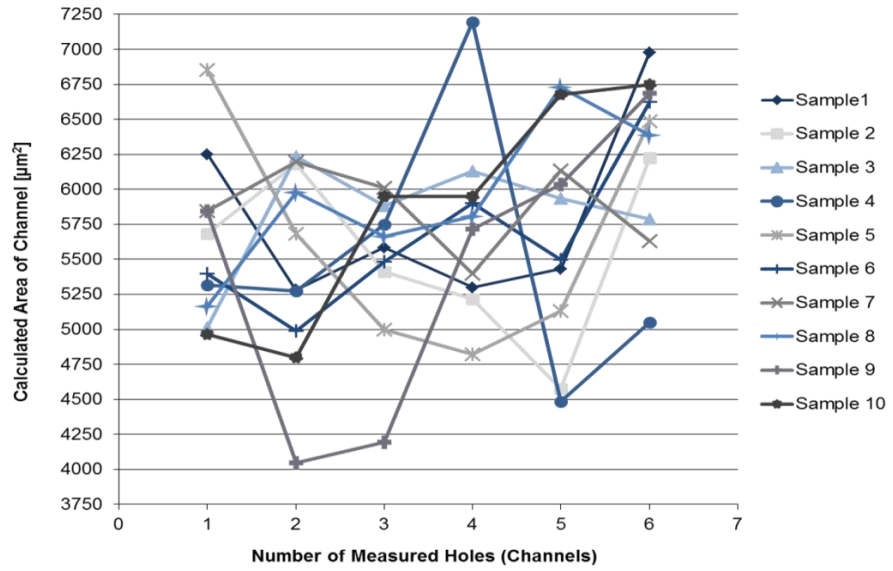


**Figure 6.18 Calculated area for six arbitrarily chosen shoulders on ten randomly chosen samples containing either 8 or 24 channels manufactured with Trumpf TruFiber laser**

Figure 6.19 exhibits the 60 measurements taken from the calculated 'hole' areas (channel areas). In contrast to the shoulder areas, the channel areas varied in a lesser range of 4000 µm$^2$ to 7000 µm$^2$.

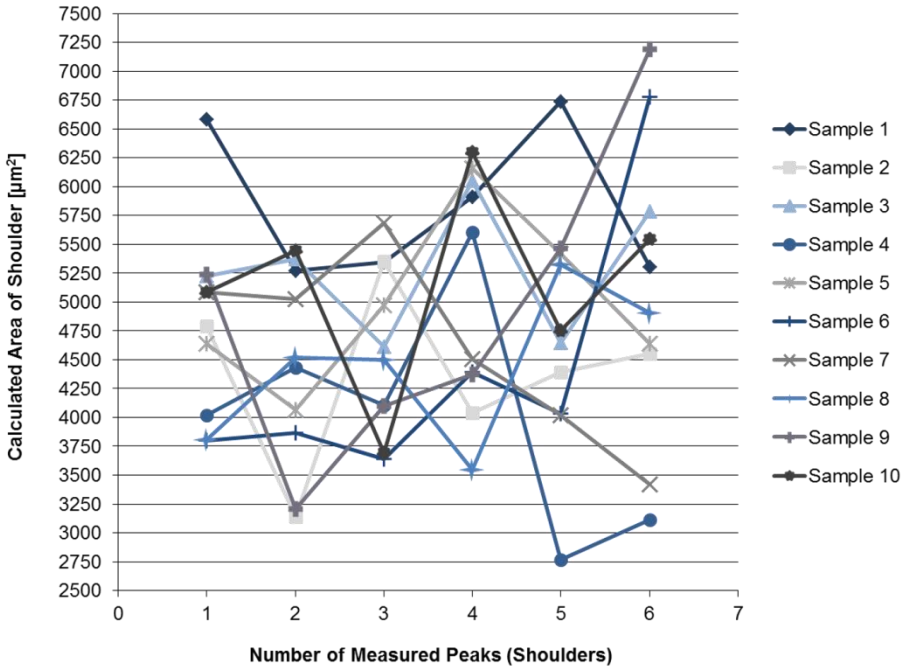


**Figure 6.19 Calculated area for six arbitrarily chosen channels on ten randomly chosen samples containing either 8 or 24 channels manufactured with Trumpf TruFiber laser**

In general, it was anticipated that the areas of the channels would show greater consistencies than the shoulders as the melting of the channel area was easier to control than the melt displacement due to the fluidity of the melt and the spatter generation. The single graphs illustrated greater consistency of the channel area results compared to the single shoulder graphs. The lines of the single channel samples appeared to be straighter compared to the shoulder lines. However, sample four and nine exhibited great variations in the values. Comparison of the two diagrams indicated a relationship between the areas of the shoulders and the areas of the channels. A substantial amount of the single graphs were in good agreement with each other.

In Figure 6.20, the mean calculated areas for all six values of the channels and shoulders are displayed for the ten samples.

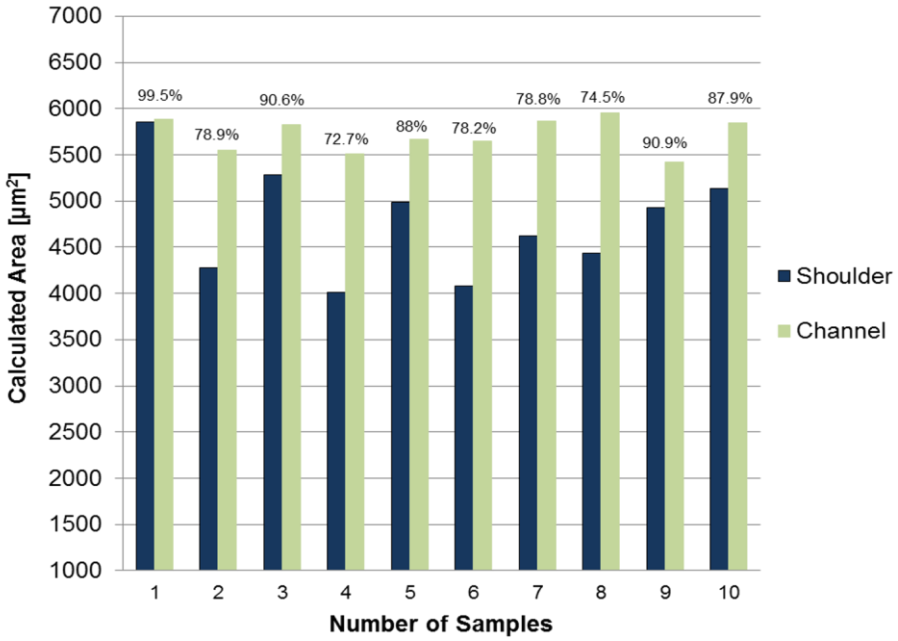


**Figure 6.20 Mean average for six arbitrarily chosen channel/shoulder areas on ten randomly chosen samples containing either 8 or 24 channels manufactured with Trumpf TruFiber laser**

The greatest conformity between shoulder and channel area was seen for samples 1, 3 and 9. As explained for Figure 6.19 and also indicated for Figure 6.18, the mean area of the channels remained approximately the same for all ten samples. The mean channel area varied between 5300 µm$^2$ and 6000 µm$^2$. This suggested that the channel width and depth for channels produced by the

Trumpf TruFiber laser could be controlled as substantial consistencies over the whole sample range was noticed. The shoulder area however varied to a greater extent between 4000 $\mu m^2$ and 6000 $\mu m^2$. It was inferred that the shoulders were more difficult to be controlled than the channels. Consistency of the shoulders was achieved in terms of shoulder manufacturing itself but was apparently less consistent in width and height. The percentages shown in Figure 6.20 relate to the percentage of removed and deposited material to the side of the channel. For all samples over 70 % of the material was deposited. This suggested that the material was melted by the laser and only a percentage of approximately 1 % to 30 %, dependent on the sample, either vaporised or was displaced in form of spatter. However, in section 5.3.4 it was suggested that the shoulder material consisted of $Al_2O_3$ instead of pure Al. As the volume of $Al_2O_3$ forming the shoulder will be different to the volume of pure aluminium removed from the channel due to their different densities ($Al_2O_3$ = 3.95 $g/cm^3$ and Al = 2.73 $g/cm^3$), it was found difficult to compare the removed and replaced material. Taking the formation of $Al_2O_3$ into account meant that the mass of the deposited Al would decrease as $Al_2O_3$ is a mixture of 52.9 % Al and 47.1 % Oxygen. Hence, the volume of the displaced Al would decrease as well. It was not possible to say if for the samples exhibiting a percentage of 70 % displaced material, 30 % were vaporised or experienced a change in volume due to the formation of $Al_2O_3$.

## 6.4 Review

The aim of the chapter was to produce samples with channels and shoulders which would enable high volume fractions of fibres to be embedded. Hence, the repeatability and consistency of the channels and shoulders was important in order to filter influences on future fibre embedment. The manufacturing of channels was a novelty for fibre embedding and further expands the research on fibre embedding approaches. Additionally, this approach could expand the research for other delicate components which may be embedded in future UC applications.

Tests on the distances between channels showed that a distance of less than 0.25 mm between the channels was possible to manufacture. To secure a non-interference of the channels, shoulders and HAZ, it was decided that distances above 0.5 mm could be chosen for channel production. It was hoped that a greater distance between adjacent channels would enhance bonding of the foils. A strategy for high number channel production was developed taking into account four considerations: firstly, the embedding orientation of fibres, secondly the available space on the UC sample, thirdly future fibre dimensions and fourthly the overall aid of the channels for fibre embedment. It was determined that samples consisting of 24 channels with a distance of 0.75mm between adjacent fibres were appropriate to allow high fibre volume fractions of fibres to be embedded. However, the understandings of close spacing between the channels and shoulders could contribute to future fibre embedding when for example different sizes of fibres should be embedded or higher numbers of fibres. To what extent the spacing between the channels plays a role in bond formation would be investigated in chapter 8.

Especially multiple passes manufactured with the Trumpf TruFiber laser showed a promising overall channel/shoulder appearance. The SPI redPower Fiber laser exhibited a less distinct channel/shoulder appearance which was likely due to the one-time radiation of the channels and the loss of power. In addition, for the SPI redPower fiber laser the consistency and repeatability of a high amount of channels was less encouraging and more difficult to control than for the Trumpf TruFiber laser which was again attributed to the lack of power experienced with the SPI redPower laser. The Trumpf TruFiber laser showed a high consistency and repeatability for channel/shoulder production. The analysis also indicated that the depth of the channels was consistent, whereas the shoulder parameters were harder to be controlled.

As the results for the SPI redPower laser for air and nitrogen showed approximately the same results, it was decided that only one of the two gases should be used for further investigations. Even though the channel/shoulder outlines for air were more promising, nitrogen was chosen to be further

explored. The reason for this was that air as a processing gas was already going to be explored for fibre embedding with samples manufactured with the Trumpf TruFiber 300 W laser and it was suggested that nitrogen as an inert gas possibly provides a different insight into the bonding mechanism especially in terms of oxide formation.

# Chapter 7.
# Impact of Pre-Processed Laser Channels on Precise Positioning and Secure Embedment of SiC Fibres into UC Matrices

## 7.1 Introduction

Production of Al 3003-H18 samples containing 24 channels was successfully carried out in chapter 6. In chapter 7, the research was aimed at fundamental understanding of fibre embedding into channels which was an essential part of the hypothesis. The primary focus in this chapter was the assistance of the pre-processed channels for accurate fibre positioning during UC as well as preserving the integrity of the fibres after UC.

To understand the deformation behaviour of the one-sided shoulder during UC and to investigate the possible impact on fibre integration, samples without fibres were consolidated before fibre embedment. Investigation of the assistance of pre-processed channels on accurate positioning of fibres was carried out by measuring their distances after UC. The fibre behaviour inside the channel and the integrity were characterised and analysed by macroscopic SEM inspection.

## 7.2 Methodology

### 7.2.1 Deformation Behaviour of One-Sided Shoulder

To evaluate the plastic deformation behaviour of the shoulder, samples were manufactured without fibres. This examination was expected to give insight on the deformation behaviour and possible aid of the shoulder for fibre embedment as well as the plastic deformation behaviour of the upper foil with regards to channel and shoulder. Additionally, it was considered necessary to evaluate the influence of the shoulder position during UC as well as the influence of the welding direction (perpendicular and parallel) on the deformation of channel and shoulder during UC. Furthermore, it was of special interest to investigate how the shoulder deforms - especially with regards to oxide distribution along the interface - when located behind the channel and welding perpendicularly channels as displayed in Figure 7.1.

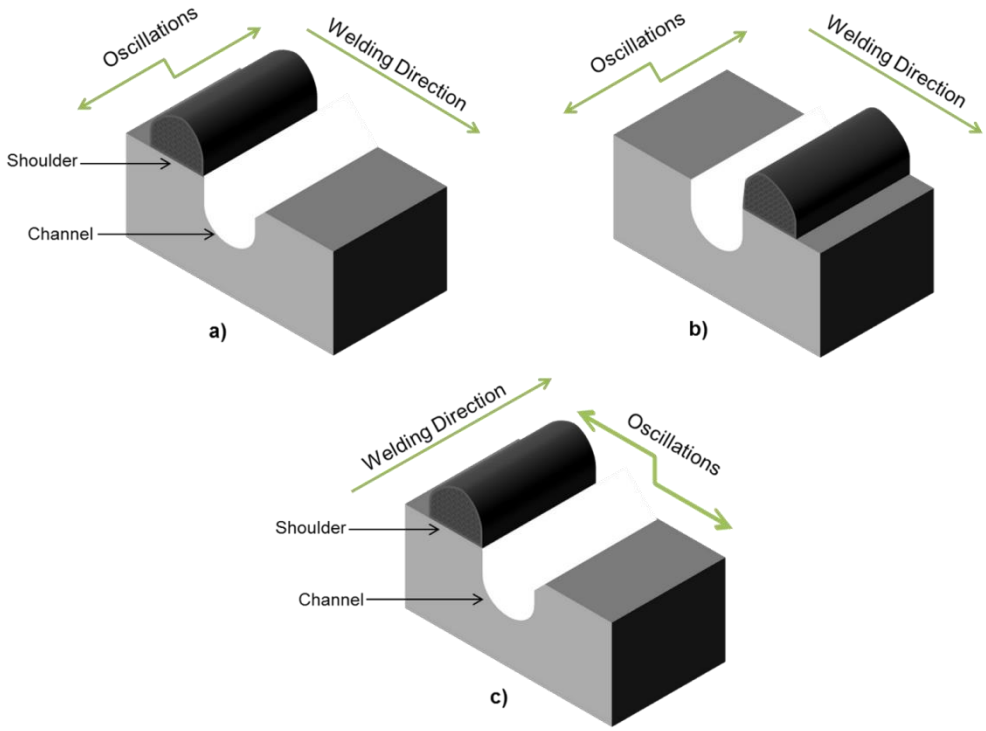


**Figure 7.1 Variable shoulder positioning a) shoulder in front of channel perpendicular to welding direction, b) shoulder behind channel perpendicular to welding direction, c) shoulder in front of channel for channel parallel to welding direction**

The manufacturing procedure was as follows: Samples from chapter 6 containing 24 channels were consolidated as-received by welding one foil on top of the channel area by using the parameters from 4.2.1. To understand the influence of UC on the shoulder deformation, care was taken to cover the different positions of the shoulder. Three possible shoulder positions were located which could influence the bonding quality (see Figure 7.1).

1. Samples containing channels perpendicular to welding direction. The shoulder was located before the channel with regards to welding direction.

2. Samples containing channels perpendicular to welding direction. The shoulder was located behind the channel with regards to welding direction.

3. Samples containing channels parallel to the welding direction. The shoulder was located on the side of the channel with regards to welding direction.

For samples containing channels parallel to the welding direction it was not considered necessary to investigate both shoulder directions. The behaviour of one shoulder under pressure and oscillations would suggest the behaviour of the other one. In order to get a better visualisation of the deformation behaviour of the shoulders, additional samples were produced for all shoulder positions which contained copper foil. High purity copper foil was chosen due to two reasons: firstly, it was readily available and secondly is a relatively soft material which deforms easily during UC compared to Al 3003-H18 (Sriraman et al., 2010). The foil (50 µm thick) was placed in between the sample containing channels and the upper foil. This was done for samples containing 8 channels to ensure that bonding will take place between the upper and lower foils. The welding procedure was carried out under the same conditions described before.

Analysis of the plastic behaviour of non-fibre samples was carried out via microscopic inspection which will be explained in sections 7.2.4 and 7.2.5. The samples were not chemically etched in order to avoid a biased reaction of the microstructure (Friel, 2011). Images covering the whole channel/shoulder area were taken.

### 7.2.2 Fibre Selection

The selection of the fibre type to analyse the aid of the channel/shoulder was based on the following considerations: Firstly, the fibre type should aid the analysis of fibre behaviour within the newly processed channels in terms of positioning, accuracy and security. Secondly, the fibre type should aid to examine the influence of the channel and shoulder on plastic flow and bonding during UC (examined in chapter 8). Ergo, the attention was concentrated on studying the channel/shoulder/fibre behaviour rather than the behaviour of the fibre itself. It was reasoned that three different types of fibres, Ni-Ti SMA, optical fibres and SiC, would be possible to embed due to their availability and use in earlier UC research (Kong et al., 2004b; Kong, 2005a; Friel and Harris, 2010). However, SMA's are prone to undergo phase changes at elevated temperatures (Van Humbeeck, 2001; Parlinska et al., 2001; Friel, 2011) and optical fibres may be sensitive to damage (Kong and Soar, 2005a). Both may therefore alter accurate information of the influence of the channel during fibre embedment and additionally, are cost-effective. For those reasons, SiC fibres were chosen to be embedded. SiC fibres have been studied in earlier research regarding bond formation and mechanical fibre behaviour (Kong, 2005; Yang et al., 2007; Li and Soar, 2008; Li and Soar, 2009a; Yang et al., 2009; Yang et al., 2010) during UC.

The fibre chosen for this study was a SiC sigma fibre (SM-1240) and was supplied by Qinetiq. The fibre consisted of a 10 µm tungsten core and an outer diameter of 100 µm, with a double coating of approximately 1 µm titanium boride and approximately 1 µm carbon. The hard nature and high strength of the SiC fibre allowed high pressure and oscillations to be used (Yang et al., 2007) with minimal fibre distortion (Kong and Soar, 2005b).

Additional practical factors to take into account when handling SiC fibres include: Firstly, SiC fibres are difficult to shape due to their brittle nature (Stacey, 1988) and possible issues for accurately positioning the fibres in the channel have to be expected. Secondly, their brittleness might lead to fibre breakage due to the oxide formation detected in chapter 5 or fibre breakage due

to oscillation stress and pressure during UC. Thirdly, the interfaces of the matrix material (Al) and fibres (C) might chemically react (Rajan et al., 1998; Kong and Soar, 2005b).

### 7.2.3 Fibre Embedding Procedure

Previous studies concerned with fibre integration via UC used differing methods to hold the fibres in place: a custom designed fixture (Yang et al., 2007), random placement within the foils (Kong and Soar, 2005b; Li and Soar, 2007; Yang et al., 2009) and clamping the fibres (Friel and Harris, 2010). All the studies embedded the fibres over the whole sample length (parallel to the welding direction). However, for future applications it may not always be possible or necessary to embed fibres over the whole length or fibres need to be embedded in different directions. In comparison to previous studies concerned with the possibility of embedding of fibres and their behaviour post-UC, this study emphasised the aid of channels and shoulders to embed fibres. As the manufactured channels had a length of 15 mm, integration of parallel fibres over the whole length of the UC sample was not conducive for studying the influence of the channel and shoulder. Additionally, as fibres were also embedded in perpendicular direction, clamping was not feasible.

To overcome the vital aspect on how to fixate fibres in the channels before UC was carried out by (Chan, 2011) and is shown in Figure 7.2.

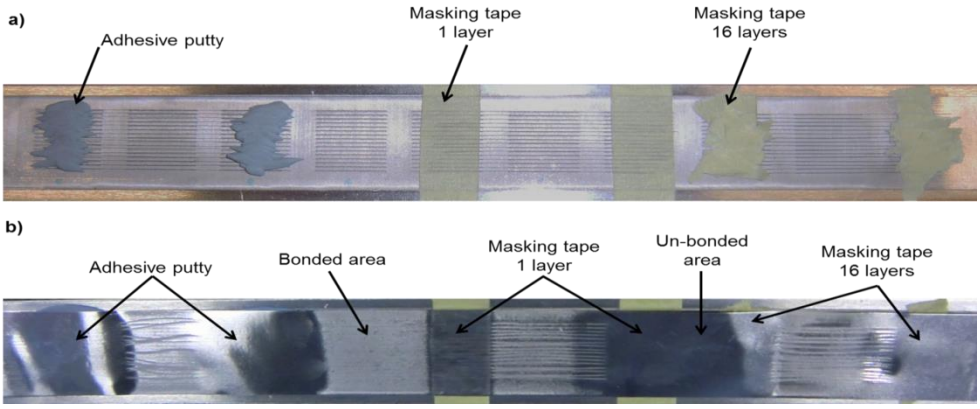


**Figure 7.2 Fibre fixation with adhesive putty and masking tape a) before and b) after UC (Chan, 2011)**

Trials on embedding fibres were carried out with two types of adhesive tape and adhesive putty. The adhesive putty and masking tape results can be seen in Figure 7.2 a) and b). The results showed that masking tape gave the best results for both, holding the fibres firmly in place and good bonding. The use of an adhesive was abandoned for two reasons: liquid adhesives need time to harden and therefore time until the fibres are positioned and secondly they are difficult to be applied in an accurate manner and might diffuse into the foil materials and bonding areas between the foils which may affect bonding (Chan, 2011).

For the samples with fibres placed perpendicular to the welding direction: the masking tape needed to be applied to the area which was not consolidated and therefore not in contact with the sonotrode, as can be seen in Figure 7.3. Indirect contact between the tape and the sonotrode resulted in non-bonding which is also indicated in Figure 7.2 b) as the non-bonded areas. As the best results were achieved with masking tape, this method was copied for every sample produced in this study.

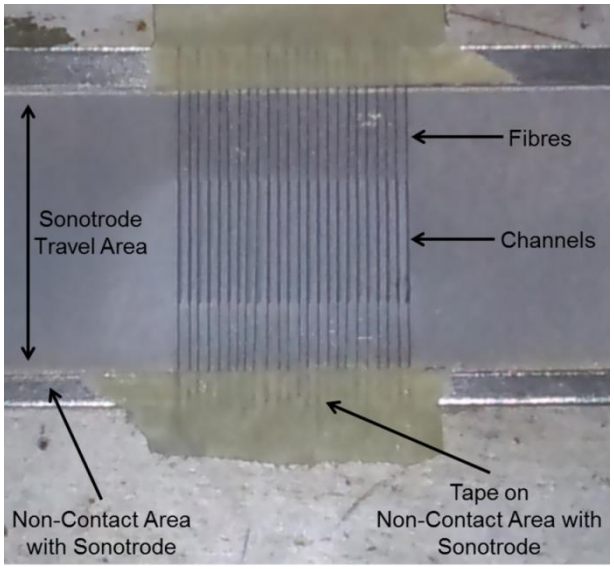


**Figure 7.3 Fibre embedment of 24 Fibres and fixation with masking tape before UC**

A schematic arrangement of the UC process for fibre embedding is illustrated in Figure 7.4. After placing the SiC fibres in the channels and applying masking

tape, the sample was placed on the anvil of the UC machine (Figure 7.4 a)). A new strip of foil was carefully placed over the old welded area and clamped on (Figure 7.4 b)). The parameters were then set to ultrasonically consolidate the new strip of foil. In order to avoid deviations in bond quality and to avoid new variable parameters, amplitude, pressure and welding speed were kept the same as for UC sample processing before laser processing (see section 4.2.1) with 20 µm, 1400 N and 40 mm/s respectively. After setting the parameters, the new foil was welded to the old foils (Figure 7.4 c)).

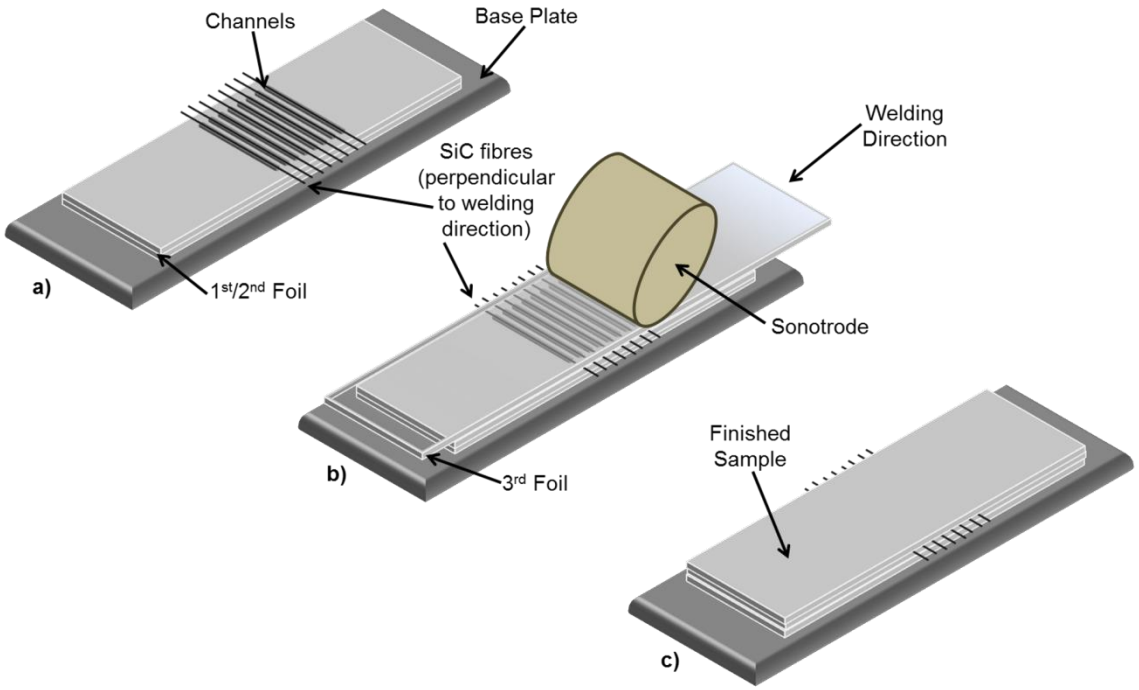


**Figure 7.4 Schematic overview of fibre embedding procedure for eight fibres perpendicular to welding direction**

Fibres were integrated into the samples based on the results obtained from chapter 6. Table 7.1 gives an overview of the produced samples. Hence, embedding was conducted on samples produced by nitrogen and air. Three samples (each containing 24 fibres which corresponded to 10.4 Volume % based on the area for fibre embedding) for each fibre orientation were produced for nitrogen samples. For air, five samples, also containing 24 fibres (corresponded to 10.2 Volume %), were manufactured for each fiber orientation. An exception was made for samples produced at the Fraunhofer Institute which

contained 24 fibres. The reason for this was that the channel/shoulder geometry of channels produced with air was more detailed. It was hoped to get a clearer understanding of the influence of channel and shoulder on embedding high volume fractions of fibres and additionally the secure fibre placement.

**Table 7.1 Overview of produced samples containing fibres**

| Gas Type | No. of Fibres | Welding Direction | No. of Samples | Total Samples | Total Fibres |
|---|---|---|---|---|---|
| Nitrogen | 8 | Parallel | 3 | 28 | 336 |
| | | Perpendicular | 3 | | |
| | 24 | Parallel | 3 | | |
| | | Perpendicular | 3 | | |
| Air | 8 | Parallel | 3 | | |
| | | Perpendicular | 3 | | |
| | 24 | Parallel | 5 | | |
| | | Perpendicular | 5 | | |

### 7.2.4 Macroscopic Observation of Welded Fibre Samples

After ultrasonically consolidating the fibre samples, the samples shown in Figure 7.4 c) were macroscopically inspected. The reason for this was that some samples after UC showed foil, fibre and surface damage which indicated insufficient bonding. Images of the samples were taken and grouped into the different types of surface damage.

### 7.2.5 Sample Preparation for Microscopic Inspection

After macroscopic inspection, all of the samples were cross-sectioned perpendicular to the fibre direction using a cutting disk (Buehler Isomet Low Speed Saw) which is displayed in Figure 7.5. The cutting disk, instead of the Struers Labotom cutting machine from section 4.2.5., was used because the fibres were considered delicate due to their brittleness. The cutting machine was equipped with a small diamond blade (Series 15HC Diamond) and allows precision cutting at low and controlled speeds. A 100 g mass was used to push the blade through the material and the speed was set to 90 Revolutions per

minute. Earlier studies comparing the two cutting machines showed that the fibres were likely to break during the cross-sectioning of samples due to the brittle nature of the SiC and the manually controllable force and speed inserted by cutting samples with the Struers Labotom (Chan, 2011). To avoid fibre breakage during sample preparation, it was decided to use the Buehler Isomet for all samples containing fibres.

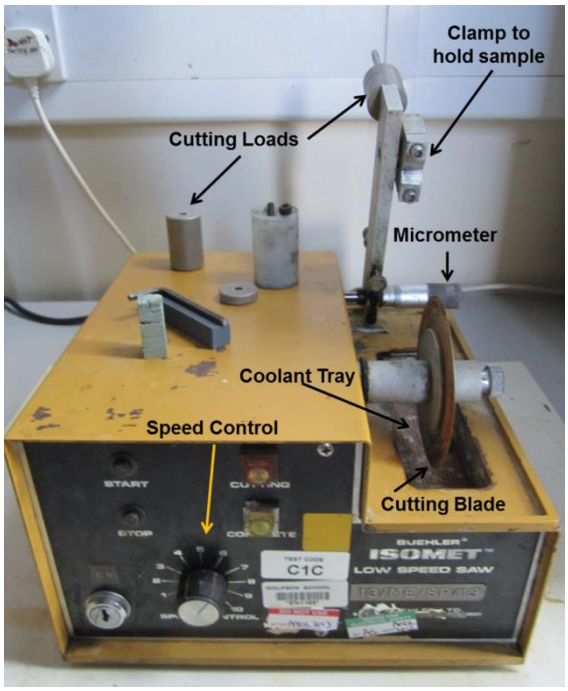


**Figure 7.5 Buehler Isomet Low Speed Saw for cutting of the delicate fibre samples**

After cutting, the samples were mounted into Buehler Konductomet II at a pressure of 20 kN and then polished to a surface finish of 0.1 µm as described in section 4.2.5. In order to reveal more details about the fibre/channel area as well as the interfaces in-between the fibres, all samples were then further polished to a surface finish of 0.05 µm by applying colloidal silica solution. Colloidal silica in contrast to Keller's Reagent exhibited only a mild etching effect and is frequently used for a finer polishing finish (Wernick and Pinner, 1972; Mills, 1985). Images were taken of the fibres in order to assess their integrity after UC. After microscopic and SEM inspection of the samples (7.2.6), the samples were then etched with Keller's Reagent to examine the channel/fibre/HAZ area in greater detail.

### 7.2.6 SEM Assessment of Samples

SEM assessment was carried out for two reasons: firstly, to determine the aid of the channel to accurately position fibres within the channel, analysis was carried out by measuring the distances between the fibres. Secondly, images at higher magnifications of the fibres allowed the inspection in greater detail. The SEM equipment has been described in section 5.2.4. The magnifications varied for the different features to be inspected as shown in Table 7.2.

**Table 7.2 Overview of different magnifications (area dependent)**

| Number of Fibres | Magnification | Visible Area |
|---|---|---|
| 8/24 | x40-x80 | Interfaces between fibres |
| 8/24 | x250 | Interface between two fibres |
| 8/24 | x750 | Fibre and Channel Area |
| 8/24 | x1000 | Broken Fibres |

Measurement of the distances was performed by measuring the distance between the centres of two fibre cores as shown in Figure 7.6.

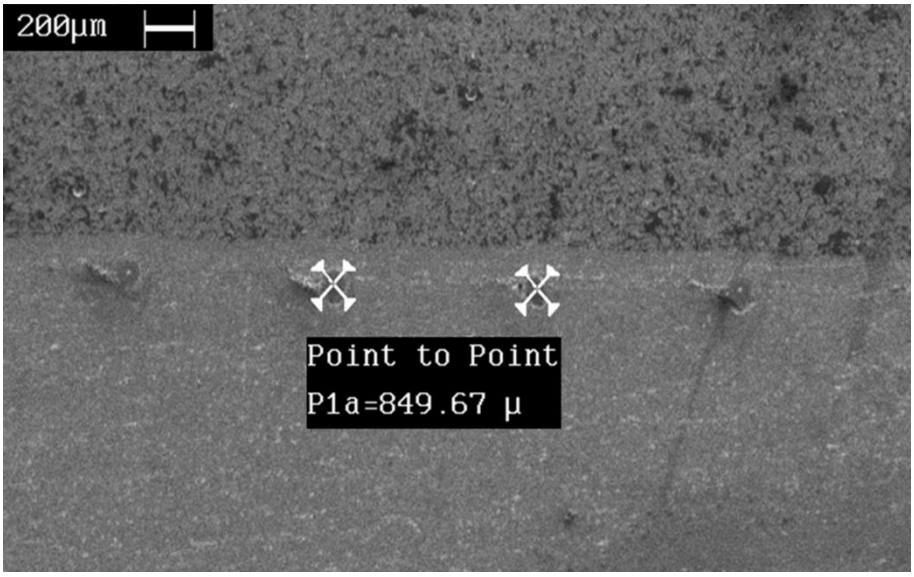


**Figure 7.6 SEM distance measurement from centre to centre of fibre cores for a sample containing 24 fibres**

The fibre core of a SiC fibre appeared as a white point during SEM and was therefore readily distinguishable (see Figure 7.6). The LEO SEM 440 was run with the LEO 32 user interface which allowed setting and controlling the different parameters for taking images. Additionally, the interface provided the possibility to measure distances on images. Measurements were carried out by using point-to-point analysis and allowed measuring the distance between the fibre cores. The distance between the channels was set to 2 mm for 8 fibres and 750 µm for 24 fibres measured from the starting point of the laser to the edge of the next channel for samples manufactured with the SPI 200 W laser. Samples manufactured with the Trumpf TruFiber 300 W laser had a distance of 2 mm for 8 fibres and 800 µm due to those channels exhibiting a greater width. Two examples for 8 and 24 fibres can be seen in Figures 7.7 and 7.8.

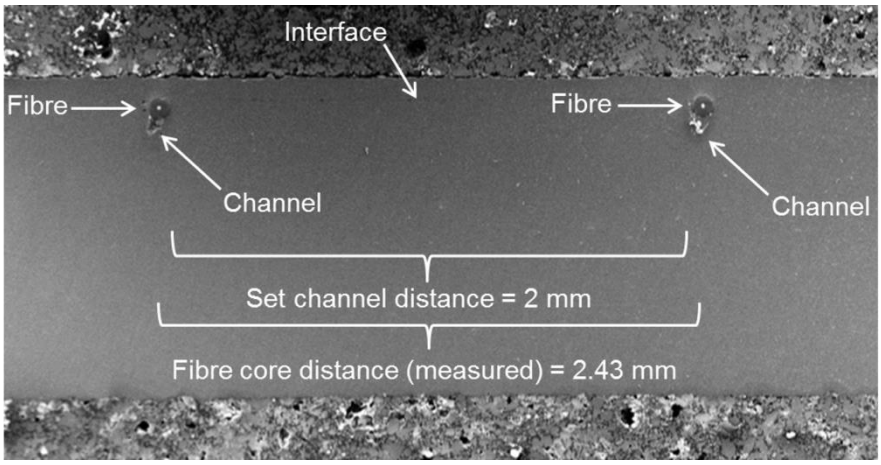


**Figure 7.7 Display of two from eight fibres in nitrogen channels (magnification of x50)**

A total of six samples was analysed for 8 fibres embedded in the parallel direction and six samples for perpendicularly embedded fibres. Those six samples were further divided into three samples for nitrogen and three samples for air. A total of 48 fibres was analysed for each embedding direction. The same amount of samples was analysed for 24 embedded fibres (i.e. for 24 fibres, 144 single fibres were analysed). The single measurements for every sample were then analysed and compared to each other. To further clarify the distances between the 24 fibres, the average distances and the resulting

standard deviation for the three samples in parallel and perpendicular direction for nitrogen and air were calculated.

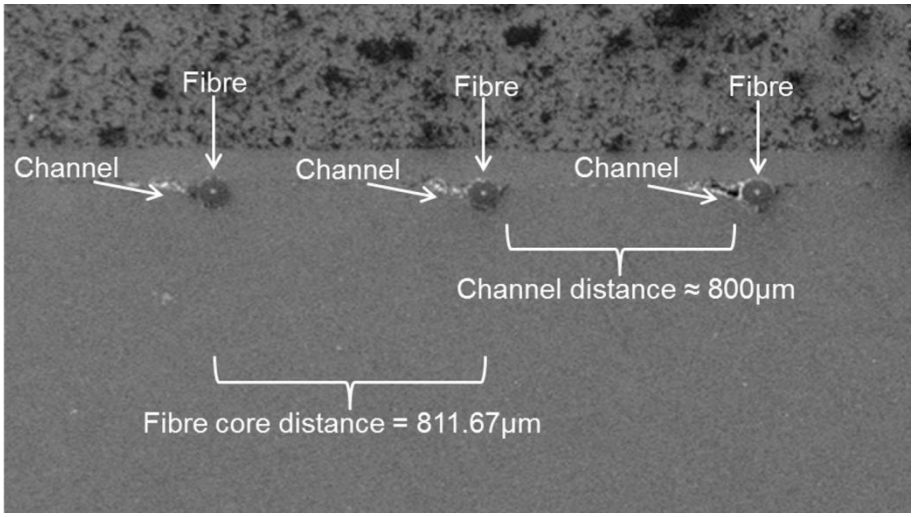


**Figure 7.8 Display of 3 from 24 fibres in air channels (magnification of x50)**

## 7.3 Results and Discussion

### 7.3.1 Examination of Shoulder Deformation after UC without Fibres

As the shoulder was only observed on one side of the channel and consisted of aluminium and aluminium oxide (see 5.3.4), examination of the shoulder behaviour before fibre embedding was considered important. The shoulder behaviour was particularly important for fibres embedded in perpendicular direction for which the results were to determine how to orientate the samples for UC to possibly gain the maximum information on fibre embedding. Three directions were analysed:

1. *Deformation in Perpendicular Direction – Shoulder in front of the Channel*

Figure 7.9 represents a deformed shoulder after UC. The deformed shoulder is clearly noticeable due to its bright white colour which arises from the oxides. The shoulder was deformed around the outer edge of the channel and all along the inner channel border into the channel. Furthermore, the shoulder was shattered possibly due to the brittle nature of the aluminium oxide which

fractured under the dynamic forces applied during UC. The upper foil seemed to have plastically deformed around the shoulder as well as into the channel as expected which was indicated due to the change in alloying element composition. However, the material in the channel appeared porous with multiple oxide inclusions, i.e. the matrix did not deform smoothly and consistently into the channel.

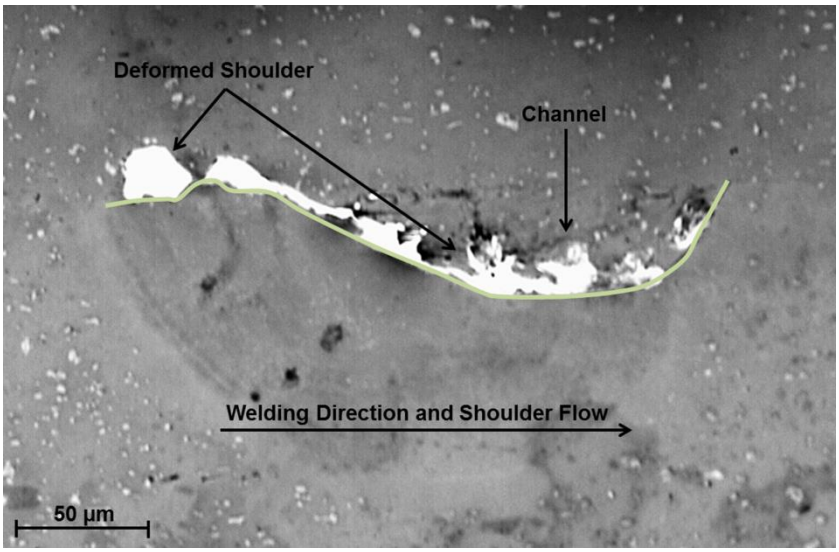


**Figure 7.9 Deformed shoulder in front of channel with regards to welding direction**

In Figure 7.10, a representative image of the embedded copper foil is displayed. As can be seen in Figure 7.10, the copper foil sheared at the shoulder which was observed for 80 % of the inspected shoulders.

It appeared that the copper foil was sheared at the upper edge of the shoulder, however after the highest point of the shoulder was reached, the copper foil deformed alongside the rest of the dispersed shoulder. The reason for the copper foil shearing was likely due to the hardness of the shoulder in combination with the dynamic forces applied as copper foil was relatively soft. Again, it was observed that the copper foil deform along the channel outline. Yet, a gap between the channel outline and the copper foil was visible due to the shoulder material being fractured along the channel outline as well as the recast layer.

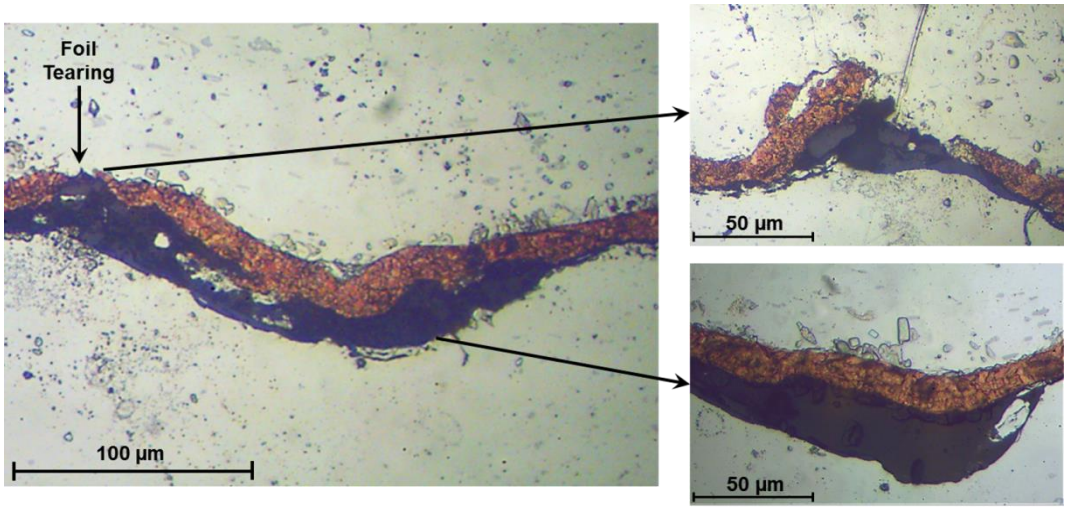


**Figure 7.10 Copper foil flow around shoulder to enable visibility of plastic flow (shoulder before channel)**

*2. Deformation in Perpendicular Direction – Shoulder behind the Channel*

In Figure 7.11, a representative image of a deformed shoulder which was behind the channel with regards to the welding direction can be seen. The shoulder deformed under the dynamic forces; however the shoulder was dispersed behind the channel.

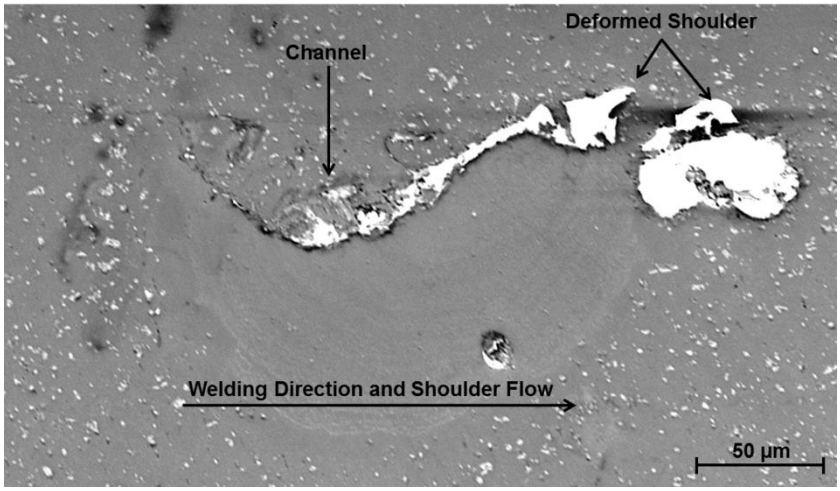


**Figure 7.11 Deformed shoulder behind the channel with regards to welding direction**

As opposed to aiding the shoulder material to flow into the channel, the shoulder material was dispersed along the weld line behind the channel. As

already mentioned for Figure 7.9, the material inside the channel appeared to be porous.

In Figure 7.12, the copper foil along the weld line for a shoulder behind the channel can be seen. As shown for copper foil deformation for the shoulder before the channel, the copper foil sheared again above the shoulder. The copper foil for samples exhibiting the shoulder behind the channel also deformed along the channel line. However, the copper foil did not narrowly deform along the channel geometry. A gap was visible between the copper foil and the channel which had also been noticed for Figure 7.10. Compared to the gap in Figure 7.10, the gap was narrower. This was due to dispersion of the fractured shoulder behind the shoulder. As a result, the copper foil was more deformed into the channel.

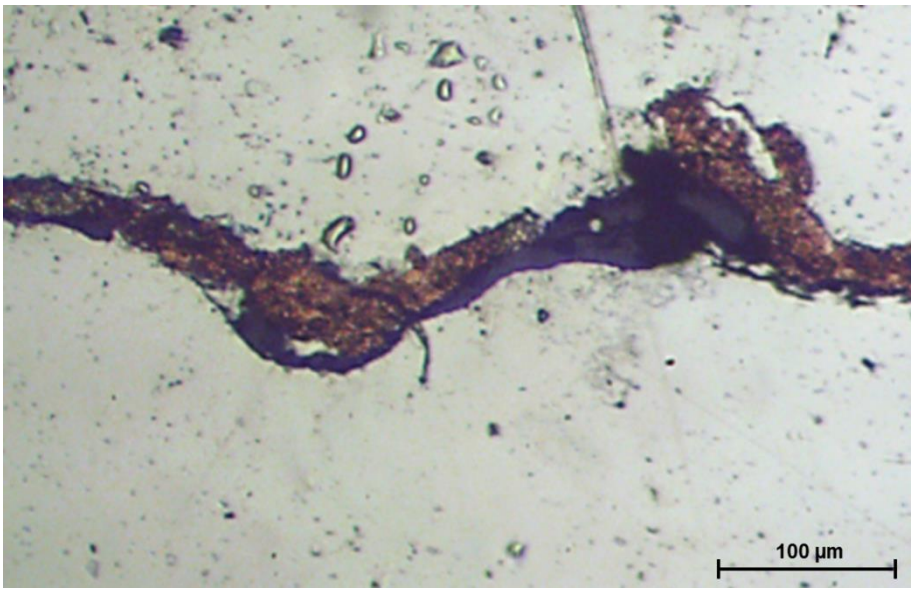


**Figure 7.12 Copper foil flow around the channel/shoulder (shoulder behind channel)**

As shown for copper foil deformation for the shoulder before the channel, the copper foil sheared again above the shoulder. The foil shearing for both shoulder positions and the better deformation of copper foil along the channel outline for a shoulder behind the channel suggested that shoulder position will have an influence on fibre embedding. Due to the results, it was decided to embed fibres perpendicular to the welding direction with the shoulder before the

channels. The reason was that the shoulder deformed (fractured) into the channel whereas for shoulders behind the channel the shoulder was of no use for deformation. Furthermore, the gap between the copper foil and the channel was an indicator that fibres may deform equally and leaving a gap between the fibre and the upper foil. Secure integration of fibre may thus be endangered as fibres could encounter a hard layer of $Al_2O_3$.

*3. Deformation of the shoulder in parallel direction*

In Figure 7.13 an example of the deformed shoulder welded parallel to the welding direction of the sonotrode can be seen. In parallel direction, the shoulder exhibited deformation either into the channel or before the channel. It was suggested that the shoulder, due to the applied oscillations, sheared the shoulder in both directions.

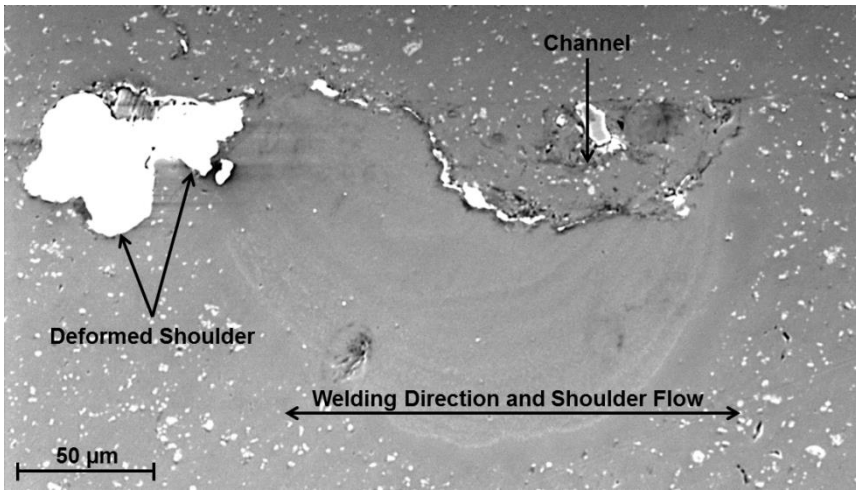


**Figure 7.13 Deformed parallel shoulder with regards to welding direction**

The main part of the shoulder was found outside of the channel for all analysed channels. As well as seen for the other two directions, the material inside the channel exhibited porosity; yet, not flowing smoothly into the channel. Furthermore, the area exhibiting porosity covered the whole channel rather than the lower part for perpendicular channels. Hence, plastic deformation in perpendicular direction was possibly different to parallel direction.

Different to the flow behaviour of the copper foil along the channel outline for perpendicular fibres, parallel samples containing copper foil, showed a hole above the channel as displayed in Figure 7.14. The hole was either non-filled or the hole was filled with mounting material. The copper foil appeared to have prevented the upper foil deforming into the channel. In addition, the copper foil sheared above the channel in some cases. Interestingly, the copper foil did not shear before the channel or after even though oxides were detected there as well. Instead, the copper foil deformed along the oxides. This might be an indication, that the shearing force for parallel and perpendicular channels may be different or as the shoulder was dispersed to both sides, the main shearing force was applicable above the channel instead of above the shoulders. Another interesting aspect was that the copper foil showed signs of wrinkling. This might be due to the oscillations which are applied over the whole length of the channel.

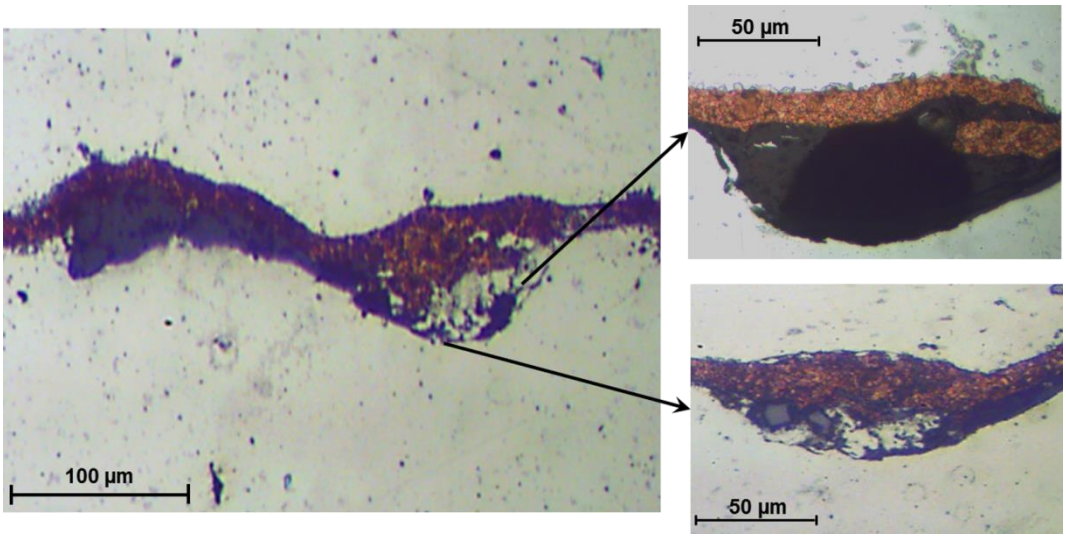


**Figure 7.14 Deformation of copper foil for a sample parallel in welding direction**

### 7.3.2 Macroscopic Inspection of Foil Surface after Fibre Embedment

Two types of surface irregularities were evident for all the samples after UC. The first was classified as insufficient welding of which typical examples can be seen for both fibre embedding directions in Figures 7.15 and 7.16.

The tape for holding the fibres in place was only attached to the area which was not actively involved in consolidation of the foils (see Figure 7.15). After UC, the fibre geometry was readily visible as imprints in the upper foil whereas the shoulder and channel geometry was hardly detectable. The upper part of the fibre/matrix area was insufficiently welded which could be noticed from the colour of the foil which resembled the original foil, whereas the lower part exhibited a satisfactory weld. The appearance of insufficient bonding and satisfactory bonding both appeared throughout the samples containing perpendicularly embedded fibres. However, a trend was noticed for a lesser bonding quality at the edges of the upper foil.

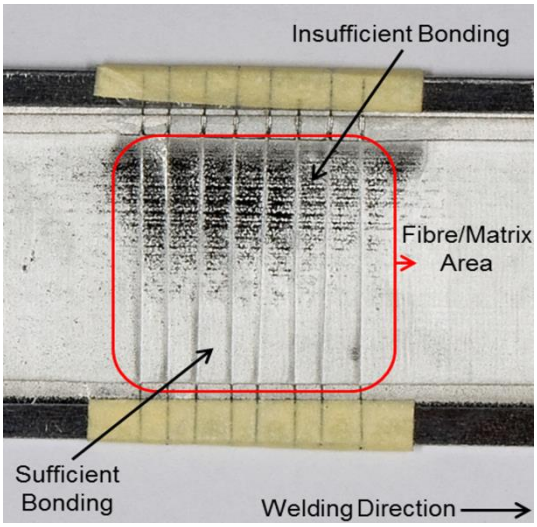


**Figure 7.15 Insufficient bonding in consolidated fibre area**

The classification of sufficient or insufficient bonding was identified by an increase of surface roughness. The surface roughness occurred as a result of the contact between the sonotrode and matrix material, induced by the applied pressure and ultrasonic motion during UC (Friel et al., 2010; Edmonds and Harris, 2011). Therefore, insufficient bonding was identified when the to-be bonded area appeared smooth and with high reflectivity similar to the surface of the original foil.

In comparison to fibres embedded perpendicular to the welding direction, insufficient bonding for parallel embedded fibres mainly occurred in the area of

the tape edges as shown in Figure 7.16. The tape supposedly constrained the two joined foils. After a distance of 1 mm to 3 mm from the tape edges sufficient bonds were detected. The bonding quality within the channel area for parallel embedded fibres was more sufficient than for perpendicularly embedded fibres.

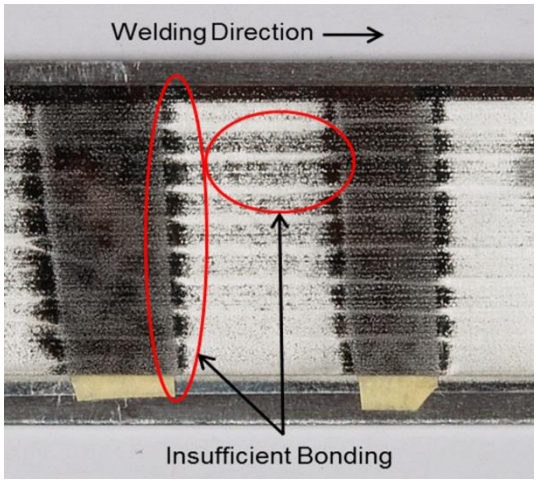


**Figure 7.16 Insufficient bonding due to masking tape and in fibre area**

In Figure 7.17, foil tearing (the second type of damage) is shown. Foil tearing only appeared for perpendicularly placed fibres. The upper foil showed sufficient welding to the lower foil which was detected by the change in reflectivity of the upper foil. However, the upper foil was not bonded to the lower foil and foil tearing occurred along the fibre/channel/upper foil line.

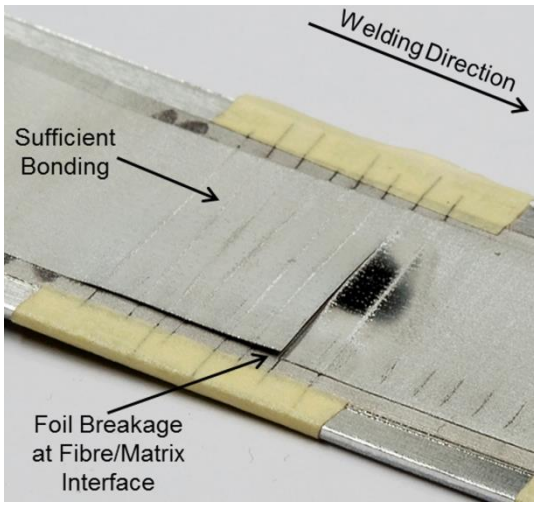


**Figure 7.17 Foil tearing at fibre/matrix Interface**

The three different effects, insufficient bonding due to directly inserted obstacles, insufficient bonding without any obstacles and foil tearing, will be explained below:

Insufficient bonding due to directly inserted obstacles in the form of tape has been noticed for fibres placed parallel to the welding direction (Figure 7.16). The tape served as a cavity during bonding of the two aluminium foils as the tape prevented the top foil from bonding to the lower foil. Shortly after the tape, the metal-to-metal contact was achieved and successful bonding started over a relatively small area which was due to the channel length of 15 mm. At the beginning and the end of the metal-to-metal contact area, partial bonding was observed for 1-3 mm. The same amount of unbonded area has been observed at the start of sonotrode contact for every consolidated foil as can be seen in Figure 7.18.

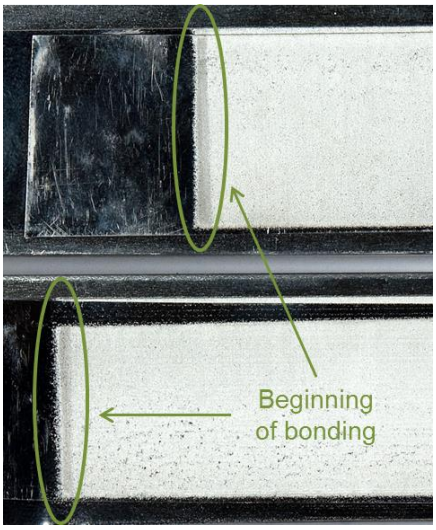


**Figure 7.18 Beginning of bonding at the starting point of the sonotrode**

There appeared to be a short time frame after the start of the sonotrode oscillations until the oscillations were fully applied to the foil. For this reason, it is believed that a short timeframe was needed for oscillations and contact pressure to be accomplished.

Insufficient bonding for Al 3003-H18 has been observed before by Kulakov and Rack (2009). They observed areas which less damage along the bottom edge

of the foils due to non-uniform contact pressure. In this study, three reasons were considered as to why the contact pressure was not uniform along the weld direction: Firstly, the contact pressure of the sonotrode was not evenly distributed. Secondly, the applied tape prevented the formation of evenly distributed contact pressure. Thirdly, fibres, channels and shoulders were responsible for a non-uniform contact pressure due to possibly non-uniform embedding and height difference. It was suggested that a combination of these was responsible for the partial bonding. For the first and third consideration, an increase in contact pressure might help to overcome insufficient bonding.

Macroscopic inspection of foil tearing showed that bonding took place as the whole channel area showed a difference in reflectivity. This suggested that foil tearing happened after welding. Both, fibres and shoulders could have acted as stress raisers in the foil material which therefore could have exceeded the maximum of stress possible and as a result the foil ripped. Another suggestion was that due to the contact pressure, the foil behaved like a wave and as the sonotrode travelled along the sample, yielding took place until further yielding was not possible anymore. Hence, in combination with the dynamic forces the foil would tear apart. The investigation in chapter 5 showed that the shoulder mainly consists of $Al_2O_3$ which is a hard material (Mondolfo, 1976). Additionally, SiC fibres have a high hardness. As the tearing of the foil was observed at the interface of shoulder/fibre/foil area, it was proposed that the interaction of dynamic forces in combination with the hard material might have led to tearing of the foil material.

Depending on the fibre direction, shear stress induced in combination with dynamic forces (see Figure 2.2) will be differently for the fibres. In Figure 7.19 the dynamic forces which are delivered through the sonotrode and acting upon the fibres for the two embedding directions are displayed. Perpendicular embedded fibres (7.19a)) receive the dynamic forces (due to contact pressure and oscillations) over the whole length in a short period of time but over a relatively big area due to the embedding direction, whereas fibres in parallel

direction (7.19b)) receive the dynamic forces over a longer period of time and a smaller area.

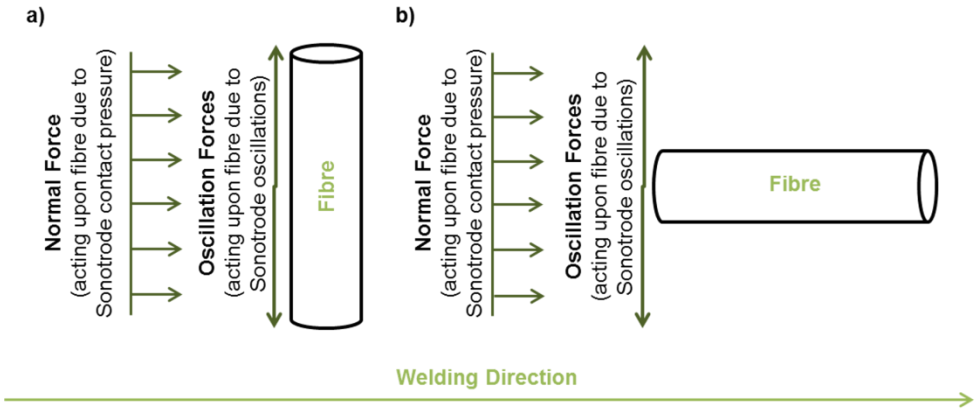


**Figure 7.19 Dynamic forces acting upon a) a perpendicular fibre and b) a parallel fibre with regards to welding direction**

For this reason, foil tearing is more likely to happen in the perpendicular direction than in parallel direction. It was proposed that a combination of the fibre direction in combination with the hardness of the material and shoulder might be the reason for foil tearing. This would be in accordance to an earlier study of Yang et al. (2007) in which best bonding results were achieved at 45° whereas 0° (parallel) and 90° (perpendicular) showed lower bonding strength (higher bonding quality in perpendicular direction). Depending on the fibre placement, the fibres and shoulders will receive different shear stresses (Doumanidis and Gao, 2004). Therefore it was suggested by Yang et al. (2007) that the shear stress in 45° direction is higher which causes higher plastic flow to embed fibres.

Interestingly, as can be seen in Figure 7.20, the sample which only contained channels was welded adequately and showed no signs of insufficient bonding.

**Figure 7.20 Sample containing channels without fibres before cross-sectioning**

The channels were welded perpendicular to the welding direction; yet no foil tearing was observed for the samples. This indicated that the main reason for non-bonding and foil tearing was the fibre integration instead of laser processed channels and shoulders.

### 7.3.3 Analysis of Accurate Fibre Positioning and Placement

Analysis of accurate positioning of fibres was carried out to determine the influence of the channels (and shoulders) to prevent fibres (in particular high volumes of fibres) from rolling or movement during consolidation. In Figure 7.21, the distances between the fibre centres for 8 fibres in nitrogen samples are displayed. As mentioned in the methodology (see 7.2.6), the distance between channel edge to channel edge was set to 2 mm. Thus, the distance between the fibre cores was also approximately 2 mm. The mean average distance between the parallel embedded fibre centres was calculated to be 2.12 mm. For perpendicular embedded fibres, the mean average between the fibre centres was 2.20 mm and therefore slightly higher than for parallel fibres. It can be seen that all distances ranged from 2 mm to 2.8 mm with an exception for the last fibre of “Parallel 3” which had a distance of 1 mm as this fibre rolled out of the channel towards the fibre before. There was no trend noticed for a better positioning of fibres in parallel or perpendicular direction – the single values seemed to vary in random orders.

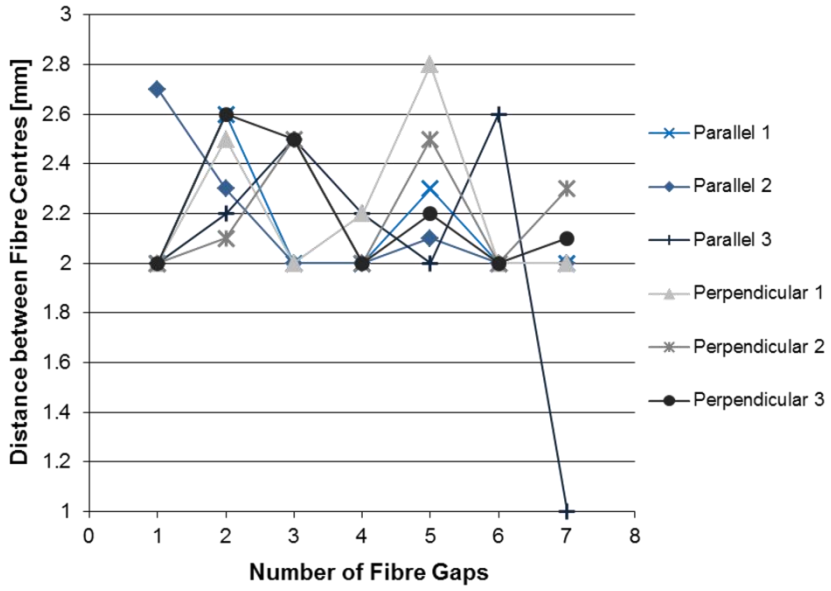


**Figure 7.21 Distances between fibre centres for nitrogen with eight embedded fibres**

Figure 7.22 displays the distances between the fibre centres for 8 fibres positioned in an air sample. As can be seen, the values ranged from 1.8 mm and 2.4 mm. The mean average values were 2.07 mm in perpendicular and 2.06 mm in parallel direction. A difference between the embedding directions was again not noticed. The high values for fibre number six in perpendicular direction 1 and 2 was due to the movement of the fibre away from the previous.

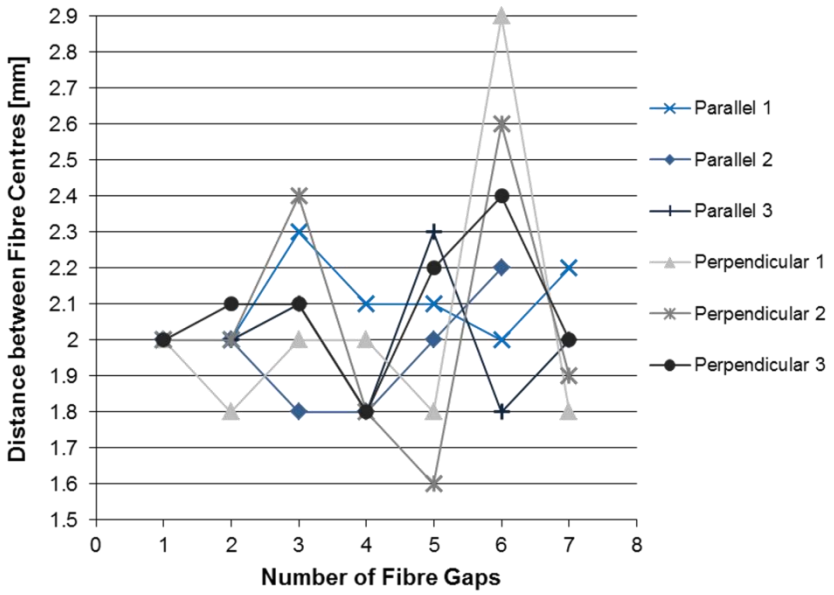


**Figure 7.22 Distances between fibre centres for air with eight embedded fibres**

The single values for 24 fibres in nitrogen samples are shown in Figure 7.23.

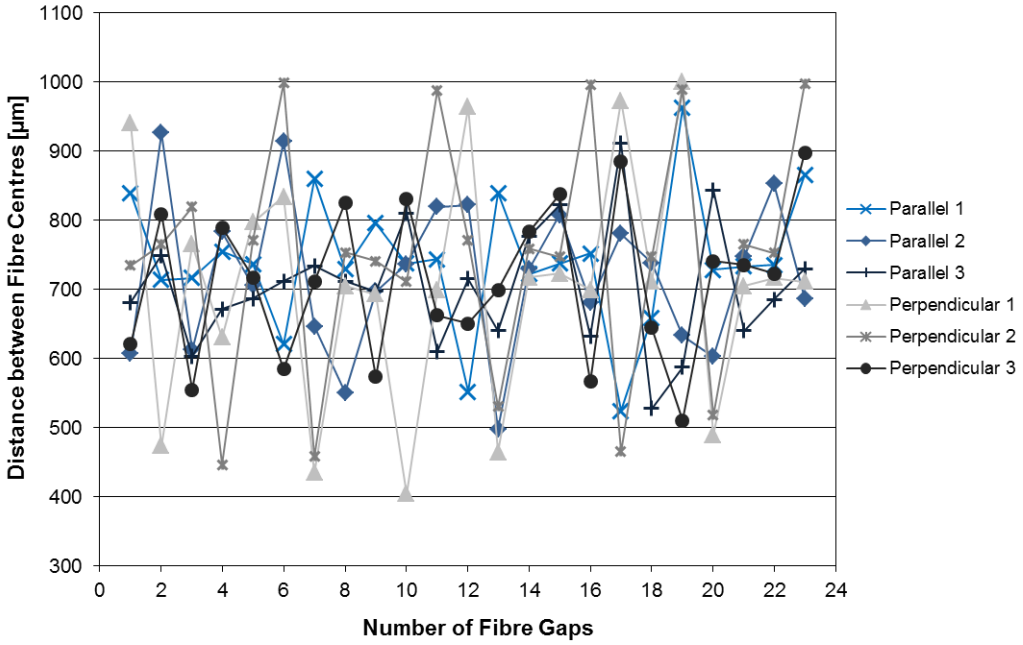


**Figure 7.23 Distances between fibre centres for nitrogen with 24 embedded fibres**

The single values ranged from 400 µm to 1 mm. Closer inspection of the data revealed that this range applied for fibres embedded perpendicular to the welding direction, whereas the values for parallel embedded fibres ranged from 525 µm to 920 µm. Hence, fibres embedded parallel to the welding direction moved less than perpendicularly embedded fibres. Additionally, for parallel embedded fibres the single values were spaced more closely. For further clarification and to summarise the values, the average distances of the three samples for each fibre direction are displayed in Figure 7.24.

The mean average of all the fibre values for the parallel samples was 722 µm and was similar to the value for the perpendicular samples (724 µm). As displayed in the diagram, all average values alternated around this value. Yet, perpendicular fibres ranged in a wider distance (see also Figure 7.23). As both directions shared approximately the same mean average value, a trend of better positioning in one of the directions was not observed.

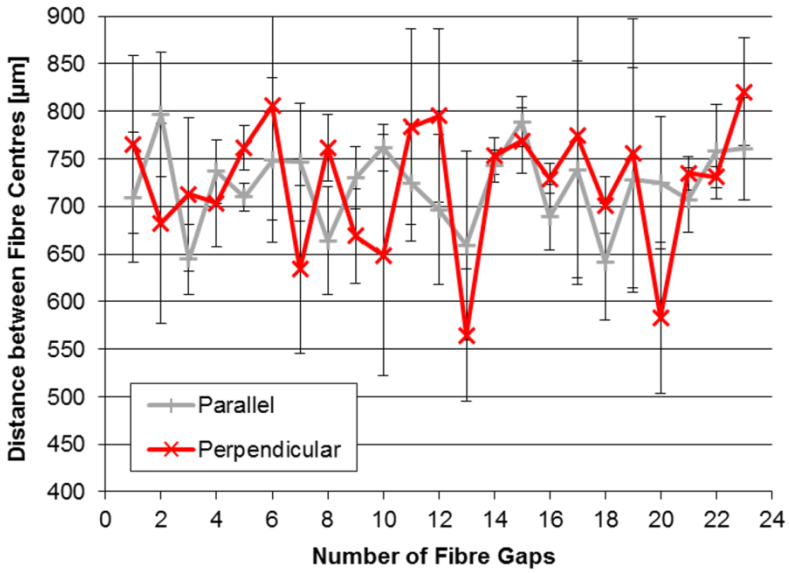


**Figure 7.24 Average distances between fibre centres for both welding directions (nitrogen - 24 embedded fibres)**

The single values of the 72 fibres embedded in parallel and 72 fibres embedded in perpendicular direction for air samples are given in Figure 7.25.

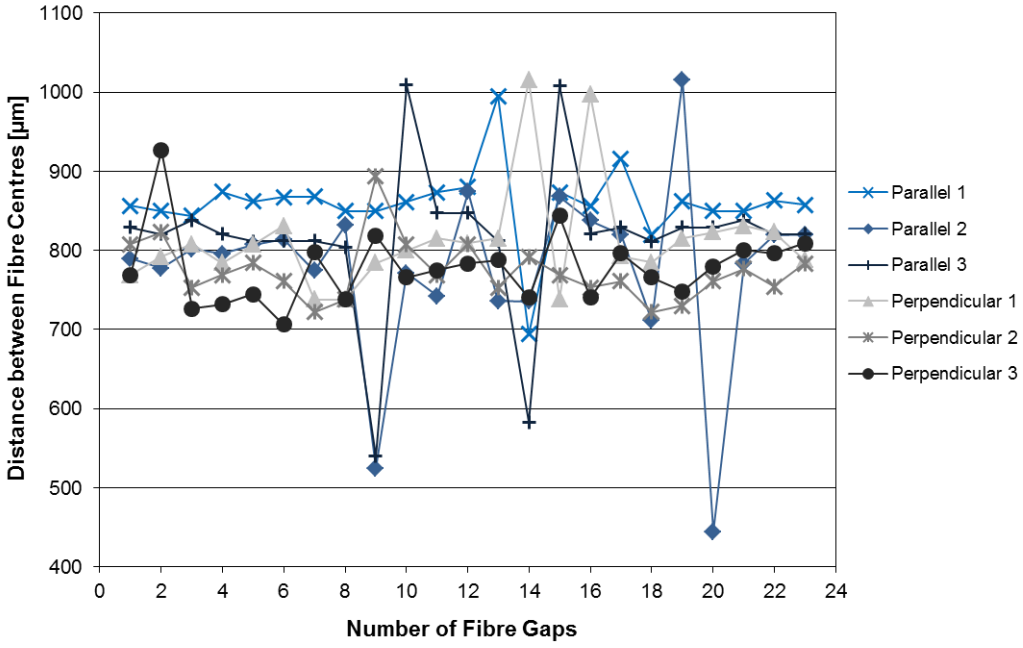


**Figure 7.25 Distances between fibre centres for air with 24 embedded fibres**

Most of the values ranged from 700 µm to 1010 µm which in comparison to nitrogen was a narrower range. It was noted that some values were far out of

the above mentioned range – for example: sample parallel 2, fibre 9 (525 µm) and fibre 20 (445 µm). The explanation for this difference (one exhibiting a shorter distance and the other one exhibiting a longer distance) for two consecutive fibres (see sample parallel 2, sample gap values 19 and 20) was that if one fibre was displaced from the channel, the distance to the following fibre became shorter however the distance to the previous fibre became longer (see Figure 7.21 and 7.22). Opposed to the results for nitrogen, air showed that especially parallel fibres instead of perpendicular fibres showed a wider range (445 µm to 1010 µm). The reason for these values was possibly that fibres moved out of the channel due to their propensity to roll and the dynamic forces applied from the sonotrode which will be discussed later on.

In Figure 7.26, the average distances for the fibres from parallel and perpendicular samples are displayed.

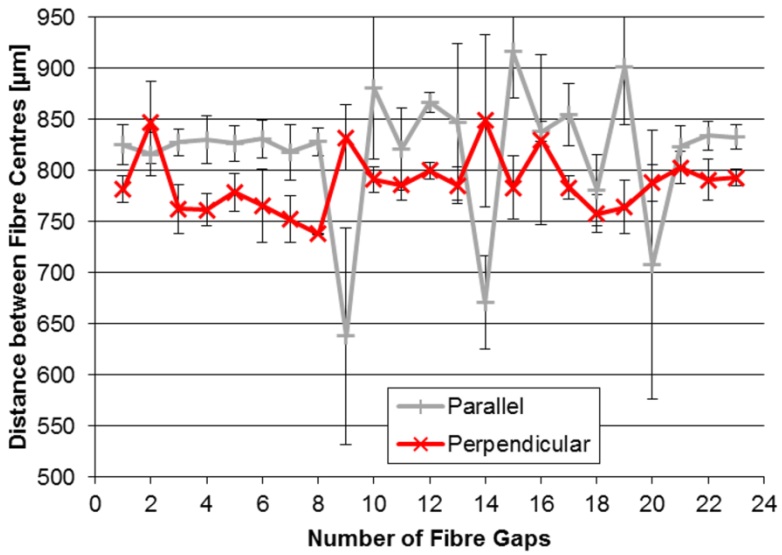


**Figure 7.26 Average distances between fibre centres for both welding directions (Air - 24 embedded fibres)**

The mean average for all the fibres embedded in parallel direction was 818 µm; the mean average for fibres embedded in perpendicular direction was 788 µm. Again, a significant deviation for the mean average value for both directions was not noticed. Yet, compared to nitrogen samples, the overall distance between the fibre centre averages was more consistent which can be seen from the

standard deviations from the single average distance values of the three samples for nitrogen and air (see Figure 7.24 and 7.26).

Little current knowledge exists about secure and accurate positioning of high fibre volumes. Studies concerned with fibre embedding focused on the plastic flow rather than secure and accurate fibre positioning as mentioned in 7.2.3. An example of fibre embedding of a high amount of fibres within an aluminium matrix can be seen in Figure 7.27.

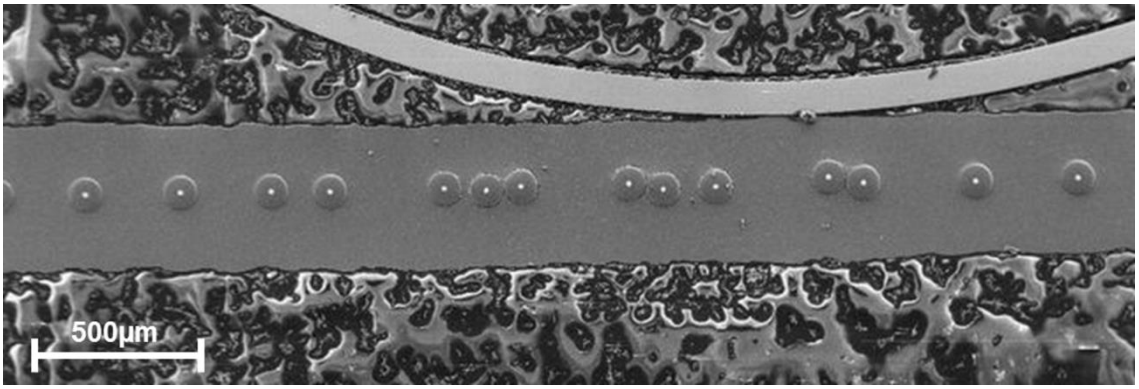


**Figure 7.27 Random distribution of SiC fibres in matrix without channels (Kong, 2005)**

The fibres in Figure 7.27 were not evenly distributed and in some cases the fibres were in contact with each other. Kong (2005) found that fibres in close proximity can disturb each other while also impeding bond formation (Friel and Harris, 2010). The reason for this is that fibres are moving due to the applied oscillations. Hence, fibre positioning is important when a high amount of fibres shall be embedded in order to guarantee their integrity after consolidation.

In Figure 7.28, a representative image of 24 fibres embedded in channels within an Al 3003-H18 matrix for this study is displayed. As anticipated and in comparison to Figure 7.27, all fibres stayed in the channel and were evenly distributed across the interface length.

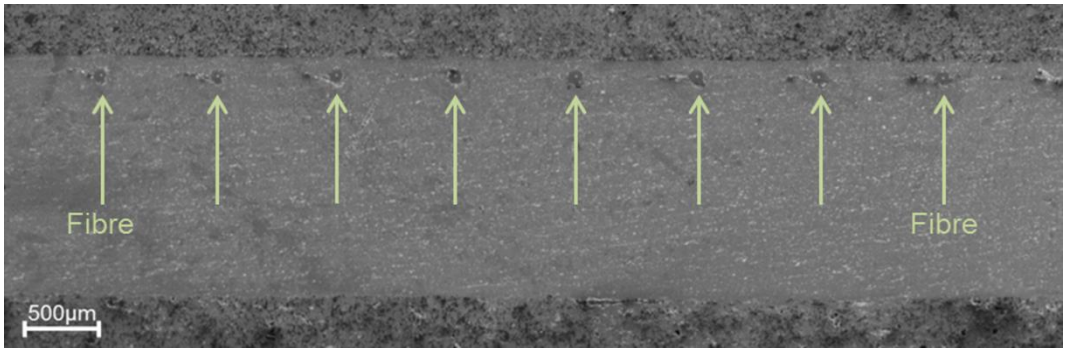


**Figure 7.28 Evenly spaced SiC fibres in matrix after embedding in channels**

To further clarify the aid of the channels for accurate fibre positioning, all fibres for samples containing 24 fibres were analysed. The result can be seen in Table 7.3 which displays the percentage of fibres remaining in the channel after UC.

**Table 7.3 Analysis of fibre positioning behaviour for 24 fibres in both directions**

| Gas Type | Embedding Direction | Total of Embedded Fibres | No of Fibres in Channel | Percentage of Fibres in Channel [%] |
|---|---|---|---|---|
| *Nitrogen* | Parallel | 72 | 52 | 72.2 |
| | Perpendicular | 72 | 46 | 63.9 |
| *Air* | Parallel | 120 | 109 | 90.8 |
| | Perpendicular | 120 | 118 | 98.3 |

The results revealed that fibres in nitrogen samples were less likely to stay in the channels after UC. Only 72 % for parallel embedded fibres and 63 % for perpendicular embedded fibres were found to be in the channel. The results for air samples indicated that for both directions over 90 % of the fibres remained in the channels after UC. In fact, fibres placed in perpendicular direction had a value as high as 98.3 % which means that nearly all fibres were observed to be in the channel.

For nitrogen, the secure positioning of fibres was less compared to air. In Figure 7.29, an example for fibre movement is presented. As this behaviour was observed for nearly 30 % of the fibres embedded in parallel direction for

nitrogen samples and for nearly 40 % of perpendicular embedded fibres it was suggested that accurate positioning was difficult to control due to the channel depth. The outline of the channels for air was more distinct and deeper channels were manufactured (see section 5.3.1).

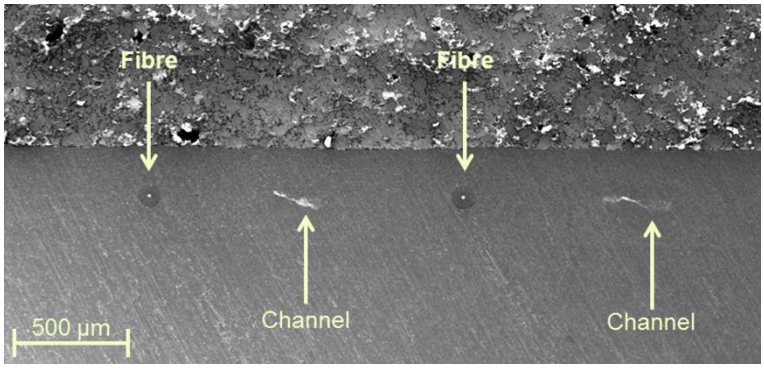


**Figure 7.29 Fibres not in channels after UC**

Hence, these channels helped to keep fibres in their place during UC. Additionally, the embedding direction may have influenced the movement of fibres which could explain a difference in movement for both directions for nitrogen samples. Parallel embedded fibres received the normal force and oscillations from the sonotrode over their whole length during UC, whereas perpendicularly embedded fibres received the normal force and oscillations over their diameter (see Figure 7.19). It was suggested that the perpendicular fibres in combination with less deep channels were, due to the normal applied force, pushed along the welding direction. Furthermore, the rolling direction of the fibres was in favour to move along the welding direction. On the contrary, air samples showed that perpendicular embedded fibres gave higher percentages. It was anticipated that, due to the deeper channels, the oscillation force was the main influence on fibre movement which made the fibres oscillate around their genuine rolling direction. Hence, depending on the channel depth, either normal or oscillation force may act on the fibres.

### 7.3.4 Aid of the Channel for Secure Positioning of Fibres

Channel and shoulder manufacturing within the UC samples was intended to meet two conditions: firstly aiding the positioning of fibres and secondly enhancing the secure placement of fibres. In order to analyse the second condition, the fibres were inspected to analyse their integrity after UC. An example of an intact fibre (desired) and a fibre exhibiting cracks (undesired) is represented in Figure 7.30. Fibre cracking was observed in every analysed sample.

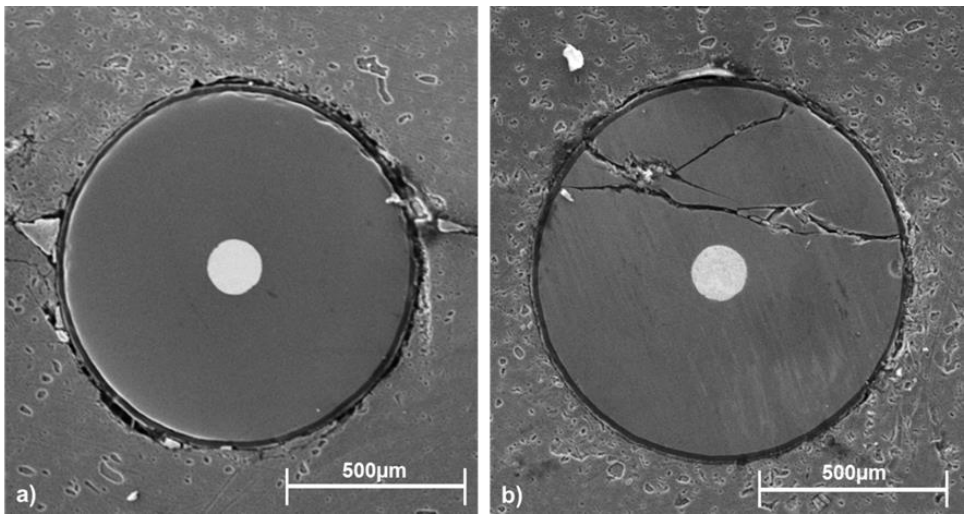


**Figure 7.30 Fibre appearance after UC a) intact fibre and b) cracked fibre**

The degree of cracking varied from sample to sample, however every sample exhibited at least one cracked fibre. The severity of the cracking varied. Representatives of shattered fibres are given in Figure 7.31. One damaged fibre is shown in Figure 7.31 a) and 7.31 c). Figure 7.31 b) shows the core of two shattered fibres. Shattering was mostly observed in nitrogen samples.

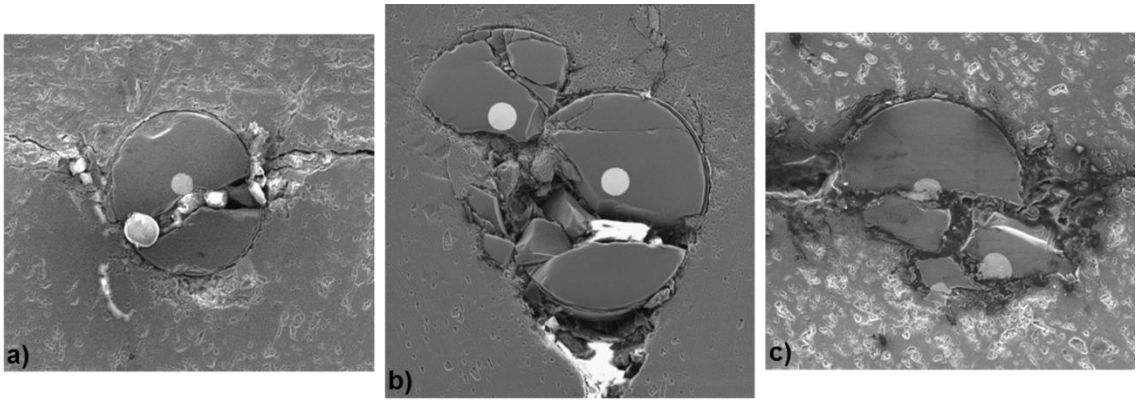


**Figure 7.31 Examples of shattered fibres a) and b) shattered fibre in channel, c) shattered fibre along the weld line**

In order to analyse the shattered fibres in relation to movement of the fibres, the percentage of cracked fibres for samples containing 24 fibres was calculated. The results are displayed in Table 7.4.

**Table 7.4 Analysis of fibre breakage for 24 fibres**

| Gas Type | Embedding Direction | Total of Embedded Fibres | No of Fibres in Channel | No of Cracked Fibres | Percentage of Cracked Fibres [%] |
|---|---|---|---|---|---|
| *Nitrogen* | Parallel | 72 | 52 | 8 | 11.1 |
| | Perpendicular | 72 | 46 | 6 | 8.3 |
| *Air* | Parallel | 120 | 109 | 5 | 4.2 |
| | Perpendicular | 120 | 118 | 4 | 3.3 |

As already seen from the results for fibre movement, air samples exhibited superior results than nitrogen samples. The percentage of cracked fibres in parallel direction was 4.2 % and 3.3 % for perpendicular places fibres. For parallel embedded nitrogen samples the percentage of cracked fibres was over 10 % and a little less in perpendicular direction. Interestingly, for both directions, parallel embedded fibres showed a higher percentage for fibre cracking. One possible explanation could have been that parallel embedded fibres endured the dynamic forces from the pressure and oscillations over the whole fibre

length which has been discussed before. Perpendicularly placed fibres only endured dynamic forces for a fraction of the time compared to parallel fibres. This could have enforced fibre cracking for parallel embedded fibres.

Another reason for fibre breaking could have been the channel/shoulder geometry itself. Especially in parallel direction, fibres were prone to be pressed and moved in both directions which was facilitated by their rolling direction in combination with the oscillations. As one side of the channel exhibited the recast layer which consisted of $Al_2O_3$, the fibres were partly pressed against a hard layer of oxides. This in combination with the pressure applied might have caused the fibres to break more easily. In comparison, fibres placed in perpendicular direction were pressed against the channel side which did not exhibit recast formation (see Figure 7.9). Additionally, the cracking in both directions might have been enforced by the oxides that were distributed into the channel and around the fibres (see 7.31). The hard oxides could have aided the cracking of fibres in combination with the dynamic shear forces. As seen for the plastic deformation of the copper foils, the copper foil always deformed with a gap along the channel geometry. It was believed that the fibres were facing this gap during consolidation as well. As the only possibility for the gap formation was the layer of recast and oxides from the shoulder, the fibres impinged on a hard layer which could have caused breakage.

A third possibility was that the fibres had to face the hardness of the recast and oxide layer but also the hardness of the HAZ. As seen in chapter 5, the microstructure of the HAZ changed and the possibility of the creation of a hard HAZ was proposed. Therefore the fibres were pressed against a hard HAZ not only at the bottom of the channel but also on the side. The investigation of the hardness of the HAZ will be investigated in chapter 8.

Research investigations into fibre cracking or shattering for SiC fibres were not found during literature surveying. However, reference samples with 24 fibres embedded exhibited cracking as well which was an indicator that cracking of the SiC happened due to the dynamic forces applied. The reference samples showed both shattering and cracking. It was believed that the dynamic forces

played a major role in fibre embedding but due to the combination of the channel/shoulder the fibres were more likely to experience breakage.

## 7.4 Review

The investigation on the deformation of the shoulder gave an indication on how the shoulder will deform during fibre embedding. Particularly the shoulder position (before or behind the channel) for fibres embedded perpendicular to the welding direction was of interest as the deformation induced by the sonotrode will determine the plastic flow around the fibre. It was found that the shoulder behind the channel deformed along the interface after the channel which would not benefit plastic flow reduction during fibre embedding. Hence, shoulders were located to be in front of the channel for fibre embedding.

Macroscopic inspection of the samples after UC showed insufficient bonding for fibre placement in perpendicular and parallel direction. In perpendicular direction, foil tearing was observed which was attributed to the combination of the hardness of SiC fibres, fibre direction and dynamic forces (oscillations and pressure) causing shearing of the foil.

One of the main focuses of this chapter was the accurate placement of a high number of fibres within the channels. Samples containing up to 10.5 % volume fraction of fibres were consolidated. It was successfully shown that channels assisted the accurate positioning of the fibres which contributed substantially to the understanding of fibre movement/rolling behaviour during UC. In comparison to deeper channels for air, less deep channels for nitrogen showed less accurate placement of fibres. However, both gas types showed little variations in the distance ranges for accurate placement with nitrogen having a slightly higher range. For air over 90 % of the parallel embedded fibres for samples containing 24 fibres were observed to be in the channel after UC. Perpendicular placed fibres showed a remarkable amount of over 98 %. Nitrogen showed lesser results which was again credited to the smaller depth of the channels.

The other main focus of chapter 7 was the preservation of the fibre integrity after consolidation. It was observed that a certain degree of fibre cracking happened in every sample for both gas types whereas fibre shattering was mainly observed in nitrogen samples. It was suggested that the recast layer and shoulder may have contributed to the fibre breakage due to their hardness and dispersion around the fibres. What impact exactly contributed to the breakage of fibre will be investigated in chapter 8. The number of broken fibres was higher for nitrogen than for air which could be attributed to the different depths of the channels. Furthermore, the embedding direction of fibres was observed to have an influence on fibre breakage. Fibres in parallel direction broke more easily than fibres in perpendicular direction which was suggested to be the influence of dynamic forces over the whole fibre length during UC. The influence of the embedding direction for fibre breakage during UC has been investigated for the first time and contributes to the further understanding of the impact the dynamic forces may have on delicate materials with regards to future embedding research and application.

# Chapter 8.
# Impact of Laser Channels and Fibres on Bond Formation and Microstructure post UC

## 8.1 Introduction

The purpose of chapter 7 was the investigation of fibre behaviour in the pre-processed channels. Chapter 8 was focused on the detailed understanding of plastic flow behaviour of the shoulders to aid secure fibre encapsulation. Furthermore, the process of bond formation for high number fibre embedding in combination with the newly manufactured channels and shoulders was investigated.

The bond quality for fibre embedded samples was examined by using LWD measurements and then compared to samples which did not contain fibres (see section 7.2.1) to understand the influence of the fibres on bonding behaviour. The role of oxide formation variability inaugurated by laser processing was scrutinised to possibly discover relationships of different gases, bond formation and fibre embedment. Microstructural changes within the HAZ, which were discovered in section 5.3.3, were further explored in terms of material property changes to further understand their influence on bond formation and fibre breakage.

## 8.2 Methodology

### 8.2.1 Classification of Bonding Quality

To determine the bond density for the fibre embedded samples, the LWD was measured. The LWD is described as the percentage of the physically bonded area ($L_B$) to the total interface length ($L_T$) (Janaki Ram et al., 2006a). The equation to calculate the LWD can be seen in section 2.1.6.

Even though the LWD procedure had been exercised before (Kong et al., 2003; Janaki Ram et al., 2006a; Li and Soar, 2009b; Friel et al., 2010; Hopkins et al., 2012), LWD measurement for fibre embedded samples differed from the generally applied LWD procedure: Instead of cutting the samples at the start/middle/finish sections (Kong et al., 2003; Friel et al., 2010), the samples were cut at the middle of the fibre/channel area as can be seen in Figure 8.1a. Furthermore, the samples in this study consisted of fibres and channels and to allow comparison with earlier studies, LWD measurements needed to be carried out at the interfaces in between the fibres (see Figure 8.1b).

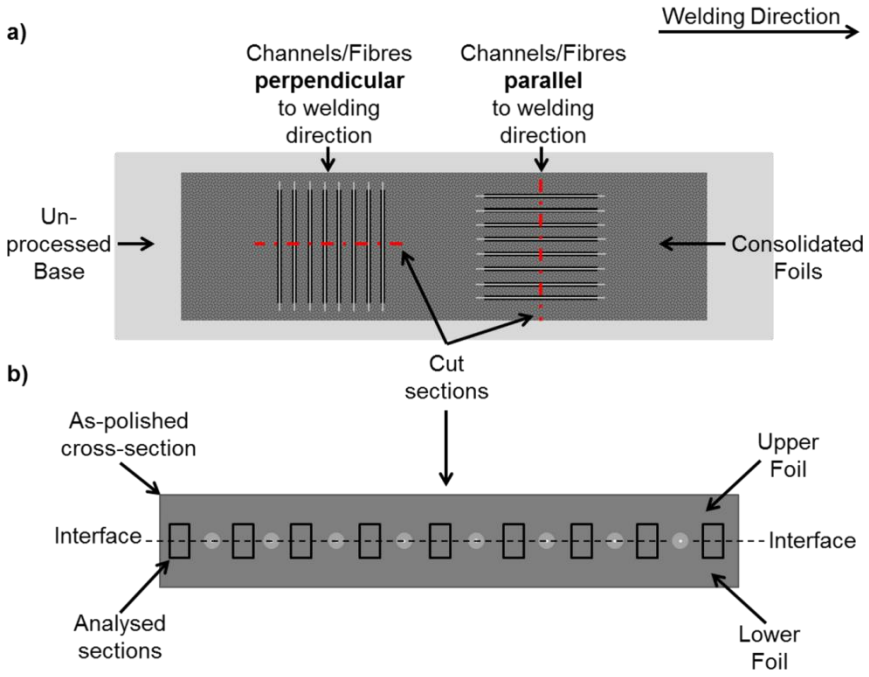


**Figure 8.1 Schematic overview of LWD measurements for a sample containing eight fibres a) cutting sections for channel/shoulder and b) measured interfaces in between the fibres**

To measure the LWD, the already cross-sectioned and mounted samples (see section 7.2.5) were used. The as-polished samples were examined using the same microscope as detailed in section 4.2.5. For each assist gas type (nitrogen and air) six samples containing eight fibres were chosen – three welded perpendicular to the fibre direction and three welded parallel to the fibre direction. The same set of samples was chosen for 24 embedded fibres. For samples consisting of eight fibres, nine images of 100x magnification were taken evenly spaced out in between the fibres. For 24 fibres, 13 images were taken which corresponded to the interfaces between every other fibre.

The microscopic images were then visually analysed by measuring the physically bonded area (excluding welding defects) and the total interface length as shown in Figure 8.2.

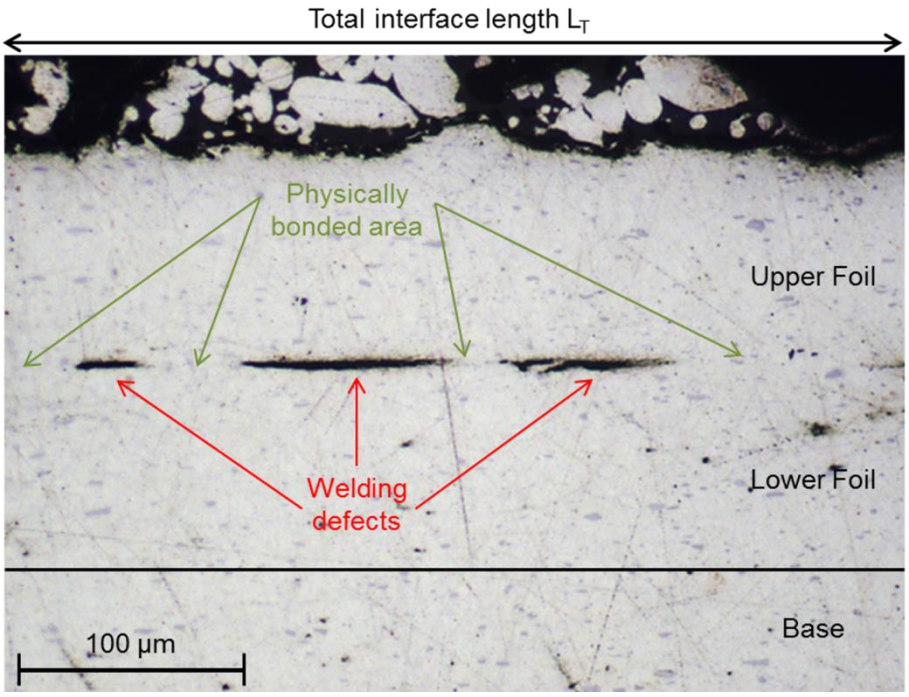


**Figure 8.2 Welding defects calculation with regards to the total measured interface length**

The LWD was calculated by using Equation 1 (see 2.1.6). An average LWD was then calculated for every sample by using the single LWD values.

To explore the impact of the fibres on bonding quality, LWD measurements were also carried out on samples containing only channels as described in

section 7.2.1. The LWD was only measured for samples containing 24 channels as the main focus of the study was to investigate high volume fractions of fibres. Furthermore, samples containing eight channels contained copper foil which would have skewed the measurements. The same LWD measurement procedure as for samples containing fibres was applied.

### 8.2.2 SEM and EDX Mapping of Fibre and Interface Area

To understand the channel/shoulder influence on the bonding quality, SEM images were taken from the area which surrounded the fibre as has been explained in 7.2.6. Additionally to the images of the fibre area, images were also taken from the interfaces between the fibres and close to the shoulder/interface transition. SEM images displayed the oxides introduced by the shoulder in bright white colours which made locating the shoulder distribution along the interface and surrounding the fibres easier than with an optical microscope. To gather further detail about the distribution of the oxides, as well as the distribution of alloying elements, EDX maps and line scans were taken for the above mentioned areas which has been described in 5.2.4.

### 8.2.3 Nanoindentation Set-up and Analysis

Nanoindentation testing was carried out in order to understand the heat influence of the laser on the microstructure of the HAZ. Furthermore, it has been suggested and investigated that fibre embedment and the resulting plastic deformation of the upper foil was accompanied by grain size reduction and work-hardening around the fibres by Li and Soar (2008), Friel and Harris (2010) and Mariani and Ghassemieh (2010). Hence, a change in hardness, due to the microstructural modification within the HAZ, would have either increased the hardness around the fibre or decreased the work-hardening. In either case, a change in hardness would have altered the overall properties of Al 3003-H18 a second time. Furthermore, as the HAZ was in direct contact with the fibre, fibre embedment could have been affected by an increase or decrease in hardness. For the case of a harder microstructure, the fibres would have received dynamic

forces and pressure from above as well as pressure from a harder microstructure from underneath. It was possible that fibre breakage observed in 7.3.4 was due to an increase in hardness. The HAZ after laser treatment has been a popular research subject in terms of hardness for welding, cladding and alloying (Dubourg, 2002; Khaleeq-ur-Rahman, 2010; Borowski and Bartkowiak, 2010).

***Explanation of Oliver-Pharr Method***

For this study, nanoindentation was preferred to microhardness testing as the area to be measured was small and hardness and elastic modulus were readily obtained. For traditional techniques such as Vickers or Brinell the indentations need to be measured after hardness testing in order to calculate the hardness. Nanoindentation continuously records the displacement of an indenter into a material by applying a load. Load and penetration depth are monitored during loading and unloading which results in a loading – unloading diagram. An example of a loading – unloading diagram can be seen in Figure 8.3. The elastic and plastic properties of the material determine the shape of the diagram.

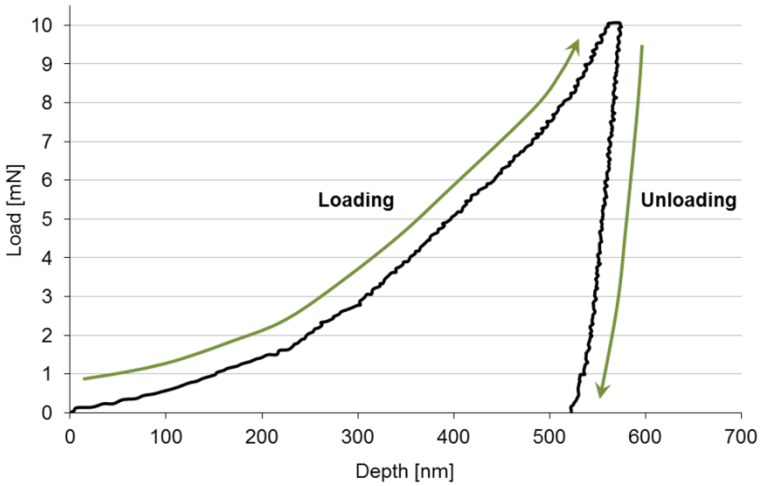


**Figure 8.3 Typical loading – displacement curve for aluminium**

The maximum indentation depth is determined as $h_{max}$ which represents elastic and plastic deformation. The final indentation depth after unloading to zero is $h_f$

which represents the final plastic depth of the material. The contact depth $h_c$ denotes the area for calculating hardness and indentation modulus (Chen et al., 2009). The contact depth $h_c$ and the hardness are determined by the method of Oliver and Pharr (1992):

The hardness (H) of the material is determined from the peak load ($P_{max}$) and the projected area of contact (A):

$$H = \frac{P_{max}}{A} \tag{4}$$

To obtain the elastic modulus, the unloading portion of the depth-load curve is analysed according to a relation depending on the contact area:

$$C_C = \frac{\pi^{0.5}}{\left(2E_r \times A^{0.5}\right)} \quad \text{where:} \tag{5}$$

$C_c$ is contact compliance and $E_r$ the reduced modulus. The reduced modulus is defined as:

$$\frac{1}{E_r} = \frac{1-v_i^2}{E_i} + \frac{1-v_s^2}{E_s} \quad \text{where:} \tag{6}$$

$v_s$ = Poisson's ratio for the sample (1.38), $v_i$ = Poisson's ratio for the indenter (0.07 for Berkovich Indenter), $E_s$ = Young's modulus for the sample (70.4 GPa) and $E_i$ = Young's modulus for the indenter (1141GPa).

***Nanoindentation System Overview***

Hardness testing was carried out on the Nano Test 600 which is a nanoindentation device developed by Micro Materials Ltd., UK. The basic principle is the measurement of the motion between a diamond stylus and the to-be indented surface of a sample. The schematic assembly can be seen in Figure 8.4. A pendulum is rotating around a frictionless pivot. On top of the pendulum, a coil is attached to a permanent magnet. If a current is present, the coil will be attracted towards the magnet which then produces the movement of the diamond stylus towards the sample surface and hence indentation. The displacement of the diamond stylus is measured via two capacitor plates which are connected to the diamond stylus holder. As the stylus moves towards the sample, the capacitance between the two plates will change which is recorded

via a capacitor bridge. The maximum movement of the stylus is defined by a limit stop. A balance weight is located below the capacitor plates in order to balance the mass of the coil and the sample.

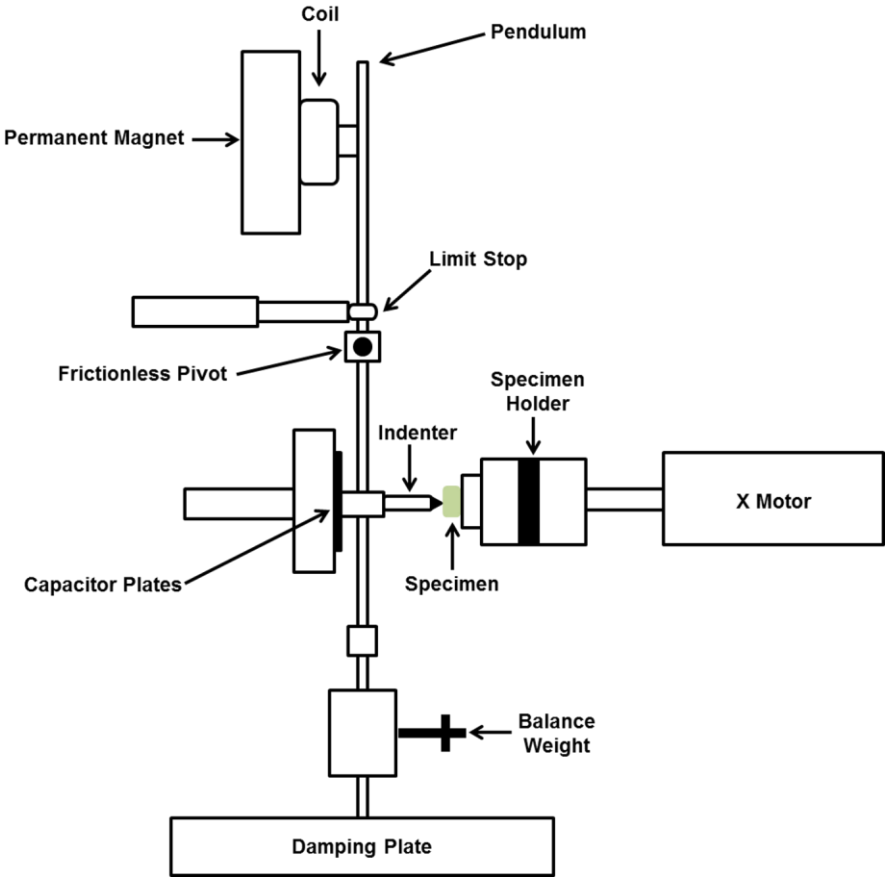


**Figure 8.4 Schematic overview of the Nano Test 600 machine**

The specimens are mounted to a specimen holder which can be applied to a stage driven by three DC motors (XYZ) which allow micrometre positioning ranges in XYZ direction.

### *Hardness Testing Procedure*

To test the hardness of the Al 3003-H18 samples, nine test samples were chosen: three samples contained only channels produced by air, three samples contained channels produced by air with fibres embedded and three samples which contained channels produced with nitrogen and with fibres embedded. Additionally, a control sample without fibres or channels was tested in order to

compare the results. The sample types were chosen due to the following reasons:

→ To investigate the microstructure for multiple passes after laser processing.

→ To investigate the influence of fibre embedding after UC.

→ To investigate the microstructure of nitrogen as those samples experienced less heat treatment (single pass) compared to air (multiple passes).

In order to investigate the hardness, the already cross-sectioned and mounted samples were re-polished to a surface finish of 0.05 µm Ra with colloidal silica to achieve an even surface. The samples were then mounted with an adhesive to a specimen holder which could be attached to the nanoindentation machine.

To test the influence of laser processing, fibre embedding and UC on the samples, a test method displayed in Figure 8.5 was applied.

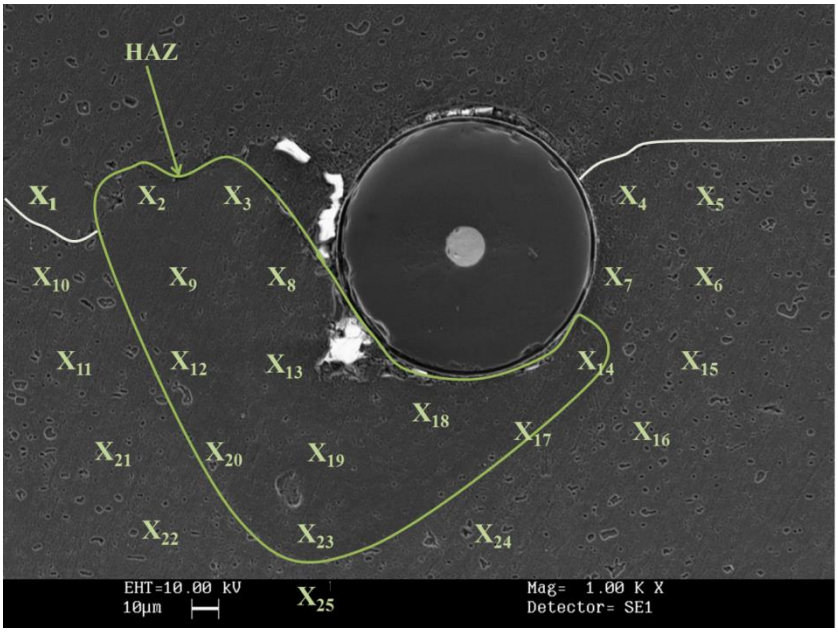


**Figure 8.5 Test method for nanoindentation to analyse effect of HAZ and fibre**

In order to gather information about the microstructure, 25 indents were measured along the HAZ and in the bulk material. To repeat the same test method for all the samples, an integrated microscope was used in order to find

the first indent position. The following 24 positions for the samples were then set by creating a test series. As the HAZ for nitrogen samples was smaller, only 19 indents were measured. The indents for the original foil were measured along the weld line into the bulk material covering an area which theoretically coincided with the HAZ for air samples. For the measurements, a three faced Berkovich diamond indenter was used (Lucca et al., 2010). The loading range was set to NT 1 which allowed loading rates of up to 10 mN to be applied. The indentations were carried out in load controlled mode and a load of 10 mN with a loading rate of 1 mN/s was set. To reduce creep, a dwell time of 15 s was set.

After indentation, the data was analysed by using the integrated NanoTest data analysis software. Analysis was carried out fitting the unloading curve from 100 % to 40 % of the peak load via power-law fitting which calculates $P_{max}$ and the contact depth $h_c$.

The software then calculates the diamond area function after Oliver and Pharr (1992) which relates the cross-sectional area of a plane through a diamond to the distance of the plane from the tip. Knowledge of this function allows the contact area and thus the hardness of the material to be calculated.

## 8.3 Results and Discussion

### 8.3.1 Bonding Quality

The bonding quality was measured in terms of LWD calculations. Bond assessment was carried out for samples containing 8 fibres, 24 fibres and samples containing channels but no fibres for both assist gases. In Figure 8.6, an image of a nitrogen sample containing 24 fibres is displayed. The upper foil was completely delaminated from the lower foil. In Figure 8.7, delamination was not observed but it was also difficult to gain sufficient data about the bond quality as a gap of 2 µm was observed. Every sample that contained 24 fibres showed either delamination, separation or insufficient bonding. Hence, it was not possible to gather sufficient data for LWD calculations for samples containing high fibre volumes.

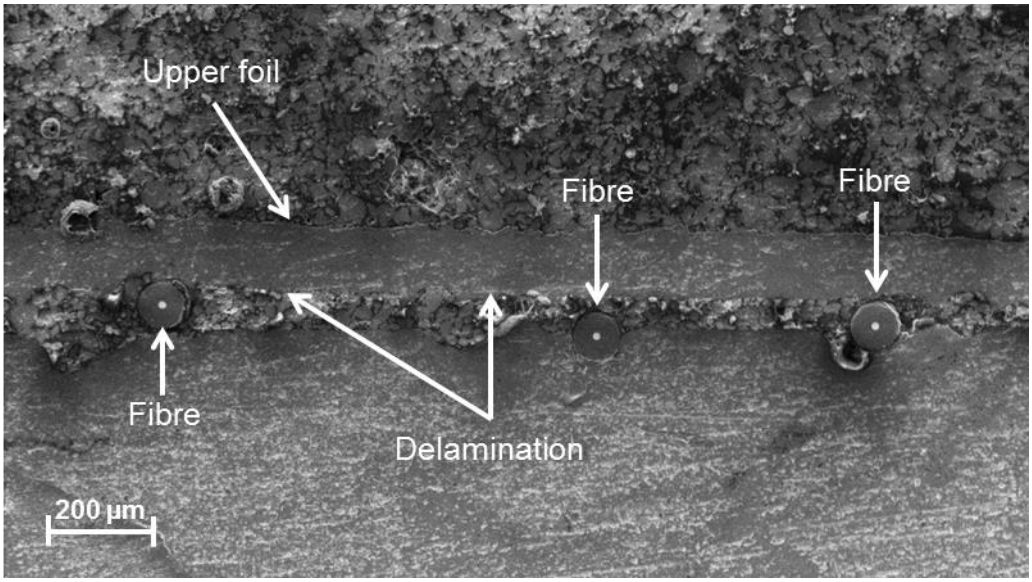


**Figure 8.6 Delamination of upper and lower foil prohibiting LWD measurements**

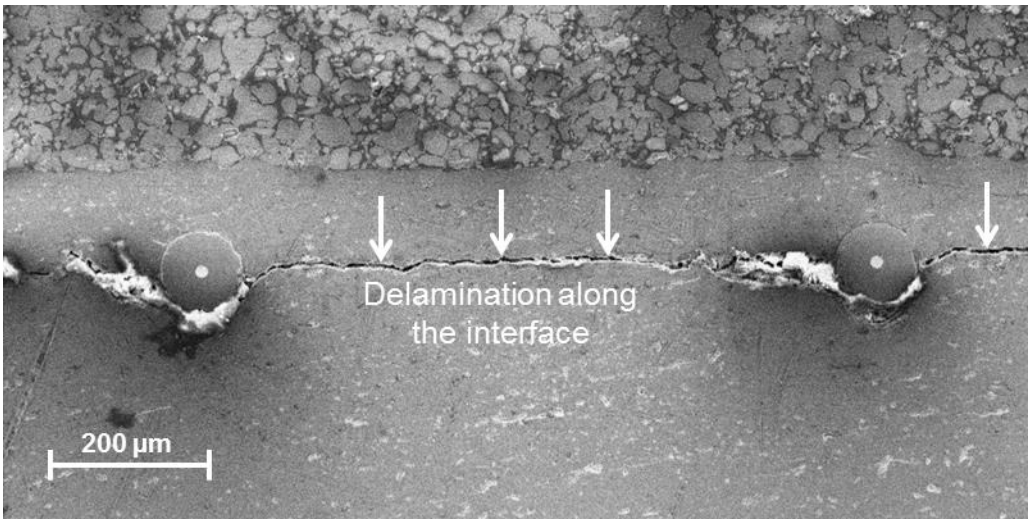


**Figure 8.7 Beginning of delamination between upper and lower foil**

For this reason, LWD calculations were only carried out for samples containing eight fibres and for samples containing channels but no fibres. The results for samples containing eight fibres produced with air as the assist gas are shown in Figure 8.8. It can be seen that the bond quality is lower for fibres embedded in parallel direction than in perpendicular direction. In perpendicular direction, the fibres exhibit bonding qualities of over 80 %.

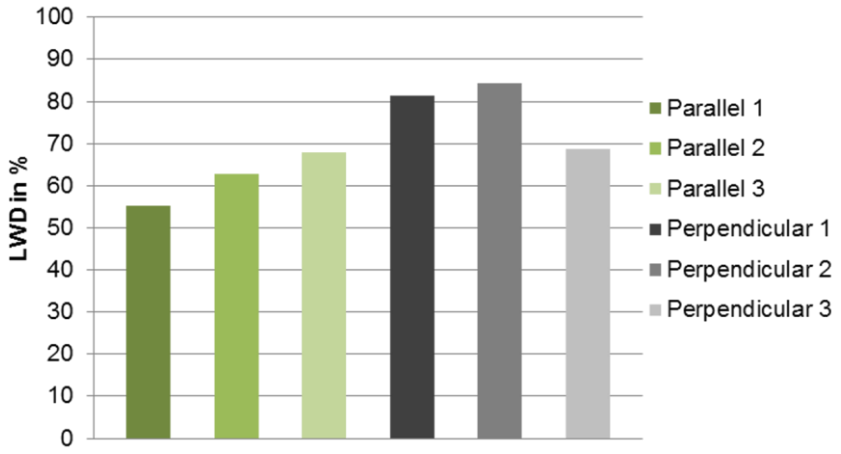


**Figure 8.8 LWD percentages for eight fibres in air samples for both directions after UC**

In Figure 8.9, the LWD results for samples produced with nitrogen and eight fibres are displayed.

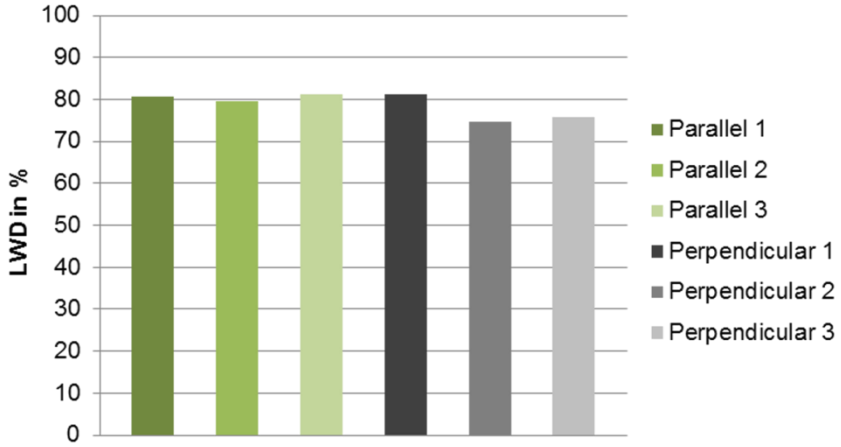


**Figure 8.9 LWD percentages for eight fibres in air samples for both directions after UC**

For both directions, LWD results of over 70 % were found. Opposed to the results seen for Figure 8.8, samples produced with nitrogen showed slightly lesser values for perpendicular embedded fibres. Hence, it was suggested that fibre direction has no effect on bonding quality. The reason for a lower bonding quality for air samples may have been that the oxides for perpendicularly embedded fibres were dispersed into the channel because the shoulder was in front of the channel. For parallel embedded fibres, the oxides could have dispersed to both sides of the shoulders which would have prohibited bonding.

Furthermore, nitrogen samples opposed to air samples comprised of less pronounced shoulders and channels (see 6.3.3) which was suggested to indicate that shoulders and channels prohibit sufficient bond formation.

In Figure 8.10, the results of the samples analysed in parallel and perpendicular direction for 24 channels created with air are displayed.

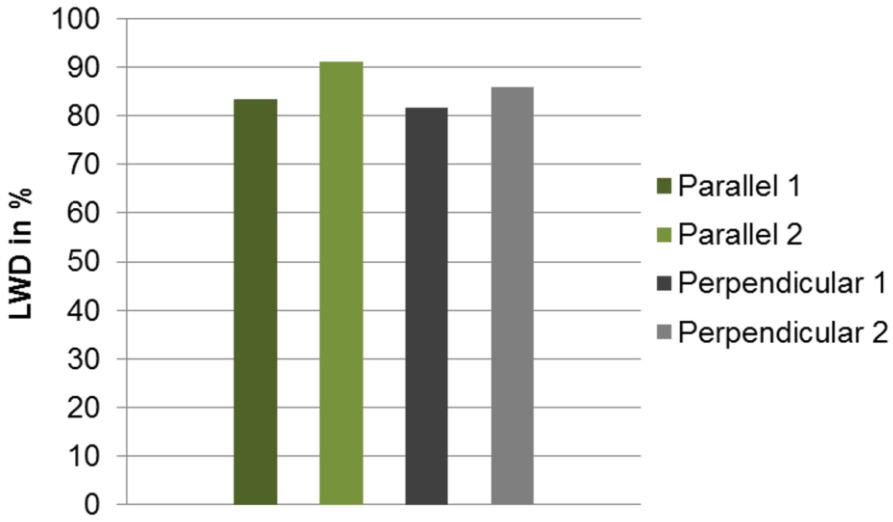


**Figure 8.10 LWD percentages for parallel and perpendicular channels without fibres after UC**

Both directions exhibited over 80 % bonding quality. This was slightly higher than for 8 fibres for both gas types – yet very similar. This was compared to the results of Friel (2011) and Kong (2005) in the expected range for samples without fibres considering that the amplitude for the measurements in this study was higher (20 µm). Furthermore, compared to the results by Kong et al. (2003) for Al 6061-O, the results showed better bonding quality which will be discussed below:

Kong et al. (2003) found after ultrasonically consolidating Al 6061, persistent oxide films which produced low bonding qualities of less than 50 % for various parameter combinations. However, peel tests showed that resistance to peeling was high and it was suggested that brittle ceramic bonds had formed. Matsuoka (1994) presented that ceramic bonds can form which exhibit mechanical properties as the parent alloy. This study already identified the existence of

$Al_2O_3$ around the shoulders and channels. Welding of the channels without fibres also meant that gaps which inhibited bonding were existent. However, the LWD percentage was still high. With regards to the study of Kong et al. (2003) the oxides were only existent at certain areas along the weld line which suggested that bonding can recover from regions were bonding is not possible. Furthermore, bonding around the shoulder may take place by ceramic bonding of $Al_2O_3$ and the upper aluminium foil as proposed by Kong et al. (2003) and Matsuoka (1994).

For 24 embedded fibres, two reasons could be proposed to have caused the delamination of foils. Firstly, the introduction of many fibres increased the area of non-bonding and secondly, the contact area for oscillations decreased with more fibres. As can be seen for the welding of 8 fibres and air, the bonding quality decreased. This might have been due to the introduction of fibres in combination with the oxides from the shoulder. For 24 fibres, the area of bonding was decreased by an increase in non-bonded areas due to oxides and fibres. Additionally, the area in which bonding would have been possible (between the channels) was considerably lowered when compared to 8 fibres. However, as bonding for 24 channels showed good bonding qualities, it was believed that the addition of the fibres was the main reason for the delamination of the upper foil instead of the oxides.

In Figure 8.11 an image of a sample containing 24 channels is displayed. Bonding was observed even though the Al2O3 shoulder got dispersed along the weld line (left) and the upper foil deformed around the shoulder. After the shoulder, bonding started again until the channel started. Due to the lack of bonding area from the channel, no bonding took place along the channel (similar to Figure 7.14 for parallel channels) and started again after the next channel/shoulder combination.

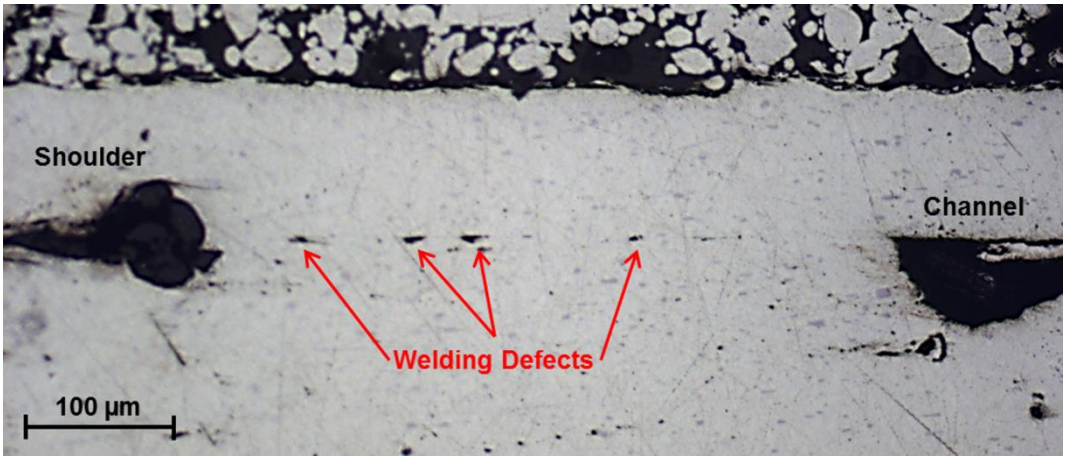


**Figure 8.11 Voids at interface for a sample without fibres but channels**

In Figure 8.12, another phenomenon which was noted during SEM is displayed: fibres possibly rolled out during UC and the upper foil deformed around them.

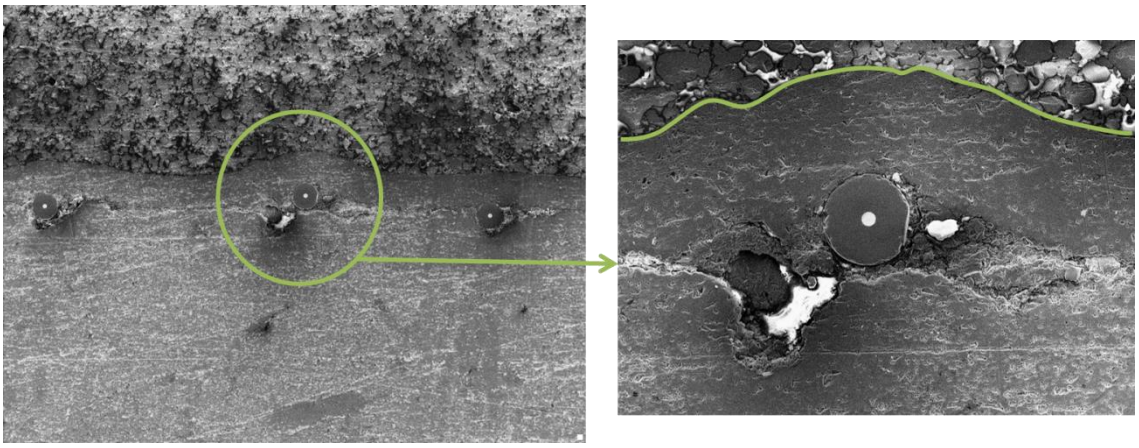

**Figure 8.12 Deformation of upper foil around a fibre not in channel**

The upper foil deformed in the shape of the fibre and significantly around the fibre as well. This was due to the fibre being harder than the aluminium matrix. Thus, instead of fracturing or compressing the fibre, the foil deformed. As the fibre was able to resist the oscillations and contact pressures applied, it was suggested that the fracturing of the fibres, observed in 7.3.4 was not influenced by dynamic forces but because of the $Al_2O_3$ inside the channel and the possibly harder HAZ.

In Figure 8.13, fibre imprints into the channel area and into the upper foil are displayed. The imprints suggested that the fibres integrated well into both foils during UC. However, due to their mechanical entrapment rather than chemical and the lack of bond formation between the foils, the fibres were displaced after UC.

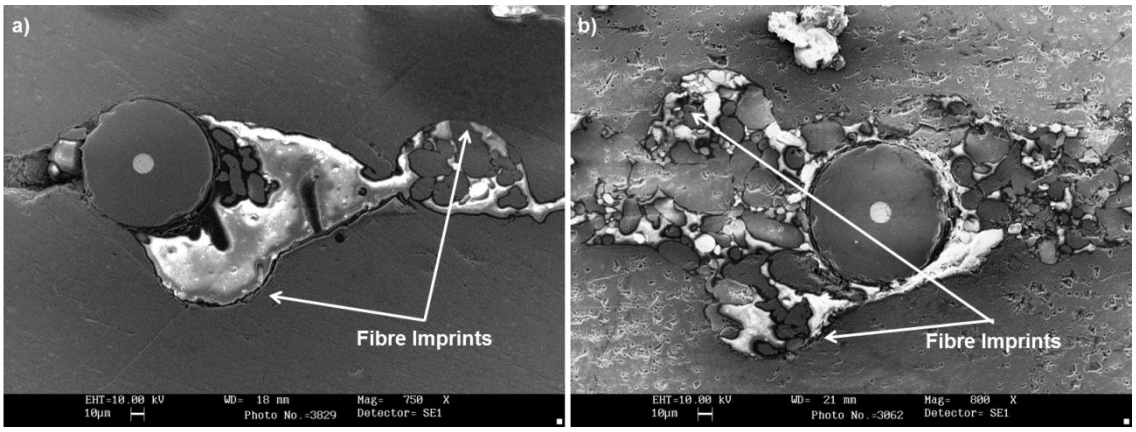


**Figure 8.13 Imprints of fibres into the upper and lower foils a) air and b) nitrogen**

It can be seen that during hot mounting of the samples, the Konductomet powder entered into the channel and the deformed areas of the fibre (different microstructure). The reason for this was that insufficient bonding took place and during cutting of small sections for microscopic and SEM inspection the foils delaminated. From Figure 8.13, it can also be noticed that the upper foil was a bit more deformed around the fibre than the lower foil. This could be an indication for a hardened channel zone.

### 8.3.2 Plastic Flow Behaviour of Matrix Material

The analysis of the plastic flow behaviour of the shoulder and of the foils around the fibres showed that the shoulder did not aid the embedding process which was expected from the results from chapter 7. Three different examples of fibres samples are displayed in Figure 8.14. The interface between the upper and lower foil was visible.

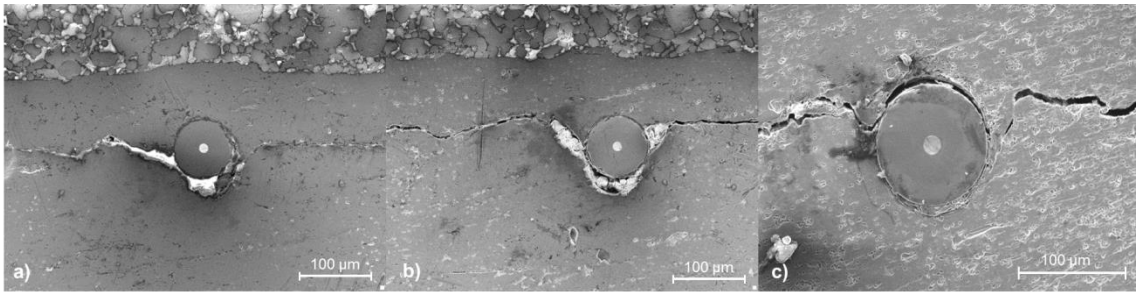


**Figure 8.14 Examples deformation of upper foils around fibres**

For every embedded fibre which stayed in the channel, it was observed that the channel indeed helped to position the fibres. In Figure 8.14 a) and b), the imprints of the fibres into the channel geometry were visible. As there was no delamination, the imprints for the upper foils were less noticeable. It was believed that the channels did aid the fibres to be securely positioned during UC. Nonetheless, the plastic flow around the fibres was assumed to be insufficient to safely encapsulate the fibres which resulted in loose fibre integration in addition to the non-deformation of the shoulder feature.

In Figure 8.15, a fibre which got encapsulated during UC is shown. During mounting of the sample, the upper foil got displaced due to insufficient bonding between the foils.

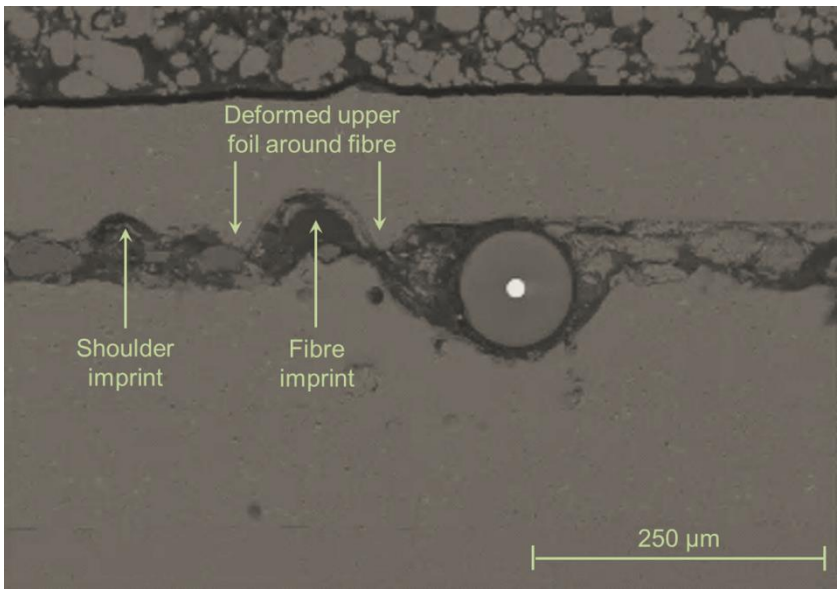


**Figure 8.15 Deformation of the upper foil around the fibre and shoulder**

It can be seen that dependent on the integration of the fibre into the channel, the upper foil deformed accordingly which is also recognisable in Figure 8.14 c). The upper foil in both Figures formed two shoulders next to the fibre. Furthermore, the upper foil also deformed around the shoulder which could be an indication of an increase in hardness.

It was proposed that there is quite a range of deformation behaviour during consolidation which could help to facilitate bonding requirements depending on the to-be embedded objects. If an object is securely integrated in a channel for example, less deformation is required. If an object is not securely positioned in a channel more deformation will be required. It was concluded that channels aid not only the positioning of fibres but also limited the amount of plastic flow around the fibre when the channel is deep enough. This endorses research on plastic flow around fibres by Kong (2005) who found that an imprint of a fibre before embedding helped facilitate plastic flow.

In Figure 8.16, an embedded fibre is shown. Integration without gaps into the lower matrix material was observed.

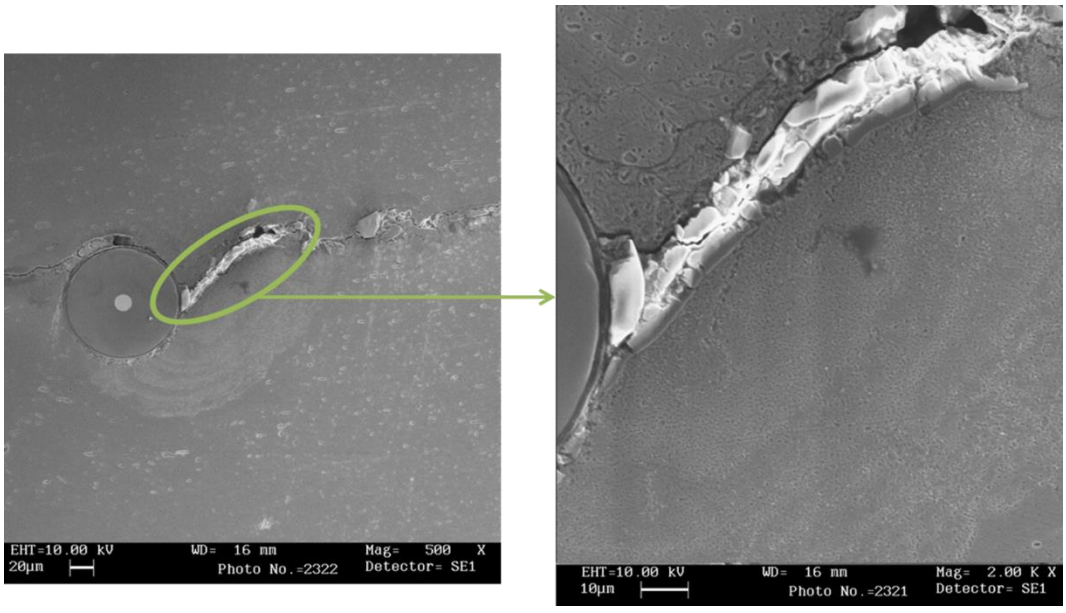


**Figure 8.16 Fibre embedded in an air sample with visible shoulder/recast layer**

Shoulder dispersal or the recast layer was not found in the channel but instead next to the fibre. The upper foil deformed well around them and around the fibre. The upper part of the fibre exhibited a gap. In the magnified image (x2000) it was observed that a gap along the recast or shoulder dispersal appeared. The gap was small; however this may be an indication that the upper foil was not able to bond to the $Al_2O_3$. As a gap between fibre and upper foil was also observed, it was suggested that bonding was hindered by the appearance of the coating of the fibre. SiC fibres were coated with the ceramic titanium diboride and $Al_2O_3$ is a ceramic as well – the combination of both over a large area might have led to the narrow unbonded gap. On the other side, the recast appeared to be adhered well to the HAZ. This would further endorse the proposal that the fibres in combination with the shoulders caused the delamination of the foils.

In Figure 8.17, a magnified shoulder area is exhibited. The upper foil deformed well around the HAZ and as well around the $Al_2O_3$ particles.

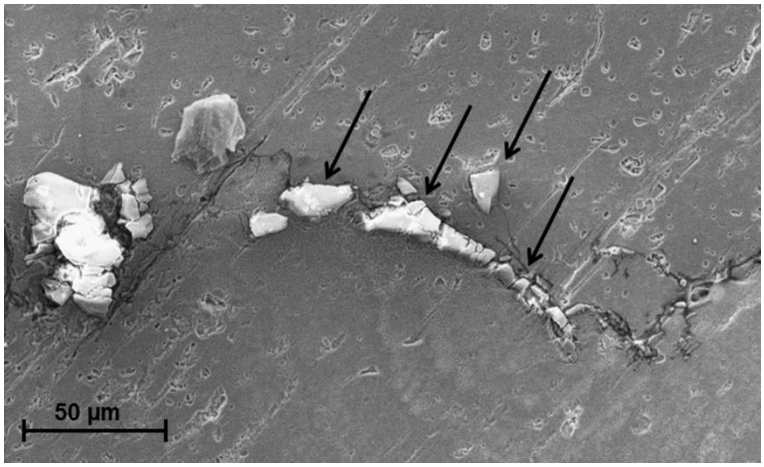


**Figure 8.17 Deformation of upper foil around HAZ and $Al_2O_3$ particles**

The gap was less visible, however it was observed that there was a clear distinction between the upper and lower foil – a weld line was visible. In addition, the upper foil deformed around the HAZ which was evidence that the HAZ was harder than the original foil material.

### 8.3.3 EDX of Interface and Fibre Area

To clarify the oxide distribution around the fibre and possibly along the interface, EDX maps and line scans were taken. Figure 8.18 displays an EDX map for an interface to identify if the oxides were dispersed along the interface due to the rolling of the sonotrode which would have facilitated non-bonding. As can be seen, hardly any oxides were noticed along the weld interface as barely red colour could be recognised in the map for oxygen. EDX mapping was not capable of detecting any oxides along the weld interfaces for any samples tested. The reason for this was that a possible oxide layer would have been only a few nanometres thick and the resolution from the EDX would have been too high. Oxide layers have been detected by using EBSD (Johnson, 2008; Dehoff and Babu, 2010).

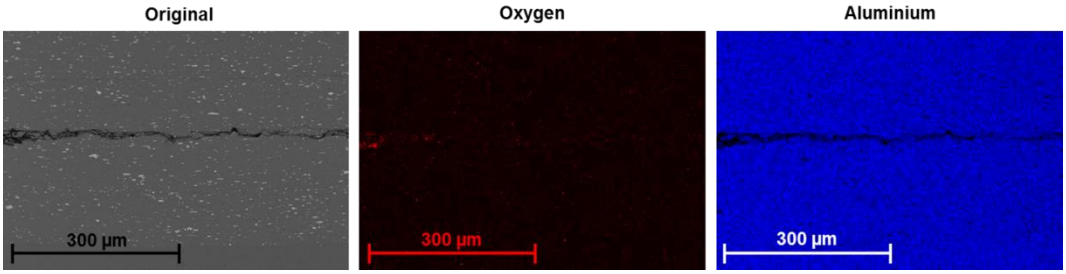


**Figure 8.18 EDX Mapping of an interface (EDX map for oxygen (red) and aluminium (blue))**

In Figure 8.19, EDX maps of a fibre embedded in an air sample can be seen. The foil delaminated and an imprint on the upper foil was detected. $Al_2O_3$ was detected all along the shoulder area as fractured shoulder pieces as well as in the interface area. It was also observed that $Al_2O_3$ was also dispersed all along the slope to the bottom of the channel. This correlated with the EDX analysis for oxygen detection without integrated fibres in chapter 5 (see Figure 5.16). Additionally, fractured aluminium and silicon pieces from the fibre were detected which possibly happened due to grinding of the sample.

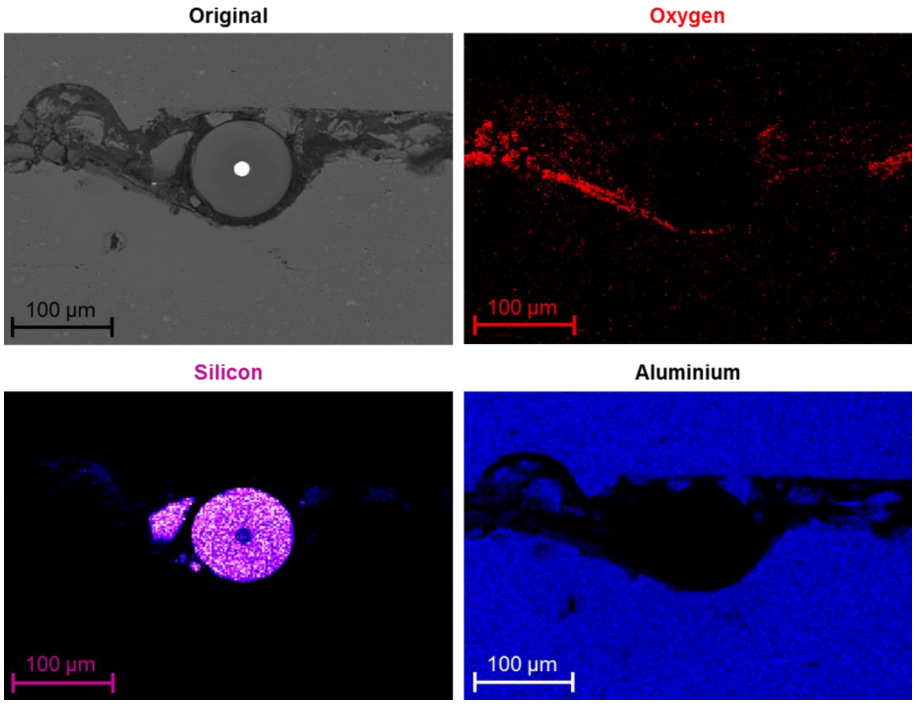


**Figure 8.19 EDX maps of selected elements for a fibre embedded in an air sample**

Figure 8.20 presents a line scan for a fibre embedded in an air sample.

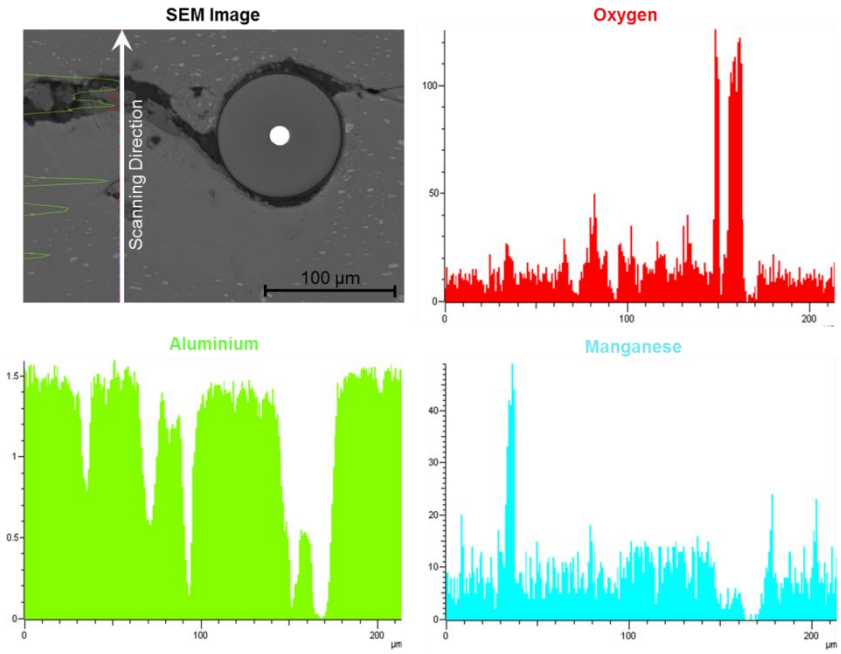


**Figure 8.20 Linescan for an air sample to detect oxygen around the shoulder**

Two distinct peaks for oxygen were apparent when the shoulder and the area above the shoulder were scanned. A compact concentration was found for Mn

in the HAZ area which became less compact further along the HAZ until the end of the HAZ.

In Figure 8.21 EDX maps for an air sample in which the fibre was well embedded is presented. A significant amount of plastic flow occurred around and especially behind the fibre.

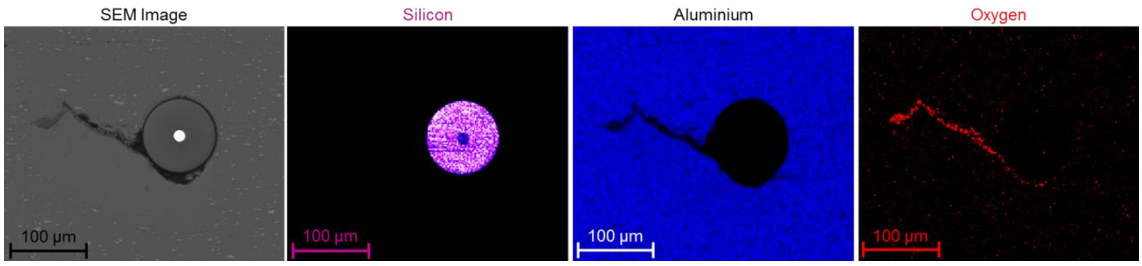


**Figure 8.21 EDX maps of selected elements for an embedded fibre without delamination**

It appeared that the upper foil deformed well around the oxygen area. In addition, no weld lines were detected along the interface.

Figure 8.22 presents a line scan for a nitrogen sample with a copper foil embedded between the foils.

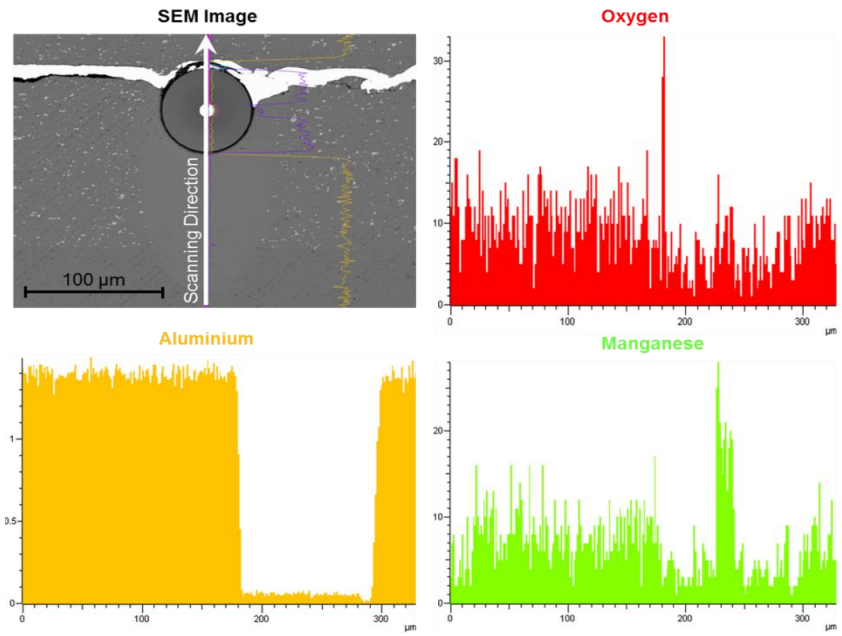


**Figure 8.22 Linescan for a nitrogen sample to detect oxygen around the fibre**

The deformation of the copper foil resembled the deformation behaviour noticed in Figure 8.15. An oxygen peak occurred at the interface of channel bottom and fibre. This peak may have occurred due to the formation of an oxide layer at the channel top after laser processing. However, no further significant oxygen peaks were detected. The fibre was well embedded into the channel and the overall channel area showed less shattering and shearing of material than for air.

In Figure 8.23, EDX maps for another nitrogen sample with a copper foil between the Al foils are presented. Oxygen was only detected in the copper foil area and less noticeable around the fibre. In comparison with the air samples, the oxygen was less noticeable. A reason for this was that firstly nitrogen is an inert gas which did not react with the aluminium as much as oxygen in air does and secondly, the shoulders in nitrogen were smaller.

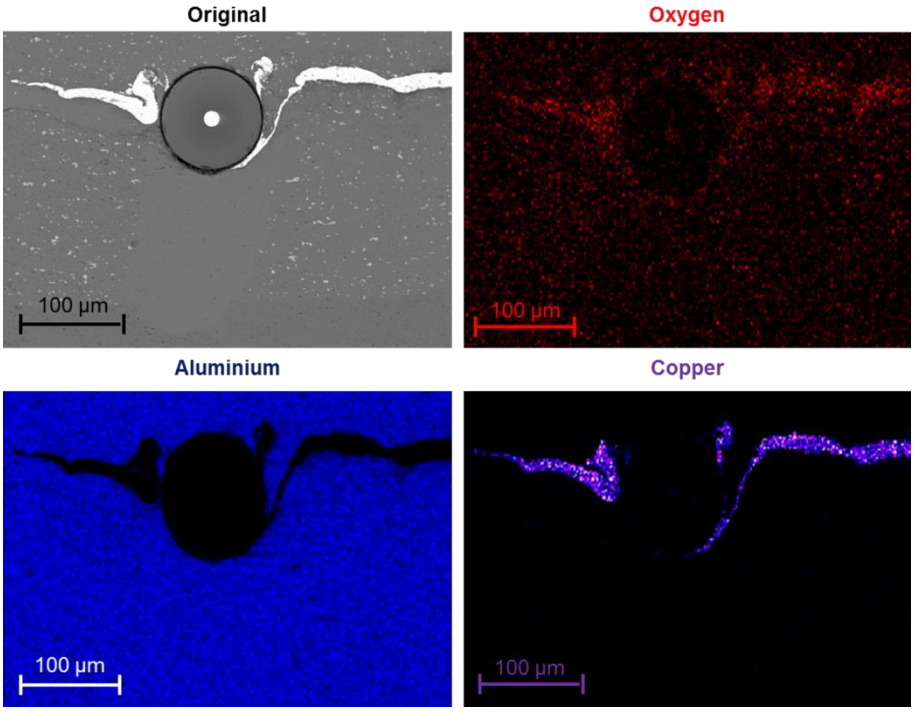


**Figure 8.23 EDX maps of selected elements for a fibre embedded in a nitrogen with copper foil.**

The copper foil was observed to be sheared before the fibre. Behind the fibre the copper foil nearly deformed around the bottom of the fibre. As can be seen

the copper foil deformed in welding direction and was possibly sheared when approaching the hard fibre.

In Figure 8.24, representative EDX maps of the main alloying elements in the matrix material and the fibre materials are given for a fractured fibre. EDX was carried out to understand the distribution of the fractured fibre in relation to the welding direction and welding forces. It can be observed from results for silicon that the fibre fractured but remained in the channel area. The titanium coating of the fibre was mainly found around the fibre as single clusters yet also in the channel area. However, from the EDX maps it was not possible to correlate the influence of the welding direction on the fibre fracturing.

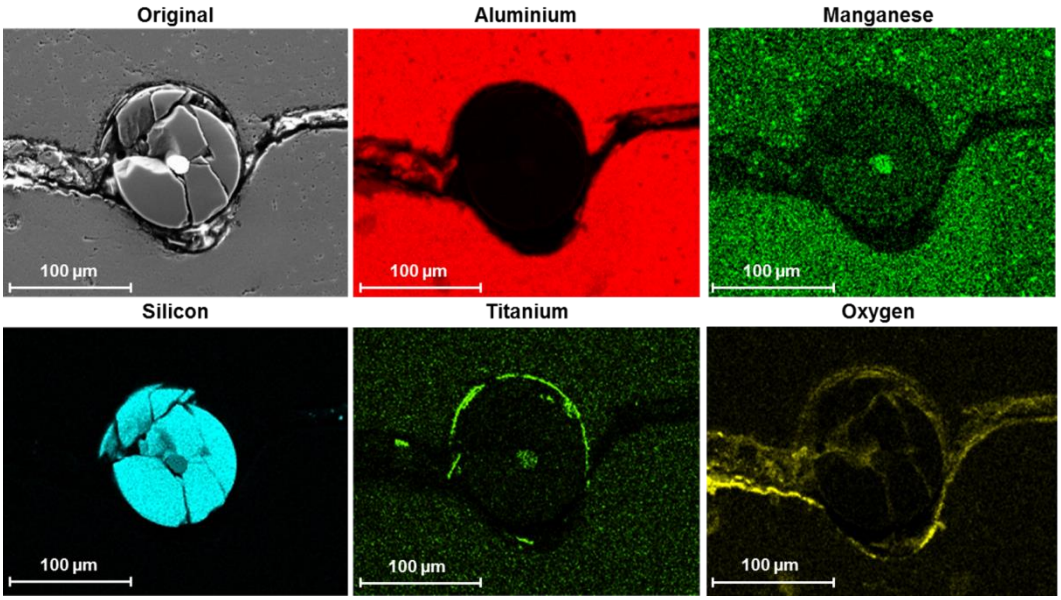


**Figure 8.24 EDX maps for selected elements to reveal behaviour of fractured fibre**

In Figure 8.25, a good example for the oxide formation around the fibre embedded in air can be seen. As $Al_2O_3$ is very brittle, it breaks up in clusters. The oxide clusters were clearly visible underneath the fibre and along the channel slope. This was further evidence for $Al_2O_3$ generation due to the assist gas during laser processing of the channel.

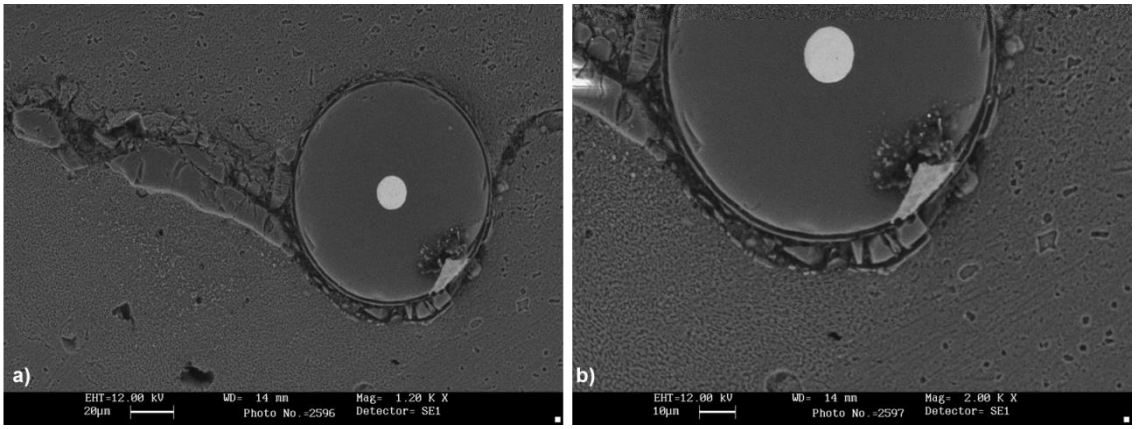


**Figure 8.25 Oxide cluster formation around a fibre**

Figure 8.26 displays two samples manufactured with air in which the fibre was not positioned in the channel. This allowed having a closer look at the inside of the channel. From Figure 8.25 a) it can be seen that the inside of the channel was distorted and dispersed with shattered material.

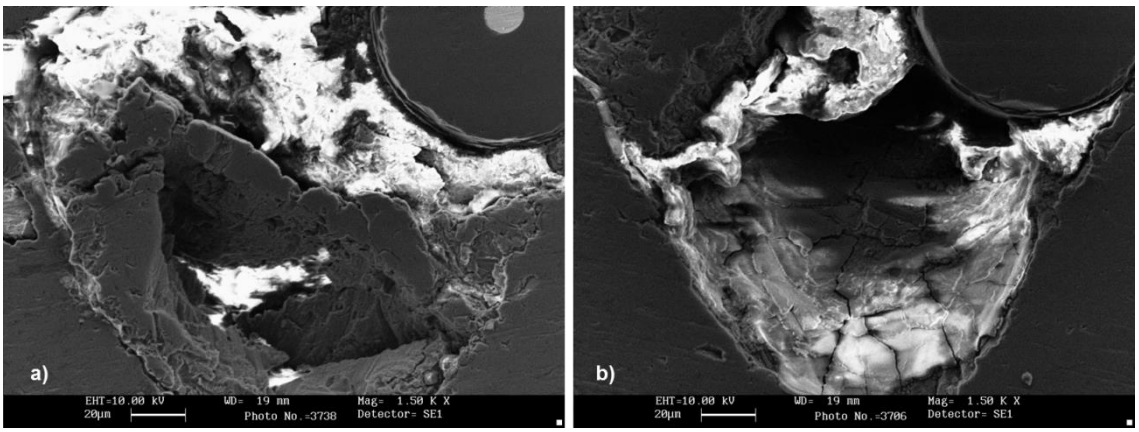


**Figure 8.26 Detailed view of channel bottom without a fibre**

Evidence for an oxide layer can be found from Figure 8.26 b). As the fibre must have moved out of the channel after UC as the imprint was visible, it was possible to inspect the inside along the channel length. It was observed that the whole bottom part of the channel was covered in brittle clusters which were likely $Al_2O_3$ which had been identified along the channel interface in Figure 8.25. However, in Figure 8.25 a backscattered image is shown which inverted the bright white colour of the oxide. Additionally, as the fibres in Figure 8.26 a) and b) still showed an intact titanium diboride coating, the coating did

not influence the oxide layer. Figure 8.27 confirms the results by Yang et al. (2010). The fibres were not chemically embedded but mechanically.

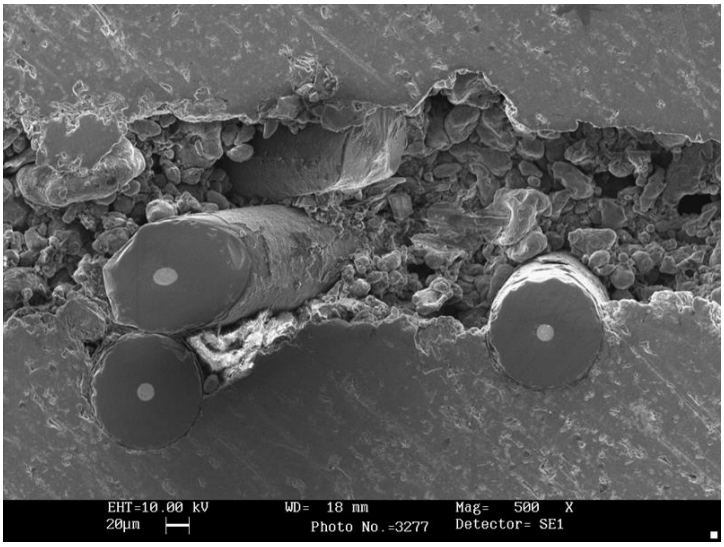


**Figure 8.27 Fibre appearance after delamination**

### 8.3.4 Nanoindentation Testing

Nanoindentation testing was carried out for three different sample types in order to investigate the hardness of the HAZ after laser processing. It was believed that the multiple passes and the accompanying change of the microstructure would not only change the mechanical properties of the material but also influence the fibre embedding. For this reason, three samples with channels but without fibres, three samples containing channels and fibres and three samples produced with nitrogen were compared to a reference sample without fibres.

The hardness results of the reference sample changed from higher values at the ultrasonically consolidated interface (1.0 GPa) (see Figure 8.5 for x1, x2, x3) to less hardness values (0.85 GPa) corresponding to points x22, x24 and x25 in Figure 8.5. Additionally, higher hardness values, ranging from 1.2 GPa to 1.5 GPa, were randomly observed within the data. The reason for this was that Al 3003-H18 consists of dispersed alloying elements of Mn, Si, Fe and Cu to increase the strength. Due to the resolution of the microscope it was not possible to identify these dispersed particles before indentation. In Figure 8.28,

three representative unloading curves for the hardness at the interface, the hardness away from the interface and hard particles are displayed.

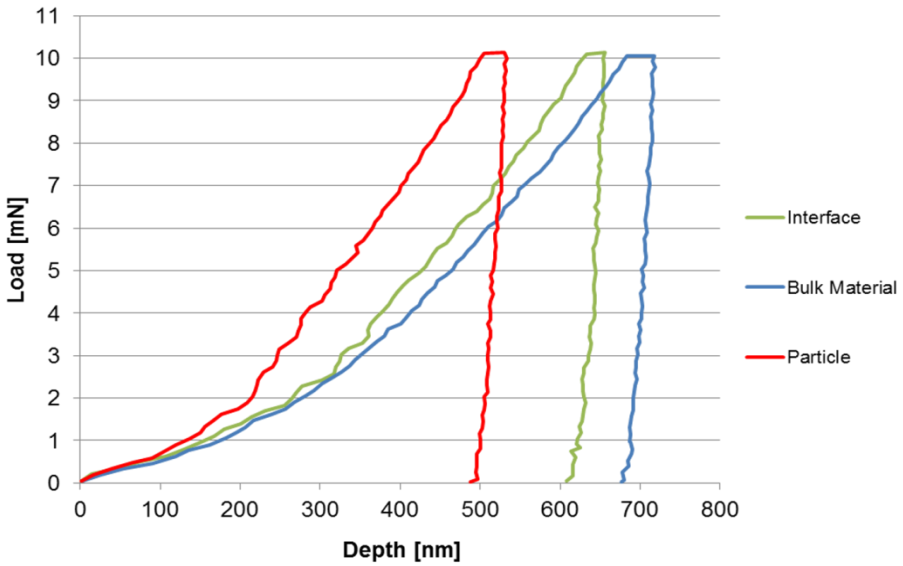


**Figure 8.28 Nanoindentation unloading curves for reference sample**

From the results it was seen that work-hardening and a reduction in grain size due to the oscillation amplitude at the reference samples' interface was possible as suggested by Li and Soar (2009a), Schick et al. (2010) and Friel and Harris (2010).

The results of the three different sample types after laser processing varied strongly due to the different indentation zones. However, trends were noticeable which will be explained below for the different sample types.

→ Only channels: Samples only containing channels showed an average hardness for all three samples of 1.12 GPa which was higher than for the reference sample. Towards the inner channel borders the hardness increased up to 1.74 GPa. The trend was observed for all three samples.

→ Air channels with fibres: The samples showed an average hardness of 1.25 GPa. Hence, the hardness was higher than with only channels. Consistent higher hardness values (higher than for samples containing only channels) were found around the fibre.

→ Nitrogen channels with fibres: Those samples showed an average hardness of 0.96 GPa. This value was lower than for the other two sample types and as well lower than the value of the UC interface. However, again a hardness increase was noticed for nanoindentation points close to the fibres.

In Figures 8.29 to 8.31 the corresponding hardness values are displayed.

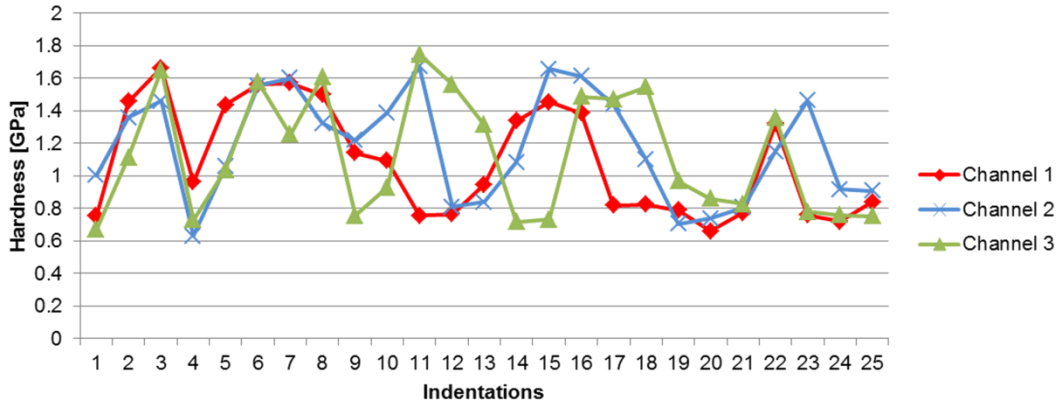


**Figure 8.29 Hardness values for only channels corresponding to the 25 measurement points from Figure 8.5**

The alternating structure arose due to the measurement technique employed. It can be seen that the low values corresponded to the values outside of the HAZ and the higher values inside the HAZ. The highest values for all three sample types were discovered near the channel outline or the fibre respectively. The reason why the data in Figures 8.29 and 8.30 shattered opposed to Figure 8.31 was because the channels manufactured by air showed a less discrete outline as well as inconsistent areas (possible inclusions).

The reason why the values for nitrogen are lower than the values for air or only the channels is due to a lower heat input into the material. The channels were processed with a power of 140 W, as opposed to 250 W for the air samples. Furthermore, due to the multiple laser passes, the heat input for air was five times higher. Another factor was that nitrogen as an inert gas provided less heat input than air (Steen, 2010). All these factors contributed to lower values next to the fibres but also to an overall increase of hardness values in the laser-affected zone.

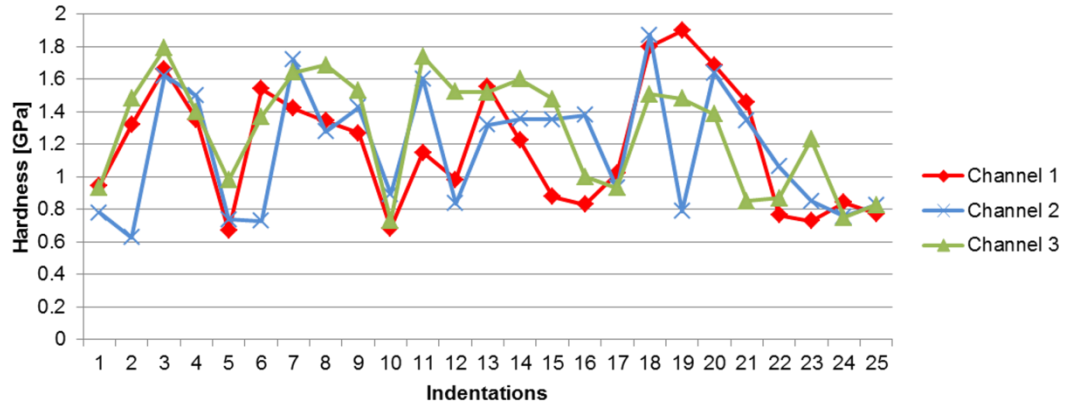


**Figure 8.30 Hardness values for channels produced with air and fibres corresponding to the 25 measurement points from Figure 8.5**

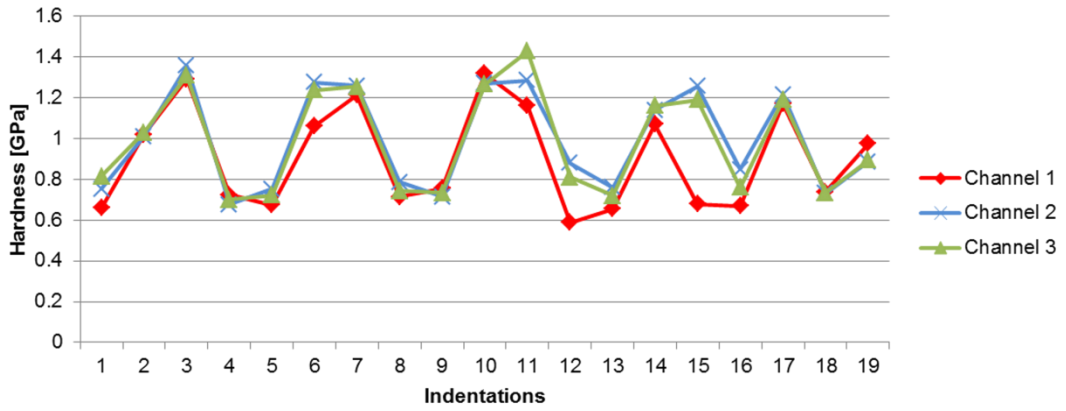


**Figure 8.31 Hardness values for channels produced with nitrogen and fibres corresponding to the 19 measurement points from Figure 8.5**

Li and Soar (2009a) found a hardness increase in a region of 20 µm around the SiC fibres. This result was found for the air and nitrogen sample as well. Comparison of the samples only containing channels and the air sample showed that the samples containing fibres had higher values near the fibre (up to 1.9 GPa) than the values near the channel outline without fibres (up to 1.7 GPa). Hence, it can be assumed that the plastic flow around the fibres was experienced even with the HAZ. However, opposed to Li and Soar (2009a), the hardness results were found to be higher. The reason for this can be attributed to the fact that solute rejection as was discovered in 5.3.3 possibly caused a pile-up of manganese around the periphery of the channel outline as this was

the area that solidified last. As Mn is responsible for strengthening of Al 3003 this area was expected to have higher hardness values. Additionally, the whole HAZ showed high hardness values for air and only channels due to the finer microstructure. Hence hardness values before fibre embedding were already higher than for Li and Soar's samples (2009a). Additionally, results by Friel and Harris (2010) suggested that previous UC before fibre embedding was increasing the plastic flow and decreasing the grain size at the bottom of the fibre. Substantiation to this result can be observed from the results in Figures 8.28 and 8.29; the values that were measured underneath the fibres were higher than for the other values measured around the fibre.

## 8.4 Review

Chapter 8 was intended to aid the understanding of the plastic behaviour of the shoulders during UC in order to further bonding while embedding a high number of fibres. LWD measurements were only carried out for samples containing eight fibres and for samples only containing channels. Measurement of the LWD was not possible for 24 embedded fibres due to delamination of the foils or long intervals of non-bonding which led to non-usable results. The LWD for eight fibres reached up to 80 % with variation depending on the channel direction. Channels without fibres showed high bonding qualities up to 90 %. Two possible mechanisms might have led to delamination or insufficient bonding of the foils containing 24 fibres: Firstly, insufficient area for bonding and secondly clean metal contact was disabled by oxides from the shoulder and HAZ area as well as from the SiC fibres. As samples containing no fibres showed good bonding results, it was suggested that the fibres may be the hindrance for bond formation rather than insufficient space or oxide formation. This knowledge contributed to further understand the problem of high volume fibre embedding.

The shoulder, which was, as stated in the hypothesis, supposed to aid decreasing the necessary plastic flow, was either dispersed into the channel or around the channel edges. Therefore, a decrease of plastic flow around the

fibres was not observed which may have proved the hypothesis to be wrong. However, it was noticed that the upper foil deformed in the shape of the fibres and also deformed along the $Al_2O_3$. Depending on how deeply the fibres were embedded into the channels, the upper foil deformed accordingly. Hence, there is some latitude in which the plastic flow of the upper foil appears which would be interesting for embedding different sizes of objects.

EDX line scans and maps for areas surrounding the fibres gave evidence that the oxides, which were introduced during laser processing and manipulation of the melt, get dispersed along the channel geometry and around the shoulders. This hindered especially secure fibre positioning into the channels produced with air which had been observed in chapter 7 before. On the contrary to chapter 7, samples produced with nitrogen showed less evidence of oxide formation (aluminium nitride) in the channel which accounted for better embedding of fibres. Hence, fibre breakage may have only occurred for nitrogen due to the lesser depth of the channel which promoted insecure positioning.

Nanoindentation testing showed that the HAZ area produced with multiple passes showed a increase in hardness compared to the original samples. An increase in hardness was noticed for samples containing fibres which was in accordance to previous studies. Hence, it can be concluded that fibres introduce stresses which lead enhanced plastic deformation. There was no difference noticed for samples containing fibres and samples only containing channels which was opposed to research work before which showed that harder material can be found especially above and below the fibre. Therefore work-hardening might have been decreased or eliminated during laser processing and the resulting HAZ. The hardness for nitrogen was found to be lower than for air samples but still higher than for original foils.

# Chapter 9.
# Conclusions

The objective of this body of research was to investigate the aid of laser manufactured channels and shoulders to protect and position high quantities of fibre during UC integration. The interdisciplinary context of combining laser processing and UC was a novel and unique approach on high quantity fibre embedding via UC which helped pushing UC further in the direction of smart material fabrication.

Research into single pass channel fabrication proved to be difficult in relation to the achievable penetration depth. It was concluded that the focused spot size of the laser was able to deliver enough intensity to the material, however it was not possible to couple sufficient heat into the aluminium sample due to high absorption and thermal conductivity as well as low powers. A different approach of multi-pass channel fabrication with higher powers circumvented high initiation powers for melting and led to the desired channel depths (≥ 70 µm) for further integration of SiC fibres with a diameter of 100 µm. The experimental investigations for channel width and depths demonstrated that different channel diameters can be achieved by variation of the laser power and traverse speed which facilitates future precise channel manufacturing for different fibre types such as optical fibres or SMA with varying diameters to enhance smart material research.

Multiple passes produced melt which was distributed in the form of shoulders at the channel borders and approximately 80 % of the melt was displaced. It was concluded that the assist gas pressure as well as the melt induced recoil pressure overcame the surface tension of the liquid metal and expelled the

melt. The shoulder material, due to the influence of air as the assist gas, consisted of aluminium and oxide. However, surface tension gradients led to one-sided shoulder build-up. The novel approach of utilising the produced melt rather than avoidance (Low et al., 2003) may, in combination with the formation of aluminium oxide, expand laser drilling operations in which surface corrosion resistance is needed. The fibre laser which was chosen due to the excellent focusing capabilities proved to be a successful tool for channel/shoulder manufacturing in the micrometre range. Excellent results were presented for narrow and controlled channel/shoulder production to embed high quantities of fibres.

The high heat input by multiple laser passes and the high thermal conductivity of aluminium produced a wide HAZ exhibiting a cellular/dendritic structure with alternating inter-cellular/inter-dendritic Mn-rich areas due to microsegregation. The intended purpose to use a highly focused beam to reduce the amount of heat dissipating into the material was not fulfilled. It was inferred that the avoidance of microstructural changes in the UC aluminium samples due to the material properties was not possible. Hardness investigations in the HAZ showed a higher hardness for the laser processed sample than for the original UC sample. Fibre embedding further contributed to a hardness increase which was supporting the results of Friel et al. (2010) and Li and Soar (2009a). Hence, the work hardening theory proposed by the two authors due to fibre embedding in UC was seconded. However, it has to be borne in mind that melting of the aluminium produced different preconditions for work hardening which makes the results difficult to compare.

The investigation of accurate positioning of fibres due to channels gave compelling evidence that channels aid the positioning of a high quantity of fibres (up to 10.5 %) by avoiding fibre entanglement. Especially channels which exhibited the desired channel depth for SiC fibre placement showed remarkable results with over 90 % of the fibres embedded for both directions. A drawback was that fractured fibres were observed in all samples. Fibre shattering was attributed to the hardness of the channel, the shoulder material and low channel

depths. It can be deduced that deeper channels provided a secure environment for fibres which will be of important knowledge for embedding of delicate fibres or components. The direction of fibre embedding has been researched for the first time in relation to fibre behaviour. It was shown that fibres parallel to the welding direction experienced higher distortions than fibres embedded perpendicular which was attributed to the dynamic forces induced during UC. Hence, for fibre embedding it is important to consider the embedding direction to achieve maximum plastic flow which seconds results by Yang et al. (2007). In addition, the influence of the dynamic forces on the embedded components needs to be taken into account.

The major objective of the dissertation to investigate the aid of the shoulders to decrease the amount of plastic deformation while embedding high quantities of fibres was challenging. 24 fibres were embedded; however the formation of bonding was unsuccessful as delamination of the upper foil was observed. This has been observed before by Li and Soar (2009a). Hence, channel and shoulder processing did not aid the plastic flow for bond formation. It was concluded that the oxides from the coating of the fibre in combination with the aluminium oxide of the shoulder inhibited sufficient bonding. Additionally, high quantity fibre embedding proved to be difficult as the UC sample only had a limited amount of space available which restricted the available space for intimate contact between upper and lower foil when embedding high quantities of fibres.

# Chapter 10.
# Recommendations on Further Work

Based on the research carried out in this thesis, several areas have been identified which would benefit from further investigation.

→ **Materials Research**

The research has shown that Al 3003-H18 is difficult to process with a laser due to the thermal conductivity and low coupling efficiency. UC has been proven to be a multi-material process. Hence, the investigation on different materials such as titanium which exhibits higher coupling efficiency could improve channel/shoulder formation via laser processing. Conversely, a softer material with regards to UC could facilitate plastic flow and thus deformation around the fibres.

→ **Further Assist Gas Investigation**

Research has shown that molten material could be deposited on the channel edges. Nitrogen proved to create channels/shoulders with less oxide concentration. As nitrogen is an inert gas, higher laser power for desirable channel/shoulder formation would be needed. Additionally, as nitrogen may form AlN by absence of $Al_2O_3$, argon could serve as a potential assist gas to avoid oxide formation.

→ **High Power Lasers**

As the coupling efficiency for Al 3003-H18 was not sufficient enough, higher power could be sufficient to induce melting. Fiber lasers operating at higher power ≥ 500 W could be used in CW mode to induce faster melting by obtaining

the same BPP. Faster melting would reduce the heat input into the material and limit the HAZ.

→ **Nozzle Placement**

Research into off-axially placed nozzles has shown to be able to control the melt direction. Side-gas could be favourable in terms of producing a shoulder on one side of the channel which has been shown to be favourable for plastic flow around the fibres for perpendicular direction during UC. It would also be worth investigating if one shoulder which due to the displacement of the melt to one side is higher enables better plastic flow.

→ **Deeper Channels**

Difficulties in shoulder formation via laser processing may be bypassed by producing deeper channels in which fibres can completely subside. Furthermore, the channels should be deep enough to allow higher edges of material which could be deformed during UC.

→ **Controlling of Channel Geometries**

Following chapter 5 in which channels with different width and depth were produced, investigation into controlled production of special channel geometries for different sizes of objects for embedding could be investigated. Here pulsed laser may be favourably. Controlled ablation could produce the required channel sizes for embedding different objects. However, as ablation is usually produced by vaporisation of the material, shoulders may not be producible anymore. Additionally, numerical modelling could be applied to predict different channel and shoulder shapes.

→ **Softening of HAZ**

When using an aluminium alloy for channel/shoulder processing, heat-treatable alloys have shown to soften within the HAZ. The softening mechanism could be used to facilitate fibre embedding as a softer material would need less effort to deform around the fibre which could reduce high UC amplitudes.

→ **Different Channel Layout**

The channel layout investigated allowed several fibres to be placed in a small area of the UC samples. At least for perpendicularly embedded fibres or fibres placed in an 45° angle towards the welding direction, large volume fractions of fibres could be embedded in channels which could have a wider distance between them. Wider space between the channels would allow a wider area for bonding between the upper and lower foil.

→ **Cladding/Skinning of Fibres**

Bonding between the foils was believed to be low due to the introduction of two different types of oxides – titanium diboride and $Al_2O_3$. As mechanical entrapment rather than chemical embedding was observed, it would seem possible to reduce the amount of oxides by skinning the SiC fibres or alternatively use a different coating which does not consist of ceramics for the fibres. This process might enhance bonding by reducing the oxide area.

→ **Automated Fibre-Laying System**

As shown in chapter 7, fibre placement was difficult before UC. A system which could easily position fibres in the required direction would aid the overall embedding process significantly. As industrial UC machines integrate an automated foil feeding system, they would also benefit from an automated fibre feeding system as well to further exploit fibre embedding.

→ **High-Wear Surfaces**

The hardness of the channel and HAZ might be used to create high-wear resistant surfaces which could provide a long lifetime or specific fluidic sliding surfaces for fluid dynamic structures. The need for wear resistant coatings and post-processing could be eliminated. In combination with the non-deformation of the foils into the channels during UC, internal structural high-wear resistant channels could be produced which would enable a different application for industrial use of UC.

→ **Utilisation of the shoulder material**

The shoulder material can be used to protect certain areas which are highly inclined to corrosion by adding the required amount of corrosion resistance. This has been performed in laser processing by alloying the surface (Li et al., 1996) but not by using the melt of an area to distribute the melt for corrosion.

# Bibliography

Ainslie, B.J., 1991. A review of the fabrication and properties of erbium-doped fibers for optical amplifiers. Journal of Lightwave Technology, 9(2), pp.220-227.

Alda, J., 2003. Laser and Gaussian beam propagation and transformation, Encyclopedia of Optical Engineering. Marcel Dekker: New York, pp.999-1013.

Allameh, S.M., Mercer, C., Popoola, D. and Soboyeyo, W.O., 2005. Microstructural characterization of ultrasonically welded aluminum. Journal of Engineering Materials and Technology, 127(1), pp.65-74.

Antonio, I., Lorenzo, P., Fabrizi, F. and Pappalardo, M., 2006. A high displacement ultrasonic actuator based on a flexural mechanical amplifier. Sensors & Actuators: A. Physical, 125(2), pp.118-123.

Arata, Y. and Miyamoto, I., 1997. Some fundamental properties of high power laser beam as a heat source (Report 2): $CO_2$ laser absorption characteristics of metal. Transactions of the Japan Welding Society, 3(1), pp.152-162.

Armon, E., Hill, M., Spalding, I.J. and Zvirin, Y., 1989. Metal drilling with a $CO_2$ laser beam. II. Analysis of aluminum drilling experiments. Journal of Applied Physics, 65(12), pp.5003-5006.

Armstrong, W.D., Lorentzen, T., Brøndsted, P. and Larsen, P.H., 1998. An experimental and modeling investigation of the external strain, internal stress and fiber phase transformation behavior of a NiTi actuated aluminum metal matrix composite. Acta Materialia, 46(10), pp.3455-3466.

Astashev, V.K. and Babitsky, V.I., 1998. Ultrasonic cutting as a nonlinear (vibro-impact) process, Ultrasonics, 36(1), pp.89-96.

ASM International, 1990. ASM Handbook Volume 2, Properties and selection: nonferrous alloys and special-purpose materials, 10th Edition, ASM International, Metals Park, Ohio.

ASM International, 1993, ASM Handbook Volume 6, Welding, Brazing and Soldering. 10th Edition, ASM International, Metals Park, Ohio.

Bachmann, F., 2003. Industrial applications of high power diode lasers in materials processing. Applied Surface Science, 208, pp.125-136.

Bai, Z.K., Wang, A.H. and Xie, C.S., 2006. Laser grooving of $Al_2O_3$ plate by a pulsed Nd:YAG laser: Characteristics and application to the manufacture of gas sensors array heater. Materials Science and Engineering A, 435, pp.418-424.

Balta, J.A., Bosia, F., Michaud, V., Dunkel, G., Botsis, J. and Månson, J.-A., 2005. Smart composites with embedded shape memory alloy actuators and fibre Bragg grating sensors: activation and control. Smart Material Structures, 14(4), pp.457–465.

Bannantine, J.A., Comer, J.J. and Handrock, J.L., 1990. Fundamentals of Metal Fatigue Analysis. Englewood Cliffs, New Jersey: Prentice Hall, p. 273.

Basu, S. and DebRoy, T., 1992. Liquid metal expulsion during laser irradiation. Journal of Applied Physics, 72(8), pp.3317-3322.

Basting, D., Pippert, K. and Stamm, U., 2002. History and future prospects of excimer laser technology. Riken Review, 43, pp.14-22.

Baziz, L., Nouiri, A. and Yousef, Y., 2006. Influence of a nanosecond pulsed laser on aluminium alloys: distribution of oxygen. Laser Physics, 16(12), pp.1643-1646.

Beck, Th., Reng, N. and Weber, H., 2000. Optical fibres for material processing lasers. Optics and Lasers in Engineering, 34(4), pp.255-272.

Bergström, D., 2005. The Absorptance of Metallic Alloys to Nd:YAG and Nd:YLF Laser Light. Licentiate Thesis, Lulea University.

Bergström, D., Powell, J. and Kaplan, A.F.H., 2007a. Absorptance of nonferrous alloys to Nd:YLF and Nd:YAG laser light at room temperature. Applied Optics, 46(8), pp.1290-1301.

Bergström, D., Powell, J. and Kaplan, A.F.H., 2007b. The absorptance of steels to Nd:YLF and Nd:YAG laser light at room temperature. Applied Surface Science, 253(11), pp.5017–5028.

Bertelli, F., Meza, E.S., Goulart, P.R., Cheung, N., Riva, R. and Garcia, A., 2011. Laser remelting of Al–1.5 wt% Fe alloy surfaces: Numerical and experimental analyses. Optics and Lasers in Engineering, 49(4), pp.490-497.

Beyer, E., Mahrle, A., Lütke, M., Standfuss, J. and Brückner, F., 2012. Innovation in high power fiber laser applications. In: Hornea, E.C., ed., Fiber Lasers IX: Technology, Systems, and Applications, Proc. of SPIE Vol. 8237, 21 January, 2012, San Francisco, USA, pp.823717-1-823717-11.

Byer, R.L., 1988. Diode Laser—Pumped Solid-State Lasers. Science, 239(4841), pp.742-747.

Birks, T.A., Knight, J.C. and Russell, P.S., 1997. Endlessly single-mode photonic crystal fiber. Optics Letters, 22(13), pp.961-963.

Blake, A. and Mazumder, J., 1985. Control of magnesium loss during laser welding of Al-5083 using a plasma suppression technique. Journal of Engineering for Industry, 107, pp.275-280.

Bouafia, M., Bencheikh, A., Bouamam, L. and Weber, H., 2004. $M^2$ quality factor as a key to mastering laser beam propagation. In: Wyrowski, F., ed., Photonics Europe. International Society for Optics and Photonics, pp.130-140.

Boller, C., 2000. Next generation structural health monitoring and its integration into aircraft design. International Journal of Systems Science, 31(11), pp.1333-1349.

Borowski, J. and Bartkowiak, K., 2010. Investigation of the influence of laser treatment parameters on the properties of the surface layer of aluminum alloys. Physics Procedia, 5, pp.449-456.

Brandes, E.A. and Brook, G.B., Eds., 1998. Smithells metals reference book. Butterworth-Heinemann: Oxford.

Brodyanski, A., Born, C. and Kopnarski, M., 2005. Nm-scale resolution studies of the bond interface between ultrasonically welded Al-alloys by an analytical TEM: a path to comprehend bonding phenomena. Applied Surface Science, 252(1), pp.94-97.

Byer, R.L., 1988. Diode laser-pumped solid-state lasers. Science, 239(4841), pp.742-747.

Cabrera, N. and Mott, N.F., 1949. Theory of the oxidation of metals. Reports on Progress in Physics, 12(1), pp.163-184.

Canning, J., 2006. Fibre lasers and related technologies. Optics and Lasers in Engineering, 44(7), pp.647-676.

Caristan, C.L., 2004. Laser cutting guide for machining. Society of Manufacturing Engineers: Dearborn, Michigan.

Carter, W.H., 1980. Spot size and divergence for Hermite Gaussian beams of any order. Applied optics, 19(7), pp.1027-9.

Chan, C.L. and Mazumder, J., 1987. One-dimensional steady-state model for damage by vaporization and liquid expulsion due to laser-material interaction. Journal of Applied Physics, 62(11), pp.4579-4586.

Chan, I., Mazumder, J. and Chen, M.M., 1988. Effect of surface tension gradient driven convection in a laser melt pool: three-dimensional perturbation model. Journal of Applied Physics, 64(11), pp.6166-6174.

Chan, D.K.L., 2011. Smart materials - embedding of fibres in aluminium. Unpublished Master's Thesis, Loughborough University, UK.

Chen, Y.F., Liao, T.S., Kao, C.F., Huang, T.M., Lin, K.H. and Wang, S.C., 1996. Optimization of fiber-coupled laser-diode end-pumped lasers: influence of pump-beam quality. IEEE Journal of Quantum Electronics, 32(11), pp.2010-2016.

Chen, X. and Wang, H.X., 2001. A calculation model for the evaporation recoil pressure in laser material processing. Journal of Physics D: Applied Physics, 34(17), pp.2637-2642.

Chen, K., Lawrence Yao, Y. and Modi, V., 2001. Gas dynamic effects on laser cut quality. Journal of Manufacturing Processes, 3(1), pp.38-49.

Chen, C.-L., Richter, A. and Thomson, R.C., 2009. Mechanical properties of intermetallic phases in multi-component Al–Si alloys using nanoindentation. Intermetallics, 2009, 17(8), pp.634-641.

Cheng, X. and Li, X., 2007. Investigation of heat generation in ultrasonic metal welding using micro sensor arrays. Journal of Micromechanics and Microengineering, 17(2), pp.273-282.

Cheng, X., Datta, A., Choi, H., Zhang, X. and Li, X., 2007. Study on embedding and integration of microsensors into metal structures for manufacturing applications. Journal of Manufacturing Science and Engineering, 129(2), pp.416-426.

Choi, W.C. and Chryssolouris, G., 1995. Analysis of the laser grooving and cutting processes. Journal of Physics D - Applied Physics, 28(5), pp.873–878.

Chong, T.C., Hong, M.H. and Shi, L.P., 2010. Laser precision engineering: from microfabrication to nanoprocessing. Laser & Photonics Reviews, 4(1), pp.123-143.

Chryssolouris, G., Bredt, J., Kordas, S. and Wilson, E., 1988a. Theoretical aspects of a laser machine tool. Journal of Engineering for Industry, 110(1), pp.65-70.

Chryssolouris, G., Sheng, P. and Choi, W.C., 1988b. Investigation of laser grooving for composite materials. CIRP Annals – Manufacturing Technology, 37(1), pp.161-164.

Chun, M.K. and Rose, K., 1970. Interaction of high-intensity laser beams with metals. Journal of Applied Physics, 41(2), pp.614-620.

Chung, D.L.L., 1998. Self-monitoring structural materials. Materials Science and Engineering R, 22(2), pp.57-78

Cieslak, M.J. and Fuerschbach, P.W., 1988. On the weldability, composition, and hardness of pulsed and continuous Nd: YAG laser welds in aluminum alloys 6061, 5456, and 5086. Metallurgical Transactions B, 19(2), pp.319-329.

Clyne, T.W. and Withers, P.J., 1993. An introduction to metal matrix composites. Cambridge University Press: Cambridge.

Daniels, H.P.C., 1965. Ultrasonic welding. Ultrasonics, 3(4), pp.190-196.

Dausinger, F., 2000. Laser welding of aluminum alloys: from fundamental investigation to industrial application. In: Chen, X., Fujioka, T. and Matsunawa, A., Eds. Proceedings of SPIE Vol. 3888, High-Power Lasers in Manufacturing, pp.367-379.

David, S.A. and Vitek, J.M., 1989. Correlation between solidification parameters and weld microstructures. International Materials Reviews, 34(1), pp.213-245.

David, S.A., Babu, S.S. and Vitek, J.M., 2003. Welding: solidification and microstructure. JOM, 55(6), pp.14-20.

Dawson, G.R., Winsper, C.E., Sansome, D.H., 1970. Application of high- and low-frequency oscillations to the plastic deformation of metals (2). Metal Forming, 37(9), pp. 254-261.

Dawson, J.W. et al., 2008. Analysis of the scalability of diffraction-limited fiber lasers and amplifiers to high average power. Optics Express, 16(17), pp.13240-13266.

Dehoff, R.R. and Babu, S.S., 2010. Characterization of interfacial microstructures in 3003 aluminum alloy blocks fabricated by ultrasonic additive manufacturing. Acta Materialia, 58(13), pp.4305-4315.

De Mol van Otterloo, J.L., Bagnoli, D. and De Hosson, J.T.M., 1995. Enhanced mechanical properties of laser treated Al-Cu alloys: A microstructural analysis. Acta Metallurgica et Materialia, 43(7), pp.2649-2656.

De Vries, E., 2004. Mechanics and mechanisms of ultrasonic metal welding. Ph. D. Ohio State University.

Dhupal, D., Doloi, B. and Bhattacharyya, B., 2008. Parametric analysis and optimization of Nd : YAG laser micro-grooving of aluminum titanate (Al2TiO5) ceramics. International Journal of Advanced Manufacturing Technology, 36(9-10), pp.883-893.

Diehl, R., 2000. High-power diode lasers: fundamentals, technology, applications. Springer: London, Berlin.

Domack, M.S. and Baughman, J.M., 2005. Development of nickel-titanium graded composition components. Rapid Prototyping Journal, 11(1), pp.41-51.

Dominic, V., MacCormack, S., Waarts, R., Sanders, S., Bicknese, S., Dohle, R., Wolak, E., Yeh, P.S. and Zucker, E., 1999. 110W fibre laser. Electronics Letters, 34(14), pp.1158-1160.

Doumanidis, C. and Gao, Y., 2004. Mechanical modeling of ultrasonic welding. Welding Journal, 83(4), pp.140s-146s.

Du, K., Biesenbach, J., Ehrlichmann, D., Habich, U., Jarosch, U., Klein, J., Loosen, P., Niehoff, J. and Wester, R., 1995. Lasers for materials processing: specifications and trends. Optical and Quantum Electronics, 27(12), pp.1089-1102.

Dubey, A.K. and Yadava, V., 2008. Laser beam machining – A review. International Journal of Machine Tools & Manufacture, 48(6), pp.609–628.

Dubourg, L., Pelletier, H., Vaissiere, D., Hlawka, F. and Cornet, A., 2002. Mechanical characterisation of laser surface alloyed aluminium–copper systems. Wear, 253(9), pp.1077-1085.

Duley, W.W., 1983. Laser processing and analysis of materials. Plenum Press: New York.

Eaves, A.E., Smith, A.W., Waterhourse, W.J., and Sansome, D.H., 1975. Review of the application of ultrasonic vibrations to deforming metals. Ultrasonics, 13(4), pp.162-170.

Edmonds, H.C. and Harris, R.A., 2011. The effect of electro-discharge machined sonotrode topology on interlaminar bonding in ultrasonic

consolidation. In: Ounaies, Z., Seelecke, S.S. (Eds.), Proceedings of SPIE 7978, Behavior and Mechanics of Multifunctional Materials and Composites, pp. 797814-1-797814-13.

Einstein, A., 1916. Emission and Absorption of Radiation in Quantum Theory. Deutsche Physikalische Gesellschaft.Verhandlungen, 18, pp.318-323.

Einstein, A., 1917. On the Quantum Theory of Radiation. Physikalische Zeitschrift, 18, pp.121-128.

Endriz, J.G., Vakili, M., Browder, G.S., Devito, M., Haden, J.M., Harnagel, G.L. and Yao, H.C., 1992. High power diode laser arrays. IEEE Journal of Quantum Electronics, 28(4), pp.952-965.

Ewing, J.J., 2000. Excimer laser technology development. IEEE Journal of Selected Topics in Quantum Electronics, 6(6), pp.1061-1071.

Faerber, M., 1995. Gases for increased productivity of laser processing. Optical and Quantum Electronics, 27(12), pp.1449-1455.

Falk, J., 1983. Measurement of laser beam divergence. Applied optics, 22(8), pp.1131-1132.

Fan, T.Y. and Byer, R.L., 1988. Diode laser-pumped solid-state lasers. IEEE Journal of Quantum Electronics, 24(6), pp.895-912.

Fan, T.Y., 1990. Diode-Pumped Solid State Lasers. Lincoln Laboratory Journal, 3(3), pp.413-425.

Farooq, K. and Kar, A., 1999. Effects of laser mode and scanning direction on melt pool shape. Journal of Applied Physics, 85(9), pp.6415-6420.

Fenoughty, K.A., Jawaid, A. and Pashby, I.R, 1994. Machining of advanced engineering materials using traditional and laser techniques. Journal of Materials Processing Technology, 42(4), pp.391-400.

Fink, W.L., 1949. Physical metallurgy of aluminium alloys. American Society for Metals: Cleveland, Ohio.

Flatau, A.B. and Chong, K.P., 2002. Dynamic smart material and structural systems. Engineering Structures, 24(3), pp.261-270.

Franke, V., Klotzbach, U., Panzner, M., and Püschel, R.. 2007. Potentials of fiber laser technology in microfabrication. In: Pfleging, W., Lu, Y., Washio, K., Bachmann F.G., and Hoving, W., eds. Proc. of SPIE Vol. 6459, Laser-based Micro- and Nanopackaging and Assembly, pp.64590J-1-64590J-10.

Friel, R.J. and Harris, R.A., 2010. A nanometre-scale fibre-to-matrix interface characterization of an ultrasonically consolidated metal matrix composite. Proceedings of the Institution of Mechanical Engineers, Part L: Journal of Materials Design and Applications, 224(1), pp.31-40.

Friel, R. J., Johnson, K. E., Dickens, P. M. and Harris, R. A., 2010. The effect of interface topography for Ultrasonic Consolidation of aluminium. Materials Science and Engineering A, 527(16), pp.4474-4483.

Friel, R.J., 2011. Investigating the effect of ultrasonic consolidation on shape memory alloy fibres. Ph.D. Loughborough University.

Friel, R.J. and Harris, R.A., 2013. Ultrasonic additive manufacturing–a hybrid production process for novel functional products. Procedia CIRP, 6, pp.35-40.

Fujii, H.T., Sriraman, M.R. and Babu, S.S., 2011. Quantitative evaluation of bulk and interface microstructures in Al-3003 alloy builds made by very high power ultrasonic additive manufacturing. Metallurgical and Materials Transactions A, 42(13), pp.4045-4055.

Gabzdyl, J. and Brodsky, M., 2010. Micro-cutting with nanosecond pulsed fiber lasers. ICALEO, 29th International Congress on Applications of Lasers & Electro-Optics Conference Proceedings, p. M901.

Galea, S.C. and Baker, A.A., 2001. Smart structures approaches for health monitoring of aircraft structures. In: Sood, D.K., Lawes, R.A. and Varadan, V.V., eds. Proc. SPIE 4235, Smart Structures and Devices, 340, 13 December 2000, Melbourne, Australia, pp.340-354.

Ganesh, R.K., Bowley, W.W., Bellantone, R.R. and Hahn, Y., 1996. A model for laser hole drilling in metals. Journal of Computational Physics, 125(1), pp.161-176.

Gao, Y. and Doumanidis, C., 2002. Mechanical analysis of ultrasonic bonding for rapid prototyping. Journal of Manufacturing Science and Engineering, 124(2), pp.426-435.

Geiger, M., 1994. Synergy of Laser Material Processing and Metal Forming. CIRP Annals - Manufacturing Technology, 43(2), pp.563-570.

George, J. and Stucker, B., 2006. Fabrication of lightweight structural panels through ultrasonic consolidation. Visual and Physical Prototyping, 1(4), pp.227-241.

Gibson, I., Rosen, D.W. and Stucker, B., 2010. Additive manufacturing technologies: rapid prototyping to direct digital manufacturing. Springer: New York, London.

Giesen, A., Hiige, H., Voss, A., Wittig, K., Brauch, U. and Opower, H., 1994. Scalable concept for diode-pumped high-power solid-state lasers. Applied Physics B, 58(5), pp.365-372.

Gillner, A., Holtkamp, J., Hartmann, C., Olowinsky, A., Gedicke, J., Klages, K., Lüdger, B. and Beyer, A., 2005. Laser applications in microtechnology. Journal of Materials Processing Technology, 167(2), pp.494–498.

Gower, M.C., 2000. Industrial applications of laser micromachining. Optics Express, 7(2), pp.56-67.

Graff, K. F., Short, M. and Norfolk, M., 2010. Very high power ultrasonic additive manufacturing (VHP UAM) for advanced materials. In: Proceedings of the 21st Solid Freeform Fabrication Symposium, Austin, Texas, USA, pp.82-89.

Gunduz, I. E., Ando, T., Shattuck, E., Wong, P.Y., and Doumanidis, C. C., 2005. Enhanced diffusion and phase transformations during ultrasonic welding of zinc and aluminum. Scripta Materialia, 52(9), pp.939-943.

Grudinin, A.B., Payne, D.N., Turner, P.W., Nilsson, L.J.A., Zervas, M.N., Ibsen, M., Durkin, M.K., University of Southampton. 2004. Multi-fibre arrangements for high power fibre lasers and amplifiers. United States Patent 6826335.

Haboudou, A., Peyre, P., Vannes, A.B. and Peix, G., 2003. Reduction of porosity content generated during Nd: YAG laser welding of A356 and AA5083 aluminium alloys. Materials Science and Engineering: A, 363(1), pp.40-52.

Hahnlen, R., Dapino, M.J., Short, M. and Graff, K., 2009. Aluminum-matrix composites with embedded Ni-Ti wires by ultrasonic consolidation. In: Henderson, B.K. and McMickell, M.B., eds. Industrial and Commercial Applications of Smart Structures Technologies: Proc. of SPIE 7290, 8-12 March 2009, San Diego, USA., pp.729009-1-729009-12.

Hahnlen, R. and Dapino, M.J., 2010. Active Metal-matrix Composites with Embedded Smart Materials by Ultrasonic Additive Manufacturing. In: McMickell, M.B. and Farinholt, K.M., eds. Industrial and Commercial Applications of Smart Structures Technologies: Proc. of SPIE Vol. 7645, pp.76450O-1- 76450O-12.

Halbwax, M., Sarnet, T., Delaporte, Ph., Sentis, M., Etienne, H., Torregrosa, F., Vervisch, V., Perichaud, I. and Martinuzzi, S., 2008. Micro and nano-structuration of silicon by femtosecond laser: Application to silicon photovoltaic cells fabrication. Thin Solid Films, 516(20), pp.6791-6795.

Hamada, K., Lee, J.H., Mizuuchi, K., Taya, M. and Inoue, K., 1998. Thermomechanical behavior of TiNi shape memory alloy fiber reinforced 6061 aluminum matrix composite. Metallurgical and Materials Transactions A, 29(13), pp.1127-1135.

Hand, D.P., Su, D., Naeem, M. and Jones, J.D.C., 1996. Fiber optic high-quality Nd:YAG beam delivery for materials processing. Optical Engineering, 35(2), pp.502-506.

Han, L. and Liou, F.W., 2004. Numerical investigation of the influence of laser beam mode on melt pool. International Journal of Heat and Mass Transfer, 47(19), pp.4385–4402.

Hanna D. C., Percival, R.M., Perry, I.R., Smart, R.G., Suni, P.J., Townsend, J.E. and Tropper, A.C., 1988. Continuous-wave oscillation of a monomode ytterbium-doped fibre laser. Electronics Letters 24(17), pp.1111-1113.

Hanna D. C., Percival, R.M., Perry, I.R., Smart, R.G., Suni, P.J. and Tropper, A.C., 1990. An Ytterbium-doped Monomode Fibre Laser: Broadly Tunable Operation from 1.010 μm to 1.162 μm and Three-level Operation at 974 Nm, Journal of Modern Optics, 37(4), pp.517-525.

Hansen, K.P. et al., 2011. Airclad fiber laser technology. Optical Engineering, 50(11), pp.111609-111609.

Hansson, I. and Thoelen, A., 1975. Plasticity due to superimposed macrosonic and static strains. Ultrasonics, 16(2), pp.57-64.

Harman, G., & Albers, J. (1977). The ultrasonic welding mechanism as applied to aluminum-and gold-wire bonding in microelectronics. IEEE Transactions on Parts, Hybrids, and Packaging, 13(4), pp. 406-412.

Hartl, D.J. and Lagoudas, D.C., 2007. Aerospace applications of shape memory alloys. Proceedings of the Institution of Mechanical Engineers, Part G: Journal of Aerospace Engineering, 221(4), pp.535-552.

Hausken, T., 2012. A Record-Breaking year for Lasers. Laser Technik Journal, 3, pp.20-21.

Hecht, J., 2002. Understanding Fiber Optics. 4th ed. Prentice Hall: Upper Saddle River, NJ.

Hecht, J., 2008. Understanding lasers: an entry-level guide. 3rd ed. IEEE Press: New York.

Hecht, J., 2010. Short history of laser development. Optical Engineering, 49(9), pp.091002-1-091002-23.

Hegge, H.J. and De Hosson, J.Th.M., 1990.Solidification structures during laser treatment. Scripta Metallurgica et Materiala, 24(3), pp.593-598.

Hirose, A., Kobayashi, K.F. and Todaka, H., 1997. $CO_2$ laser beam welding of 6061-T6 aluminum alloy thin plate. Metallurgical and Materials transactions A, 28(12), pp.2657-2662.

Quantitative evaluation of softened regions in weld heat-affected zones of 6061-T6 aluminum alloy—Characterizing of the laser beam welding process

Hirose, A., Kurosawa, N., Kobayashi, K., Todaka, H. and Yamaoka, H., 1999. Metallurgical and Materials Transactions A, 30(8), pp.2115-2120.

Hitz, C., 1989. Understanding laser technology: an intuitive introduction to basic and advanced laser concepts, 2nd ed. PennWell Books: Tulsa.

Hocheng, H. and Pan, C.T., 1999; The effects of cryogenic surroundings on thermal-induced damage in laser grooving of fiber-reinforced plastic. Machining Science And Technology, 3(1), pp.77-90.

Hodgson, N. and Weber, H., 1993. Influence of spherical aberration of the active medium on the performance of Nd:YAG lasers. IEEE Journal of Quantum Electronics, 29(9), pp.2497-2507.

Hopkins, C.D., Dapino, M.J. and Fernandez, S.A., 2010. Statistical characterization of ultrasonic additive manufacturing Ti/Al composites. Journal of Engineering Materials and Technology, 132(4), pp.041006-1-041006-9.

Hopkins, C.D., Wolcott, P.J., Dapino, M.J., Truog, A.G., Babu, S.S. and Fernandez, S.A., 2012. Optimizing ultrasonic additive manufactured Al 3003 properties with statistical modeling. Journal of Engineering Materials and Technology, 134(1), pp.011004-1-011004-10.

Hopkinson, N., Hague, R. and Dickens, P., eds., 2006. Rapid manufacturing an industrial revolution for the digital age. John Wiley & Sohns, Ltd.: Chichester.

Hoult, T., Ingram, S. and Jannssen, A., 2006. Addressing challenging micro-processing applications and materials with fiber lasers. In: Brown, A.J.W., Nilsson, J., Harter, D.J. and Tünnermann, A., eds., Proc. of SPIE Vol. 6102, Fiber Lasers III: Technology, Systems, and Applications, pp.610202-1-610202-7.

Horley. R., Norman, S. and Zervas, M.N., 2007. Progress and development in fibre laser technology. In: Titterton, D.H. and Richardson, M.A., eds. Proceedings of SPIE 6738, pp.6738K-1 – 6738K-10.

Hügel, H., 2000. New solid-state lasers and their application potentials. Optics and Lasers in Engineering, 34(4), pp.213-229.

Hulst, A.P., 1972. Macrosonics in industry 2. Ultrasonic welding of metals, Ultrasonics, 10(6), pp.252-261.

Humphreys, F.J. and Hatherley, M., 2004. Recrystallization and related annealing phenomena. 2nd ed. Pergamon Press: Oxford.

Huntington, C. and Eagar, T. W., 1983. Laser welding of aluminum and aluminum alloys. Welding Journal, 62(4), pp.105s-107s.

Hurlebaus, S. and Gaul, L., 2006. Review Smart structure dynamics. Mechanical Systems and Signal Processing, 20(2), pp.255–281.

Incropera, F.P. and DeWitt, D.P., 2002. Fundamentals of heat and mass transfer. 5th ed. John Wiley & Sons: New York.

Ion, J.C., 2005. Laser processing of engineering materials: principles, procedure and industrial application. Elsevier Butterworth-Heinemann: Oxford.

Iula, A., Parenti, L., Fabrizi, F. and Pappalardo, M., 2006. A high displacement ultrasonic actuator based on a flexural mechanical amplifier. Sensors & Actuators: A. Physical, 125(2), pp.118-123.

Ivarson, A., Powell, J. and Magnusson, C., 1991. The role of oxidation in laser cutting stainless and mild steel. Journal of Laser Applications, 3(3), pp.41-45.

Izumi, O., Oyama, K. and Suzuki, Y., 1966. Effects of superimposed ultrasonic vibration on compressive deformation of metals. Transactions of the Japan Institute of Metals, 7(3), pp.162-167.

Janaki Ram, G.D., Yang, Y., George, J., Robinson, C. and Stucker, B., 2006a. Improving linear weld density in ultrasonically consolidated parts. In: Proceedings of the 17th Solid Freeform Fabrication Symposium. WH Freeman, pp. 692-708.

Janaki Ram, G.D., Yang, Y. and Stucker, B.E., 2006b. Effect of process parameters on bond formation during ultrasonic consolidation of aluminium alloy 3003. Journal of Manufacturing Systems, 25(3), pp.221-238.

Janaki Ram, G.D., Robinson, C., Yang, Y. and Stucker, B.E., 2007a. Use of ultrasonic consolidation for fabrication of multi-material structures. Rapid Prototyping Journal, 13(4), pp.226-235.

Janaki Ram, G. D., Yang, Y., Nylander, C., Aydelotte, B., Stucker, B. E. and Adams, B. L., 2007b. Interface microstructures and bond formation in ultrasonic consolidation. In: Proceedings of the 18th Solid Freeform Fabrication Symposium, Austin, Texas, USA, PWS-Kent, pp.266-283.

Johnson, K., Higginson, R., Dickens, P., West, G., Gupta, A. and White, D., 2007. Formation of nano-grains during biaxial high frequency fully reversed loading. In: Proceedings of the Materials Science and Technology, Detroit, 2007. Warrendale: Association for Iron and Steel Technology, pp.2618-2629.

Johnson, K.E., 2008. Interlaminar subgrain refinement in ultrasonic consolidation. Ph.D. Loughborough University.

Johnson, K., 2009. Ultrasonic Consolidation – A viable Method of Smart Structure Manufacture. 4th International Conference on Rapid Manufacturing, Loughborough, UK, 8-9 July.

Johnson, K., Edmonds, H.C., Higginson, R.L. and Harris, R.A., 2011. New discoveries in ultrasonic consolidation nano-structures using emerging analysis techniques. Proceedings of the Institution of Mechanical Engineers, Part L: Journal of Materials Design and Applications, 225(4), pp.277-287.

Jones, J.B. and Powers, J.J., 1956. Ultrasonic welding. Welding Journal, 35(8), pp.761-766.

Jordon, J.B., Horstemeyer, M.F., Solanki, K. and Xue, Y., 2007. Damage and stress state influence on the Bauschinger effect in aluminum alloys. Mechanics of Materials, 39(10), pp.920-931.

Joshi, K.C., 1971. The formation of ultrasonic bonds between metals. Welding Journal, 50(12), pp.840-848.

Juarez Islas, J.A., Jones, H. and Kurz, W., 1988. Effect of solidification front velocity on the characteristics of aluminium-rich Al-Mn alloy solutions extended by rapid solidification. Materials Science and Engineering, 98, pp.201-205.

Junger, J. and Schmidt, K., 2007. Excimer Lasers–Reliability and Higher Power Area Key Product Trends. Laser Technik Journal, 4(3), pp.31-33.

Kainer, K.U. ed., 2006. Metal Matrix Composites. Wiley-VCH: Weinheim, Germany.

Kalita, S.J., 2011. Microstructure and corrosion properties of diode laser melted friction stir weld of aluminum alloy 2024 T351. Applied Surface Science, 257(9), pp.3985-3997.

Kam, D.H. and Mazumder, J., 2008. Three-dimensional biomimetic microchannel network by laser direct writing. Journal Of Laser Applications, 20(3), pp.185-191.

Kamimuki, K., Inoue, T., Yasuda, K., Muro, M., Nakabayashi, T. and Matsunawa, A., 2002. Prevention of welding defect by side gas flow and its monitoring method in continuous wave Nd:YAG laser welding. Journal of Laser Applications, 14(3), pp.136-145.

Kantor, A., Scott, J.E. and Latham, W.P., 1996. Effects of mode structure on three-dimensional laser heating due to single or multiple rectangular laser beams. Journal of Applied Physics, 80(2), pp.667-674.

Kao, K.C. and Hockham, G.A., 1966. Dielectric-fibre surface waveguides for optical frequencies. Proceedings of the Institution of Electrical Engineers, 113(7), pp.1151-1158.

Kaplan, A.F.H., 2011. Analysis and modeling of a high-power Yb:fiber laser beam profile. Optical Engineering, 50(5), pp.054201-1- 054201-6.

Kar, A. and Mazumder, J., 1990. Two-dimensional model for material damage due to melting and vaporization during laser irradiation. Journal of Applied Physics, 68, pp.3884-3891.

Kar, A., Rockstroh, T. and Mazumder, J., 1992. Two-dimensional model for laser-induced materials damage: Effects of assist gas and multiple reflections inside the cavity. Journal of Applied Physics, 71(6), pp.2560-2569.

Kawahito, Y., Matsumoto, N., Abe, Y. and Katayama, S., 2012. Laser absorption of aluminium alloy in high brightness and high power fibre laser welding. Welding International, 26(4), pp.275-281.

Kearns, W.H., ed., 1980. Welding Handbook Vol.3, Resistance and solid-state welding and other joining processes, 7th ed. American Welding Society: Miami.

Khaleeq-ur-Rahman, M., Butt, M.Z., Samuel, A. and Siraj, K., 2010. Investigation of laser irradiation effects on the hardness of Al 5086 alloy under different conditions. Vacuum, 85(3), pp.474-479.

Killi, A., Zawischa, I., Sutter, D., Kleinbauer, J., Schad, S., Neuhaus, Jörg, and Schmitz, C., 2008. Current status and development trends of disk laser. In: Clarkson, W.A., Hodgson, N, and Shori, R.K., eds., Technology Solid State Lasers XVII: Technology and Devices, Proc. of SPIE Vol. 6871, pp. 68710L-1 68710L-10.

Kleine, K.F., Whitney, B. and Watkins, K.G., 2002. Use of Fiber Lasers for Micro Cutting Applications in the Medical Device Industry. In: Proceedings of the 21st International Congress on Applications of Laser and Electro-Optics (ICALEO ’02).

Kliner, D.A.V., et al., 2011. 4-kW fiber laser for metal cutting and welding. In: Dawson, J.W. and Honea, E.C., eds., Fiber Lasers VIII: Technology, Systems, and Applications, Proceedings of SPIE Vol. 7914, San Francisco, USA, January 22, pp.79148-1 -79148-8.

Knight, J.C., 2003. Photonic crystal fibres. Nature, 424(6950), pp.847-851.

Koester, C.J., Snitzer, E., 1964. Amplification in a Fiber Laser. Applied Optics, 3(10), pp.1182-1186.

Koester, C., 1966. 9A4-Laser action by enhanced total internal reflection. IEEE Journal of Quantum Electronics, 2(9), pp.580-584.

Körner, C., Mayerhofer, R., Hartmann, M. and Bergmann, H., 1996. Physical and material aspects in using visible laser pulses of nanosecond duration for ablation. Applied Physics A, 63(2), pp.123-131.

Kogelnik, H. and Li, T., 1966. Laser beams and resonators. Proceedings of the IEEE, 54(10), pp.1312-1329.

Kong, C.Y., Soar, R.C. and Dickens, P.M., 2003. Characterisation of aluminium alloy 6061 for the ultrasonic consolidation process. Materials Science and Engineering A, 363(1), pp.99-106.

Kong, C.Y., Soar, R.C. and Dickens, P.M., 2004a. Optimum process parameters for ultrasonic consolidation of 3003 aluminium. Journal of Materials Processing Technology, 146(2), pp.181-187.

Kong, C.Y., Soar, R.C. and Dickens, P.M., 2004b. Ultrasonic consolidation for embedding SMA fibres within aluminium matrices. Composite Structures, 66(1-4), pp.421-427.

Kong, C.Y., 2005. Investigation of ultrasonic consolidation for embedding active/passive fibres in aluminium matrices. Ph.D. Loughborough University.

Kong, C.Y. and Soar, R.C., 2005a. Method for embedding optical fibers in an aluminium matrix by ultrasonic consolidation. Applied Optics, 44(30), pp. 6325-6333.

Kong, C.Y. and Soar, R.C., 2005b. Fabrication of metal–matrix composites and adaptive composites using ultrasonic consolidation process. Materials Science and Engineering A, 412(1), pp.12–18.

Kong, C.Y., Soar, R.C. and Dickens, P.M., 2005. A model for weld strength in ultrasonically consolidated components. Proceedings of the Institution of Mechanical Engeneers, Part C: Journal of Mechanical Engineering Science, 219(1), pp.83-91.

Koplow, J.P., Kliner, D.A. and Goldberg, L., 2000. Single-mode operation of a coiled multimode fiber amplifier. Optics Letters, 25(7), pp.442-444.

Kou, S. 2002. Welding metallurgy. 2nd ed. John Wiley & Sons, Inc.: Hoboken, New Jersey.

Kratky, A., Schuöcker, D., and Liedl, G., 2008. Processing with kW fibre lasers: advantages and limits. In: XVII International Symposium on Gas Flow and

Chemical Lasers and High Power Lasers. International Society for Optics and Photonics, pp.71311X-71311X.

Kruth, J.-P., Leu, M.C and Nakagawa, T., 1998. Progress in additive manufacturing and rapid prototyping. CIRP Annals - Manufacturing Technology, 47(2), pp.525-540.

Kudesia, S.S., Solana, P., Rodden, W.S.O., Hand, D.P, and Jones, J.D.C., 2002. Appropriate regimes of laser drilling models containing melt eject mechanisms. Journal of Laser Applications, 14(3), pp.159-164.

Kulakov, M. and Rack, H.J., 2009. Control of 3003-H18 aluminum ultrasonic consolidation. Journal of Engineering Materials and Technology, 2009, 131(2), pp.021006-1-021006-6.

Kulakov, M. and Rack, H.J., 2010. Surface damage during ultrasonic consolidation of 3003-H18 aluminum. Rapid Prototyping Journal, 16(1), pp.12-19.

Kumar, S., 2010. Development of functionally graded materials by ultrasonic consolidation. CIRP Journal of Manufacturing Science and Technology, 3(1), pp.85-87.

Kumar, A. and Gupta, M.C., 2010. Laser machining of micro-notches for fatigue life. Optics and Lasers in Engineering, 48(6), pp.690-697.

Kurkov, A.S., 2007. Oscillation spectral range of Yb-doped fiber lasers. Laser Physics Letters, 4(2), pp.93-102.

Kurz, W. and Trivedi, R., 1994. Rapid solidification processing and microstructure formation. Materials Science and Engineering: A, 179, pp.46-51.

Kurz, W. and Fisher, D.J., 1998. Fundamentals of solidification. 4th ed. Trans Tech Publications: Aedersmannsdorf.

Kwon, H., Baek, W.K., Kim, M.S., Shin, W.S. and Yoh, J.J., 2012. Temperature-dependent absorptance of painted aluminum, stainless steel 304, and titanium for 1.07 μm and 10.6 μm laser beams. Optics and Lasers in Engineering, 50(2), pp.114-121.

Lallemand, G., Jacrot, G., Cicala, E. and Grevey, D.F., 2000. Grooving by Nd:YAG laser treatment. Journal of Materials Processing Technology, 99(1), pp.32-37.

Langenecker, B., 1966. Effects of ultrasound on deformation characteristics of metals. IEEE Transactions on Sonics and Ultrasonics, 13(1), pp.1-8.

Leech, P.W., 1989. The laser surface melting of aluminum-silicon-based alloys. Thin Solid Films, 177(1), pp.133-140.

Levy, G.N., Schindel, R. and Kruth, J.P., 2003. Rapid manufacturing and rapid tooling with layer manufacturing (LM) technologies, state of the art and future perspectives. CIRP Annals-Manufacturing Technology, 52(2), pp.589-609.

Levy, G.N., 2010. The role and future of the laser technology in the additive manufacturing environment, Physics Procedia, Part A, 5, pp.65-80.

Li, L., 2000. The advances and characteristics of high-power diode laser materials processing. Optics and Lasers in Engineering, 34(4), pp.231-253.

Li, X and Prinz, F., 2003. Embedded Fiber Bragg Grating Sensors in Polymer Structures Fabricated by Layered Manufacturing. Journal of Manufacturing Processes, 5(1), pp.78-86.

Li, R., Ferreira, M.G.S., Almeida, A., Vilar, R., Watkins, K.G., McMahon, M.A. and Steen, W.M., 1996. Localized corrosion of laser surface melted 2024-T351 aluminium alloy. Surface & Coatings Technology, 81(2), pp.290-296.

Li, D. and Soar, R., 2007. Optimum process parameters and influencing factors for embedding SiC fibres in Al 6061 O matrix through ultrasonic consolidation. In: Materials Science and Technology, Association for Iron and Steel Technology, pp. 3048-3064.

Li, D. and Soar, R.C., 2008. Plastic Flow and work hardening of Al alloy matrices during ultrasonic consolidation fibre embedding process. Materials Science and Engineering A, 498(1), pp.421-429.

Li, D. and Soar, R.C., 2009a. Characterization of process for embedding SiC fibres in Al 6061 O matrix through ultrasonic consolidation. Journal of Engineering Materials and Technology, 131(2), pp.021016-1-021016-5.

Li, D. and Soar, R., 2009b. Influence of sonotrode texture on the performance of an ultrasonic consolidation machine and the interfacial bond strength. Journal of Materials Processing Technology, 209(4), pp.1627-1634.

Limpert, J. Schreiber, T. Clausnitzer, T. Zöllner, K. Fuchs, H. Kley, E. Zellmer, H. and Tünnermann, A., 2002. High-power femtosecond Yb-doped fiber amplifier. Optics Express, 10(14), pp.628-38.

Limpert, J., Liem, A., Zellmer, H. and Tünnermann, A., 2003. 500 W continuous-wave fibre laser with excellent beam quality. Electronics Letters, 39(8), pp.645-647.

Limpert, J. et al., 2006. Extended single-mode photonic crystal fiber lasers. Optics Express, 14(7), pp.2715-20.

Limpert, J., Röser, F., Klingebiel, S., Schreiber, T., Wirth, C., Peschel, T., Eberhardt, R. and Tünnermann, A., 2007. The Rising Power of Fiber Lasers and Amplifiers. IEEE Journal of Selected Topics in Quantum Electronics, 13(3), pp.537-545.

Limpert, J. et al., 2009. High Repetition Rate Gigawatt Peak Power Fiber Laser Systems: Challenges, Design, and Experiment. IEEE Journal of Selected Topics in Quantum Electronics, 15(1), pp.159-169.

Lindroos, V.K. and Talvitie, M.J., 1995. Recent advances in metal matrix composites. Journal of Materials Processing Technology, 53(1), pp.273-284.

Liu, Z., Chong, P.H., Butt, A.N., Skeldon, P. and Thompson, G.E., 2005. Corrosion mechanism of laser-melted AA 2014 and AA 2024 alloys. Applied Surface Science, 247(1), pp.294-299.

Low, D.K.Y, Li, L. and Corfe, A.G., 2000a. The influence of assist gas on the mechanism of material ejection and removal during laser percussion drilling. Proceedings of the Institution of Mechanical Engineers, Part B: Journal of Engineering Manufacture, 214(7), pp.521-527.

Low, D.K.Y., Li, L. and Corfe, A.G., 2000b. Effects of assist gas on the physical characteristics of spatter during laser percussion drilling of NIMONIC 263 alloy. Applied Surface Science, 154, pp.689-695.

Low D.K.Y. and Li, L., 2001. An investigation into melt flow dynamics during repetitive pulsed laser drilling of transparent media. Optics and Laser Technology, 33(7), pp.515-522.

Low, D.K.Y, Li, L., Corfe, A.G. and Byrd, P.J., 2001. Spatter-free laser percussion drilling of closely spaced array holes. International Journal of Machine Tools and Manufacture, 41(3), pp.361-377.

Low, D.K.Y., Li, L. and Byrd, P.J., 2002. Hydrodynamic physical modeling of laser drilling. Journal of Manufacturing Science and Engineering, 124(4), pp.852-862.

Low, D.K.Y., Li, L., Byrd, P.J., 2003. Spatter prevention during the laser drilling of selected aerospace materials. Journal of Materials Processing Technology, 139(1), pp.71-76.

Lucca, D.A., Hermann, K. and Klopfstein, M.J., 2010. Nanoindentation: measuring methods and applications. CIRP Annals - Manufacturing Technology, 59(2), pp.803-819.

Luijendijk, T., 2000. Welding of dissimilar aluminium alloys. Journal of Materials Processing Technology, 103(1), pp.29-35.

Mai, C.-C. and Lin, J., 2003. Supersonic flow characteristics in laser grooving. Optics and Laser Technology, 35(8), pp.597-604.

Mai, C.-C. and Lin, J., 2006. An investigation of the surface contours in laser grooving. The International Journal of Advanced Manufacturing Technology, 28(1), pp.76–81.

Maiman, T.H., 1960. Stimulated Optical Radiation in Ruby. Nature, 187, pp. 493-494.

Mariani, E. and Ghassemieh, E., 2010. Microstructure evolution of 6061 O Al alloy during ultrasonic consolidation: an insight from electron backscatter diffraction. Acta Materialia, 58(7), pp.2492-2503.

Matsuoka, S., 1994. Ultrasonic welding of ceramic/metal. Journal of Materials Processing Technology, 47(1), pp.185-196.

Matsuoka, S. and Imai, H., 2009. Direct welding of different metals used ultrasonic vibration. Journal of Materials Processing Technology, 209(2), pp.954-960.

Mayer, A., 2012. Laser materials processing market reaches record high. Advanced Optical Technologies, 1(5), pp.345–348.

McCafferty, E., Shafrin, E.G. and McKay, J.A., 1981. Microstructural and surface modification of an aluminum alloy by rapid solidification with a pulsed laser. Surface Technology, 14(3), pp.219-223.

McNally, C.A., Folkes, J. and Pashby, I.R., 2004. Laser drilling of cooling holes in aeroengines: state of the art and future challenges. Materials Science and Technology, 20(7), pp.805-813.

Meijer, J. 2004. Laser beam machining (LBM), state of the art and new opportunities. Journal of Materials Processing Technologies, 149(1), pp.2-17.

Meyer, B., Tempus, G., Doyen, H., Emanowski, D., Hirsch, T. and Mayr, P., 2000. Dispersoid-free zones in the heat-affected zone of aluminum alloy welds.

Metallurgical and Materials Transactions A, 31(5), pp.1453-1459.

Mills, K., 1985. Metals Handbook Vol.9, Metallography and microstructures, 9th ed. American Society for Metals: Metals Park, Ohio.

Mohanty, P. and Mazumder, J., 1998. Solidification behavior and microstructural evolution during laser beam-material interaction. Metallurgical and Materials Transactions B, 29(6), pp.1269-1279.

Mondolfo L.F., 1976. Aluminium alloys: structure and properties, Butterworth: London.

Moon, D.W. and Metzbower, E.A., 1983. Laser beam welding of aluminum alloy 5456. Welding Journal, 62(2), pp.53s-58s.

Mou, C., Saffari, P., Li, D., Zhou, K., Zhang, L., Soar, R. and Bennion, I., 2008. Embedded fibre Bragg grating array sensors in aluminium alloy matrix by ultrasonic consolidation. In: 19th International Conference on Optical Fibre Sensors. International Society for Optics and Photonics, pp.70044B-70044B.

Mou, C., Saffari, P., Li, D., Zhou, K., Zhang, L., Soar, R. and Bennion, I., 2009. Smart structure sensors based on embedded fibre Bragg grating arrays in aluminium alloy matrix by ultrasonic consolidation. Measurement Science and Technology, 20, pp. 034013-034018.

Müller, H.-R., Kirchhof, J., Reichel, V. and Unger S., 2006. Fibers for high-power lasers and amplifiers. Comptes Rendus – Physique, 7(2), pp.154–162.

Nair, S.V., Tien, J.K. and Bates, R.C., 1985. SiC-reinforced aluminium metal matrix composites. International Metals Reviews, 30(1), pp.275-290.

Nakamura, T. and Suresh, S., 1993. Effects of thermal residual stresses and fiber packing on deformation of metal-matrix composites. Acta Metallurgica et Materialia, 41(6), pp.1665-1681.

Nelson, C. and Christ, J. 2012. Predicting laser beam characteristics. Laser Technik Journal, 1, 36-39.

Neppiras, E.A., 1965. Ultrasonic welding of metals. Ultrasonics, 3(3), pp.128-135.

Ng, G.K.L. and Li, L., 2001. The effect of laser peak power and pulse width on the hole geometry repeatability in laser percussion drilling. Optics and Laser Technology, 33(6), pp.393-402.

Norman, S. et al., 2004. Latest development of high-power fiber lasers in SPI. In: Lasers and Applications in Science and Engineering, International Society for Optics and Photonics, pp. 229-237.

O'Brien, R.L., 1991. Welding Handbook Vol. 2, Welding Processes, 8th ed. American Welding Society: Miami, pp.783-812.

Obielodan, J.O. and Stucker, B.E, 2009. Further Exploration of Multi-Material Fabrication Capabilities of Ultrasonic Consolidation Technique. In: 20th Solid Freeform Fabrication Symposium. University of Texas, Austin, 3-5 August 2009, Austin, Texas, USA.

Obielodan, J.O., Ceylan, A. and Marr, L.E., 2010. Multi-material bonding in ultrasonic consolidation. Rapid Prototyping Journal, 16 (3), pp.180-188.

Okada, M., Shin, A., Miyagi, M. and Matsuda, H., 1963. Joint mechanism of ultrasonic welding. Japan Institute of Metals, 4, pp.250-256.

Oliver, W.C. and Pharr, G.M., 1992. An improved technique for determining hardness and elastic modulus using load and displacement sensing indentation experiments. Journal of Materials Research, 7(6), pp.1564-1583.

O'Neill, W., Voglsanger, M., Elboughey, A. and Steen, W.M., 2001. On the selective removal of steel by laser-assisted vortex machining. Proceedings of the Institution of Mechanical Engineers, Part B: Journal of Engineering Manufacture, 215(8), pp.1051-1064.

Pakdil, M., Cam, G., Kocak, M. and Erim, S., 2011. Microstructural and mechanical characterization of laser beam welded AA6056 Al-alloy. Materials Science and Engineering: A, 528(24), pp.7350-7356.

Pan, C.T. and Hocheng, H., 1996. The anisotropic heat-affected zone in the laser grooving of fiber-reinforced composite material. Journal of Materials Processing Technology, 62(1-3), pp.54-60.

Paschotta, R., Nilsson, J., Tropper, A.C. and Hanna, D.C., 1997. Ytterbium-doped fiber amplifiers. IEEE Journal of Quantum Electronics, 33(7), pp.1049-1056.

Paschotta, R., 2007. Laser Sources for Ultrashort Pulses – Oscillators and Amplifiers for Various Applications. Laser Technik Journal, 4(1), pp.49-51.

Paschotta, R., 2008. Encyclopedia of Laser Physics and Technology. Wiley-VCH Verlag GmbH & Co. KGaA: Weinheim.

Paschotta, R., 2009. Fiber amplifiers – part 1. Laser Technik Journal, 6(5), pp.48-49.

Patel, R.S. and Brewster, M.Q., 1990. Effect of oxidation and plum formation on low power Nd:YAG laser metal interaction. Journal of Heat Transfer, Transaction of ASME, 112(1), pp.170-177.

Parent, A., Morin, M. and Lavigne, P., 1992. Propagation of super-Gaussian field distributions. Optical and Quantum Electronics, 24(9), pp.S1071-S1079.

Parlinska, M., Clech, H., Balta, J.A., Michaud, V., Bidaux, J.E., Manson, J.A. and Gotthardt, R., 2001. Adaptive composites with embedded shape memory alloys. Le Journal de Physique IV, 11(PR4), pp.197-204.

Pecholt, B., Vendan, M., Dong, Y. and Molian, P., 2008. Ultrafast laser micromachining of 3C-SiC thin films for MEMS device fabrication. International Journal of Advanced Manufacturing Technology, 39(3-4), pp.239-250.

Pfeiler, W., ed., 2007. Alloy physics : a comprehensive reference. Wiley-VCH: Weinheim.

Phillips, R.L. and Andrews, L.C., 1983. Spot size and divergence for Laguerre Gaussian beams of any order. Applied optics, 1983, 22(5), pp.643-4.

Pierron, N., Sallamand, P. and Mattaï, S., 2007. Study of magnesium and aluminum alloys absorption coefficient during Nd:YAG laser interaction. Applied Surface Science, 253(6), pp.3208-3214.

Pinto, M.A., Cheung, N., Filippini Ierardi, M.C. and Garcia, A., 2003. Microstructural and hardness investigation of an aluminum-copper alloy processed by laser surface melting. Materials Characterization, 50(2-3), pp. 249-253.

Pohlman, R. and Lehfeldt, E., 1966. Influence of Ultrasonic Vibration on Metallic Friction. Ultrasonics, 4(4), pp.178-185.

Polmear, I.J., 2006. Light alloys from traditional alloys to nanocrystals, 4$^{th}$ Edition. Elsevier/Butterworth-Heinemann: Burlington.

Poole, S.B., Payne, D.N. and Fermann, M.E., 1985. Fabrication of low-lossoptical fibres containing rare-earth ions. Electronics Letters, 21(17), 737-738.

Poprawe, R. and Schulz, W., 2003. Development and application of new high-power laser beam sources. Riken Review, pp.3-10.

Poprawe, R., Schulz, W. and Schmitt, R., 2010. Hydrodynamics of material removal by melt expulsion: Perspectives of laser cutting and drilling. Physics Procedia, 5(A), pp.1-18.

Porneala, C. and Willis, D.A., 2006. Observation of nanosecond laser-induced phase explosion in aluminum. Applied Physics Letters, 89(21), pp.211121-1-211121-3.

Powell, J., Ivarson, A. and Magnusson, C., 1993. Laser cutting of steels: a physical and chemical analysis of the particles ejected during cutting. Part II. Journal of Laser Applications, 5(1), pp.25-31.

Powell, J., 1998. CO2 laser cutting. 2nd ed., Springer: Berlin, Heidelberg, New York.

Powell, J., Petring, D., Kumar, R.V., Kaplan, A. and Voisey, K.T., 2009. Laser-oxygen cutting of mild steel: the thermodynamics of the oxidation reaction. Journal of Physics D: Applied Physics, 42(1), pp.015504-015514.

Powell, J. and Kaplan, A.F.H., 2012. Laser cutting technology - a commercial perspective. Laser Technik Journal, 9(2), pp.39-41.

Qi, H., Chen, T., Yao, L. and Zuo, T., 2009. Micro machining of micro channel on the polycarbonate substrate with CO2 laser direct-writing ablation. Optics and Lasers in Engineering, 47(5), pp.594–598.

Quintino, L., Costa, A., Miranda, R., Yapp, D., Kumar, V. and Kong, C.J., 2007. Welding with high power fiber lasers - A preliminary study. Materials and Design, 28(4), pp.1231-1237.

Rajan, T.P.D, Pillai, R.M. and Paj, B.C., 1998. Reinforcement coatings and interfaces in aluminium metal matrix composites. Journal of Materials Science, 33(14), pp.3491-3503.

Ramasamy, S. and Albright, C.E., 2000. $CO_2$ and Nd:YAG laser beam welding of 6111-T4 aluminum alloy for automotive applications. Journal of Laser Applications, 12(3), pp.101-115.

Ready, J. F. and Farson, D. F., 2001. LIA handbook of laser materials processing. Laser Institute of America/Magnolia: Orlando, Florida.

Recarte, V., Pérez-Landazábal, J.I., Ibarra, A., Nób, M.L., and San Juan, J., 2004. High temperature β phase decomposition process in a Cu–Al–Ni shape memory alloy. Materials Science and Engineering: A, 378(1-2), pp.238-242.

Reg, Y., Leitz, K.H. and Schmidt, M., 2011. Influence of processing gas on the ablation quality at ns-laser beam ablation. Physics Procedia, 12, pp.182-187.

Richardson, D.J., Nilsson J. and Clarkson, W.A., 2010. High power fiber lasers: current status and future perspectives [Invited]. Journal of the Optical Society of America, 27(11), pp.B63-B91.

Riveiro, A., Quintero, F., Lusquiños, F., Comesaña, R. and Pou, J., 2010. Parametric investigation of $CO_2$ laser cutting of 2024-T3 alloy. Journal of Materials Processing Technology, 210(9), pp.1138-1152.

Riveiro, A., Quintero, F., Lusquiños, F., Comesaña, R. and Pou, J., 2010b. Influence of assist gas nature on the surfaces obtained by laser cutting of Al–Cu alloys. Surface & Coatings Technology, 205(7), pp.1878-1885.

Riveiro, A., Quintero, F., Lusquiños, F., Comesaña, R., Del Val, J. and Pou, J., 2011. The role of the assist gas nature in laser cutting of aluminum alloys. Physics Procedia, 12, pp.548-554.

Robinson, C.J., Stucker, B., Lopes, A.J., Wicker, R., Palmer, J.A., 2006. Integration of direct-write (DW) and ultrasonic consolidation (UC) technologies to create advanced structures with embedded electrical circuitry. 17th Solid Freeform Fabrication Symposium, Austin, Texas, 14-16 August. Society of Manufacturing Engineers, pp.60-69.

Ryen, O., Nijs, O., Sjölander, E., Holmedal, B., Ekström, H.-E. and Nes, E., 2006. Strengthening Mechanisms in Solid Solution Aluminum Alloys. Metallurgical and Materials Transactions A, 37A(6), pp.1999-2006.

Sánchez-Amaya, J.M., Delgado, T., González-Rovira, L. and Botana, F.J., 2009. Laser welding of aluminium alloys 5083 and 6082 under conduction regime. Applied Surface Science, 255(23), pp.9512-9521.

Sánchez-Amaya, J.M., Boukha, Z., González-Rovira, L., Navas, J., Martín-Calleja, J., and Botana, F.J., 2011. Laser texturization to improve absorption and weld penetration of aluminum alloys. Journal of Laser Applications, 24(1), pp.012002-1-012002-7.

Savage, W.F., Nippes, E.F. and Erickson, J.S., 1976. Solidification mechanisms in fusion welds. Welding Journal, 76, pp.213-s-221-s.

Schaller, R., 2003. Metal matrix composites, a smart choice for high damping materials. Journal of Alloys and Compounds, 355(1), pp.131–135.

Schick, D. E., Hahnlen, R. M., Dehoff, R., Collins, P., Babu, S. S., Dapino, M. J. and Lippold, J. C., 2010. Microstructural Characterization of Bonding Interfaces in Aluminum 3003 Blocks Fabricated by Ultrasonic Additive Manufacturing. Welding Journal, 89(5), pp.105s-115s.

Schick, D., Babu, S.S., Foster, D.R., Dapino, M., Short, M. and Lippold, J.C., 2011. Transient thermal response in ultrasonic additive manufacturing of aluminum 3003. Rapid Prototyping Journal, 17(5), p.369-379.

Schneider, M., Berthe, L., Fabbro, R., Muller, M. and Nivard, M., 2007. Gas investigation for laser drilling. Journal of Laser Applications, 19(3), pp.165-169.

Schneider, M., Berthe, L., Fabbro, L. and Muller, M., 2008. Measurement of laser absorptivity for operating parameters characteristic of laser drilling regime. Journal of Physics D: Applied Physics, 41(15), pp.155502-155507.

Schröder, D., Werner, E., Franke, A., Wagner, L., Bonati, G., Dörfel, F. and Gabler, T., 2010. Roadmap to low cost high brightness diode laser power out of the fiber. In: LASE, International Society for Optics and Photonics, pp.758309-758309.

Semak, V. and Matsunawa, A., 1997. The role of recoil pressure in energy balance during laser materials processing. Journal of Physics D: Applied Physics, 30(18), pp.2541-2552.

Semak, V.V.,Knorovsky, G.A., MacCallum, D.O. and Roach, R.A., 2006. Effect of surface tension on melt pool dynamics during laser pulse interaction. Journal Of Physics D-applied Physics, 39(3), pp.590-595.

Shamsaei, S. and Ghoreishi, M., 2011. The effect of power density, scanning velocity, and pulse frequency on residual stress in laser grooving process. Proceedings of the Institution of Mechanical Engineers, Part B: Journal of Engineering Manufacture, 225(10), pp.1772-1783.

Sheng, P. and Chryssolouris, G., 1995. Theoretical model of laser grooving for composite materials. Journal of Composite Materials, 29(1), pp.96-112.

Shiganov, I.N., Kholopov, A.A. and Ioda, E.I., 2012. Special features of laser welding of aluminium alloys. Welding International, 26(3), pp.231-235.

Shoh, A., 1975. Industrial applications of ultrasound-A review I. high-power ultrasound. IEEE Transactions on Sonics and Ultrasonics, 22(2), pp.60-70.

Siggard, E.J., Madhusoodanan, A.S., Stucker, B. and Eames, B., 2006. Structurally embedded electrical systems using Ultrasonic Consolidation (UC). 17th Solid Freeform Fabrication Symposium, Austin, Texas, 14-16 August.

Siddiq, A. and Ghassemieh, E., 2008. Thermomechanical analyses of ultrasonic welding process using thermal and acoustic softening effects. Mechanics of Materials, 40(12), pp.982-1000.

Siddiq, A. and Ghassemieh, E., 2008. Fibre embedding in aluminium alloy 3003 using ultrasonic consolidation process—thermo-mechanical analyses. The International Journal of Advanced Manufacturing Technology, 54(9), pp.997-1009.

Siddiq, A. and El Sayed, T., 2012. A thermomechanical crystal plasticity constitutive model for ultrasonic consolidation. Computational Materials Science, 51(1), pp.241-252.

Siegman, A.E., 1990. New developments in laser resonators. In: Proc. SPIE 1224, Optical Resonators, pp. 2-14.

Siegman, A.E., 1998. How to (maybe) measure laser beam quality. In: Dowley, M.W., ed., DPSS Lasers: Application and Issues, Vol. 17 of OSA Trends in Optics and Photonics Series (Optical Society of America, Washington, D.C., 1998), pp.184-199.

Silfvast, W.T., 2004. Laser Fundamentals. 2nd Edition, Cambridge University Press: Cambridge, England.

Siu, K.W. and Ngan, A.H.W, 2011. Understanding acoustoplasticity through dislocation dynamics simulations. Philosophical Magazine, 91(34), pp. 4367-4387.

Siu, K.W., Ngan, A.H.W. and Jones, L.P., 2011. New insight on acoustoplasticity - Ultrasonic irradiation enhances subgrain formation during deformation. International Journal of Plasticity, 27(5), pp.788-800.

Smith, R.G., 1972. Optical power handling capacity of low loss optical fibers as determined by stimulated Raman and brillouin scattering. Applied Optics, 11(11), pp.2489-94.

Snitzer, E., 1989. Rare earth fibre lasers. Journal of the Less-Common Metals, 148(1), pp.45-58.

Sohn, H., 2007. Effects of environmental and operational variability on structural health monitoring. Philosophical Transactions: Mathematical, Physical and Engineering Sciences, 365(1851), pp.539-560.

Sojiphan, K., Sriraman, M.R. and Babu, S.S., 2010. Stability of microstructure in Al 3003 builds made by very high power ultrasonic additive manufacturing. In: Proceedings of the 21st International Solid Freeform Fabrication Symposium, Austin, Texas, USA: Wohlers Associates, Inc., pp.362–371.

Solana, P., Kapadia, P., Dowden, J., Rodden, W.S., Kudesia, S.S., Hand, D.P. and Jones, J.D., 2001. Time dependent ablation and liquid ejection processes during the laser drilling of metals. Optics Communications, 191(1), pp.97-112.

Sowerby, R., Uko, D.K. and Tomita, Y., 1979. A review of certain aspects of the Bauschinger effect in metals. Materials Science and Engineering, 41(1), pp.43-58.

Spillman Jr, W.B., Sirkisz, J.S. and Gardiner, P.T., 1996. Smart materials and structures: what are they?. Smart Material Structures, 5(3), pp.247–254.

Sriraman, M.R., Babu, S.S. and Short, M., 2010. Bonding characteristics during very high power ultrasonic additive manufacturing of copper. Scripta Materialia, 62(8), pp.560-563.

Sriraman, M.R., Gonser, M., Fujii, H.T., Babu, S.S. and Bloss, M., 2011. Thermal transients during processing of materials by very high power ultrasonic additive manufacturing. Journal of Materials Processing Technology, 211(10), pp.1650-1657.

Sriraman, M.R., Gonser, M., Foster, D., Fujii, H.T., Babu, S.S. and Bloss, M., 2012. Thermal transients during processing of 3003 Al-H18 multilayer build by very high-power ultrasonic additive manufacturing. Metallurgical and Materials Transactions B, 43(1), pp.133-144.

Stacey, M.H., 1988. Production and characterisation of fibres for metal matrix composites. Materials Science and Technology, 4(3), pp.227-230.

Steen, W. M., 2003a. Laser Material Processing, 3rd ed., Springer: London.

Steen, W.M., 2003b. Laser material processing—an overview. Journal of Optics A: Pure and Applied Optics, 5(4), pp.S3-S7.

Steen, W.M. and Mazumder, J., 2010. Laser Material Processing. 4th ed., Springer: London.

St-Onge, I., Detalle, V. and Sabsabi, M., 2004. Periodic variations of plasma optical emission during repetitive pulsed-laser irradiation of aluminum in ambient air. Applied Physics A, 79(4), pp.1361-1364.

Stournaras, A., Salonitis, K., Stavropoulos, P. and Chryssolouris, G., 2009. Theoretical and experimental investigation of pulsed laser grooving process.

The International Journal of Advanced Manufacturing Technology, 44(1-2), pp.114–124.

Tam, S.C., Williams, R., Yang, L.J., Jana, S., Lim, L.E.N., Lau, M.W.S., 1990. A review of the laser processing of aircraft components. Journal of Materials Processing Technology, 23(2), pp.177-194.

Tamaoki, S., Kaneuchi, M., Baird, B., Paudel N. and Wieland, K.A., 2010. Development of wide operational range fiber laser for processing thin film photovoltaic panels. In: Proc. of ICALEO, Paper M1306, 26-30 September, Anaheim, USA, 29th International Congress on Applications of Lasers & Electro-Optics.

Tani, G., Tomesani, L. and Campana, G., 2003. Prediction of melt geometry in laser cutting. Applied Surface Science, 208, pp.142-147.

Timmermann, A., Meinschien, J., Bruns, P., Burke, C. and Bartoschewski, D., 2008. Next generation high-brightness diode lasers offer new industrial applications. In: Lasers and Applications in Science and Engineering, International Society for Optics and Photonics, pp. 68760U-68760U.

Tünnermann A., Zellmer H., Schöne W., Giesen, A. and Contag, K., 2000. New concepts for diode-pumped Solid-State Lasers. In: Diehl, R., ed. High-Power Diode Lasers. Springer Verlag: Berlin Heidelberg, pp.369-408.

Tünnermann, A., 2005. High power CW fiber lasers – present and future. Laser Technik Journal, 2(2), pp.54-56.

Tünnermann, A., Schreiber, T., Röser, F., Liem, A., Höfer, S., Zellmer, H., Nolte, S., and Limpert, J., 2005. The renaissance and bright future of fiber lasers. Journal of Physics B: Atomic, Molecular and Optical Physics. 38(9), pp.S681-S693.

Tünnermann A., Schreiber T. and Limpert J., 2010. Fiber lasers and amplifiers: an ultrafast performance evolution. Applied Optics, 49(25), pp.F71-F78.

Tunna, L., O'Neill, W., Khan, A. and Sutcliffe, C., 2005. Analysis of laser micro drilled holes through aluminium for micro-manufacturing applications. Optics and Lasers in Engineering, 43(9), pp.937-950.

Tuttle, R.B., 2007. Feasibility study of 316L stainless steel for the ultrasonic consolidation process. Journal of Manufacturing Processes, 9(2), pp.87-93.

Tzou, H.S., Lee, H.-J. and Arnold, S.M., 2004. Smart Materials, Precision Sensors/Actuators, Smart Structures, and Structronic Systems. Mechanics of Advanced Materials and Structures, 11(4-5), pp.367-393.

Ursu, I., Apostol, I., Craciun, D., Dinescu, M., Mihailescu, I.N., Nistor, L. and Konov, V.I., 1984. On the influence of surface condition on air plasma formation near metals irradiated by microsecond TEA $CO_2$ laser pulses. Journal of Physics D: Applied Physics, 17(4), pp.709-720.

Van Humbeeck, J., 2001. Shape memory alloys: a material and a technology. Advanced Engineering Materials, 3(11), pp.837-850.

Venkat, S., Albright, C.E., Ramasamy, S. and Hurley, J.P., 1997. $CO_2$ Laser Beam Welding of Aluminum 5754-O and 6111-T4 AIIoys. Welding Journal, 76, 275s-282s.

Voisey, K.T., Cheng, C.F. and Clyne, T.W., 2000. Quantification of melt ejection phenomena during laser drilling. In: MRS Proceedings, Vol. 617, Cambridge University Press, pp.J5-6.

Voisey, K.T., Kudesia, S.S., Rodden, W.S.O., Hand, D.P., Jones, J.D.C. and Clyne, T.W., 2003. Melt ejection during laser drilling of metals. Materials Science & Engineering A, 356(1), pp.414-424.

Von Allmen, M., 1976. Laser drilling velocity in metals. Journal of Applied Physics, 47(12), pp.5460-5463.

Von Allmen, M., 1987. Laser-beam interactions with materials. Springer Verlag: Berlin, Heidelberg.

Wan, Y.Z., Wang, Y.L., Luo, H.L., Dong, X.H. and Cheng, G.X., 2000. Effects of fiber volume fraction, hot pressing parameters and alloying elements on tensile strength of carbon fiber reinforced copper matrix composite prepared by continuous three-step electrodeposition. Materials Science and Engineering: A, 288(1), pp.26-33.

Watkins, K.G., Liu, Z, McMahon, M., Vilar, R and Ferreira, M.G.S., 1998. Influence of the overlapped area on the corrosion behaviour of laser treated aluminium alloys. Materials Science & Engineering A, 252(2), pp.292-300.

Weare, N.E., Antonevich, J. and Monroe, R., 1960. Fundamental studies of ultrasonic welding. Welding Journal, 39(8), 331s-341s.

Weber, H., 1998. Resonators for high-power solid state lasers: the fight for beam quality. In: Proceedings of SPIE 3267, Laser Resonators, pp.2-13.

Weckman, D.C., Kerr, H.W. and Liu, J.T., 1997. The effects of process variables on pulsed Nd: YAG laser spot welds: Part II. AA 1100 aluminum and comparison to AISI 409 stainless steel. Metallurgical and Materials Transactions B, 28(4), pp.687-700.

Wei, Z.G., Sandstroem, R. and Miyazaki, S., 1998. Review Shape-memory materials and hybrid composites for smart systems: Part I Shape-memory materials. Journal of Materials Science, 33(15), pp.3743-3762.

Wernick, S. and Pinner, R., 1972. The surface treatment and finishing of aluminium and its alloys Vol. 1, 4th ed., Robert Draper LTD: Teddington.

White, D., Solidica, INC. 2003a. Ultrasonic object consolidation. United States Patent 6,519,500 B1.

White, D.R., 2003b. Ultrasonic Consolidation of Aluminium Tooling. Advanced Materials and Processes, 161(1), pp.64-65.

Winsper, C.E., Dawson, G.R., Sansome, D.H., 1970. An introduction to the mechanics of oscillatory metalworking. Metals and Materials, 4(4), pp.158-162.

Wirth, C. et al., 2011. High average power spectral beam combining of four fiber amplifiers to 8.2 kW. Optics Letters, 36(16), pp.3118-20.

Wong, T.T. and Liang, G.Y., 1997. Effect of laser melting treatment on the structure and corrosion behaviour of aluminium and AlSi alloys. Journal of Materials Processing Technology, 63(1), pp.930-934.

Wong, T.T., Liang, G.Y. and Tang, C.Y., 1997. The surface character and substructure of aluminium alloys by laser-melting treatment. Journal of Materials processing technology, 66(1), pp.172-178.

Woods, S., 2009. Understanding materials processing lasers. Laser Technik Journal, 6(5), pp.23-26.

Wu, M.H. and Schetky, L.McD., 2000. Industrial applications for shape memory alloys. In: Russel, S.M. and Pelton A.R., eds. SMST-2000 Proceedings of the International Conference on Shape Memory and Superelastic Technologies, 30 April – 4 May, Pacific Grove, USA, pp.171-182.

Wu, Y., Li, I.L., Fu, L. and Ruan, S.C., 2009. Characterization of microstructures induced in the workpiece of aluminum alloy by excimer laser micromachining. Applied Surface Science, 255(23), pp.9409-9412.

Xiao, Y., Brunet, F., Kanskar, M., Faucher, M., Wetter, A. and Holehouse, N., 2012. 1-kilowatt CW all-fiber laser oscillator pumped with wavelength-beam-combined diode stacks. Optics Express, 20(3), pp.3296-3301.

Xie, J. and Kar, A., 1997. Mathematical modeling of melting during laser materials processing. Journal of Applied Physics, 81, pp.3015-3022.

Xie, J. and Kar, A., 1999. Laser welding of thin sheet steel with surface oxidation. Welding Journal, 78, pp.343s-348s.

Xu, X. and Willis, D.A., 2002. Non-equilibrium phase change in metal induced by nanosecond pulsed laser irradiation. Journal of Heat Transfer, 124(2), pp.293-298.

Yang, Y., Janaki Ram, G.D. and Stucker, B., 2006. Process parameters optimization for ultrasonically consolidated fiber-reinforced metal matrix composites. In: Proceedings of the 17th Solid Freeform Fabrication Symposium, Austin, Texas, USA: Wohlers Associates, Inc., pp.754-769.

Yang, Y., Janaki Ram, G.D. and Stucker, B.E., 2007. An experimental determination of optimum processing parameters for Al/SiC metal matrix composites made using ultrasonic consolidation. Journal of Engineering Materials and Technology, 129(4), pp.538-549.

Yang, Y., 2008. Fabrication of Long-Fiber-Reinforced Metal Matrix Composites Using Ultrasonic Consolidation. Ph. D. Utah State University.

Yang, Y., Janaki Ram, G.D. and Stucker, B.E., 2009. Bond formation and fiber embedment during ultrasonic consolidation. Journal of Materials Processing Technology, 209(10), pp.4915-4924.

Yang, Y., Stucker, B.E. and Janaki Ram, G.D., 2010. Mechanical properties and microstructures of SiC fiber-reinforced metal matrix composites made using ultrasonic consolidation. Journal of Composite Materials, 44(26), pp.3179-3194.

Yilbas, B.S. and Sami, M., 1997. Liquid ejection and possible nucleate boiling mechanisms in relation to the laser drilling process. Journal of Physics D: Applied Physics, 30(14), pp.1996-2005.

Yilbas, B.S. and Abdul Aleem, B.J., 2006. Dross formation during laser cutting process. Journal of Physics D: Applied Physics, 39(7), pp.1451-1461.

Yu-Qing, W. and Ben-Liam, Z., 1998. Effect of a fiber coating on the fabrication of fiber reinforced metal-matrix composites. Journal of Materials Processing Technology, 73(1-3), pp.78-81.

Zenteno, L., 1993. High-power double-clad fiber lasers. Lightwave Technology, Journal of, 11(9), pp.1435-1446.

Zhang, Y. and Faghri, A., 1999. Vaporization, melting and heat conduction in the laser drilling process. International Journal of Heat and Mass Transfer, 42(10), pp.1775-1790.

Zhang, C.S., Deceuster, A. and Li, L., 2009. A Method for Bond Strength Evaluation for Laminated Structures with Application to Ultrasonic Consolidation. Journal of materials engineering and performance, 18(8), pp.1124-1132.

Zhao, H., White, D.R. and DebRoy, T., 1999. Current issues and problems in laser welding of automotive aluminium alloys. International Materials Reviews, 44(6), pp.238-266.

# Appendix A

# Hardness Results

A. Hardness Results for Original Sample

| Indent Number | Hardness [GPa] |
|---|---|
| 1 | 1.054 |
| 2 | 1.005 |
| 3 | 1.104 |
| 4 | 1.076 |
| 5 | 1.008 |
| 6 | 1.016 |
| 7 | 0.928 |
| 8 | 0.834 |
| 9 | 0.782 |
| 10 | 0.891 |
| 11 | 0.834 |
| 12 | 0.811 |

B. Hardness Results for Sample containing Channels

| | Sample Number | | |
|---|---|---|---|
| | **1** | **2** | **3** |
| Indent Number | Hardness [GPa] | | |
| 1 | 0.753 | 1.004 | 0.669 |
| 2 | 1.458 | 1.36 | 1.115 |
| 3 | 1.663 | 1.462 | 1.652 |
| 4 | 0.962 | 0.631 | 0.728 |
| 5 | 1.437 | 1.057 | 1.036 |
| 6 | 1.563 | 1.555 | 1.577 |
| 7 | 1.57 | 1.601 | 1.256 |
| 8 | 1.5 | 1.324 | 1.61 |
| 9 | 1.142 | 1.218 | 0.757 |
| 10 | 1.094 | 1.39 | 0.93 |
| 11 | 0.756 | 1.673 | 1.747 |
| 12 | 0.764 | 0.811 | 1.562 |
| 13 | 0.947 | 0.839 | 1.314 |
| 14 | 1.337 | 1.085 | 0.717 |
| 15 | 1.454 | 1.657 | 0.731 |
| 16 | 1.385 | 1.614 | 1.488 |

C. Hardness Results for containing channels (continued)

| | | | |
|---|---|---|---|
| 17 | 0.82 | 1.439 | 1.472 |
| 18 | 0.826 | 1.1 | 1.548 |
| 19 | 0.789 | 0.705 | 0.967 |
| 20 | 0.662 | 0.738 | 0.862 |
| 21 | 0.774 | 0.807 | 0.827 |
| 22 | 1.321 | 1.15 | 1.359 |
| 23 | 0.758 | 1.464 | 0.78 |
| 24 | 0.72 | 0.917 | 0.758 |
| 25 | 0.841 | 0.908 | 0.754 |

D. Hardness Results for Sample produced with Air and Fibres

| | Sample Number | | |
|---|---|---|---|
| | 1 | 2 | 3 |
| Indent Number | Hardness [GPa] | | |
| 1 | 0.948 | 0.781 | 0.935 |
| 2 | 1.321 | 0.627 | 1.483 |
| 3 | 1.664 | 1.623 | 1.793 |
| 4 | 1.353 | 1.499 | 1.398 |
| 5 | 0.671 | 0.738 | 0.981 |
| 6 | 1.54 | 0.73 | 1.372 |
| 7 | 1.422 | 1.719 | 1.643 |
| 8 | 1.343 | 1.28 | 1.687 |
| 9 | 1.27 | 1.427 | 1.529 |
| 10 | 0.685 | 0.892 | 0.73 |
| 11 | 1.151 | 1.603 | 1.74 |
| 12 | 0.983 | 0.836 | 1.522 |
| 13 | 1.557 | 1.32 | 1.521 |
| 14 | 1.225 | 1.355 | 1.6 |
| 15 | 0.878 | 1.354 | 1.4776 |
| 16 | 0.832 | 1.38 | 1 |
| 17 | 1.023 | 0.933 | 0.931 |
| 18 | 1.8 | 1.872 | 1.507 |
| 19 | 1.9 | 0.789 | 1.481 |
| 20 | 1.688 | 1.64 | 1.385 |
| 21 | 1.458 | 1.348 | 0.852 |
| 22 | 0.766 | 1.064 | 0.87 |
| 23 | 0.73 | 0.853 | 1.231 |
| 24 | 0.842 | 0.757 | 0.749 |
| 25 | 0.775 | 0.828 | 0.827 |

E. Hardness Results for Samples produced with Nitrogen and Fibres

| | Sample Number | | |
|---|---|---|---|
| | **1** | **2** | **3** |
| Indent Number | Hardness [GPa] | | |
| 1 | 0.661 | 0.754 | 1.03 |
| 2 | 1.021 | 1.012 | 1.31 |
| 3 | 1.292 | 1.357 | 0.701 |
| 4 | 0.724 | 0.676 | 0.723 |
| 5 | 0.674 | 0.754 | 1.237 |
| 6 | 1.061 | 1.275 | 1.254 |
| 7 | 1.214 | 1.26 | 0.743 |
| 8 | 0.715 | 0.787 | 0.734 |
| 9 | 0.756 | 0.715 | 1.267 |
| 10 | 1.32 | 1.271 | 1.43 |
| 11 | 1.162 | 1.286 | 0.81 |
| 12 | 0.588 | 0.88 | 0.72 |
| 13 | 0.656 | 0.76 | 1.162 |
| 14 | 1.07 | 1.141 | 1.189 |
| 15 | 0.679 | 1.256 | 0.76 |
| 16 | 0.67 | 0.848 | 1.189 |
| 17 | 1.17 | 1.216 | 0.734 |
| 18 | 0.738 | 0.731 | 0.894 |
| 19 | 0.974 | 0.887 | 1.03 |